THÈSE

En vue de l'obtention du

DOCTORAT DE L'UNIVERSITÉ DE TOULOUSE

Délivré par :

Institut National Polytechnique de Toulouse (Toulouse INP)

Discipline ou spécialité :

Dynamique des fluides

Présentée et soutenue par :

Mme ELENA-ROXANA POPESCU

le mardi 2 juillet 2019

Titre :

Numerical simulation of the interaction between an external flow, laminar or turbulent, and liquid/vapor phase change

---

Ecole doctorale :

Mécanique, Energétique, Génie civil, Procédés (MEGeP)

Unité de recherche :

Institut de Mécanique des Fluides de Toulouse (IMFT)

Directeur(s) de Thèse :

MME CATHERINE COLIN

M. SÉBASTIEN TANGUY

Rapporteurs :

M. FABRICE LEMOINE, UNIVERSITÉ LORRAINE

M. FRANÇOIS XAVIER DEMOULIN, UNIVERSITE DE ROUEN

Membre(s) du jury :

M. DOMINIQUE LEGENDRE, TOULOUSE INP, Président

M. BENJAMIN LEGRAND, CENTRE NATIONAL D'ETUDES SPATIALES CNES, Invité

M. FABRICE MATHEY, AIR LIQUIDE, Invité

Mme CATHERINE COLIN, TOULOUSE INP, Membre

M. SÉBASTIEN TANGUY, UNIVERSITE TOULOUSE 3, Membre

M. YOHEI SATO, INSTITUT PAUL SCHERRER, Membre

Résumé

Dans le réservoir d'un satellite, le carburant cryogénique peut se transformer en vapeur à cause de la présence d'un gradient de température à la paroi, induit par le rayonnement solaire ou la diffusion thermique résiduelle des moteurs du lanceur. La quantité de vapeur transformée peut fortement augmenter la pression à l'intérieur du réservoir. En raison d'une connaissance incomplète des ces phénomènes, aujourd'hui, les opérations faites pour régulariser la pression interne entraînent une perte de carburant. Il est donc très important d'étudier le changement de phase liquide/vapeur et les processus physiques mis en jeu au niveau de l'interface. C'est dans ce contexte que se situe cette thèse, dont l'objectif est d'obtenir une meilleure compréhension des phénomènes susmentionnés au moyen de la Simulation Numérique Directe (DNS). Le travail est divisé en trois parties : l'interaction entre un liquide à température de saturation et un écoulement externe de vapeur sous-refroidie ou surchauffée, en régime laminaire et turbulent, et l'interaction entre des mouvements de convection naturelle et le changement de phase liquide/vapeur.

Tout d'abord, le régime laminaire est étudié. Dans ce cadre, une étude paramétrique est menée dont l'objectif est de trouver des lois de comportements pour le transfert thermique et le coefficient de frottement à l'interface entre un liquide statique à température de saturation et un écoulement de couche limite de vapeur. Nous étudions à la fois la vaporisation et la condensation.

La seconde partie de cette thèse est dédiée à la simulation numérique d'un écoulement de couche limite turbulente d'une vapeur surchauffée en interaction avec un champ de vitesse induit par de la vaporisation. Pour cela, un injecteur de turbulence est implémenté dans le code et validé pour la configuration de l'évolution spatiale d'une couche limite turbulente sur une plaque plane avec transfert thermique. Ensuite, une étude sur l'influence du champ de vitesse induit par la vaporisation sur le nombre de Nusselt, le coefficient de frottement, le nombre de Stanton et les différentes quantités turbulentes est réalisée.

Enfin, nous menons une étude numérique préliminaire sur une configuration décrivant l'écoulement convectif dans un réservoir cryogénique. Un nouveau solveur est implémenté dans le code utilisé afin de prendre en compte les variations de la densité. Des résultats préliminaires sont obtenus sur l'influence du nombre de Grashof sur le flux thermique à l'interface liquide/vapeur.

Mots-clés : vaporisation, condensation, nombre de Nusselt, couche limite turbulente, convection naturelle

Abstract

In a launcher tank, the cryogenic fuel can suffer a liquid/vapor phase change due to a thermal gradient induced by solar radiation or by engines residual thermal diffusion. The quantity of vapor released by the phase change process can highly increase the internal pressure. Due to a poor knowledge of these phenomena, at present, the operations led to regulate the internal pressure induce fuel loss. It is therefore of great importance to investigate the liquid/vapor phase and the physical processes taking place at the interface. This is the context of the present thesis, that takes place in an effort to extract better understanding of the above underlined phenomena by means of Direct Numerical Simulation (DNS). The work is split into three studies : the interaction between a liquid pool at saturation and an external flow of subcooled or superheated vapor, both in laminar and turbulent regime flows, and the interaction between natural convection mouvements and liquid/vapor phase change.

Firstly, the laminar regime flow is investigated. In this framework, a parametric study is conducted with the objective of finding behaviour laws for the heat transfer and the friction coefficient at the interface between a static liquid pool at saturation temperature and a laminar boundary layer flow of vapor. Both vaporization and condensation are studied.

The second project was on the numerical simulation of a turbulent boundary layer flow of superheated vapor interacting with the velocity field induced by vaporization. To this extent, a turbulent fluctuations injector is implemented and validated for the spatial development of a boundary layer flow over a flat plate with heat transfer. A study on the influence of the velocity field induced by vaporization on the Nusselt number, the friction coefficient, the Stanton number and the turbulent quantities is conducted.

Finally, we lead a preliminary numerical study on a configuration describing the interaction between natural convection flow and liquid/vapor phase change in a cryogenic tank. A new solver is implemented in the in house code to account for the density variations in the liquid. Preliminary results are obtained on the influence of the Grashof number on the thermal flux at the liquid/vapor interface.

Keywords : vaporization, condensation, Nusselt number, turbulent boundary layer, natural convection

Acknowledgements

I remember some years ago hearing a PhD student complaining that she lacked time to finish her thesis and that it was too hard to manage the corresponding pressure and stress. At that time, I was thinking: "I am sure she did not organize her work as she should have. When I will be a PhD student, I will do better and do not have this kind of problem." And now, after 3 years and a half, I have finally defended my thesis and I can loudly say that I was wrong. The evolution of a thesis depends on so many factors, and our will to do our best is only a tiny part of all of these. Inter alia, the work and personal environment have a major role, and therefore, in what follows, I will try to acknowledge and thank the ones involved directly or indirectly in the conduct of this thesis.

I will begin by acknowledging my supervisors, Catherine Colin and Sébastien Tanguy. First, I would like to thank you, Catherine, you always took the time to read my presentations and reports and give me your feedback. You were often available and listening to my needs and your speech at the end of my defense particularly touched me. Sébastien thank you for allowing me to work in the world of numerical simulation. You believed in our first paper, even when I was doubting its value. If at the beginning of this thesis I lacked initiative, working with you allowed me to become independent and acquire in this way vast scientific knowledge, and I thank you for that.

I would want to acknowledge and thank CNES and AirLiquide for founding this thesis. Additionally, I acknowledge CINES and IDRIS for the allocated compute hours allowing me to lead massive parallel computations.

I want to acknowledge the DIVA team and particularly Romain and Guillaume, your help was precious. You always took the time to listen and discuss the problems I was encountering with DIVA code, thank you to both of you.

I want to thank the entire staff and colleagues from IMFT. First, thank you Greg, you allowed me to get used to the harmless jokes on the Romanians. You was always there, listening to me complaining of everything, giving me advices, sharing your knowledge, and I will not forgot all of your compliments on my clothes, merci beaucoup Greg! Next, I want to thank all of my colleagues that, amongst other things, initiated me to trail. Thank you Paul, Flo, Seb, Alexis, Guillaume and Tawfik (and I hope I forgot no one), you helped me move out several times and each time without having an elevator, that was so cool of you guys!

During this thesis I have met and got close to so many. Particularly, Tawfik and Marc, thank you for our small coffee breaks that were always comforting. Loïc, as you are always saying, it is difficult to find someone we are able to speak with so much honesty as we did and I thank you for that. I want to thank Lucia for all of her advices at the beginning of my thesis. Annagrazia, my co-office, thank you for the pep talks and our hilarious discussions. Gianluca, my thoughts go to you too. Nadia, thank you for being there any time I was in need.

There are some people that were there from the beginning, meaning my arrival in France and I think that without them I would certainly not be here. I will begin by thanking Mr. Boisson for his help and precious guidance. Next, Bastien, you and your family took me as a family member

and helped me as I was one of you, and I thank you so much for that.

And now, I will acknowledge and thank Rafael, the one who went along with me during this last hard year of thesis. You were always there to listen to my problems and my complains. You encouraged me to be stronger and to better manage the pressure. I know it was not easy to tolerate all my moods and I thank you so much for that. And finally, I would want to thank my parents, and particularly my mother to whom I owe everything and I dedicate this work. Tu imi dai curaj si incredere pentru a continua, m-ai invatat sa fiu puternica, multumesc mult mami!

Contents

Introduction

Industrial context

The interaction between liquid/vapor phase change and an external flow plays an important role in various fields, such as in combustion applications, weather forecasting, heat exchangers or climate modeling. The study of such a phenomena represents, first of all, a theoretical and a scientific challenge. In addition, having a better understanding of the heat and mass transfers in such a configuration could allow a performance enhancement of numerous industrial devices.

In particular, the space sector is also concerned by this field in the case of a space launcher, and this, at different steps of the mission: launching phase, ballistic flight, orbit insertion, etc.

When launching a space rocket, a part of the embedded liquid propellant (ergol) is stored in cryogenic tanks for later employement, during space manoeuvres. However, the tanks are heated through solar radiation or engines thermal dissipation. Thus, the temperature of the tank wall is highly increased. The thermal gradient between the tank wall and the contained ergol generates liquid/vapor phase change. The presence of vapor increases the internal pressure of the tank, which, in the context of the tank pressurization, leads to fuel loss. Hence, a better understanding of the liquid/vapor phase change and its interaction with the induced flows in a cryogenic tank could allow an optimisation of the embarked liquid propellant.

It is in this industrial context that the present thesis is placed. The tool used to tackle this subject is direct numerical simulation (DNS). The DNS of the entire cryogenic tank, together with all the involved physical phenomena, is, of course, out of reach, for computational costs and complexity reasons. Industrial codes are already employed for the simulation of a cryogenic tank. However, the lack of a good resolution of the interface between liquid and vapor phases prevents an accurate computation of the mass and heat transfers induced by the phase change. The intended concept would be to determine, by means of DNS, behaviour laws for the thermal and mass transfers at the liquid/vapor interface, laws that will further be used to model the interface in the industrial codes.

The main objective of this thesis has therefore been to simulate configurations describing the interaction between the liquid/vapor phase change and the internal cryogenic tank flows, with the focus on the interface thermal transfer.

Numerical approach

The choice of the computational configuration was not straightforward. Depending on the various phases of the flight mission, the involved physical phenomena differ. These changes are driven, inter alia, by the presence or the absence of gravitational accelerations. These two configurations are described in what follows, begining with the microgravity regime.

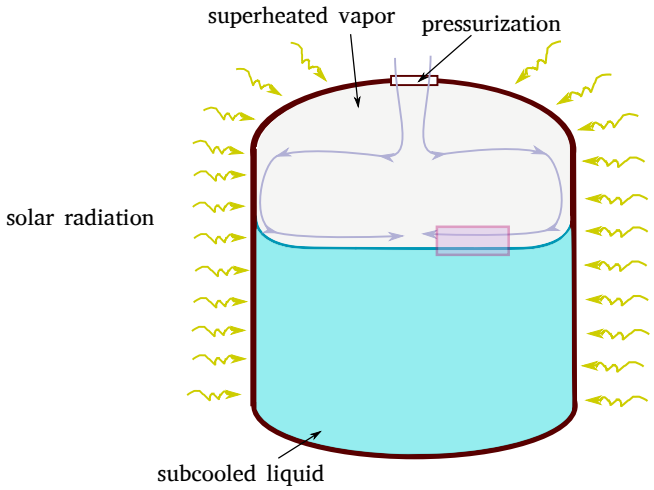

Figure 1: Schematics of the cryogenic tank subjected to microgravity, during the presurrization of the subcooled liquid by a superheated vapor. The tank wall is heated through solar radiation. The red rectangle represents the zone where the DNS will be used to characterize the vapor flow and the phase change at the liquid/vapor interface.

In space, the ergol is drained from the cryogenic tank for different manoeuvres, such as the orbit insertion or change of position. In order to maintain a certain internal pressure, the subcooled liquid is pressurized by a superheated vapor or a non-condensable gas. Considering the absence of the gravitational field, this procedure also allows to pack the liquid propellant. A schematic of this configuration is showed in figure 1. The approach employed for the simulation of such a configuration in microgravity has been to consider only a narrow zone at the liquid/vapor interface where the vapor flow can be modeled by a boundary layer flow, schematized by a red rectangle in figure 1. The liquid phase is considered to be static and at saturation temperature while a thermal gradient is imposed in the vapor phase. Both laminar and turbulent regimes are investigated. The influence of the liquid/vapor phase change on the interface thermal flux evolution and on the development of the laminar or turbulent boundary layer are studied.

On the other hand, during the launching phase, the tank is subjected to high gravitational accelerations, while heated through engines thermal diffusion. Residual gravitational accelerations can also be generated in space, when the engines are reignited for the orbit insertion of the satellite. Figure 2 illustrates a schematic of the tank under these conditions. The gravitational field induces a thermal stratification in the liquid, while phase change occurs at the liquid/vapor interface. Convective motions are generated in the liquid phase, that will interact with the liquid/vapor phase change. Note that, for this industrial application, the regime is turbulent, with values of the Grashof number of order $\sim 10^{10}$. The DNS of turbulent natural convection is complex and have a high computational cost. For these reasons, the numerical approach is to consider a 2D laminar configuration of a two phase flow containing a subcooled liquid and a vapor flow initially at saturation temperature. The solar radiation heat flux is modeled by imposing a wall conduction heat flux. Laminar natural convection flow, defined by a Grashof number of $\sim 10^6$, is induced in the liquid. Even if, in terms of flow regime, the studied configuration is different from the industrial configuration, this can be seen as a first step before pursuing with more precise studies. Additionally, the preliminary results obtained with the 2D configuration will allow a better understanding of the physical phenomena involved when natural convection mouvements interact with liquid/vapor phase change.

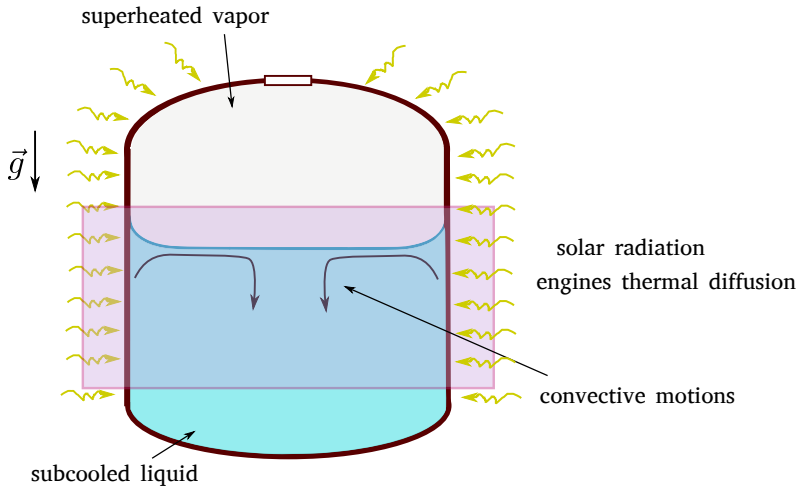

Figure 2: Schematics of the cryogenic tank subjected to gravitational accelerations, containing a subcooled liquid pressurized by a superheated vapor. The tank wall is heated through solar radiation or/and engines thermal diffusion. The red rectangle represents the numerical configuration studied in the present thesis.

Before describing the outline of the thesis, it is important to stress that, often, the studied configurations, both by numerical or experimental approaches, differ from the very complex industrial problems. However, this does not diminish, in any way, their scientific and theoretical importance. Moreover, the interlock of decoupled physical phenomena or of simplistic configurations, allows in the end the comprenhension of more complex industrial processus.

Outline of the Thesis

The work carried out during the course of this thesis is presented as follows.

Chapter 1 is dedicated to the description of the in house code, DIVA, used for the direct numerical simulation of the above described configurations. The numerical methods implemented to solve the physical model translating the behaviour of two-phase flows with phase change are presented: the Level-Set method for the interface capture, the projection method for the Navier-Stokes equations, and the Ghost Fluid Thermal Solver for Boiling used to solve the energy conservation equation.

In chapter 2, we present a numerical study to characterize the interaction between a superheated or subcooled external laminar vapor flow shearing a static and plane liquid pool at saturation temperature. Our purpose was to find, for this configuration, correlations on the Nusselt number accounting for the modification of the local thermal gradient on the interface due to the vaporization or condensation induced flow. As the local structure of the flow is also modified in the vicinity of the liquid-vapor interface, our study includes an analysis on the interfacial viscous friction when phase change occurs.

In practical applications, most flows which occur are turbulent. Therefore, the subsequent topic of our work concerns the interaction between a turbulent boundary layer flow and the velocity field induced by liquid/vapor phase change. To this extent, the spatial evolution of a turbulent boundary layer flow on a flat plate has first to be simulated. This work is described in chapter 3. After a thorough overview of the existing numerical methods for the generation of turbulent fluctuations, the chosen method is described and validated. Next, the results obtained are presented

and discussed. A particular attention is also paid to the computational constraints related to the simulation of turbulent boundary layer flows.

In chapter 4, we investigate the interaction between a spatially developing turbulent boundary layer flow and a normal velocity field induced by liquid/vapor phase change. This is first conducted qualitatively, by analysing the normal velocity field, the vorticity magnitude field and the isosurfaces of the Q criterion. Next, a study on the influence of the phase change onto the turbulent quantities is presented. Several Jakob numbers are studied and a preliminary physical analysis is proposed for the obtained profiles. Additionally, we take interest on the impact of the phase change onto the Nusselt number evolution. This is given in the continuity of the work on the laminar regime where correlations on the Nusselt number are proposed.

In chapter 5, the focus is on the liquid phase where natural convection motions develop and interact with the liquid/vapor phase change. A 2D computational configuration is considered, where the density variations in the liquid phase are treated using the low-Mach approximation while the vapor phase is incompressible. The vapor is initially at saturation temperature and the liquid is subcooled. Wall conduction is considered for the boundary conditions on the vertical walls. A natural convection flow is induced in the liquid and its interaction with the liquid/vapor phase change is investigated. Different values of the Grashof number are studied and a discussion on its influence on the thermal flux is given. The study is in progress and opens to many perspectives.

Finally, the work ends with conclusions together with recommendations for future work.

Chapter 1

Numerical methods

Contents

The numerical study of the interaction between an external flow and the liquid/vapor phase change has been conducted using the in house code, DIVA. The code DIVA, that states for Interfacial Dynamics for Atomization and Vaporization, allows for direct numerical simulation of two-phase flows with phase change. In this chapter, this numerical tool is described.

1.1 Introduction

In this chapter we try to provide a comprehensive overview of two-phase flows numerical simulation. To this extent, the first section tackles the three major aspects of two-phase flows simulation, i.e. the interface localization, the formalism to solve the corresponding physical equations and the treatment of the interface discontinuities. In the second part of this chapter, the code DIVA is described. First, the methods for interface localization are described, then the physical equations translating the behaviour of two-phase flows with phase change are presented. Finally, the numerical methods implemented to solve this physical model are expounded: the Level-Set method for the interface capture, the projection method for the Navier-Stokes equations, and the Ghost Fluid Thermal Solver for Boiling used to solve the energy conservation equation.

1.2 General background on two-phase flows numerical simulation

Two-phase flows simulations entail the use of a numerical model allowing above all to locate the interface between the two phases. Additionally, algorithms for solving the physical equations as well as treating the discontinuities across the interface are needed. A general background on these aspects is given in what follows.

1.2.1 Interface localization

The notion of interface is inherent in the context of two-phase flows. A large amount of literature relevant to interfaces exists. For example, in the classical work of Germain [25], the interface separating two immiscible fluids is defined as a geometric surface at which a discontinuity in properties occurs. Jump conditions through the interface are derived from the classical balance laws for mass, momentum and energy.

To numerically simulate two-phase flows, each phase distribution as well as the interface position have to be known at all times. Two approaches describing the time evolution of an interface can be distinguished: the Lagrangian or Interface-Tracking methods and the Eulerian or Interface-Capturing methods.

The Lagrangian approach implies the use of markers or particles without mass whereas in the Eulerian approach a scalar field defining the presence of a fluid or of the interface is used. Both the markers and the scalar field are convected by the local velocity field throughout the entire domain. In what follows, a survey of the existing methods is given.

1.2.1.1 Lagrangian methods

Numerous Lagrangian methods exist. One of the first is the Mark and Cell method (MAC) proposed by Harlow and Welch [30] where lagrangian markers are placed only in the region of one of the phases. The major drawback of this method is the large number of markers needed to correctly model the fluids distribution (figure 1.1a). To adress this, Daly [17] proposes a slighthly different method where markers are dispersed only on the interface. Nevertheless, to obtain an accurate position of the interface, the distance between two consecutive points has to remain small enough and regular. This leads us to the Front Tracking methods, introduced by Glimm *et al.* [14, 28]. The markers are regularly distributed along the interface, forming segments in 2D and triangles in 3D (figure 1.1b). The most common version of this method was proposed by Unverdi and

Tryggvason [105]. This type of approach is not the most appropriate to the simulation of the interaction between several interfaces, in the case of rupture or coalescence.

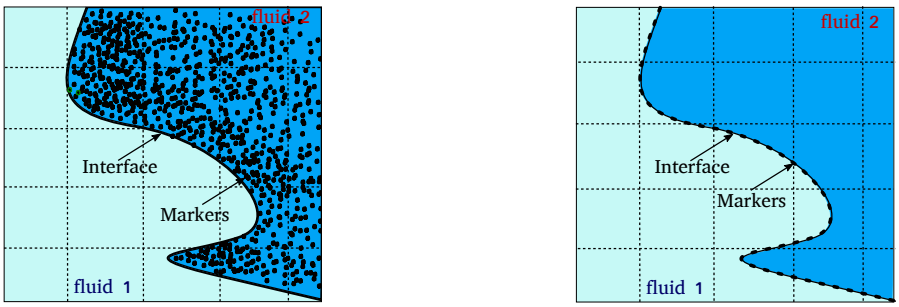

(a) MAC (b) Front Tracking

Figure 1.1: Illustration of Lagrangian methods.

The Boundary Fitted methods, another Lagrangian approach, involves that the mesh grid is adapted to the interface shape. This allows modeling the interface jump conditions as classical boundary conditions. Since the mesh grid is aligned with the interface, the accuracy is greatly improved. Nevertheless, the main drawback is that the mesh grid is evolving with the interface and has to be reconstructed at each time step. The computation time is therefore greatly increased. This type of approach has particularly be used for bubble rising simulations [18, 89].

1.2.1.2 Eulerian methods

The Eulerian methods are based on the definition of a particular scalar field within the global fixed mesh grid. This scalar field is advected by the local velocity at each time iteration. It allows in this way to compute the localization of the two fluids as well as the interface position. The Eulerian methods can be divided into two major categories: the Volume of Fluid (VOF) and the Level-Set methods.

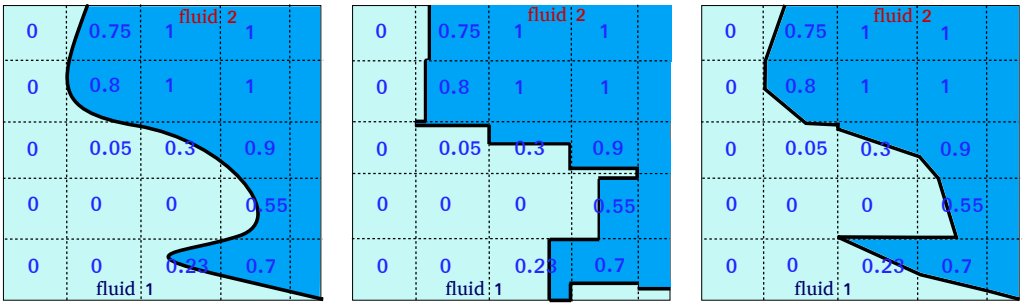

(a) VOF (b) VOF SLIC (c) VOF SPLIC

Figure 1.2: Different VOF methods: initial form and C values (a), interface reconstruction with the SLIC (b) and SPLIC (c) algorithms.

The VOF method, proposed by Hirt and Nichols [33], uses a scalar function C characterizing the volume fraction of one of the two fluids present in the cell grid (figure 1.2a). Thus, if the fluid occupies the entire cell, $C = 1$ whereas if the cell is filled only with the second fluid, $C = 0$. It

follows naturally that the cell crossed by the interface contains the two fluids and $0 < C < 1$. The scalar field C is advected by the local velocity field $\mathbf{u}$,

$$\frac{\partial C}{\partial t} + \mathbf{u} \cdot \nabla C = 0. \tag{1.1}$$

The scalar field C is constant in each fluid region and varies greatly across the interface. Consequently, a very accurate discretization is needed for the computation of the convective term from equation (1.1). The advantage of the VOF method is its mass conservation in time. Nonetheless, the computation of the geometric properties, such as the interface curvature and the normal vector, is not straightforward. This is caused by the fact that the precise location of the interface is unknown. Indeed, a reconstruction algorithm is necessary at each time step in order to reconstitute the interface using the discrete values of the function C. Noh and Woodward [68] introduced the first reconstruction algorithm, the SLIC (Simple Line Interface Calculation) where the interface is formed by line segments aligned with the mesh principal directions (figure 1.2b). An improvement of the SLIC method is proposed by Youngs [110] where the interface is now approximated by a line segment non-aligned with the mesh (figure 1.2c). This method, named PLIC (Piecewise Line Interface Calculation) uses the values of the field C at the grid neighbouring points to calculate the line segment orientation in the corresponding cell. Since the introduction of the VOF methods, numerous modifications have been done in order to improve the accuracy of the temporal evolution of the interface, as well as the calculation of its geometric properties (see [7, 9, 29, 51, 78, 80, 85, 91]).

The second category of Eulerian approaches is represented by the Level-Set method, introduced by Osher and Sethian [69]. A scalar field ϕ corresponding to the signed distance to the interface is defined in the entire computational domain Ω. The latter is decomposed into two regions Ω^+ and Ω^-, representatives of the two respective fluids,

$$\Omega^+ = \{\mathbf{x} \in \Omega \,|\, \phi(\mathbf{x}) > 0\}, \tag{1.2}$$

$$\Omega^- = \{\mathbf{x} \in \Omega \,|\, \phi(\mathbf{x}) < 0\}, \tag{1.3}$$

whereas the interface is characterised by the level 0 of the ϕ function

$$\Gamma = \{\mathbf{x} \in \Omega \,|\, \phi(\mathbf{x}) = 0\}. \tag{1.4}$$

It is therefore possible to define, by extension, a level lines ensemble Γ_k in the computational domain Ω, located at a distance $|d_k|$ from the interface (figure 1.3),

$$\Gamma_k = \{\mathbf{x} \in \Omega \,|\, \phi(\mathbf{x}) = |d_k|\}. \tag{1.5}$$

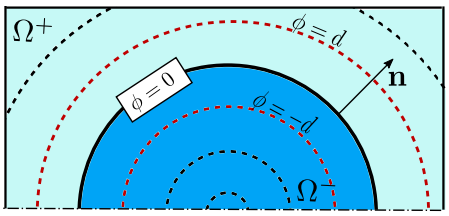

Figure 1.3: Level set function corresponding to a circular interface.

As a result, the computation of the physical properties of each fluid, such as the density ρ and the dynamic viscosity μ, is direct.

The temporal evolution of the interface is done by the use of the following advection equation,

$$\frac{\partial \phi}{\partial t} + \mathbf{u} \cdot \nabla \phi = 0. \tag{1.6}$$

This type of equation is known to develop discontinuous solutions even if the initial field is continuous. Hence, a robust scheme has to be employed to deal with possible singularities.

Compared to others Interface-Capturing methods, the Level-Set method allows a simple and accurate computation of the interface geometric properties. The normal vector to the interface is calculated with

$$\mathbf{n} = \frac{\nabla \phi}{||\nabla \phi||}, \tag{1.7}$$

and the interface curvature can be deduced with

$$\kappa = \nabla \cdot \mathbf{n} = \nabla \cdot \left(\frac{\nabla \phi}{||\nabla \phi||} \right). \tag{1.8}$$

On the other hand, this method has two major drawbacks. Firstly, the existence of high shearing or streching zones in the velocity field can considerably spread or tighten the level lines, degrading therefore the geometric properties of the Level Set function. Indeed, the advection equation (1.6) is solved for all the level lignes Γ_k, whereas the displacement speed is known only for the interface, since their definition is purely mathematical. Sussman *et al.* [99] proposed to solve a redistancing equation which forces ϕ to be a signed distance to the interface for every time step, without changing the zero level curve location. To this extent, the following equation

$$\frac{\partial d}{\partial \tau} = \text{sign}(\phi) \left(1 - |\nabla d|\right) \tag{1.9}$$

is iterated for a few fictitious time steps τ. The interface position is conserved by imposing the initial condition $d\left(\mathbf{x}, t, \tau = 0\right) = \phi(\mathbf{x}, t)$.

Secondly, the numerical dissipation of the advection equation (1.6) discretization can cause mass losses. Additionally, during the redistancing step (1.9), the interface position can be slightly changed and induces a gain or loss in mass. Nevertheless, the interface perturbation remains low if the mesh grid is refined enough. As for the numerical dissipation of the advection equation, this can be adressed, inter alia, by the use of a more accurate discretization scheme.

1.2.2 Modeling two-phase flows

In this section, we present the physical equations and the numerical approach used in the configuration of two-phase flows. All thermodynamic properties are considered to be constant. The specific case of variable density will be discussed later.

1.2.2.1 Physical equations

An incompressible one-phase fluid flow, in a domain Ω, is described by the Navier-Stokes equations,

$$\nabla \cdot \mathbf{u} = 0, \tag{1.10}$$

$$\rho \left(\frac{\partial \mathbf{u}}{\partial t} + \left(\mathbf{u} \cdot \nabla \right) \mathbf{u} \right) = -\nabla p + \nabla \cdot \left(2\mu \bar{\bar{\mathbf{D}}} \right) + \rho \mathbf{g}, \tag{1.11}$$

with t the time, ρ and μ the fluid density and dynamic viscosity, respectively, $\mathbf{u} = (u, v, w)$ the velocity field, p the pressure field, $\mathbf{g}$ the gravitational acceleration and $\bar{\bar{\mathbf{D}}}$ the strain tensor defined by

$$\bar{\bar{\mathbf{D}}} = \frac{\nabla \mathbf{u} + \nabla^T \mathbf{u}}{2}. \tag{1.12}$$

The thermal field is described by a simplified energy conservation equation, formulated using the enthalpy primitive variable

$$\rho C_p \left(\frac{\partial T}{\partial t} + (\mathbf{u} \cdot \nabla) \mathbf{T} \right) = \nabla \cdot (k \nabla T), \tag{1.13}$$

where T is the thermal field, C_p is the specific heat at constant pressure and k is the thermal conductivity.

We now consider that the domain Ω contains two regions Ω^+ and Ω^-, each corresponding to a different phase. As a result, the two fluids physical properties are employed respective to each fluid as: $(\rho^+, \mu^+, k^+, C_p^+)$ and $(\rho^-, \mu^-, k^-, C_p^-)$.

The liquid and the vapor phases are separated by an interface Γ, across which phase change can occur (i.e. the liquid vaporizes into vapor or the vapor condenses into the liquid). Across the interface, the continuity of the mass flux, the momentum and enthalpy balances have to be satisfied.

The interface mass flux, $\dot{m}$ is obtained by applying the mass conservation (1.10) across the interface,

$$\dot{m} = \rho_l (\mathbf{V}_l - \mathbf{V}_\Gamma) \cdot \mathbf{n} = \rho_v (\mathbf{V}_v - \mathbf{V}_\Gamma) \cdot \mathbf{n}, \tag{1.14}$$

where the interface velocity is denoted by $\mathbf{V}_\Gamma$ and $\mathbf{n}$ is the local unit vector pointing towards the liquid phase. The subscripts l and v are used to refer to the liquid and vapor phases, respectively. The jump on the velocity field across the interface can therefore be written as:

$$[\mathbf{V}]_\Gamma = \dot{m} \left[\frac{1}{\rho} \right]_\Gamma \mathbf{n}, \tag{1.15}$$

where the operator $[\cdot]_\Gamma$ accounts for the jump across the interface and it is defined by: $[f]_\Gamma = f_v - f_l$.

The momentum balance at the interface is imposed by integrating the momentum equation (1.11) across the interface and by including the effects of the surface tension,

$$\left[p - 2\mu \frac{\partial V_n}{\partial n} + \rho (\mathbf{V} \cdot \mathbf{n} - \mathbf{V}_\Gamma \cdot \mathbf{n})^2 \right]_\Gamma = \sigma \kappa, \tag{1.16}$$

which, by using equation (1.15), is rewritten as

$$[p]_\Gamma = \sigma \kappa + 2 \left[\mu \frac{\partial V_n}{\partial n} \right]_\Gamma - \dot{m}^2 \left[\frac{1}{\rho} \right]_\Gamma, \tag{1.17}$$

where σ is the surface tension, κ is the interface curvature and $\frac{\partial V_n}{\partial n}$ is the normal derivative of the normal velocity component. The first term of the right hand side of this equation is the capillary pressure from the Laplace-Young law, the second term accounts for the discontinuity of the normal viscous stress, and the last term is usually referred as the recoil pressure.

According to the second law of thermodynamics and assuming that the local equilibrium hypothesis is still valid, the interface temperature is imposed to be the saturation temperature $T_l = T_v = T_{sat}$. Integrating equation (1.13) across the interface yields

$$[\rho h (\mathbf{V}_l - \mathbf{V}_\Gamma) \cdot \mathbf{n}]_\Gamma = [-k \nabla T \cdot \mathbf{n}]_\Gamma, \tag{1.18}$$

where h defines the enthalpy. It is assumed that h depends only on the temperature. By using equation (1.15), the jump condition for the energy conservation writes

$$\dot{m} L_v = [-k \nabla T \cdot \mathbf{n}]_\Gamma, \tag{1.19}$$

with $L_v = [h]_\Gamma$ the latent heat of phase change.

The physical model that has to be solved in two-phase flow simulations is represented by the Navier-Stokes equations (1.10)-(1.11), the energy conservation equation (1.13), along with the interface jump conditions (1.15), (1.17), (1.19). Thus, in comparison with single phase flows, the resolution of two-phase flows presents two issues: the treatment of the discontinuities across the interface and modeling of the jump conditions. The two points in question will be further discussed.

There are two types of formulations for the Navier-Stokes equations, when incompressible two-phase flows are concerned: the *Whole-Domain* formulation [11, 91] and the *Jump-Condition* formulation. As their names suggest it, the *Whole-Domain* formulation implies the resolution of the physical equations in all the domain whereas in the *Jump-Condition* formulation, the physical equations are solved in each phase and jump conditions are imposed at the interface.

Concerning the treatment of the discontinuities across the interface, two approaches can be distinguished:

- the *Continuum Surface Force* formalism, where the discontinuities are smoothed over 2-3 grid cells with the aid of the Heaviside distribution H_Γ; the inconvenient of this approach is the development of parasitic currents leading to numerical instabilities.

- the *Sharp Interface* methods, where the discontinuities are treated as jump conditions, preventing the interface thickening and reducing parasitic currents magnitude.

1.2.2.2 Projection method for solving Navier-Stokes equations

The temporal discretization of the Navier-Stokes equations (1.10)-(1.11), with velocity and pressure fields unknown at the time step t^{n+1}, yields

$$\nabla \cdot \mathbf{u}^{n+1} = 0, \tag{1.20}$$

$$\rho \left(\frac{\mathbf{u}^{n+1} - \mathbf{u}^n}{\Delta t} + (\mathbf{u}^n \cdot \nabla)\, \mathbf{u}^n \right) = -\nabla p^{n+1} + \nabla \cdot \left(2\mu \bar{\bar{\mathbf{D}}}^n \right) + \rho \mathbf{g}. \tag{1.21}$$

The obtained equations are numerically solved by the use of the projection method introduced by Chorin [15] for single phase flows. The latter is based on the Hodge decomposition of any vector field into the sum of an irrotational (curl-free) vector field and a solenoidal (divergence-free) vector field. This method allows to decouple the resolution of the Navier-Stokes equations into the velocity field $\mathbf{u}$ resolution and the pressure field p resolution.

For two-phase flows, the use of this approach is not straightforward. Some modifications have to be done depending upon the chosen formulation. The method is further described for a *Jump-Condition* formalism, since it is implemented in the code DIVA.

The first step, also called the prediction step, is based on the calculation of an intermediate velocity $\mathbf{u}^*$ as

$$\mathbf{u}^* = \mathbf{u}^n - \Delta t \left((\mathbf{u}^n \cdot \nabla)\, \mathbf{u}^n - \frac{\nabla \cdot \left(2\mu \bar{\bar{\mathbf{D}}}^n \right)}{\rho} - \mathbf{g} \right). \tag{1.22}$$

Replacing this expression into equation (1.21) yields

$$\mathbf{u}^* = \mathbf{u}^{n+1} + \Delta t \frac{\nabla p^{n+1}}{\rho}, \tag{1.23}$$

and in this way we obtain the decomposition of the velocity field $\mathbf{u}^*$ into a free divergence component $\mathbf{u}^{n+1}$ according to eq. (1.20) and a component deriving from the scalar potential p. By

enforcing the free divergence on this decomposition, the Poisson equation on the pressure is obtained

$$\nabla \cdot \left(\frac{\nabla p^{n+1}}{\rho} \right) = \frac{\nabla \cdot \mathbf{u}^*}{\Delta t}. \tag{1.24}$$

with at the interface the jump condition on the pressure (1.17). It will be demonstrated in section 1.2.3 that adding a source term in the right hand side of the Poisson equation is equivalent with imposing a jump condition,

$$\nabla \cdot \left(\frac{\nabla p^{n+1}}{\rho} \right) = \frac{\nabla \cdot \mathbf{u}^*}{\Delta t} + \nabla \cdot \left(\frac{\sigma \kappa \mathbf{n} \delta_\Gamma}{\rho} \right). \tag{1.25}$$

Finally, the velocity field $\mathbf{u}^{n+1}$ can be directly deduced from the Hodge decomposition, as

$$\mathbf{u}^{n+1} = \mathbf{u}^* - \frac{\Delta t}{\rho} \left(\nabla p^{n+1} - \sigma \kappa \mathbf{n} \delta_\Gamma \right). \tag{1.26}$$

where δ_Γ is the Dirac delta function, non-zero only at the interface.

1.2.3 Ghost Fluid method

The Ghost Fluid method allows to adress the jump conditions at the interface for a system of partial differential equations discretized on a cartesian grid. This approach have been introduced by Fedkiw *et al.* [23] to compute non-viscous fluid flows with discontinuities at the interface. Later, it has been extended by Kang *et al.* to incompressible viscous two-phase flows with surface tension and gravity [43].

This approach is based on the accurate subgrid localization of the region where the discontinuity occurs thanks to the interface capture. The differential schemes are modified in order to avoid the presence of discontinuities related to the jump across the interface. For a better understanding of this procedure, figure 1.4 shows a 1D exemple. In each fluid region (purple for $x < x_\Gamma$ or blue for $x > x_\Gamma$) the real values of the function f are known. They are extended by continuity at a certain number of grid points in the region across the interface by using the known value of the jump. This so called ghost values are used in the derivation schemes to ensure the continuity while preserving the f jump value at the interface.

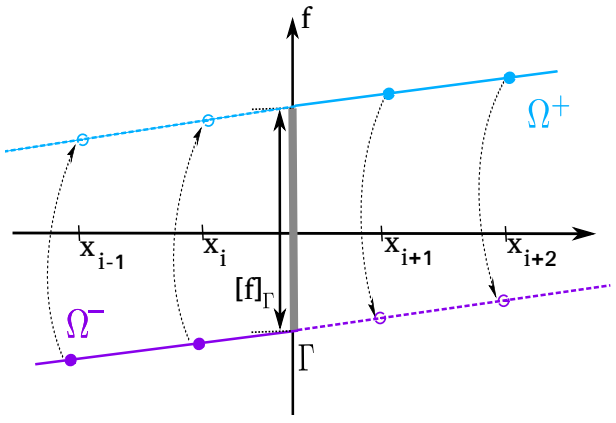

Figure 1.4: Schematics of the jump variable for Ghost Fluid method: real values (●) and ghost values (○).

The spatial discretization of the 1D Poisson equation, proposed in [61],

$$\frac{\partial}{\partial x} \left(\beta \frac{\partial f}{\partial x} \right) = R_{hs}, \tag{1.27}$$

using a centered scheme of second order, is expressed as

$$\frac{\beta_{i+1/2}\dfrac{f_{i+1}-f_i}{\Delta x}-\beta_{i-1/2}\dfrac{f_i-f_{i-1}}{\Delta x}}{\Delta x}=R_{hs}|_i, \tag{1.28}$$

where R_{hs} states for right hand side of the Poisson equation.

Further, the three possible configurations, the jump on the function $[f]_\Gamma = a(x_\Gamma)$ (fig. 1.4), the jump on the flux $\left[\beta\frac{\partial f}{\partial x}\right]_\Gamma = b(x_\Gamma)$ and the jump on the diffusion coefficient $[\beta]_\Gamma \neq 0$ are described. The three conditions can be combined and the extension to 2D or 3D configurations is straightforward.

1.2.3.1 Variable jump

We first consider the variable jump $[f]_\Gamma = a(x_\Gamma)$ at the interface Γ situated between the grid points x_i and x_{i+1}, as in figure 1.4. The spatial discretization of equation (1.27), with respect to each fluid region, yields

$$\frac{\beta_{i+1/2}\dfrac{f_{i+1}^+-f_i^-}{\Delta x}-\beta_{i-1/2}\dfrac{f_i^--f_{i-1}^-}{\Delta x}}{\Delta x}=R_{hs}|_i. \tag{1.29}$$

We recall that the symbols + and − state for the fluid region for which the value is considered: Ω^+ or Ω^-. The discretization of the first derivative contains a jump on the function f since the cell $[x_i, x_{i+1}]$ is crossed by the interface. To avoid this, the function f_{i+1}^+ is replaced by its ghost value $f_{i+1}^{G,-}$ defined as

$$f_{i+1}^{G,-} = f_{i+1}^+ - [f]_\Gamma = f_{i+1}^+ - a(x_\Gamma). \tag{1.30}$$

The discretization of the Poisson equation, without mixing terms from both fluid regions, becomes

$$\frac{\beta_{i+1/2}\dfrac{f_{i+1}^{G,-}-f_i^-}{\Delta x}-\beta_{i-1/2}\dfrac{f_i^--f_{i-1}^-}{\Delta x}}{\Delta x}=R_{hs}|_i. \tag{1.31}$$

and, by the use of the ghost value definition (1.30),

$$\frac{\beta_{i+1/2}\dfrac{\left(f_{i+1}^+-a(x_\Gamma)\right)-f_i^-}{\Delta x}-\beta_{i-1/2}\dfrac{f_i^--f_{i-1}^-}{\Delta x}}{\Delta x}=R_{hs}|_i, \tag{1.32}$$

or

$$\frac{\beta_{i+1/2}\dfrac{f_{i+1}^+-f_i^-}{\Delta x}-\beta_{i-1/2}\dfrac{f_i^--f_{i-1}^-}{\Delta x}}{\Delta x}=R_{hs}|_i+\beta_{i+1/2}\frac{a(x_\Gamma)}{\Delta x^2}. \tag{1.33}$$

The original discretization of the Poisson equation is obtained with an additional source term allowing to account for the jump condition between x_i and x_{i+1}.

In the same way, the discretization at the grid point x_{i+1} accounting for the jump condition, writes

$$\frac{\beta_{i+3/2}\dfrac{f_{i+2}^+-f_{i+1}^+}{\Delta x}-\beta_{i+1/2}\dfrac{f_{i+1}^+-f_i^-}{\Delta x}}{\Delta x}=R_{hs}|_{i+1}-\beta_{i+1/2}\frac{a(x_\Gamma)}{\Delta x^2}. \tag{1.34}$$

1.2.3.2 Flux jump

We now consider the configuration where a jump on the flux has to be imposed, defined as $\left[\beta\frac{\partial f}{\partial x}\right]_\Gamma = b(x_\Gamma)$. The spatial discretization of the Poisson equation (1.27), at a grid point x_i gives:

$$\frac{\left(\beta_{i+1/2}\dfrac{f_{i+1}-f_i}{\Delta x}\right)^+-\left(\beta_{i-1/2}\dfrac{f_i-f_{i-1}}{\Delta x}\right)^-}{\Delta x}=R_{hs}|_i, \tag{1.35}$$

with the symbols + and − corresponding to the regions where the flux is computed. The derivative between the grid points $x_{i-1/2}$ and $x_{i+1/2}$ is not continous as a result of the jump at the interface.

The ghost values of the flux are defined, by continuity, on the grid points across the interface

$$\left(\beta_{i+1/2}\frac{f_{i+1}-f_i}{\Delta x}\right)^{G,-} = \left(\beta_{i+1/2}\frac{f_{i+1}-f_i}{\Delta x}\right)^{+} - \left[\beta\frac{\partial f}{\partial x}\right]_\Gamma = \left(\beta_{i+1/2}\frac{f_{i+1}-f_i}{\Delta x}\right)^{+} - b(x_\Gamma). \quad (1.36)$$

By using the latter equation, the Poisson equation writes

$$\frac{\left(\beta_{i+1/2}\frac{f_{i+1}-f_i}{\Delta x}\right)^{+} - \left(\beta_{i-1/2}\frac{f_i-f_{i-1}}{\Delta x}\right)^{-}}{\Delta x} = R_{hs}|_i + \frac{b(x_\Gamma)}{\Delta x}. \quad (1.37)$$

1.2.3.3 Diffusion coefficient jump

The third possible configuration presumes a discontinuity on the diffusion coefficient. Considering the 1D example from figure 1.4, the discretization of the Poisson equation (1.27) includes the values $\beta_{i-1/2}$ and $\beta_{i+1/2}$. As it can be observed in fig. 1.5, the value $\beta_{i-1/2} = \beta^-$, as both the grid points x_i and x_{i-1} are located in Ω^-. To calculate $\beta_{i+1/2}$, we use the continuity of the flux at the interface, that writes

$$\beta_{i+1/2}\frac{f_{i+1}-f_i}{\Delta x} = \beta^-\frac{f_\Gamma - f_i}{(1-\theta)\Delta x} = \beta^+\frac{f_{i+1}-f_\Gamma}{\theta\Delta x}, \quad (1.38)$$

where f_Γ represents the value of f at the interface.

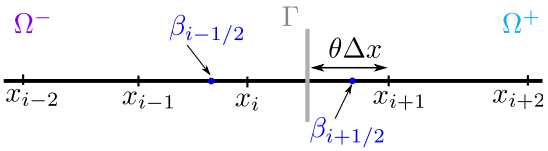

Figure 1.5: Interface-grid intersection and jump on the diffusion coefficient for Ghost Fluid method.

As a result, from the latter equation, the value of f_Γ is expressed as

$$f_\Gamma = \frac{\beta^- f_i\theta + \beta^+ f_{i+1}(1-\theta)}{\beta^-\theta + \beta^+(1-\theta)}, \quad (1.39)$$

where $\theta = \dfrac{|\phi_{i+1}|}{|\phi_i| + |\phi_{i+1}|}$, ϕ being the Level-Set function known at each grid point.

By replacing this expression in (1.38), the value of the diffusion coefficient yields

$$\beta_{i+1/2} = \frac{\beta^-\beta^+}{\beta^-\theta + \beta^+(1-\theta)}. \quad (1.40)$$

The jump on the diffusion coefficient does not imply the addition of a source term in the right hand side of the equation. Nevertheless, the coefficients of the linear system matrix are modified.

1.3 Numerical model for two-phase flows - DIVA code

In this section, the numerical solver implemented in the code DIVA is detailed. It allows the computation of incompressible two-phase flows with a jump condition on the normal velocity at the interface. Nguyen *et al.* [67] were the first to use it to capture flame discontinuities. Kang

et al. [43] and Sussman *et al.* [100] extended it for the simulation of incompressible two phase flows without phase change. The approach Ghost Fluid allowing to account for the velocity jump at the interface, when phase change occurs, was employed in several papers. Gibou *et al.* [26] and Tanguy *et al.* [102] applied it for boiling simulation. For an accurate simulation of drops evaporation, Tanguy *et al.* [101] propose an improvement of the method in order to properly impose the free divergence condition at the interface for the liquid velocity field.

The interface separating the two-phases is located using the Level-Set method, that allows splitting the computational domain Ω into two regions corresponding to each phase: Ω^+ for the liquid phase and Ω^- for the vapor phase (see details on the Level-Set method in section 1.2.1.2). A global scalar field is defined for each physical property, such as

$$\rho(\mathbf{x}) = \begin{cases} \rho^+ & \text{if } \mathbf{x} \in \Omega^+ \\ \rho^- & \text{if } \mathbf{x} \in \Omega^- \end{cases} . \tag{1.41}$$

The same goes for the dynamic viscosity μ, the specific heat C_p and the thermal conductivity k. Their discontinuity across the interface is treated using a *Sharp-Interface* approach.

The physical model is represented by the mass (1.10), momentum (1.11) and energy (1.13) conservation equations along with the corresponding interface jump conditions (1.15), (1.17) and (1.19). Its resolution is done in the framework of *Jump-Condition* formulation, with the Ghost-Fluid Method for the jump conditions treatment.

In what follows, the various steps of the solver algorithm, as well as the corresponding spatial discretizations, are given. For the sake of simplification, the 2D configuration is considered, but the extension to 3D is straightforward.

In the context of this thesis, we use a cartesian mesh grid of MAC (Marker and Cell) type, represented in figure 1.6. The formalism of this kind of mesh grid is that the different variables are not computed on the same grid. The scalar fields (pressure, Level-Set function, ...) are defined at the center of the cell grid while the velocity components are staggered at the cell face centers. The spatial discretization follows from a finite-volume approach.

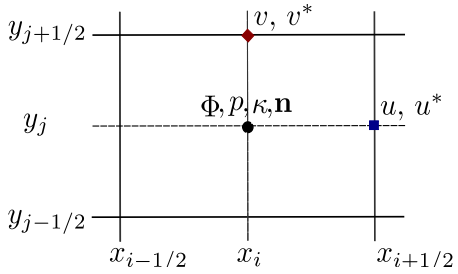

Figure 1.6: Variables definition on the mesh grid.

The different convective terms are discretized with a WENO-Z scheme [10]. The resolution of the linear systems obtained for the pressure and the thermal fields is carried out with the Black Box MultiGrid method (BBMG) [22, 63]. The details on the implementation of this solver in the DIVA code can be found in [56].

1.3.1 Level-Set discretization

The level-set function $\phi(i, j)$ is defined at the cell center. At each temporal iteration, the interface is convected using (1.6) while considering the velocity field $\mathbf{u}^n$ from the previous time step t^n. The

resolution is explicit in time, writing

$$\phi^{n+1} = \phi^n - \Delta t \left(\mathbf{u}^n \cdot \nabla\right) \phi^n, \tag{1.42}$$

with Δt the time step.

Once the level-set function is computed at the time t^{n+1}, the redistancing algorithm is applied to adjust the distance between consecutive levels. An explicit scheme is used on the fictitious time τ and the absolute value of the distance function d is obtained with the WENO-Z scheme,

$$\begin{cases} d^{m+1} & = d^m - \Delta\tau \text{sign}\left(\phi^{n+1}\right)\left(1 - ||\nabla d^m||\right) \\ d^{m=0} & = \phi^{n+1} \end{cases}, \tag{1.43}$$

where $\Delta\tau$ is the fictitious time step. A few temporal iterations are performed to obtain the algorithm convergence. Thereafter, the distance function replaces the level-set field ϕ^{n+1}. The fluids physical properties are updated using the novel value of the level-set function, as

$$\rho^{n+1}(\phi^{n+1}) = \rho^- + H_\Gamma(\phi^{n+1})\left(\rho^+ - \rho^-\right), \tag{1.44}$$

$$\mu^{n+1}(\phi^{n+1}) = \mu^- + H_\Gamma(\phi^{n+1})\left(\mu^+ - \mu^-\right), \tag{1.45}$$

with the Heaviside distribution expressed as

$$H_\Gamma\left(\Phi^{n+1}\right) = \begin{cases} 1 & \text{if } \phi^{n+1} > 0 \\ 0 & \text{if } \phi^{n+1} < 0 \end{cases}. \tag{1.46}$$

Next, the resolution of the Navier-Stokes equations, performed using the projection method, is detailed. The following sections are organized as follows: first the general algorithm is given for two-phase flows, and next, the extensions required to deal with phase change are presented.

1.3.2 Computation of the intermediate velocity

The first step in the projection method is the computation of the intermediate velocity field $\mathbf{u}^*$. In the code DIVA, the viscous term has an implicit treatment,

$$\rho^{n+1}\mathbf{u}^* - \Delta t \nabla \cdot \left(2\mu^{n+1}\bar{\bar{\mathbf{D}}}^*\right) = \rho^{n+1}\left(\mathbf{u}^n - \Delta t\left(\left(\mathbf{u}^n \cdot \nabla\right)\mathbf{u}^n - \mathbf{g}\right)\right). \tag{1.47}$$

First, the terms of the right-hand side of equation (1.47) are computed,

$$R_{hs} = \rho^{n+1}\left(\mathbf{u}^n - \Delta t\left(\left(\mathbf{u}^n \cdot \nabla\right)\mathbf{u}^n - \mathbf{g}\right)\right). \tag{1.48}$$

Next, the resolution of (1.47) leads to a large linear system where the two velocity components are coupled. This velocity field does not need an interface jump condition, however, the diffusion coefficient in the viscous term corresponding to the dynamic viscosity μ, is discountinuous across the interface. The formalism described in section 1.2.3.3 is therefore used.

The discretization of the viscous term is further detailed [52]. By applying the divergence operator and by omitting the exponents symbols $(.)^{n+1}$ and $(.)^*$, we obtain

$$\nabla \cdot \left(2\mu\bar{\bar{\mathbf{D}}}\right) = \begin{pmatrix} \dfrac{\partial}{\partial x}\left(2\mu\dfrac{\partial u}{\partial x}\right) + \dfrac{\partial}{\partial y}\left(\mu\left(\dfrac{\partial u}{\partial y} + \dfrac{\partial v}{\partial x}\right)\right) \\ \dfrac{\partial}{\partial x}\left(\mu\left(\dfrac{\partial u}{\partial y} + \dfrac{\partial v}{\partial x}\right)\right) + \dfrac{\partial}{\partial y}\left(2\mu\dfrac{\partial v}{\partial y}\right) \end{pmatrix}. \tag{1.49}$$

The projection in the $\mathbf{e}_x$ direction gives

$$\nabla \cdot \left(2\mu\bar{\bar{\mathbf{D}}}\right) \cdot \mathbf{e}_x \left|_{i+1/2,j} = \frac{\partial}{\partial x}\left(2\mu\frac{\partial u}{\partial x}\right)\right|_{i+1/2,j} + \frac{\partial}{\partial y}\left(\mu\left(\frac{\partial u}{\partial y}+\frac{\partial v}{\partial x}\right)\right)\Big|_{i+1/2,j}, \tag{1.50}$$

with, by using a second order finite difference scheme,

$$\frac{\partial}{\partial x}\left(2\mu\frac{\partial u}{\partial x}\right)\Big|_{i+1/2,j} \simeq \frac{2\mu_{i+1,j}\dfrac{u_{i+3/2,j}-u_{i+1/2,j}}{\Delta x} - 2\mu_{i,j}\dfrac{u_{i+1/2,j}-u_{i-1/2,j}}{\Delta x}}{\Delta x}, \tag{1.51}$$

$$\frac{\partial}{\partial y}\left(\mu\frac{\partial u}{\partial y}\right)\Big|_{i+1/2,j} \simeq \frac{\mu_{i+1/2,j+1/2}\dfrac{u_{i+1/2,j+1}-u_{i+1/2,j}}{\Delta y} - \mu_{i+1/2,j-1/2}\dfrac{u_{i+1/2,j}-u_{i+1/2,j-1}}{\Delta y}}{\Delta y}, \tag{1.52}$$

$$\frac{\partial}{\partial y}\left(\mu\frac{\partial v}{\partial x}\right)\Big|_{i+1/2,j} \simeq \frac{\mu_{i+1/2,j+1/2}\dfrac{v_{i+1,j+1/2}-v_{i,j+1/2}}{\Delta x} - \mu_{i+1/2,j-1/2}\dfrac{v_{i+1,j-1/2}-v_{i,j-1/2}}{\Delta x}}{\Delta y}. \tag{1.53}$$

In the same way, the projection in the $\mathbf{e}_y$ direction yields

$$\nabla \cdot \left(2\mu\bar{\bar{\mathbf{D}}}\right) \cdot \mathbf{e}_y \left|_{i,j+1/2} = \frac{\partial}{\partial x}\left(\mu\left(\frac{\partial u}{\partial y}+\frac{\partial v}{\partial x}\right)\right)\right|_{i,j+\frac{1}{2}} + \frac{\partial}{\partial y}\left(2\mu\frac{\partial v}{\partial y}\right)\Big|_{i,j+1/2}, \tag{1.54}$$

with

$$\frac{\partial}{\partial x}\left(\mu\frac{\partial u}{\partial y}\right)\Big|_{i,j+1/2} \simeq \frac{\mu_{i+1/2,j+1/2}\dfrac{u_{i+1/2,j+1}-u_{i+1/2,j}}{\Delta y} - \mu_{i-1/2,j+1/2}\dfrac{u_{i-1/2,j+1}-u_{i-1/2,j}}{\Delta y}}{\Delta x}, \tag{1.55}$$

$$\frac{\partial}{\partial x}\left(\mu\frac{\partial v}{\partial x}\right)\Big|_{i,j+1/2} \simeq \frac{\mu_{i+1/2,j+1/2}\dfrac{v_{i+1,j+1/2}-v_{i,j+1/2}}{\Delta x}) - \mu_{i-1/2,j+1/2}\dfrac{v_{i,j+1/2}-v_{i-1,j+1/2}}{\Delta x}}{\Delta x}, \tag{1.56}$$

$$\frac{\partial}{\partial y}\left(2\mu\frac{\partial v}{\partial y}\right)\Big|_{i,j+1/2} \simeq \frac{2\mu_{i,j+1}\dfrac{v_{i,j+3/2}-v_{i,j+1/2}}{\Delta y} - 2\mu_{i,j}\dfrac{v_{i,j+1/2}-v_{i,j-1/2}}{\Delta y}}{\Delta y}. \tag{1.57}$$

In order to compute rightfully the viscous term at the intermediate time step, one must solve a coupled linear system of two matrices with 9 diagonals per velocity components as

$$\begin{aligned} &a1_{i+1,j}u^*_{i+3/2,j} + a1_{i,j}u^*_{i-1/2,j} + b1_{i+1/2,j+1/2}u^*_{i+1/2,j+1} + b1_{i+1/2,j-1/2}u^*_{i+1/2,j-1} + \alpha_{i+1/2,j}u^*_{i+1/2,j} \\ &+ c1_{i+1/2,j+1/2}\left(v^*_{i+1,j+1/2} - v^*_{i,j+1/2}\right) + c1_{i+1/2,j-1/2}\left(v^*_{i+1,j-1/2} - v^*_{i,j-1/2}\right) = R_{hs}\cdot\mathbf{e}_x\left|_{i+1/2,j}\right., \end{aligned} \tag{1.58}$$

and

$$\begin{aligned} &\beta_{i,j+1/2}v^*_{i,j+1/2} + b2_{i,j+1}v^*_{i,j+3/2} + b2_{i,j}v^*_{i,j-1/2} + a2_{i+1/2,j+1}v^*_{i+1,j+1/2} + a2_{i+1/2,j+1}v^*_{i-1,j+1/2} \\ &+ c2_{i+1/2,j+1/2}\left(u^*_{i+1/2,j+1} - u^*_{i+1/2,j}\right) + c2_{i-1/2,j+1/2}\left(u^*_{i-1/2,j+1} - u^*_{i-1/2,j}\right) = R_{hs}\cdot\mathbf{e}_y\left|_{i,j+1/2}\right.. \end{aligned} \tag{1.59}$$

The matrix coefficients are deduced from equations (1.47), (1.50) and (1.54) as

$$a1_{k,l} = -\frac{2\mu_{k,l}}{\Delta x^2}\Delta t, \quad b1_{k,l} = -\frac{\mu_{k,l}}{\Delta y^2}\Delta t, \quad c1_{k;l} = -\frac{\mu_{k,l}}{\Delta x\Delta y}\Delta t, \tag{1.60}$$

$$a2_{k,l} = -\frac{\mu_{k,l}}{\Delta x^2}\Delta t, \quad b2_{k,l} = -\frac{2\mu_{k,l}}{\Delta y^2}\Delta t, \quad c2_{k;l} = -\frac{\mu_{k,l}}{\Delta x\Delta y}\Delta t, \tag{1.61}$$

$$\alpha_{i+1/2,j} = \rho^{n+1}_{i+1/2,j} - a1_{i+1,j} - a1_{i,j} - b1_{i+1/2,j+1/2} - b1_{i+1/2,j-1/2}, \tag{1.62}$$

$$\beta_{i,j+1/2} = \rho^{n+1}_{i,j+1/2} - b2_{i,j+1} - b2_{i,j} - a2_{i+1/2,j+1/2} - a2_{i-1/2,j+1/2}. \tag{1.63}$$

Lepilliez *et al.* [57] showed that, since the linear system is diagonally dominant, it can be solved efficiently with a few Gauss–Seidel iterations (< 20 iterations for typical multiphase flow configurations). For a 3D system, a third coupled matrix has to be accounted for, resulting in a 15-diagonal matrix per velocity components.

Additional aspects when phase change occurs

When phase change occurs, the jump condition (1.15) on the mass conservation equation has to be considered. Therefore, the velocity fields correponding to the vapor and the liquid are extended as it follows

$$\mathbf{u}_l^* = \begin{cases} \mathbf{u}^* & \text{if } \phi > 0 \\ \mathbf{u}^* - \dot{m}\left[\frac{1}{\rho}\right]_\Gamma \mathbf{n} & \text{if } \phi < 0 \end{cases}, \tag{1.64}$$

$$\mathbf{u}_v^* = \begin{cases} \mathbf{u}^* - \dot{m}\left[\frac{1}{\rho}\right]_\Gamma \mathbf{n} & \text{if } \phi > 0 \\ \mathbf{u}^* & \text{if } \phi < 0 \end{cases}. \tag{1.65}$$

1.3.3 Pressure field resolution

The second step of the projection method implies the resolution of the Poisson equation on the pressure (1.24). Additionally, the jump condition (1.17) has to be imposed. The formalisms described in Section 1.2.3.1 and 1.2.3.3 are therefore used. The spatial discretization of the pressure equation (1.26) is done by using the Ghost Fluid approach,

$$\frac{\beta_{i+1/2,j}\left(\frac{p_{i+1,j}-p_{i,j}}{\Delta x}\right) - \beta_{i-1/2,j}\left(\frac{p_{i,j}-p_{i-1,j}}{\Delta x}\right)}{\Delta x} \tag{1.66}$$

$$+\frac{\beta_{i,j+1/2}\left(\frac{p_{i,j+1}-p_{i,j}}{\Delta y}\right) - \beta_{i,j-1/2}\left(\frac{p_{i,j}-p_{i,j-1}}{\Delta y}\right)}{\Delta y} = R_{hs}|_{i,j} + \eta_{i,j}, \tag{1.67}$$

with $\beta = 1/\rho^{n+1}$ the diffusion coefficient,

$$R_{hs}|_{i,j} = \frac{\frac{u^*_{i+1/2,j} - u^*_{i-1/2,j}}{\Delta x} + \frac{v^*_{i,j+1/2} - v^*_{i,j-1/2}}{\Delta y}}{\Delta t}, \tag{1.68}$$

the right hand side of the Poisson equation and $\eta_{i,j}$ represents the source terms accounting for the pressure jump condition.

As explained in section 1.2.3.3, when the cell grid is crossed by the interface, the diffusion coefficient β is calculated using a harmonic mean. There are two general configurations. If the interface crosses the segment $[x_i, x_{i+1}]$, the diffusion coefficient is computed with

$$\beta_{i+1/2,j} = \begin{cases} \dfrac{\beta^-\beta^+}{\beta^-\theta^E + \beta^+(1-\theta^E)} & \text{if } \phi_{i,j} < 0 \text{ and } \phi_{i+1,j} > 0 \\ \dfrac{\beta^-\beta^+}{\beta^+\theta^E + \beta^-(1-\theta^E)} & \text{if } \phi_{i,j} > 0 \text{ and } \phi_{i+1,j} < 0 \end{cases}, \tag{1.69}$$

where

$$\theta^E = \frac{|\phi_{i+1,j}|}{|\phi_{i,j}| + |\phi_{i+1,j}|}. \tag{1.70}$$

If the interface crosses the segment $[x_{i-1}, x_i]$, the diffusion coefficient reads

$$\beta_{i-1/2,j} = \begin{cases} \dfrac{\beta^-\beta^+}{\beta^-\theta^W + \beta^+(1-\theta^W)} & \text{if } \phi_{i,j} < 0 \text{ and } \phi_{i-1,j} > 0 \\ \dfrac{\beta^-\beta^+}{\beta^+\theta^W + \beta^-(1-\theta^W)} & \text{if } \phi_{i,j} > 0 \text{ and } \phi_{i-1,j} < 0 \end{cases}, \tag{1.71}$$

where

$$\theta^W = \frac{|\phi_{i-1,j}|}{|\phi_{i,j}| + |\phi_{i-1,j}|}. \tag{1.72}$$

The discretization in the $\mathbf{e}_y$ is similar. The term $\eta_{i,j}$ corresponds to the sum of the jump conditions for each segment neighbouring the grid point (i,j) crossed by the interface. The latter are marked with the exponents E, W, N, S corresponding to the segments east, west, north, south,

$$\eta_{i,j} = \eta^E_{i,j} + \eta^W_{i,j} + \eta^N_{i,j} + \eta^S_{i,j}. \tag{1.73}$$

Each one of this terms are calculated using the formalism described in section 1.2.3.1,

$$\eta^E_{i,j} = \pm\frac{\beta_{i+1/2,j}a^E_\Gamma}{\Delta x^2}, \quad \eta^W_{i,j} = \pm\frac{\beta_{i-1/2,j}a^W_\Gamma}{\Delta x^2}, \quad \eta^N_{i,j} = \pm\frac{\beta_{i,j+1/2}a^N_\Gamma}{\Delta y^2}, \quad \eta^S_{i,j} = \pm\frac{\beta_{i,j-1/2}a^S_\Gamma}{\Delta y^2}, \tag{1.74}$$

with $\pm$ corresponding to the opposite sign as $\phi_{i,j}$ and, by definition as the pressure jump $a_\Gamma = \sigma\kappa$,

$$a^E_\Gamma = \sigma\kappa_{i,j}\theta^E + \sigma\kappa_{i+1,j}\left(1-\theta^E\right), \quad a^W_\Gamma = \sigma\kappa_{i,j}\theta^W + \sigma\kappa_{i-1,j}\left(1-\theta^W\right), \tag{1.75}$$

$$a^N_\Gamma = \sigma\kappa_{i,j}\theta^N + \sigma\kappa_{i,j+1}\left(1-\theta^N\right), \quad a^S_\Gamma = \sigma\kappa_{i,j}\theta^S + \sigma\kappa_{i,j-1}\left(1-\theta^S\right). \tag{1.76}$$

Additional aspects when phase change occurs

When phase change occurs, the pressure field is calculated in each phase domain, by considering the corresponding intermediate velocity field,

$$\nabla\cdot\left(\frac{\nabla p^{n+1}}{\rho^{n+1}}\right) = \begin{cases} \dfrac{\nabla\cdot\mathbf{u}^*_l}{\Delta t} & \text{if } \phi > 0 \\ \dfrac{\nabla\cdot\mathbf{u}^*_v}{\Delta t} & \text{if } \phi < 0 \end{cases}, \tag{1.77}$$

while imposing the following jump condition

$$[p]_\Gamma = \sigma\kappa - \dot{m}^2\left[\frac{1}{\rho}\right]. \tag{1.78}$$

We emphasize that the discontinuity on the normal viscous stress $\mu\frac{\partial V_n}{\partial n}$ is accounted for in the intermediate velocity computation and that the recoil pressure $\dot{m}^2\left[\frac{1}{\rho}\right]_\Gamma$ has little influence in the present study.

1.3.4 Extension methodology to impose the free divergence onto the velocity field

Finally, the physical velocity field yields

$$\mathbf{u}^{n+1} = \mathbf{u}^* - \frac{\Delta t}{\rho^{n+1}}\left(\nabla p^{n+1} - \sigma\kappa\mathbf{n}\delta_\Gamma\right). \tag{1.79}$$

In this last correcting step, the approximation of the Dirac δ_Γ distribution based on Liu *et al.* [61] and detailed in Lalanne *et al.* [52], is used.

In order to correctly compute the next temporal iteration, it is necessary to extend the velocity field. This will allow to relocate the Level-Set function and to calculate the convective terms at the interface.

For the extension of the velocity field in the liquid region, Tanguy *et al.* [101] propose solving the Poisson equation using a ghost pressure field p_g,

$$\nabla \cdot \left(\frac{\nabla p_g^{n+1}}{\rho_{n+1}} \right) = \frac{\nabla \cdot \mathbf{u}_l^*}{\Delta t}. \tag{1.80}$$

The extrapolated velocity field is then obtained by

$$\mathbf{u}_l^{n+1} = \begin{cases} \mathbf{u}^{n+1} & \text{if } \Phi > 0 \\ \mathbf{u}_l^{n+1} - \dot{m} \dfrac{\nabla p_g^{n+1}}{\rho^{n+1}} & \text{if } \Phi < 0 \end{cases}. \tag{1.81}$$

The extension of the velocity fields in the vapor region is equivalent to equation 1.65,

$$\mathbf{u}_v^{n+1} = \begin{cases} \mathbf{u}^{n+1} - \dot{m} \left[\dfrac{1}{\rho} \right]_\Gamma \mathbf{n} & \text{if } \Phi > 0 \\ \mathbf{u}^{n+1} & \text{if } \Phi < 0 \end{cases}. \tag{1.82}$$

So far, the Navier-Stokes equations have been solved ensuing with the computation of the pressure and the velocity fields. Next, the energy conservation equation (1.13) is treated using the so called Ghost Fluid Thermal Solver for Boiling.

1.3.5 Ghost Fluid Thermal Solver for Boiling

In the previous sections, the pressure and the velocity fields have been solved by imposing a given mass flow rate $\dot{m}$. In what follows, the numerical approach proposed by Gibou *et al.* [26] allowing to simulate boiling flows is presented. The configuration supposes pure liquids evaporating in their own vapor. There is therefore one and the same chemical specie in the liquid and vapor phase. The authors propose to solve separately the temperature fields corresponding to the liquid and vapor phases by assuming that the interface temperature is uniform and constant. The fields are then solved with the saturation temperature T_{sat} imposed at the interface as a Dirichlet condition, using the formalism proposed by Gibou *et al.* [27].

First, we compute the temperature field in the liquid phase, by solving the following linear system

$$\begin{aligned} &\rho_l C_{p_l} T_l^{n+1} - \Delta t \nabla \cdot \left(k_l \nabla T_l^{n+1} \right) = \rho_l C_{p_l} \left(T_l^n - \Delta t \mathbf{u}_l^n \cdot \nabla T_l^n \right), \quad \text{if } \phi > 0, \\ &T|_\Gamma = T_{sat}. \end{aligned} \tag{1.83}$$

next, we calculate the temperature field in the vapor phase by solving a similar linear system

$$\begin{aligned} &\rho_v C_{p_v} T_v^{n+1} - \Delta t \nabla \cdot \left(k_v \nabla T_v^{n+1} \right) = \rho_v C_{p_v} \left(T_v^n - \Delta t \mathbf{u}_v^n \cdot \nabla T_v^n \right), \quad \text{if } \phi < 0, \\ &T|_\Gamma = T_{sat}. \end{aligned} \tag{1.84}$$

Imposing an immersed Dirichlet boundary condition on an interface, described on a Cartesian grid, can be done by using the numerical method proposed by Gibou et al. in [27]. This efficient

method is second order accurate in space and leads to a simple symmetric definite positive linear system that can be solved with the Black Box MultiGrid solver. Once the temperature field has been computed, the local mass flow rate can be easily deduced from the difference between the thermal fluxes,

$$\dot{m} = \frac{[k\nabla T \cdot \mathbf{n}]_\Gamma}{L_v}. \tag{1.85}$$

The above equation contains the thermal gradient on both sides of the interface. The spatial discretization of a gradient needs a continuous field in the vicinity of the point where it is evaluated. For this, the ghost fields T_l^G and T_v^G are introduced. They represent, respectively, the extension of the real temperature field in the liquid extended in the gas and the extension of the real temperature field in the gas extended in the liquid domain. To tackle this, the method proposed by Aslam [3], described in the following section, has been implemented in the code DIVA and validated by Rueda-Villegas in [88].

1.3.6 Extrapolation techniques for a scalar field

In order to compute the fields onto the ghost grids, an extrapolation technique is necessary. Aslam proposes in [3] an extrapolation method which requires the resolution of a partial differential equation inspired from the work of Fedkiw *et al.* [23].

This method allows obtaining extrapolations of order as high as necessary. With the constant extrapolation, a continuous field is obtained in the ghost domain, distributed normal to the interface. The linear extrapolation ensures in addition the continuity of the gradient field in the normal direction. If one increases the order of the extrapolation, the continuity of the corresponding order derivative is provided. In the code DIVA, the constant, the linear and the quadratic extrapolations are implemented. In what follows we will only describe the first two.

1.3.6.1 Constant extrapolation

Let us assume the variable $\xi = T^G$, where T^G represents the gas temperature defined in the domain Ω^-. The constant extrapolation of this variable in the liquid domain Ω^+ is realized by solving the following partial differential equation

$$\frac{\partial \xi}{\partial \tau} + H(\phi)\mathbf{n} \cdot \nabla \xi = 0, \tag{1.86}$$

where τ is a fictitious time, and $H(\phi)$ the Heaviside function.

The temporal discretization of the above equation writes

$$\xi^{m+1} = \xi^m - \Delta\tau H(\phi)\left(\frac{\partial \xi^m}{\partial x}n_x + \frac{\partial \xi^m}{\partial y}n_y\right). \tag{1.87}$$

For the spatial derivatives we use an Upwind scheme,

$$\frac{\partial \xi^m}{\partial x}\Big|_{i,j} = \begin{cases} \dfrac{u^m_{i,j} - u^m_{i-1,j}}{\Delta x_{i-1}} & \text{if } (n_x)_{i,j} > 0 \\ \dfrac{u^m_{i+1,j} - u^m_{i,j}}{\Delta x_i} & \text{elsewhere} \end{cases}, \tag{1.88}$$

and

$$\frac{\partial \xi^m}{\partial y}\Big|_{i,j} = \begin{cases} \dfrac{u^m_{i,j} - u^m_{i,j-1}}{\Delta y_{j-1}} & \text{if } (n_y)_{i,j} > 0 \\ \dfrac{u^m_{i,j+1} - u^m_{i,j}}{\Delta y_j} & \text{elsewhere} \end{cases}. \tag{1.89}$$

1.3.6.2 Linear extrapolation

The linear extrapolation allows to preserve the continuity of the variable ξ and of its gradient $\nabla\xi$ in the normal $\mathbf{n}$ direction. First, the derivative $\partial_n\xi = \mathbf{n}\cdot\nabla\xi$ is computed, in the region where the variable ξ is defined, here Ω^-. The first step is to solve the following partial differential equation

$$\frac{\partial(\partial_n\xi)}{\partial\tau} + H(\phi)\mathbf{n}\cdot\nabla(\partial_n\xi) = 0, \tag{1.90}$$

allowing to extrapolate the variable derivative in the domain where it is not defined. The algorithm for a constant extrapolation, described in the previous section, is here used for the variable $\partial_n\xi$. Once $\partial_n\xi$ is computed, we need to extrapolate the variable ξ by solving a second partial differential equation,

$$\frac{\partial\xi}{\partial\tau} + H(\phi)(\mathbf{n}\cdot\nabla\xi - \partial_n\xi) = 0. \tag{1.91}$$

The temporal discretization of this equation is done in a similar way as for the constant extrapolation. Note that here, a source term is added in the right hand of the obtained equation,

$$\xi^{m+1} = \xi^m - \Delta\tau H(\phi)\left(\frac{\partial\xi^m}{\partial x}n_x + \frac{\partial\xi^m}{\partial y}n_y - \partial_n\xi^m\right). \tag{1.92}$$

More details on this extrapolation method can be found in the theses of Rueda-Villegas [88] and of Alis [1].

1.3.7 Temporal discretization

The temporal derivatives in the Navier-Stokes equations, in the energy equation as well as in the Level-Set equation of convection are discretized with a second order Runge-Kutta scheme. To ensure the computation stability, the time step is calculated by taking into account the constraints of the convection, surface tension and viscosity effects [91, 99, 43].

The convective time step is defined by

$$\Delta t_{conv} = \frac{1}{\dfrac{\max(|u|)}{\Delta x} + \dfrac{\max(|v|)}{\Delta y} + \dfrac{\max(|w|)}{\Delta z}}, \tag{1.93}$$

and the surface tension time step is expressed as

$$\Delta t_{surf\_tens} = \frac{1}{4}\sqrt{\frac{\max(\rho^+,\rho^-)}{\sigma}}\min(\Delta x\Delta y\Delta z)^{3/2}. \tag{1.94}$$

If the viscous term is treated explicitly, the corresponding time step writes

$$\Delta t_{visc} = \frac{\min(\rho^+/\mu^+, \rho^-/\mu^-)}{\dfrac{2}{\min(\Delta x^2)} + \dfrac{2}{\min(\Delta y^2)} + \dfrac{2}{\min(\Delta z^2)}}. \tag{1.95}$$

Throughout this thesis, the viscous term is computed with an implicit treatment, therefore the latter constraint on the computation time step is not considered. Finally, the global time step has to respect the following condition in order to ensure the simulation stability:

$$\frac{1}{\Delta t} > \frac{1}{\Delta t_{conv}} + \frac{1}{\Delta t_{surf\_tens}}. \tag{1.96}$$

1.4 Conclusion

The objective of this chapter was, on one side, to provide a general background on two-phase flows numerical simulation and on the other side, to give a detailed description of the numerical solver implemented in the code DIVA.

The Navier-Stokes equations are solved using the projection method, with a *Jump-Condition* formalism. The thermal field is computed by solving a simplified conservation energy equation. As the liquid-gas interface is not boundary fitted with computational grid, the suitable jump conditions can be imposed across the interface following the general guidelines of the Ghost Fluid Method to maintain the conservation of mass, momentum and energy. That is made possible by using the subgrid location of the interface with a static Level Set function whose zero level curve represents the interface. Spatial derivatives are computed with fifth order WENO-Z schemes. A Black-Box MultiGrid solver is used to solve the pressure Poisson equation and we perform an implicit temporal discretization of the viscous terms. The system of unsteady equations is solved until reaching a steady state by using a second order TVD Runge-Kutta scheme for the temporal integration.

In the next chapter, this numerical solver is used to carry out numerical simulations with the aim of characterizing the interaction between a laminar boundary layer of a superheated or subcooled vapor flow and a static liquid pool at saturation temperature.

Chapter 2

Laminar boundary layer

Contents

In the industrial context detailed in the Introduction, thermal laws are needed to predict the physical phenomena involved in the liquid/vapor phase change in a launcher cryogenic tank. To this end, the configuration of a laminar boundary layer of a superheated or subcooled vapor flow shearing a static liquid pool at saturation temperature is first considered. The results obtained for this study have been recently published in International Journal of Thermal Sciences [77].

2.1 Introduction

There is currently little information on how an external flow will modify evaporation or condensation of a liquid pool with a plane surface in spite of its significant interest in various fields, such as processes in thermal engineering, in combustion applications, weather forecasting or climate modeling. Most applications cited above involve turbulent flows and gas mixture. Nevertheless, the simpler configuration where a laminar superheated or subcooled vapor flow is shearing a saturated liquid interface has still never been solved whether theoretical, numerical or experimental approaches are considered. This would be a significant step forward before considering more complex configurations. The theory of an expanding laminar boundary layer of a fluid above a solid plate, known as the Blasius theory [8], has been generalized to account for heat transfer between the fluid and an isothermal plate by Pohlhausen in [75]. Both theories are based on a boundary layer hypothesis assuming that the velocity component in the streamwise direction is much higher than the one in the normal direction to the plate. However, when one considers an expanding boundary layer of a superheated or subcooled vapor flow over a saturated liquid, the latter assumption is no longer valid due to the phase change vapor flow that will respectively blow or aspirate the boundary layer, depending on whether vaporization or condensation occurs. The mathematical complexity of this problem being strongly increased, the resulting flow will exhibit a fully two-dimensional rotational structure for which a classical theoretical analysis can hardly be practiced. Consequently, using fully resolved numerical simulation is a promising alternative for tackling such a problem in order to improve our knowledge in the field of heat transfer in liquid-vapor flow with phase change.

Phase change heat transfer, treated using the so-called conception of the two-phase boundary layer, has been a subject of study in several papers. For example, Koh et al. made an analysis of a saturated vapor in a forced-convection flow over a flat plate in [47] and a vertical plate in [48]. The configuration with film boiling was studied for a forced-convection flow by Cess and Sparrow in [12] and for a free-convection flow by Kaneyasu and Takehiro in [42]. Regarding the interaction between liquid-vapor phase change and two-phase flows, since the seminal works of Renksizbulut and Yuen [82, 83], where correlations on Nusselt number and drag coefficient of evaporating droplets have been designed, a few studies have been dedicated to fully characterize other configurations.

Scriven [94] has proposed 1D theory of bubble growth involving an induced phase change flow motion (radial and irrotational flow). In the context of bubble growth, Ruckenstein and Davis [87] have developed a theoretical study where the external flow is approximated by a potential flow. Nevertheless, rotational effects can have influence both on the viscous friction and the heat flux as it is the case in the present study.

In this chapter, we present a numerical study to characterize the interaction between a superheated or subcooled external laminar vapor flow shearing a static and plane liquid pool at saturation temperature. The Blasius-Pohlhausen theory of an expanding laminar boundary layer over an isothermal plate can be considered as a reference solution. Our purpose is to find, for this configuration, correlations on the Nusselt number accounting for the modification of the local thermal gradient on the interface due to the vaporization or condensation induced flow. As the local structure of the flow is also modified in the vicinity of the liquid-vapor interface, our study includes an analysis on the interfacial viscous friction when phase change occurs.

2.2 Computational configuration of numerical simulations

We consider here the canonical configuration of an expanding Blasius-Pohlhausen boundary layer interacting with a saturated and static liquid pool. Our aim is to investigate the influence of

the external flow on the local heat flux, for an improved knowledge on the interaction between liquid/vapor phase change and fluid mechanics. Even though each different industrial system would require a specific quantitative study, there is a strong interest in understanding local mechanisms in academic configurations. A possible experimental set-up representative of our computations is illustrated in figure 2.1.

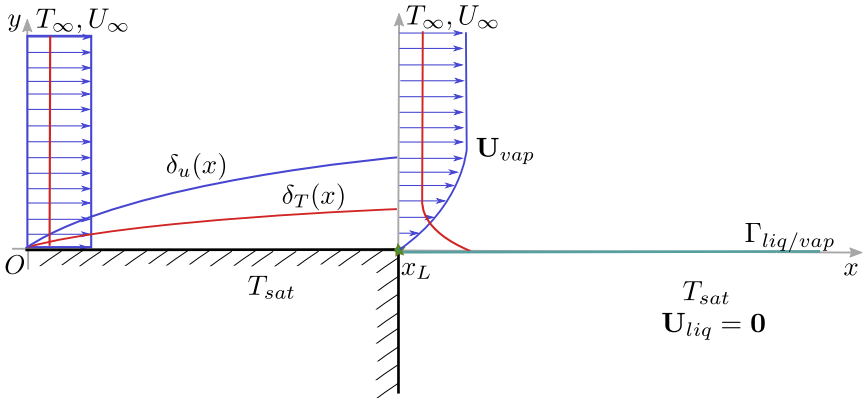

Figure 2.1: Schematics of the expanding Blasius-Pohlhausen boundary layer interacting with a saturated and static liquid pool.

The actual computational domain implemented in our simulations is the liquid/vapor domain (for $x \geqslant x_L$). The interface has a plane shape, which corresponds to the asymptotic case of a high Weber number (high surface tension value). The vapor stream is flowing in the upper part of the domain over a static saturated liquid pool located in the lower part of the computational domain.

2.2.1 Initialization and boundary conditions

An inflow boundary condition is used on the left of the domain for the injection of the superheated or subcooled vapor flow. Given that the purpose of this work is to study the influence of the liquid/vapor phase change on an expanding Blasius-Pohlhausen boundary layer, a boundary layer thickness δ_{x_L} has to be imposed at the inlet of the domain. This boundary layer thickness depends on the length of the solid plate, defined as x_L on the schematics in figure 2.1. It should be emphasized that the results of the present study will directly depend on the inlet boundary layer thickness δ_{x_L}. Such a dependence on the boundary layer thickness is classical in Fluid Mechanics and has been observed for various type of flows as reported in [64, 65] in the framework of primary atomization, for instance.

Velocity and temperature inflow profiles are computed by solving respectively the Prandtl [79] and the Pohlhausen [75] boundary layer equations:

$$f^{'''}(\eta) + \frac{1}{2} f(\eta) f^{'}(\eta) = 0, \tag{2.1}$$

and

$$\theta^{''}(\eta) + \frac{Pr}{2} f(\eta) \theta^{'}(\eta) = 0, \tag{2.2}$$

where $f = \dfrac{u}{U_\infty}$ and $\theta = \dfrac{T - T_{sat}}{\Delta T}$ are the normalized stream function and the non-dimensional temperature, respectively; $\Delta T = T_\infty - T_{sat}$ is the thermal gradient. The boundary conditions are: $\eta = 0 : f = 0, f^{'} = 0; \quad \eta \to \infty : f^{'} = 1$ for equation (2.1) and $\eta = 0 : \theta = 0; \quad \eta \to \infty : \theta = 1$ for equations (2.2). We recall that $\eta \sim \dfrac{y}{\delta}$ is the dimensionless variable, $\delta \sim \sqrt{\dfrac{\nu x}{U_\infty}}$ is the boundary

layer thickness, $Pr = \frac{\mu C_p}{k}$ is the Prandtl number. Equations (2.1) and (2.2) are solved using the Runge-Kutta fourth-order scheme combined with a recursive algorithm.

Free-boundary conditions are used on top and on the right of the computational domain, in order to avoid containment effects and to maintain isobaric conditions.

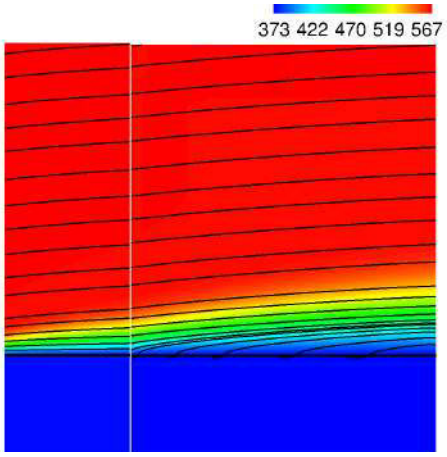

Figure 2.2: Streamlines and temperature profile [K] of a liquid pool evaporating in an superheated gas flow for $Pr = 0.98$, $Re_{x_L} = 211$, $\rho_l/\rho_v = 1623$, $Ja_{vap} = 7.38$; left - classic Blasius boundary layer, right - the boundary layer blown by the vaporization.

As the aim of this work is to characterize a steady solution of the interaction between an external flow and a static liquid pool, it is considered that the interface position is fixed in time in order to maintain a constant liquid height in the computational domain. This assumption is fitting with the schematics of a possible experimental set-up proposed in figure 2.1, if one considers an additional device that allows maintaining a constant liquid level in the liquid pool. Unlike boiling, stationary hypothesis is a classical approximation [98] when considering the evaporation of a liquid (as droplet evaporation for instance) interacting with a superheated vapor since the velocity of the vapor flow is much higher than the interface speed regression.

Moreover, it has been verified that for viscosity ratios $\frac{\mu_{liq}}{\mu_{vap}} \in [2, 56]$ the liquid motion due to the shear stress of the vapor flow on the interface can be neglected in our configurations. Consequently, only the velocity jump condition due to phase change will interact with the external flow. However, such a configuration is consistent with the static liquid hypothesis only if one assumes a sufficiently high density ratio, since the ratio between the interface velocity and the vapor velocity on the interface is close to the density ratio.

The velocity and thermal field are initialized, in the whole domain, with the Blasius-Pohlhausen dynamic and thermal boundary layer profiles, respectively.

2.2.2 Computational domain and mesh grid

To avoid the thermal singularity on the phase change mass flow rate at the inlet plane, we assume that the vapor flow has traveled a distance x_L over an isothermal solid plate before contacting the liquid pool (figures 2.2 and 2.3). Consequently, the boundary layer thickness of the vapor inlet flow depends on this distance x_L that can be accounted for in our dimensionless analysis by defining an inlet Reynolds number Re_{x_L}, such as $Re_{x_L} = \frac{\rho_v U_\infty x_L}{\mu_v}$.

The dimensions of the computational domain are (l_x, l_y) with $l_x = 6.7\delta_{x_L}$, $\delta_{x_L} = \min(\delta_u, \delta_T)$

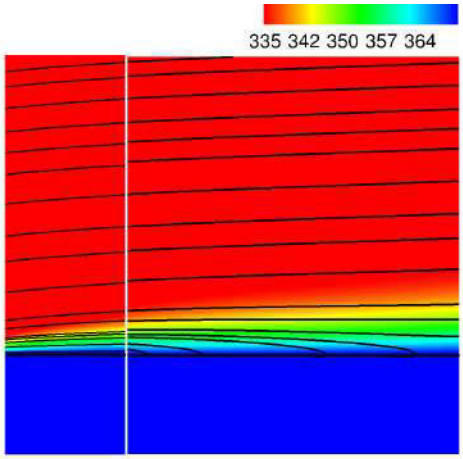

Figure 2.3: Streamlines and temperature profile [K] of a subcooled gas flow condensating in the liquid pool. for $Pr = 0.98$, $Re_{x_L} = 211$, $\rho_l/\rho_v = 1623$, $Ja_{cond} = 0.74$; left - classic Blasius boundary layer, right - the boundary layer "aspirated" by the condensation.

where $\delta_u = 4.92\dfrac{x_L}{\sqrt{Re_{x_L}}}$ and $\delta_T = \delta_u Pr^{-1/3}$ are the dynamic and the thermal boundary layers, respectively.

2.2.2.1 Convergence study

A convergence study with different mesh grids is carried out for both configurations, for a couple of liquid/vapor defined by the following dimensionless numbers: $Pr = 1.022$, $Re_{x_L} = 85.726$, $\frac{\rho_l}{\rho_v} = 17.746$, and two different values for the Jakob number: $Ja_{vap} = 3.69$ and $Ja_{vap} = 8.87$ for the vaporization and $Ja_{cond} = 0.37$ and $Ja_{cond} = 1.15$ for the condensation. The dimensionless numbers are defined as it follows: $Re_x = \dfrac{\rho_v U_\infty x}{\mu_v}$, $Pr = \dfrac{\mu_v C_{p_v}}{k_v}$, $Ja_{vap} = \dfrac{C_{p_v}(T_\infty - T_{sat})}{L}$ and $Ja_{cond} = \dfrac{C_{p_v}(T_{sat} - T_\infty)}{L}$. The subscrit '$v$' is for vapor and '$l$' is for liquid, μ is the viscosity, C_{p_v} is the specific heat, k is the thermal conductivity, $T_\infty - T_{sat}$ is the thermal gradient, U_∞ and T_∞ are the velocity and the temperature in the uniform zone outside the boundary layer.

The local dimensionless coefficient of heat transfer, known also as the local Nusselt number, is defined as

$$Nu_x = \frac{hx}{k} = \frac{\phi_I x}{k\,(T_I - T_\infty)}, \tag{2.3}$$

where h is the convective heat transfer coefficient, ϕ_I is the local heat flux at the liquid/vapor interface and T_I is the liquid/vapor interface temperature, equal to the saturation temperature T_{sat}.

At first glance, the evolution of the Nusselt number seems to be converged with the grid 256×256, for both vaporization (figure 2.4) and condensation (figure 2.5). Nevertheless, the velocity jump at $x = x_L$ from a single-phase boundary layer flow to a phase change boundary layer flow has to be captured and well resolved. As one of the objectives of this numerical study is to define correlations on the Nusselt number, high accuracy is required. Consequently, the mesh grid 1024×1024 is chosen to run the present numerical study. At the inlet, this mesh grid allows to have ~ 150 points in the boundary layer.

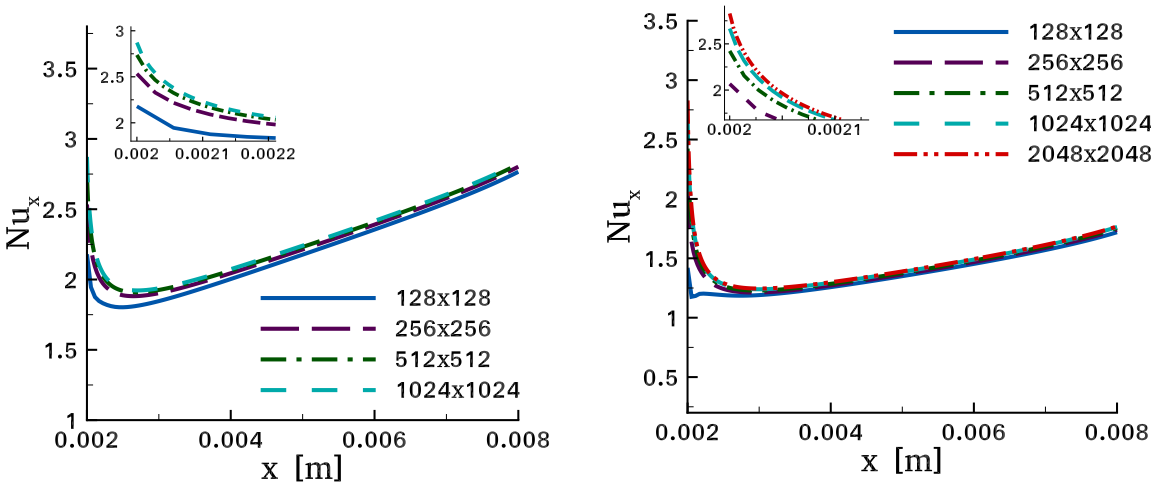

(a) $Ja = 3.69$ (b) $Ja = 8.87$

Figure 2.4: Convergence study for the evolution of the Nusselt number for the vaporization configuration, for the dimensionless numbers: $Re_{x_L} = 85.726$, $Pr = 1.022$, $\frac{\rho_l}{\rho_v} = 17.746$.

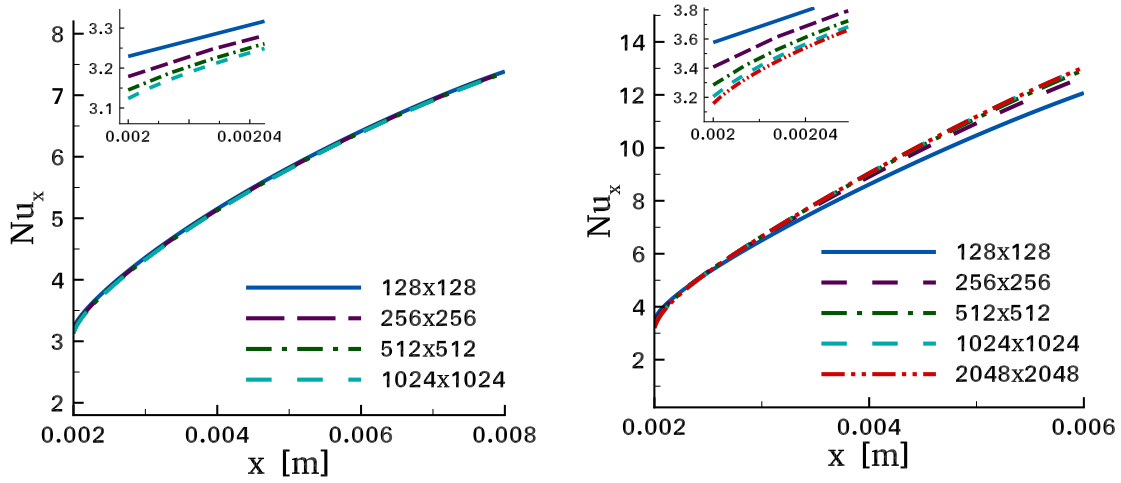

(a) $Ja = 0.37$ (b) $Ja = 1.15$

Figure 2.5: Convergence study for the evolution of the Nusselt number for the condensation configuration, for the dimensionless numbers: $Re_{x_L} = 85.726$, $Pr = 1.022$, $\frac{\rho_l}{\rho_v} = 17.746$.

2.2.2.2 Containment study

Our interest is to compute the spatial development of the thermal and dynamical boundary layers over the saturated liquid pool. Therefore, a containment study is conducted to determine the influence of the computational domain dimensions. In figure 2.6, the containment effects in the y-direction on the Nusselt number evolution are plotted. For the vaporization configuration, the dimension in the normal direction has to be $l_y = 2l_x$ (figure 2.6a), while, in the condensation configuration, $l_y = l_x$ is sufficient to ensure that the numerical solutions do not depend on the computational domain size(figure 2.6b). That can be explained considering that the vaporization has a "blowing" effect on the boundary layer and so a larger domain in the y-direction is needed to assure that the development of the boundary layer is not affected by the upper boundary

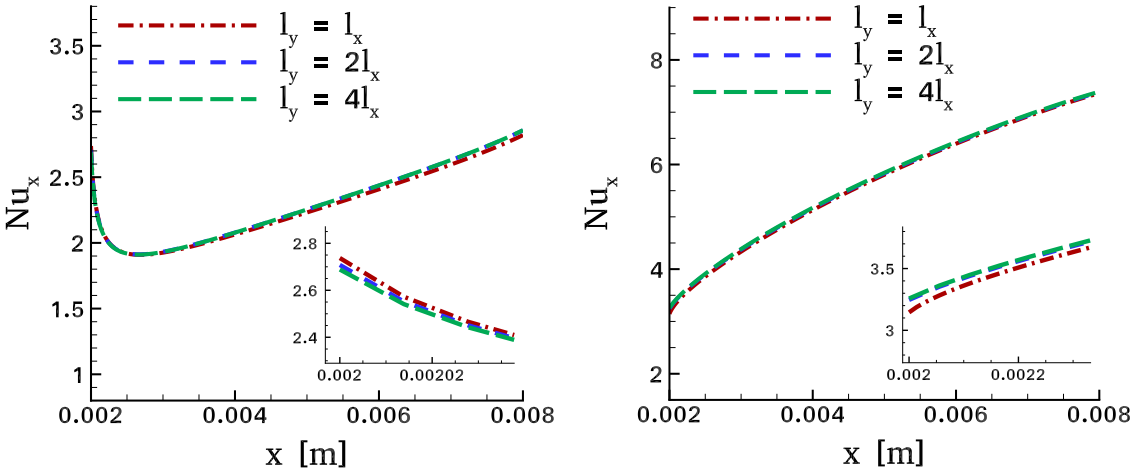

(a) Vaporization, $Ja = 3.69$ (b) Condensation, $Ja = 0.37$

Figure 2.6: Confinement study in the y-direction for the evolution of the Nusselt number, for the dimensionless numbers: $Re_{x_L} = 85.726$, $Pr = 1.022$, $\frac{\rho_l}{\rho_v} = 17.746$.

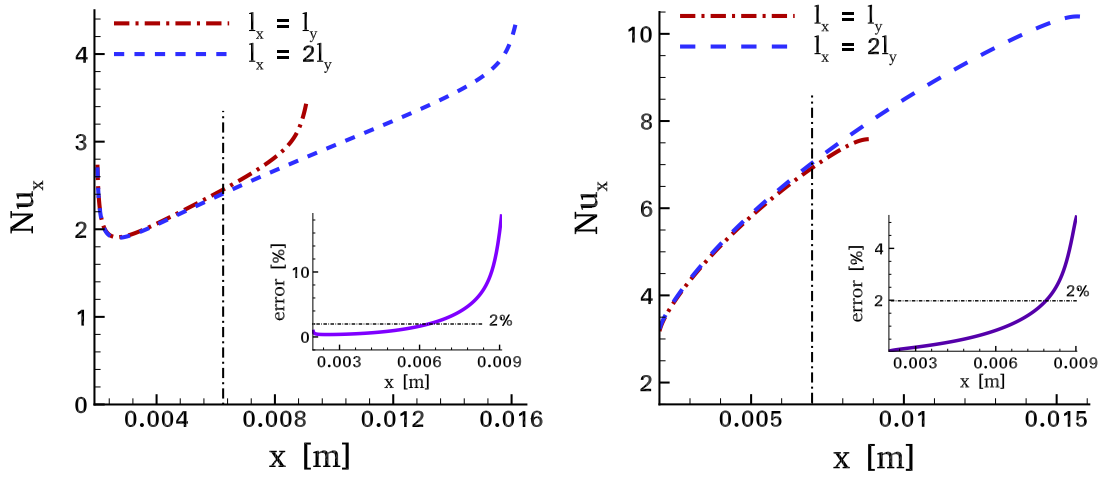

(a) Vaporization, $Ja = 3.69$ (b) Condensation, $Ja = 0.37$

Figure 2.7: Confinement study in the x-direction for the evolution of the Nusselt number, for the dimensionless numbers: $Re_{x_L} = 85.726$, $Pr = 1.022$, $\frac{\rho_l}{\rho_v} = 17.746$.

condition. Unlike vaporization, condensation aspirates the boundary layer, so containement effects have smaller influence on its spatial development.

Following, a containment effects study in the streamwise direction is realized. In figures 2.7a and 2.7b we have plotted the evolution of the Nusselt number for two computational domains: $l_x = l_y$ and $l_x = 2l_y$. In order to have a difference of less than 2% between the two corresponding curves, only 50% of the streamwise length is retained for the parametric study.

2.2.2.3 Upstream containment effects

Even though the present parametric study has been conducted using the computation configuration presented in the previous section, some additional verifications are conducted to ensure that the

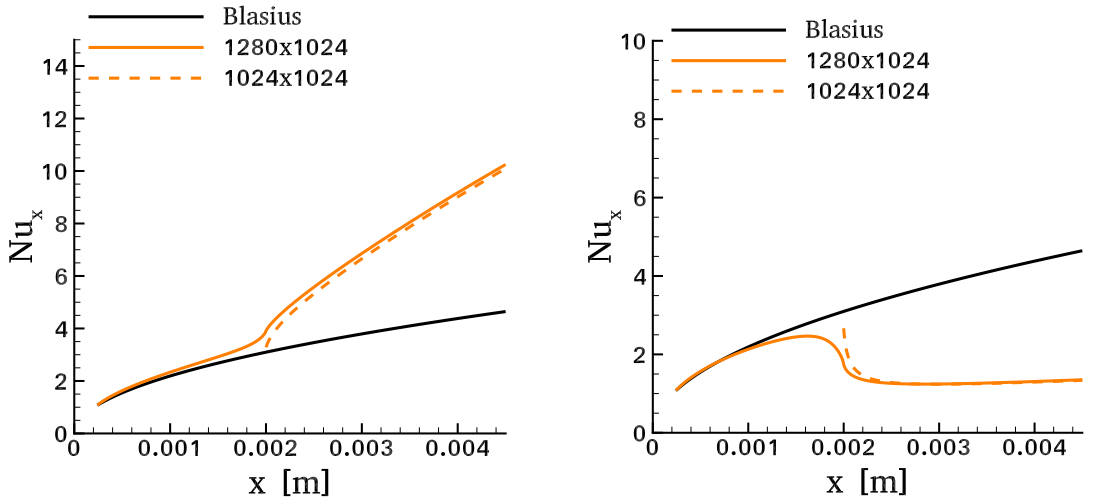

(a) Condensation, $Ja = 1.15$

(b) Vaporization, $Ja = 8.8$

Figure 2.8: The influence of the inflow boundary condition on the evolution of the Nusselt number, for the dimensionless numbers: $Re_{x_L} = 85.726$, $Pr = 1.022$, $\frac{\rho_l}{\rho_v} = 17.746$. The solid line represents the evolution of the Nusselt number when the upstream spatial evolution of the Prandtl-Pohlhausen boundary layer is simulated whereas the dashed line represents the Nusselt evolution when the Prandtl-Pohlhausen boundary layer profile is directly imposed at $x = x_L$.

upstream containment effects do not have a significant influence on the Nusselt number evolution (figure 2.8).

A conditioning section is added, where the boundary layer is spatially developing from a certain point $x = x_{L_0}$ to $x = x_L$. The phase change is plugged at x_L and we want to investigate the differences between imposing a Blasius profile at the inlet plane (dashed lines in figure 2.8) and simulating its development upstream (solid lines in figure 2.8). Even if the computational domain starts before the point $x = x_L$, the evolution of the Nusselt number is not affected at all in the far field and only weakly affected in the inlet vicinity.

To conclude, the computational domain used in our parametric study is defined by $l_y = 2l_x$ for the vaporization and $l_y = l_x$ for the condensation configuration, where $l_x = 6.7\delta_{x_L}$. The corresponding mesh grids used are 1024×2048 and 1024×1024, respective to vaporization or condensation. Additionally, after the containment study in x-direction, only the $[x_L, x_L + l_x/2]$ Nusselt evolution will be considered for the parametric study.

2.3 Results

2.3.1 Spatial evolution of the Nusselt number

The spatial evolution of the Nusselt number along the longitudinal coordinate x is showed in figure 2.9a for vaporization, and in figure 2.9b for condensation, for a couple of liquid/vapor defined by the following dimensionless numbers: $Pr = 1.022$, $Re_{x_L} = 85.726$, $\rho_l/\rho_v = 17.746$, and different values of Jakob number. One can see that the Nusselt number is lower for vaporization and higher for condensation than the Nusselt number obtained from the Blasius theory. Indeed, as observed in figure 2.2, when vaporization occurs, the thermal boundary layer being thickened due to the

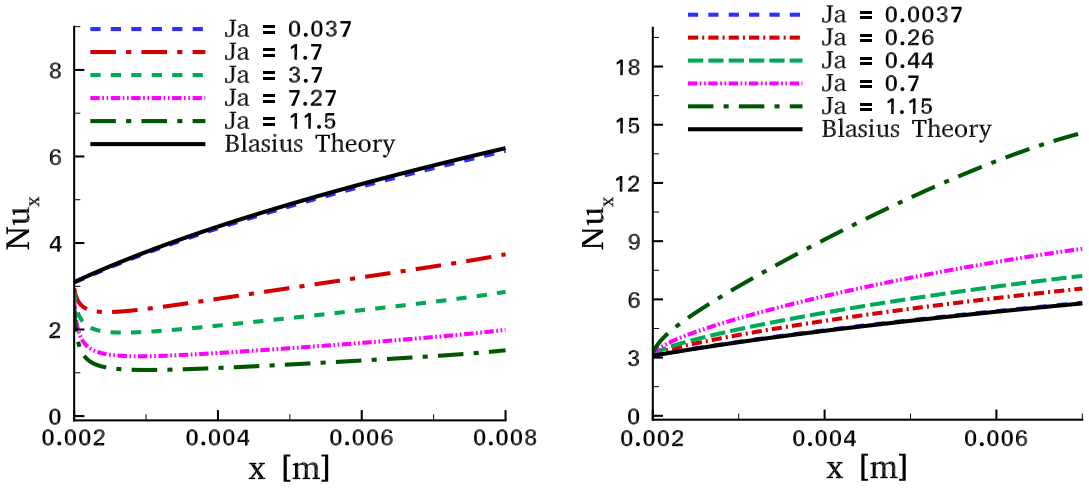

(a) Vaporization (b) Condensation

Figure 2.9: Spatial evolution of the Nusselt number for the dimensionless numbers: $Re_{x_L} = 85.726$, $Pr = 1.022$, $\rho_l/\rho_v = 17.746$ and different values of the Jakob number.

expansion flow of vapor, the heat transfer coefficient decreases. The same trend was observed by Yan and Soong in [109], where the convective heat and mass transfers along an inclined heated plate with film evaporation was studied. On the other hand, the condensation involves an aspirating flow towards the liquid/vapor interface, as it can be visualized in figure 2.3. As this flow decreases the thermal boundary layer thickness, the heat transfer coefficient is increased.

For the vaporization, the minimum value observed on the Nusselt number can be related to the rapid decrease of the heat flux in the vicinity of the inlet flow, figure 2.10a. This can be explained by the connecting zone between the Blasius-Pohlhausen expanding boundary layer (for $x < x_L$) and the established flow in interaction with the phase change (for $x >> x_L$).

On the other hand, given that the "aspirating" effect of the condensation increases the local heat flux, it is only natural to observe that the the latter has a maximum value, as it can be seen in figure 2.10b. The heat flux increases at first due to the boundary layer thinning by the condensation flow and it is followed by a decrease due to the spatial evolution of the boundary layer.

Figure 2.9 also illustrates the influence of the Jakob number on the spatial evolution of the Nusselt number. The increase of the Jakob number implies an increase of the vapor/liquid phase change and therefore the Nusselt number decreases or increases if vaporization or condensation is respectively concerned, as expected. Figures 2.9a and 2.9b are now compared in regard to the influence of the Jakob number on the Nusselt number evolution. If the Jakob number is doubled and then tripled, in the case of the boundary layer "blown" by the liquid pool vaporization, a decrease of the intervals between the succesives curves is observed, while if the boundary layer is "aspirated" by the condensation, the intervals between the succesives curves increase. These unanticipated results will be further explained, but first, the correlations on the Nusselt number will be presented.

2.3.2 Correlations on the Nusselt number

A parametric study was conducted to determine how the Nusselt number is varying with the dimensionless numbers characterizing our configuration. These dimensionless numbers can be

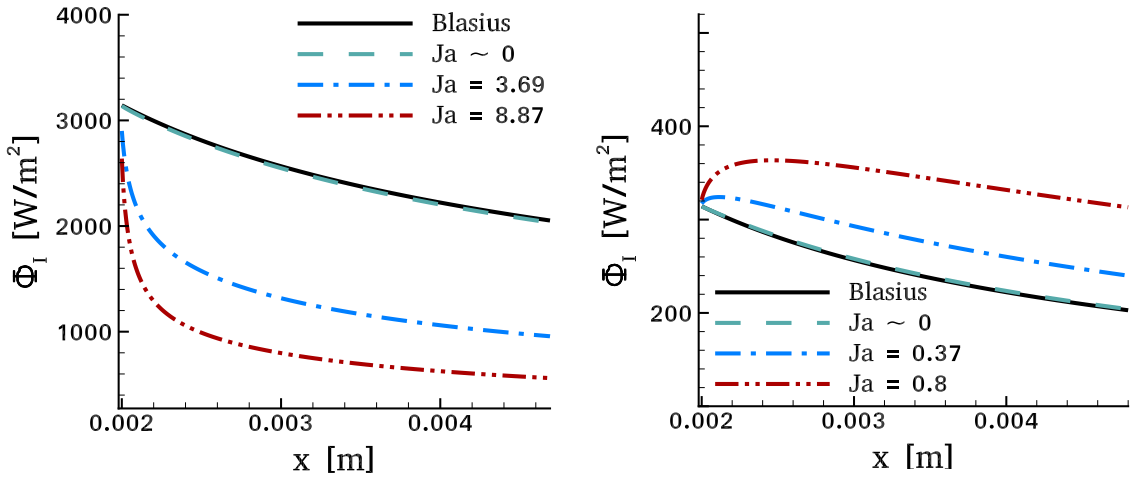

(a) Vaporization

(b) Condensation

Figure 2.10: Evolution of the local heat flux Φ_I with the x-axis for the dimensionless numbers: $Re_{x_L} = 85.726$, $Pr = 1.022$, $\rho_l/\rho_v = 17.746$ and different values of the Jakob number.

deduced from the physical equations as it follows:

- the Reynolds number Re_x from the momentum balance (1.11),
- the Prandtl number Pr from the energy conservation equation (1.13),
- the Jakob number Ja from the balance of energy at the interface (1.19),
- the density ratio $\dfrac{\rho_l}{\rho_v}$ from the jump condition on the mass conservation (1.15).

To ensure that when one dimensionless number is varied the other three are constants, the physical variables varied in this parametric study are the velocity U_∞ for the Reynolds number, the thermal conductivity of the vapor k for the Prandtl number, the latent heat L for the Jakob number and the liquid density ρ_l for the density ratio.

The range of values for our parametric study was: $Re_{x_L} = (15; 1250)$, $Pr = (0.6; 8)$, $Ja = (0.00037; 8.87)$ and $\rho_l/\rho_v = (10; 5000)$, with approximately fifty simulations for each configuration.

By fitting the numerical Nusselt number evolution obtained in all of our simulations, we have found general correlations that depend on the dimensionless numbers characterizing this configuration. In what follows, the resulting correlations are presented separately for the vaporization and for the condensation. For the sake of simplicity, the approach to find these correlations is described in Appendix A. Both correlations are designed by adding correction terms to the Nusselt number from the Blasius theory which is defined as $Nu_x^{Bl} = 0.332 Pr^{0.333} Re_x^{0.5}$.

2.3.2.1 Vaporization

The correlation for the Nusselt number with vaporization has the following expression

$$Nu_x^{vap} = Nu_x^{Bl} - \left(\alpha \left(\frac{x}{x_L} - 1\right)^n + \beta\right) H(x - x_L), \tag{2.4}$$

where $H(x - x_L)$ is the Heaviside function who has a non-zero value only for $x > x_L$, α, β and n have the following expressions

$$\alpha = 0.294 Re_{x_L}^{0.495} Pr^{0.333} \left(1 - e^{-0.0248\left(Ja\left(\frac{\rho_l}{\rho_v}-1\right)\right)}\right),$$

$$n = 0.935 Re_{x_L}^{-0.11} Pr^{-0.07} Ja^{-0.1} \frac{\rho_l}{\rho_v}^{-0.12},$$

$$\beta = 0.119 Re_{x_L}^{0.477} Pr^{0.237} \left(1 - e^{-0.0043 Ja\left(\frac{\rho_l}{\rho_v}-1\right)}\right).$$

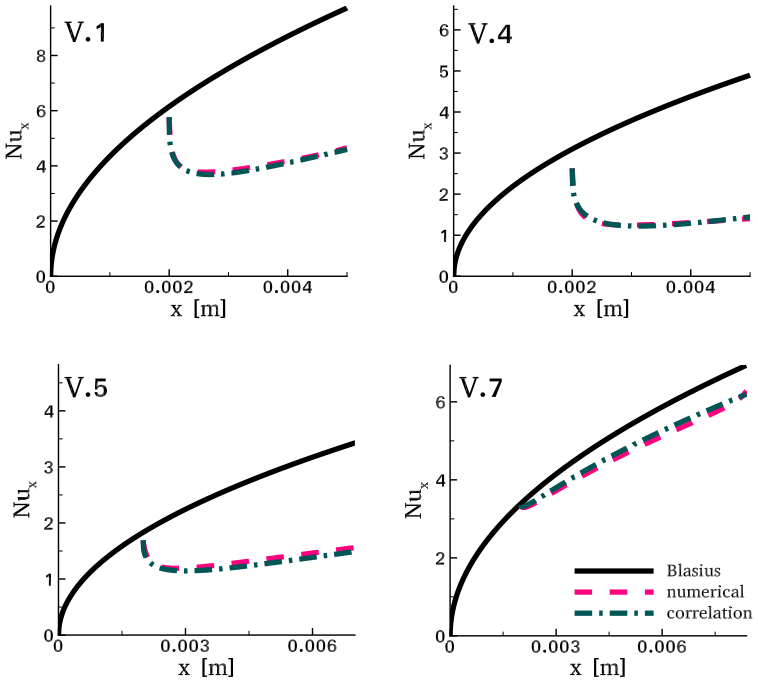

Figure 2.11: Spatial evolution of the Nusselt number for different configurations extracted from Table 2.1 for the case involving vaporization.

2.3.2.2 Condensation

In the configuration involving condensation, the correlation on the Nusselt number writes as

$$Nu_x^{cond} = Nu_x^{Bl} + \left(\gamma \left(\frac{x}{x_L} - 1\right)^m + \eta\right) H(x - x_L), \tag{2.5}$$

where γ, η and m have the following expressions

$$\gamma = 0.0854 Re_{x_L}^{0.483} Pr^{0.356} \left(e^{0.1018 Ja\left(\frac{\rho_l}{\rho_v}-1\right)} - 1\right),$$

$$m = 0.519 Re_{x_L}^{-0.045} Pr^{-0.042} e^{0.02985 Ja \frac{\rho_l}{\rho_v}},$$

$$\eta = 0.00042 Re_{x_L}^{0.426} Pr^{0.55} \left(Ja\left(\frac{\rho_l}{\rho_v} - 1\right)\right)^{1.25}.$$

2.3.3 Validation of the proposed correlations

For the sake of validation of the proposed correlations, we present in Table 2.1, for various configurations, the average relative error $\bar{\epsilon}$ and the maximum relative error ϵ_{max}, between the computed Nusselt number and the correlations. The relative error is defined as: $\epsilon = \left(Nu_x^{correl} - Nu_x^{num}\right)/Nu_x^{num}$.

The average relative error between the Nusselt number from DNS and the correlation is less than 2% for condensation and less than 5% for vaporization. The higher error in the vaporization configuration is due to the transition zone near the inlet plane $x = x_L$ (figure 2.9a). A good fit of this region was not straightforward. If one would search only the evolution of the Nusselt number far enough from the inlet plane, the correlation would be less complex and more accurate. We add also that most of the values chosen to be displayed in Table 2.1 are situated at the limits of the interval range of values studied here.

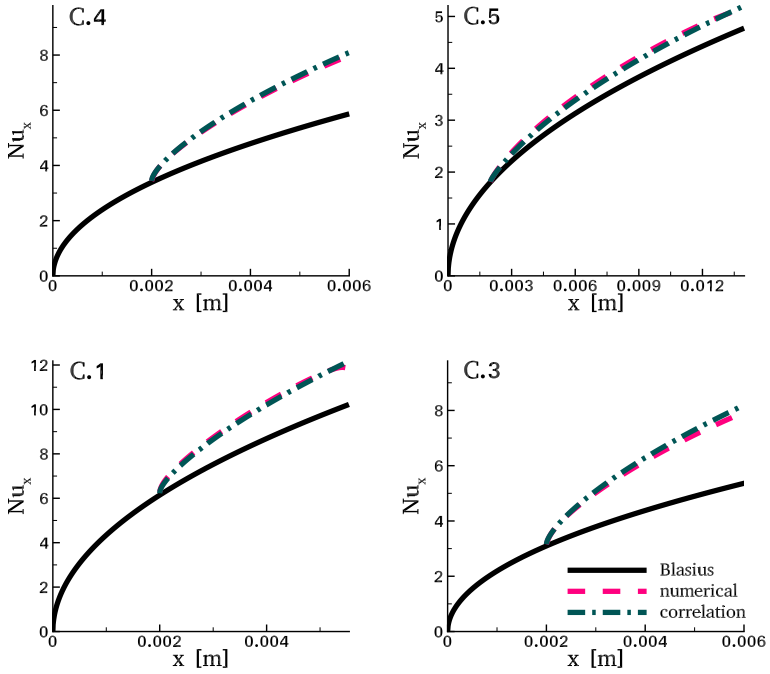

Figure 2.12: Spatial evolution of the Nusselt number for different configurations extracted from Table 2.1 for the case involving condensation.

Comparisons between the proposed correlations and numerical results are also plotted in figure 2.11 for the vaporization and in figure 2.12 for the condensation for different configurations from Table 2.1.

2.3.4 Asymptotic cases

The correlations on the Nusselt number can be simplified when considering asymptotic cases, as it will be shown in the following paragraphs.

Table 2.1: The average relative error and the maximum relative error for the Nusselt number for different couples of dimensionless numbers.

	Condensation	$\bar{\epsilon}$ [%]	ϵ_{max} [%]
C.1	$Pr = 8$, $Re_{x_L} = 85.726$ $Ja = 0.37$, $\frac{\rho_l}{\rho_v} = 17.6$	1.028	1.171
C.2	$Pr = 0.98$, $Re_{x_L} = 1250$ $Ja = 0.179$, $\frac{\rho_l}{\rho_v} = 1623$	0.58	0.75
C.3	$Pr = 1.022$, $Re_{x_L} = 85.726$ $Ja = 0.7$, $\frac{\rho_l}{\rho_v} = 17.6$	0.65	1.34
C.4	$Pr = 0.98$, $Re_{x_L} = 105.51$ $Ja = 0.179$, $\frac{\rho_l}{\rho_v} = 5000$	0.28	0.32
C.5	$Pr = 0.98$, $Re_{x_L} = 30$ $Ja = 0.179$, $\frac{\rho_l}{\rho_v} = 1623$	1.38	1.6
C.6	$Pr = 6$, $Re_{x_L} = 105.51$ $Ja = 0.179$, $\frac{\rho_l}{\rho_v} = 1623$	1.69	1.8
C.7	$Pr = 0.98$, $Re_{x_L} = 105.51$ $Ja = 0.29$, $\frac{\rho_l}{\rho_v} = 1623$	0.57	0.703
	Vaporization	$\bar{\epsilon}$ [%]	ϵ_{max} [%]
V.1	$Pr = 8$, $Re_{x_L} = 85.726$ $Ja = 3.69$, $\frac{\rho_l}{\rho_v} = 17.6$	1.56	7
V.2	$Pr = 0.98$, $Re_{x_L} = 1250$ $Ja = 0.179$, $\frac{\rho_l}{\rho_v} = 1623$	1.09	1.45
V.3	$Pr = 1.022$, $Re_{x_L} = 85.726$ $Ja = 8.87$, $\frac{\rho_l}{\rho_v} = 17.6$	2.13	9.4
V.4	$Pr = 0.98$, $Re_{x_L} = 105.51$ $Ja = 0.179$, $\frac{\rho_l}{\rho_v} = 3500$	2.4	2.8
V.5	$Pr = 1.022$, $Re_{x_L} = 30$ $Ja = 3.69$, $\frac{\rho_l}{\rho_v} = 17.6$	4.8	6
V.6	$Pr = 1.022$, $Re_{x_L} = 85.726$ $Ja = 3.69$, $\frac{\rho_l}{\rho_v} = 5$	1.8	2.69
V.7	$Pr = 0.98$, $Re_{x_L} = 105.51$ $Ja = 0.3598$, $\frac{\rho_l}{\rho_v} = 1623$	2.17	2.64

2.3.4.1 Asymptotic cases for the vaporization Nusselt number correlation

If $Ja \to 0$, the approximation of the terms depending on the Jakob number yields simpler expressions for the parameters α and β from equation (2.4),

$$\alpha(Ja \to 0) = 0.0073Ja\left(\frac{\rho_l}{\rho_v} - 1\right) Re_{x_L}^{0.495} Pr^{0.333},$$

and

$$\beta(Ja \to 0) = 0.0005Ja\left(\frac{\rho_l}{\rho_v} - 1\right) Re_{x_L}^{0.477} Pr^{0.237}.$$

This asymptotic case brings out a linear evolution of the Nusselt number, both with the Jakob number and the density ratio, for low vaporization rate.

When $Ja = 0$, the correction terms equal to 0 as the jump condition on the velocity field is zero. Hence, the boundary layers are not modified and the expression of the Nusselt number fits simply with the one obtained with the Blasius theory.

Considering the asymptotic cases $Ja \to \infty$ or $\rho_l/\rho_v \to \infty$, it can be shown that in the vaporization case, the expression of the Nusselt number tends towards a saturation value:

$$Nu_x^{vap}\left(Ja \to \infty\right) \to Nu_x^{Bl} - \left(0.294Re_{x_L}^{0.495}Pr^{0.333} + 0.119Re_{x_L}^{0.4777}Pr^{0.2374}\right).$$

It can be explained by remarking that an increase of the vapor superheat tends to increase the local heat flux on the interface, and thus, the jump on the normal velocity. As this jump condition tends to thicken the thermal boundary layer and thus to decrease the local heat flux, the saturation effect results from an equilibrium state between these two antagonistic effects.

2.3.4.2 Asymptotic cases for the condensation Nusselt number correlation

The expression of the Nusselt number in the condensation case is now presented for a low Jakob number.

If $Ja \to 0$, equation (2.5) becomes

$$Nu_x^{cond} \simeq Nu_x^{Bl} + \gamma\left(\frac{x}{x_L} - 1\right)^m H(x - x_L),$$

with

$$\gamma(Ja \to 0) = 0.0087Ja\left(\frac{\rho_l}{\rho_v} - 1\right) Re_{x_L}^{0.483} Pr^{0.356},$$

and

$$m(Ja \to 0) = 0.519Re_{x_L}^{-0.045} Pr^{-0.042},$$

considering

$$\eta(Ja \to 0) = 0.$$

As for the vaporization, when $Ja = 0$, the Nusselt number simply fits with the Blasius theory.

Moreover, if $Ja \to \infty$ or $\rho_l/\rho_v \to \infty$, an opposite trend to the one observed for vaporization is reported. In the case of condensation, the oncoming subcooled flow being aspirated towards the interface, the thickness of the thermal boundary layer is reduced. This leads to an increase of the local heat transfer as it can be visualised in figure 2.9b. It is found that in the case of condensation, no saturation effect on the Nusselt number is observed neither in the numerical simulations, nor in the expression of the proposed correlation equation (2.5). This can be understood by remarking that, compared to vaporization, in the case of condensation, the jump condition on the normal velocity is of opposite direction, favoring the local heat transfer.

These trends have also been observed when figure2.9a and figure2.9b were compared regarding to the influence of the Jakob number on the evolution of the Nusselt number.

2.3.5 Normal velocity and thermal flux interdependency

In what follows, we search to explain the Nusselt number evolution by means of an analysis on the normal velocity evolution when phase change occurs considering only the vaporization configuration.

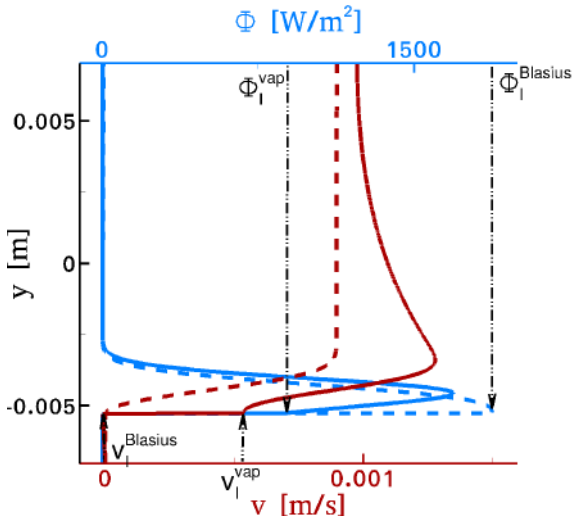

Figure 2.13: Evolution of the normal velocity v and the thermal flux Φ for the vaporization study case for $Pr = 1.022$, $Re_{x_L} = 85.726$, $\rho_l/\rho_v = 17.746$, $Ja_{vap} = 3.69$: dashed line - Blasius theory, solid line - vaporization configuration.

Figure 2.13 illustrates the evolution of the normal velocity $v\left(x^f, y\right)$ and the thermal flux $\Phi\left(x^f, y\right) = k_v \dfrac{\partial T}{\partial y}\left(x^f, y\right)$ with the y-axis for a fixed value of $x = x^f$. The interface between the liquid and the vapor phase is situated at $y_I = -5\ mm$. The normal velocity in the liquid phase can be neglected compared to the vapor phase. At the liquid/vapor interface there is an important variation of the normal velocity value between the Blasius theory and the vaporization configuration. Following, the change in the evolution of the normal velocity with y when vaporization occurs is related directly to the mass flow rate.

The thermal flux is non-zero only close to the liquid/vapor interface, as expected. Unlike the classical Blasius theory, where the thermal flux is induced only by conduction, in the phase change configuration there is a significant influence of the thermal convection in the transverse direction.Thereby, it can be understood that the discontinuity on the Nusselt number is induced by the jump condition on the normal velocity field.

2.3.6 Integrated heat flux

The integrated heat flux exchanged at the liquid/vapor interface can be calculated from the correlations on the Nusselt number (2.4) and (2.5).

2.3.6.1 Vaporization

Given the expression (2.4) of the Nusselt number when vaporization happens, the heat flux per unit of width, integrated between x_L and x is defined as

$$\Phi^{vap}(x,x_L) = \int_{x_L}^{x} \phi^{vap}(x)dx = k\left(T_\infty - T_{sat}\right)\int_{x_L}^{x} \frac{Nu^{vap}(x)}{x}dx$$
$$= k\left(T_\infty - T_{sat}\right)\left(\int_{x_L}^{x} \frac{Nu^{Bl}(x)}{x}dx - \alpha\int_{x_L}^{x} \frac{\left(\frac{x}{x_L}-1\right)^n}{x}dx - \beta\int_{x_L}^{x}\frac{1}{x}dx\right). \quad (2.6)$$

The different components of equation (2.6) are calculated as it follows

$$\int_{x_L}^{x} \frac{Nu^{Bl}(x)}{x}dx = 2\left(Nu^{Bl}(x) - Nu^{Bl}(x_L)\right), \quad (2.7)$$

$$\int_{x_L}^{x} \frac{\left(\frac{x}{x_L}-1\right)^n}{x}dx = \frac{\left(\frac{x}{x_L}\right)^n {}_2F_1\left(-n,-n;1-n,\frac{x_L}{x}\right)}{n} - \pi\csc(\pi n), \quad (2.8)$$

where $\csc(\pi n) = 1/sin(\pi n)$ is the cosecant function and ${}_2F_1\left(-n,-n;1-n;\frac{x_L}{x}\right)$ is the Gauss hypergeometric function, defined as

$${}_2F_1\left(a,b;c;z\right) = \frac{\Gamma(c)}{\Gamma(a)\Gamma(b)}\sum_{k=0}^{\infty}\left(\frac{\Gamma\left(a+k\right)\Gamma\left(b+k\right)}{\Gamma\left(c+k\right)}\frac{z^k}{k!}\right),$$

with $\Gamma(a) = (a-1)!$ the gamma function, and

$$\int_{x_L}^{x}\frac{1}{x}dx = \ln(\frac{x}{x_L}). \quad (2.9)$$

Substituting the expressions of equations (2.7), (2.8), (2.9) in equation (2.6) leads to

$$\int_{x_L}^{x}\Phi^{vap}(x,x_L)dx = k\left(T_\infty - T_{sat}\right)\left\{2\left[Nu^{Bl}(x) - Nu^{Bl}(x_L)\right] - \right.$$
$$\left. - \alpha\left[\frac{\left(\frac{x}{x_L}\right)^n {}_2F_1\left(-n,-n;1-n,\frac{x_L}{x}\right)}{n} - \pi\csc(\pi n)\right] - \beta\ln\left(\frac{x}{x_L}\right)\right\}. \quad (2.10)$$

If we also consider the region $x \in (0, x_L)$ where the boundary layer is evolving without interacting with the vaporization, the following expression for the heat flux per unit of width is obtained

$$\Phi(x,x_L) = \int_0^{x_L}\phi^{Bl}(x)dx + \int_{x_L}^{x}\phi^{vap}(x)dx = k\left(T_\infty - T_{sat}\right)\left\{2Nu^{Bl}(x) - \right.$$
$$\left. - \left[\alpha\left(\frac{\left(\frac{x}{x_L}\right)^n {}_2F_1\left(-n,-n;1-n,\frac{x_L}{x}\right)}{n} - \pi\csc(\pi n)\right) + \beta\ln\left(\frac{x}{x_L}\right)\right]H(x-x_L)\right\}. \quad (2.11)$$

The expression (2.11) of the integrated heat flux is plotted in Fig 2.14. The black curve represents the integrated flux exchanged if the boundary layer evolved without interacting with the liquid vaporization. The dotted lines depict the x-evolution of the thermal flux exchanged at the liquid/vapor interface from x_L to L_x for different values of the Jakob number. As expected, the vaporization reduces the exchanged heat flux.

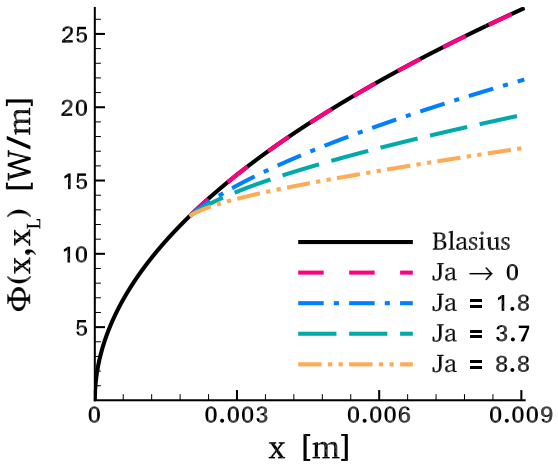

Figure 2.14: Vaporization configuration - The x-evolution of the integrated exchanged thermal flux at the interface for $Pr = 1.022$, $Re_{x_L} = 85.726$, $\rho_l/\rho_v = 17.746$ and different values of the Jakob number.

2.3.6.2 Condensation

For the configuration with condensation, the approach to calculate the exchanged heat flux is the same as for the vaporization. Considering the expression (2.5) of the Nusselt number, the exchanged heat flux per unit of width is expressed as

$$\Phi(x,x_L) = \int_0^{x_L} \phi^{Bl}(x)dx + \int_{x_L}^{x} \phi^{cond}(x)dx = k\left(T_\infty - T_{sat}\right)\Bigg\{2Nu^{Bl}(x) + \\ + \left[\gamma\left(\frac{\left(\frac{x}{x_L}\right)^m {}_2F_1\left(-m,-m;1-m,\frac{x_L}{x}\right)}{m} - \pi\csc(\pi m)\right) + \eta\ln\left(\frac{x}{x_L}\right)\right]H(x-x_L)\Bigg\}. \quad (2.12)$$

The evolution of the integrated heat flux is plotted in figure 2.15. The black curve represents the integrated flux exchanged if the boundary layer evolved without interacting with the condensation. The dotted lines depict the x-evolution of the exchanged heat flux at the liquid/vapor interface from x_L to L_x for different values of the Jakob number. The exchanged heat flux is increased by the condensation.

2.3.7 Viscous friction

We now examine the influence of the liquid/vapor phase change on the viscous friction. Given the 2D expression of the viscous stress tensor,

$$\bar{\bar{\tau}} = \begin{pmatrix} 2\mu\dfrac{\partial u}{\partial x} & \mu\left(\dfrac{\partial u}{\partial y} + \dfrac{\partial v}{\partial x}\right) \\ \mu\left(\dfrac{\partial u}{\partial y} + \dfrac{\partial v}{\partial x}\right) & 2\mu\dfrac{\partial v}{\partial y} \end{pmatrix}, \quad (2.13)$$

at the interface of normal vector $\mathbf{e}_y$, the stress vector $\mathbf{T} = \bar{\bar{\tau}}\cdot\mathbf{e}_y$ has the following normal and shear components: $\mathbf{T}\cdot\mathbf{e}_y = \mu\dfrac{\partial v}{\partial y}$ and $\mathbf{T}\cdot\mathbf{e}_x = \mu\left(\dfrac{\partial u}{\partial y} + \dfrac{\partial v}{\partial x}\right)$. Their spatial evolution is plotted in

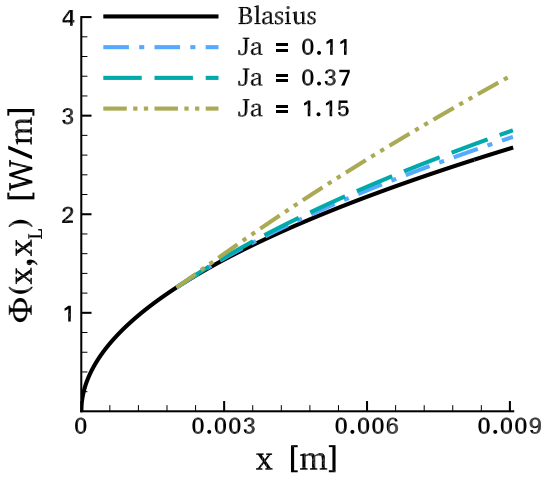

Figure 2.15: Condensation configuration - The x-evolution of the integrated exchanged thermal flux at the interface for $Pr = 1.022$, $Re_{x_L} = 85.726$, $\rho_l/\rho_v = 17.746$ and different values of the Jakob number.

figure 2.16 for the configuration with vaporization at a high Jakob number, $Ja_{vap} = 8.8$. Excluding the zone $x = x_L$, the normal component of the stress vector is negligible against the tangential component by a factor of 100. The same result is found for the classical Blasius boundary layer theory, see for example [92], where only the shear component is accounted for in the viscous friction analysis. In figure 2.16, the evolution of the shear component of the stress vector with and without vaporization (Blasius theory) has the same trend, except for the zone close to $x = x_L$. The difference in this zone comes from the singularity on the gradient computation.

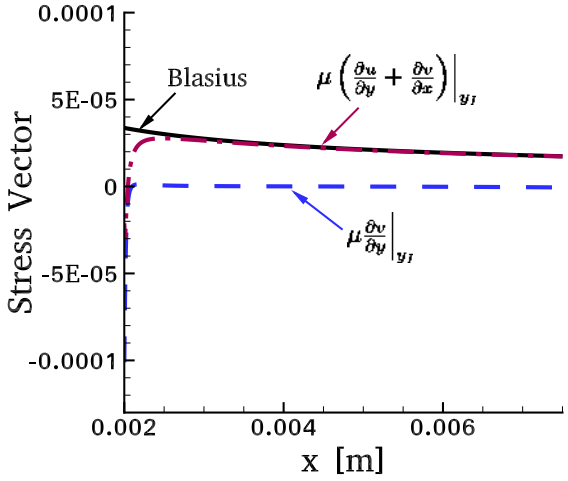

Figure 2.16: Spatial evolution of the normal and the shear components of the stress vector $\mathbf{T}$ for the dimensionless numbers $Pr = 1.022$, $Re_{x_L} = 85.726$, $\rho_l/\rho_v = 17.746$ and $Ja_{vap} = 8.8$.

We now consider the friction coefficient, expressed as the ratio between the interfacial friction and the dynamic pressure:

$$\frac{C_f}{2} = \frac{\tau_I}{\rho U_\infty^2}, \tag{2.14}$$

where τ_I is the shear component of the stress vector at the interface. We recall that for the Blasius

theory, considering $\frac{\partial u}{\partial y} >> \frac{\partial v}{\partial x}$, the friction coefficient reads

$$\frac{C_f}{2} = \frac{\mathrm{d}\delta_2}{\mathrm{d}x} = \frac{0.332}{\sqrt{Re_x}}, \tag{2.15}$$

as a result of

$$\tau_I = \mu\frac{\partial u}{\partial y} = \mu U_\infty \sqrt{\frac{\rho U_\infty}{\mu x}} f''(\eta) = \mu\frac{U_\infty}{x}\sqrt{Re_x} f''(\eta), \tag{2.16}$$

and for $y = y_I$, $f''(\eta = 0) = 0.332$.

In figure 2.17 is plotted the evolution of the friction coefficient for the three configurations, i.e. Blasius theory, vaporization and condensation. One can see that, surprisingly, the phase change does not influence the viscous friction at the liquid/vapor interface, despite the modification of the velocity field in the vicinity of the interface.

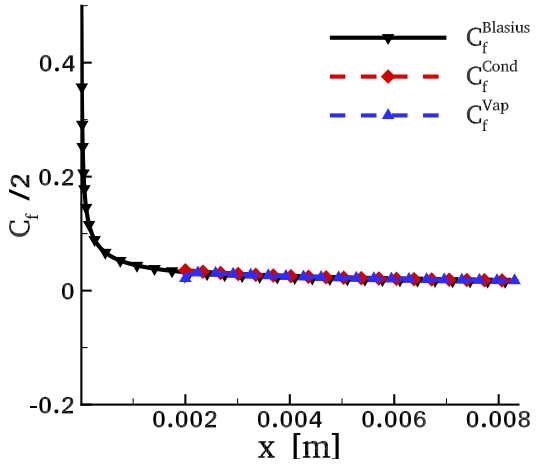

Figure 2.17: Evolution of the friction coefficient for: $Pr = 1.022$, $Re_{x_L} = 85.726$, $\rho_l/\rho_v = 17.746$, $Ja_{vap} = 3.69$ and $Ja_{cond} = 0.369$.

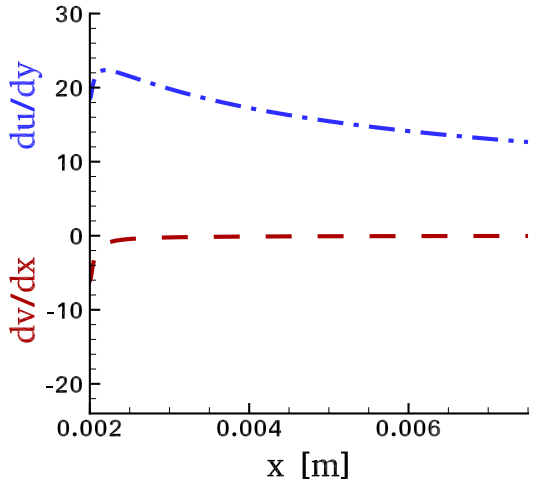

Figure 2.18: Evolution of the velocity gradients $\partial v/\partial x$ and $\partial u/\partial y$ for: $Pr = 1.022$, $Re_{x_L} = 85.726$, $\rho_l/\rho_v = 17.746$, $Ja_{vap} = 3.69$.

As it can be seen in figure 2.18, the derivative $\partial v/\partial x$ influence on the viscous coefficient is less important than the derivative $\partial u/\partial y$. Therefore, in order to justify the relevance of the result obtained above, we will further take a look at the normal velocity at the liquid/vapor interface. For the sake of simplicity we will take only the example of the vaporization.

In figure 2.19, the evolution of the tangential velocity with the y-axis is plotted for $x = \frac{l_x}{2}$. It is noteworthy that the evolution of the tangential velocity profile in the vaporization configuration is almost identical to the Blasius boundary layer velocity profile, despite the vapor blowing in the normal direction due to phase change. The liquid motion due to the shear stress of the vapor flow on the interface is negligible (see the zoom at the bottom left of the figure). Moreover, there is little modification of the tangential velocity profile at the liquid/vapor interface (for $y = -0.005$ m) (see the zoom situated in the middle right of the graphics). This explains why only marginal modifications of the interfacial friction coefficient are observed.

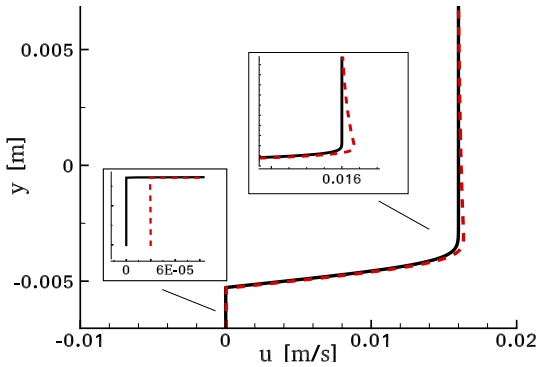

Figure 2.19: Evolution of the tangential velocity u for the vaporization study case for $Pr = 1.022$, $Re_{x_L} = 85.726$, $\rho_l/\rho_v = 17.746$, $Ja_{vap} = 3.69$: black line - Blasius theory, red dashed line - vaporization configuration. Zoom on the liquid region (the bottom left) and on the zone close to the interface (middle right).

2.4 Conclusion

Based on numerical simulations, we obtain correlations on the influence of an external flow on the vaporization or condensation of a static liquid pool. It is shown that the local flow, induced by the phase change, decreases or increases, respectively, the local heat flux, depending upon vaporization or condensation is considered.

For the vaporization configuration it was found that the Nusselt number, and therefore the heat transfer, decreases exponentially with the Jakob number until reaching a saturation value. The opposite trend is observed for the condensation, for which the Nusselt number increases as an exponential function of the Jakob number.

The obtained Nusselt number correlations have allowed to determine the expressions of the integrated heat flux over the liquid/vapor interface.

Another noteworthy result is about the viscous friction on the interface, or the tangential component of the viscous tensor, which is weakly affected by the phase change in the case of a plane interface. Additionally, given the evolution of the normal velocity v with y, the influence of the phase change on the normal component of the viscous tensor is still very weak in comparison to the tangential one, as it is the case for the classical Blasius boundary layer. Moreover, even if the profiles are not superimposed, it can be qualitatively observed that the derivative $\frac{\partial v}{\partial y}$ is in the

same order of magnitude with or without phase change. This is why we can conclude that the liquid vapor phase change has little influence on the components of the viscous stress vector.

The obtained correlations are difficult to be used for the cryogenic tank applications, considering the existing turbulent regime flow. Nevertheless, besides its academic interest, the physical analysis acquired for the laminar regime will be of use when studying the interaction between a turbulent boundary layer flow and liquid/vapor phase change. To this extent the following chapter treats of the numerical simulation of the spatial development of a turbulent boundary layer flow with heat transfer.

Chapter 3

Turbulent boundary layer modeling

Contents

In the present chapter, the numerical simulation of the spatial development of a boundary layer flow on a flat plate, with heat transfer, is presented. After a thorough overview of the existing numerical methods for the generation of turbulent fluctuations, the chosen method is described and validated. Next, the results obtained are presented and discussed. A particular attention is also paid to the computational constraints related to the used numerical solver.

In the previous chapter we have described our work on the influence of liquid/vapor phase change onto the evolution of a laminar boundary layer flow of vapor. In practical applications, most flows which occur are turbulent. Therefore, the subsequent topic of our work will be the interaction between a turbulent boundary layer flow and the velocity field induced by liquid/vapor phase change. To this extent, the spatial evolution of a turbulent boundary layer flow on a flat plate has first to be simulated. Later on, the influence of the blowing velocity induced by the phase change onto the turbulent boundary layer evolution will be investigated.

Before discussing the results obtained in the numerical simulation of the spatial development of a boundary layer on a flat plate with heat transfer, we first give a brief description of some important aspects of the physics of wall turbulence. Next, we present an exhaustive overview of the literature on the different existing approaches for the generation of turbulent inflow for spatially-developing boundary layer simulations. The chosen method to be implemented in the code DIVA is then thoroughly described. The description of the extension of the corresponding method in order to impose the thermal boundary layer inflow is afterward presented. Validations of the implemented method are done and shown, as well as some verifications and discussions on the statistics obtained for the imposed inflow data. Finally, the numerical simulation of the spatial development of a boundary layer on a flat plate with heat transfer, for a momentum thickness Reynolds number $Re_\theta = 1100$ is described.

3.1 Introduction to the physics of wall turbulence

The first section is devoted to the description of some important aspects of the physics of wall turbulence. Only those aspects which are most relevant to the numerical simulation and modeling techniques used in this thesis are considered. A detailed introduction to turbulence theory can be found in the textbooks of Schlichting [92], Hinze [32], Tennekes and Lumley [103] or Pope [76].

As seen in chapter 2, a laminar boundary layer can be reduced to a stationnary two-dimensional flow, for which Blasius [8] proposed an analytical solution in excellent agreement with experimental results [92]. When the flow moves more rapidly or occurs on a bigger scale, the motion becomes unstable and varies more and more significantly and irregularly in space and time. This flow regime is called turbulent, and irregular fluctuations are superimposed on the main stream (figure 3.1).

Reynolds [84] first defined a non-dimensional number to help predict the transition between the two flow regimes, the Reynolds number Re_x. For the configuration involving a channel flow, he determined that the transition between the two regimes occurs when Re_x reaches a critical value ($Re_x \sim 2000$). Below this value, small perturbations that occur in the flow are damped by the viscous stresses and the flow does not change with time. Beyond this limit, small perturbations that occur in the flow amplify exponentially to yield spatially organized large scale coherent structures (Schlichting [92]). These structures are often referred to as eddies or vortices, since they are associated with the rotating motions of the fluid flow. At large Reynolds numbers, the energy is transported from the main flow into the large eddies. However, energy is dissipated preponderantly by small eddies. For a wall flow, this process occurs in a narrow band inside the boundary layer, in the neighbourhood of the wall (Schlichting [92]).

So far, the turbulent flow has been inaccessible to mathematical treatment due to its complexity. The description of these phenomena can nevertheless be led using the classical tools of turbulence analysis, as for example the decomposition of the flow into a mean motion and into a fluctuation, correlative or spectral analyses, etc. A detailed presentation of these methods can be found in the textbook of Chassaing [13].

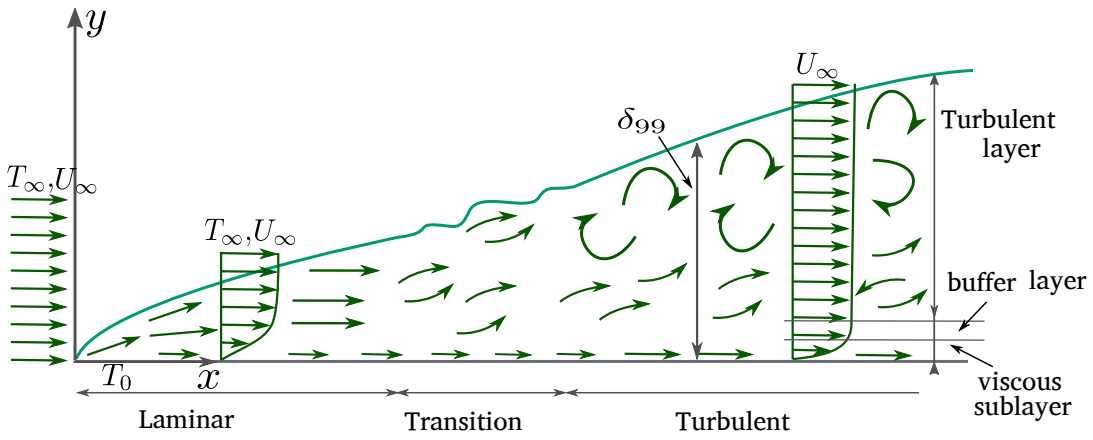

Figure 3.1: Schematics of the different regimes of a wall flow.

3.1.1 Characteristic quantities of wall turbulent flow

In order to describe a turbulent boundary layer flow, certain quantities are generally used and are defined in what follows. The mean and fluctuating parts of a variable ϕ will be hereinafter denoted by Φ and $\phi^{'} = \phi - \Phi$, respectively, except for the temperature where the mean is T and the fluctuation is θ'. The average of the fluctuations will be denoted whether by $< \cdot >$ or by $\overline{(\cdot)}$.

The boundary layer thickness δ_{99} is defined as the coordinate at which the velocity value is equal to $0.99U_\infty$. Its calculation is not conventional, therefore two other thicknesses have been in use,

$$\delta^* = \int_0^\infty \left(1 - \frac{U}{U_\infty}\right) dy, \quad \text{the displacement thickness, and,} \tag{3.1}$$

$$\theta = \int_0^\infty \frac{U}{U_\infty}\left(1 - \frac{U}{U_\infty}\right) dy, \quad \text{the momentum thickness.} \tag{3.2}$$

The displacement thickness δ^* is a measure of the fraction of the original free stream slowed down by the wall (Bejan [5]) due to the fluid viscosity

$$\delta^* U_\infty = \int_0^\infty U_\infty dy - \int_0^\infty U dy. \tag{3.3}$$

The momentum thickness θ is based on a similar argument: it is a measure of the longitudinal momentum missing at any x relative to the original ($x = 0$) amount, (Bejan [5]),

$$\theta U_\infty^2 = \int_0^\infty U_\infty^2 dy - \int_0^\infty U^2 dy - U_\infty \int_0^\infty (U_\infty - U)\, dy. \tag{3.4}$$

The ratio $H = \delta^*/\theta$ is called the shape factor and it characterizes the shape of the velocity profile in the boundary layer.

Different Reynolds numbers can be created using these quantities:

$$Re_\delta = \frac{U_\infty \delta_{99}}{\nu}, \quad Re_{\delta *} = \frac{U_\infty \delta^*}{\nu}, \quad Re_\theta = \frac{U_\infty \theta}{\nu}. \tag{3.5}$$

The local boundary layer flow is characterized by its friction coefficient, that can be written using the wall shear stress $\tau_0(x)$

$$C_f(x) = \frac{\tau_0(x)}{\frac{1}{2}\rho U_\infty^2}. \tag{3.6}$$

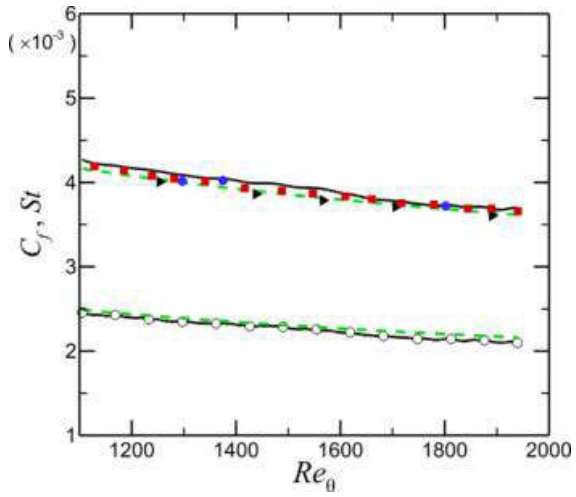

Figure 3.2: Example of the evolution of the friction coefficient C_f and the Stanton number St with Re_θ. The graph is extracted from Li *et al.* [58]. solid line - C_f obtained in [58]; line with circle - St obtained in [58]; dashed lines - turbulent correlations from Kays and Crawford [44].

Finally, the local Stanton number is a dimensionless number reporting heat-transfer coefficient in turbulent flow,

$$St_x = \frac{h(x)}{\rho C_p U_\infty}, \tag{3.7}$$

where $h(x) = q_0^{''}/(T_0 - T_\infty)$ is the heat-transfer coefficient that can be calculated using the wall heat flux $q_0^{''}(x)$.

The evolution of the friction coefficient C_f and the Stanton number St with the momentum thickness Reynolds number Re_θ is shown in figure 3.2. Both quantities decrease with Re_θ and they are related through a functional relation [44], that writes, for high Reynolds number,

$$\frac{2St}{C_f} = Pr^{-2/5}. \tag{3.8}$$

3.1.2 Turbulent boundary layer equations

For the configuration of a turbulent boundary layer, the Navier-Stokes equations reduce to x-momentum and energy equations. By applying the decomposition of the fields into a mean field and the corresponding fluctuations we obtain

$$U\frac{\partial U}{\partial x} + V\frac{\partial U}{\partial y} = -\frac{1}{\rho}\frac{dP}{dx} + \frac{1}{\rho}\frac{\partial}{\partial y}\left(\mu\frac{\partial U}{\partial y} - \rho < u'v' >\right), \tag{3.9}$$

$$U\frac{\partial T}{\partial x} + V\frac{\partial T}{\partial y} = \frac{1}{\rho C_p}\frac{\partial}{\partial y}\left(k\frac{\partial T}{\partial y} - \rho C_p < v'\theta' >\right). \tag{3.10}$$

Note that, for a flat plate at zero incidence, the pressure gradient along the wall, dP/dx, is zero.

In the momentum equation (3.9) the molecular diffusion shear stress $\mu\partial U/\partial y$ is augmented by the time-averaged eddy shear stress $(-\rho < u'v' >)$. This so called apparent shear stress τ_{app} is therefore composed by the viscous shear $\tau_\nu = \mu\partial U/\partial y$ and the turbulent shear $\tau_t = -\rho < u'v' >$ (figure 3.3)

$$\tau_{app} = \mu\frac{\partial U}{\partial y} - \rho < u'v' >= \rho\left(\nu + \epsilon_M\right)\frac{\partial U}{\partial y}, \tag{3.11}$$

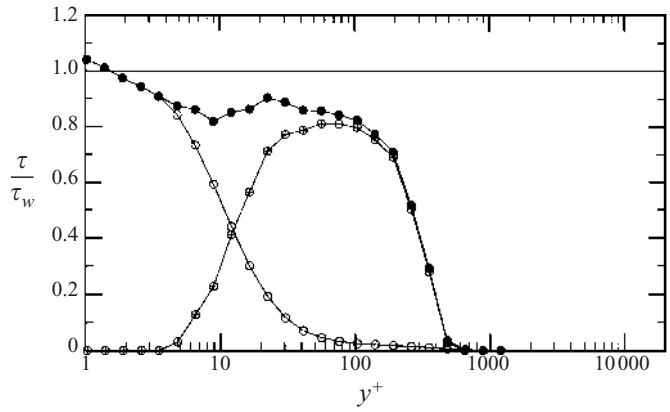

Figure 3.3: Example of shear stress distribution for $Re_\theta = 1430$. (●) - total shear stress; (⊗) - Reynolds shear stress; (○) - viscous stress. The graph is extracted from DeGraaff and Eaton [20].

where ϵ_M is the momentum eddy diffusivity.

In the same way, in energy equation (3.10), the apparent heat flux is defined as

$$-q''_{app} = k\frac{\partial T}{\partial y} - \rho C_p < v'\theta' >= \rho C_p \left(\alpha + \epsilon_H\right)\frac{\partial T}{\partial y}, \tag{3.12}$$

where α is the thermal diffusivity and ϵ_H is the thermal eddy diffusivity.

The ratio between the momentum eddy diffusivity and the thermal eddy diffusivity defines the turbulent Prandtl number $Pr_t = \epsilon_M/\epsilon_H$. Its evolution in the boundary layer is shown in figure 3.4. The turbulent Prandtl number tends to remain constant along the wall-normal direction. In the vicinity of the wall region a maximum value is obtained at the wall.

An analysis of the apparent shear stress shows that there are different zones in the boundary layer, as illustrated in figure 3.3. The inner region is defined by a negligible inertial effect, equation (3.9) resuming to

$$\left(\nu + \epsilon_M\right)\frac{\partial U}{\partial y} = \frac{\tau_0}{\rho}, \tag{3.13}$$

with τ_0 the value of τ_{app} at $y = 0$, where the Reynolds stress $-\rho < u'v' >$ vanishes (Bejan [5]). The dimensions of $(\tau_0/\rho)^{1/2}$ are those of velocity, and it is therefore known in the turbulence literature as the friction velocity

$$u_\tau = \left(\frac{\tau_0}{\rho}\right)^{1/2}, \tag{3.14}$$

and it is used for the nondimensionalization of the flow problem. In the same way, a friction temperature Θ_τ can be defined

$$\Theta_\tau = \frac{q''_0}{\rho C_p u_\tau}. \tag{3.15}$$

The outer zone is a region where the τ_{app} = constant assumption fails. It is also called the wake region and it is ruled by a balance between inertia and τ_{app}.

The boundary layer is not dominated by a single physical mechanism, therefore, the nondimensionalization of the flow problem is done by using two different length scales: the inner scale or the wall coordinates $y^+ = yu_\tau/\nu$ and the external scale $\eta = y/\delta_{99}$.

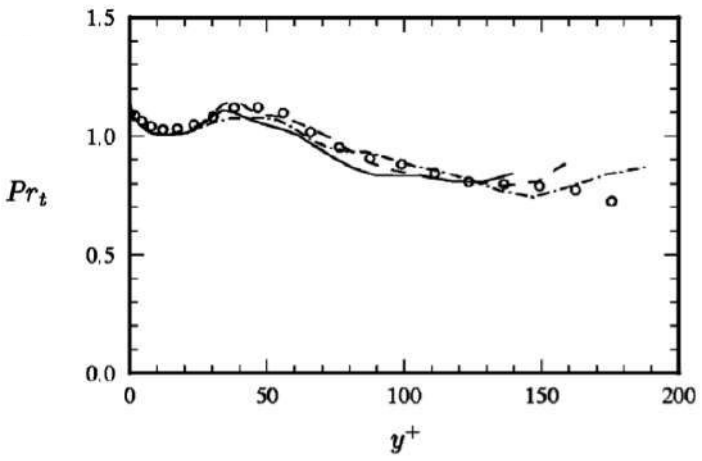

Figure 3.4: Example of the evolution of the turbulent Prandtl number Pr_t. The graph is extracted from Kong *et al.* [49];

3.1.3 Reynolds stress tensor and the turbulent kinetic energy balance equation

We have seen in equation (3.9) that the turbulence manifests itself by a highly correlated fluctuating mouvement. Its study can be made through the Reynolds stress tensor $R_{ij} =< u_i' u_j' >$. The component $< u'v' >$ appears in equation (3.9) and its influence has already been described in section 3.1.2.

The summation of the other three Reynolds stresses, ($< u'^2 >$, $< v'^2 >$, $< w'^2 >$) gives the turbulent kinetic energy $2k'$. The maximum of turbulent kinetic energy is contained in the buffer layer. The principal contribution is given by the streamwise component $< u^{'2} >$ (figure 3.5), showing the high anisotropic character of the flow close to the wall. The transverse stress $< w'^2 >$ is the second contribution to $k^{'}$, followed by the normal stress $< v'^2 >$.

DeGraaff and Eaton [20] show that the streamwise normal stress profiles $< u'^2 >^+$ presents a peak very near the wall. Their study demonstrates that the magnitude of $< u'^2 >^+$ is a strong function of Reynolds number throughout the entire inner region, except the viscous sublayer (figure 3.6). The near-wall peak occurs at $y^+ = 14$ and grows in magnitude with increasing Reynolds number. In the same work, it is shown that the energy from the mean flow is first transferred to $< u'^2 >^+$, and then redistributed by pressure and turbulent transport to the other Reynolds stresses.

The balance equation of the turbulent kinetic energy, obtained using the Navier-Stokes equations, yields

$$0 = -U\frac{\partial k^{'}}{\partial x} - V\frac{\partial k^{'}}{\partial y} + \left(- < u'v' > \frac{\partial U}{\partial y}\right) - \left(\frac{\partial < v'k' >}{\partial y}\right) - \left(\frac{\partial < v' (p/\rho) >}{\partial y}\right) + \nu\frac{\partial^2 k^{'}}{\partial y^2} - \bar{\epsilon} \quad (3.16)$$

The first two terms represent the advection. The production term ($- < u'v' > \partial U/\partial y$) writes as a coupling between the turbulent stress and the mean velocity gradient. For a boundary layer, this term is predominantly positive and it translates that the turbulence takes the energy from the mean flow and converts it in velocity fluctuations. This production center is situated close to $y^+ \simeq 12$. It can be observed in figure 3.7 that the generated energy is not entirely dissipated, a part is converted into turbulent ($\partial < v'k' > /\partial y$) and viscous $\nu\left(\partial^2 k'/\partial y^2\right)$ diffusion. In the viscous sublayer, the energy balance is reflected by the equality between the turbulent diffusion

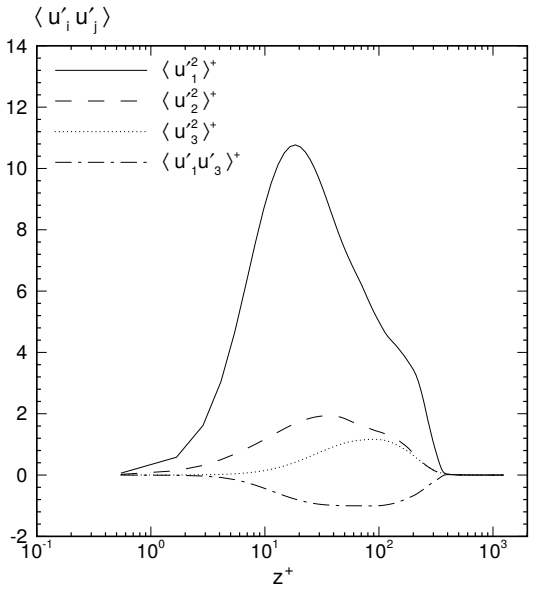

Figure 3.5: Example of Reynolds stresses profiles for $Re_\theta = 1430$. The graph is extracted from Ferrante and Elghobash [24].

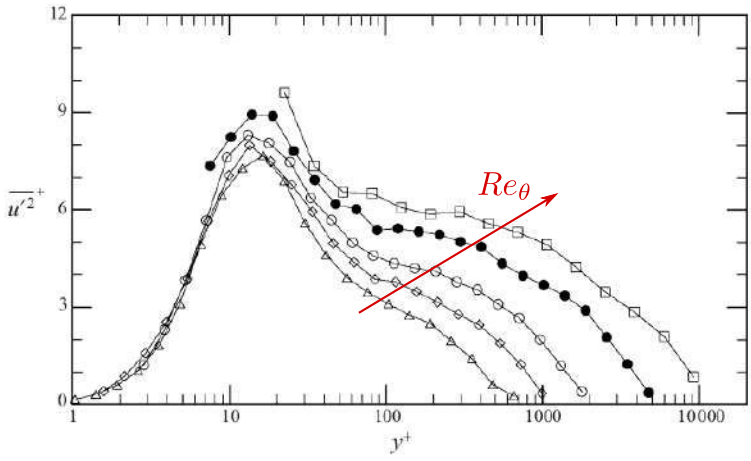

Figure 3.6: Example of $\overline{u'^2}$ profiles for different values of Reynolds number Re_θ. The graph is extracted from DeGraaff and Eaton [20].

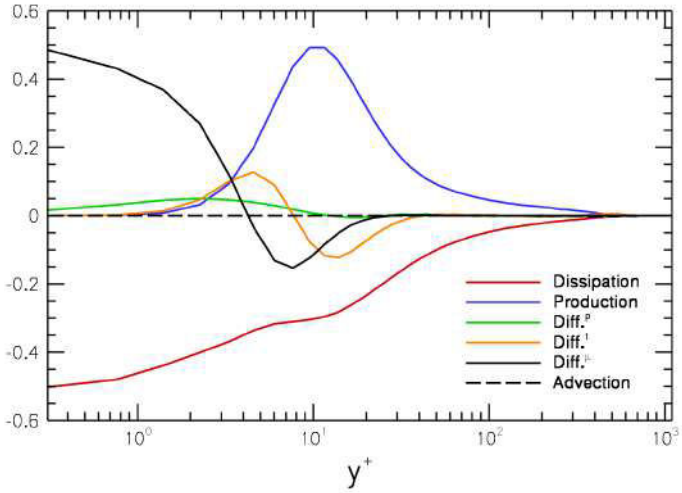

Figure 3.7: Example of the evolution of the different terms from the turbulent kinetic energy balance equation (3.16). All the terms are nondimenionalized by u_τ^4/ν. The graph is extracted from Pamies [72], who used the data from the DNS of Spalart [95].

and dissipation $\bar{\epsilon}$ terms. Finally, for $y^+ > 30$, the main equilibrium, production equals dissipation, shows that the energy provided by the mean motion is dissipated locally.

3.1.4 Mean velocity profile

The mean velocity distribution can be deduced from the definitions given previously. Close to the wall, the length scales of the vortices are very small and their energy is entirely dissipated. Additionally, considering the no-slip condition $u(0) = 0$, at the wall, the turbulent eddy shear is negligible and equation (3.13) writes

$$\nu \frac{\partial U}{\partial y} = u_\tau^2, \tag{3.17}$$

and a linear profile is obtained for the mean velocity $U^+ = y^+$. This equation is valid only on a thin zone called the viscous sublayer, which expands from the wall $y^+ = 0$ to $y^+ \sim 7$. Further in the boundary layer, the viscous effects become negligible and we obtain that all the turbulence production is dissipated. A dimensional analysis done using the turbulent kinetic energy balance (3.16) leads to

$$< u'v' > \frac{\partial U}{\partial y} = \bar{\epsilon} \sim \frac{u_\tau^3}{\kappa y}, \tag{3.18}$$

which allows obtaining

$$\frac{\partial U}{\partial y} = \frac{1}{\kappa} \frac{u_\tau}{y}. \tag{3.19}$$

Or, by using the inner length scale definition, the nondimensionalization of the above equation writes

$$y^+ \frac{\partial U^+}{\partial y^+} = \frac{1}{\kappa}. \tag{3.20}$$

We obtain from equation (3.20) the logarithmic law for the mean velocity

$$U^+ = \frac{\ln(y^+)}{\kappa} + C, \tag{3.21}$$

where $\kappa \simeq 0.4$ is the von Karman constant and $C \simeq 5$ is an integration constant. Its domain of validity expands from $y^+ = 50$ to $y^+ = 200$ [20]. The connection between the linear and logarithmic laws takes place in the buffer region.

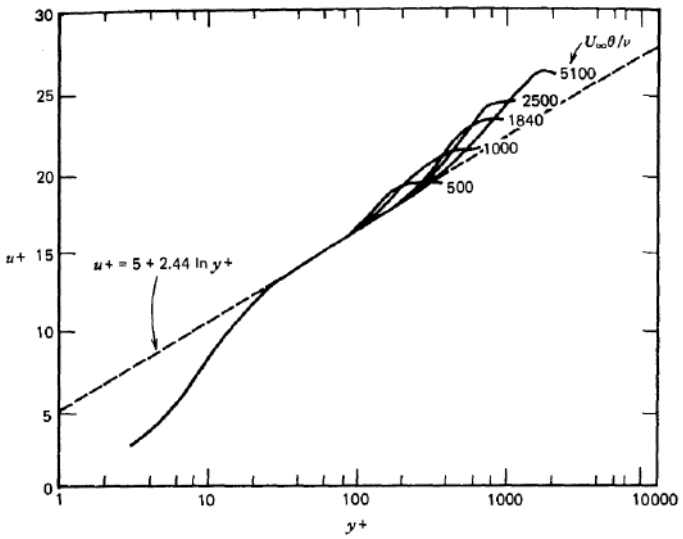

Figure 3.8: Example of mean velocity profiles for different values of the Reynolds number. The graph is extracted from Bejan [5].

This laws allows an universal description of the inner zone of the boundary layer. They are often used in experimental works to determine the friction coefficient.

Starting some distance from the wall, the external region can be poorly described by the logarithmic law (3.20). By making an analogy with the wake flows [16], a correction term is added,

$$U^+ = \frac{\ln(y^+)}{k} + \frac{2\Pi}{k}\sin^2\left(\frac{\pi y}{2\delta_{99}}\right), \tag{3.22}$$

where Π is a constant.

In figure 3.8, example of the mean velocity $U^+(y^+)$ measurements is shown for different values of the Reynolds number Re_θ. The experimental results are in very good agreement with the logarithmic law, illustrating the universality of the latter. However, as the momentum boundary layer thickness increases, the viscous sublayer occupies a smaller fraction of the boundary layer. DeGraaff and Eaton's study [20] gives a very thorough analysis on non-equilibrium boundary-layer scaling with the Reynolds number.

For the heat transfer part of the turbulent boundary layer problem, we focus on the equation (3.10) and make the assumption that, sufficiently close to the wall, the left side of (3.10) becomes negligible. With an approach analogous to the procedure used for the mean velocity profile, we obtain the mean temperature profile (Bejan [5])

$$T^+ = \begin{cases} Pr\, y^+ & \text{if } y^+ < y^+_{CSL} \\ Pr\, y^+_{CSL} + \dfrac{Pr_t}{k}\ln\dfrac{y^+}{y^+_{CSL}} & \text{if } y^+ > y^+_{CSL} \end{cases}. \tag{3.23}$$

According to Kays and Crawford [44], good agreement with temperature measurements is achieved if $Pr_t \simeq 0.9$, $k \simeq 0.41$ and $y^+_{CSL} \simeq 13.2$.

3.2 Review of the numerical simulation methods for turbulent flows

In what follows we will first remind the three numerical approaches one can use to simulate a turbulent flow: RANS, LES and DNS. We only give a brief description of these, more details can be found in Jarrin [37].

The most widely used and less costly approach for turbulent flow simulation is to simulate only the averaged quantities. The decomposition of the flow motion into a mean and a fluctuating component conducts to the Reynolds-Averaged Navier–Stokes (RANS) equations (equations (3.9) and (3.10) for a boundary layer flow). The Reynolds stresses are expressed using classical turbulence models allowing to close the flow problem.

Direct numerical simulation (DNS) of turbulent flow is the simulation of the Navier-Stokes equations without modeling assumption. All the scales of the flow are resolved by the numerical grid used. The difficulty of the DNS resides in the wide range of scales that needs to be simulated. The size of the smallest structures in the near wall layer is proportional to the viscous length scale ν/u_τ. The constraint on the grid is therefore given by the smallest scale, imposing the use of a non-uniform grid in the direction normal to the wall.

For turbulent flows at high Reynolds numbers, large-eddy simulation (LES) can be used to simulate all the flow scales larger than the mesh size while using subgrids models to describe the physics of the smaller scales. This allows for simulations less costly than the ones conducted with the DNS. Nevertheless, for wall flows at high Reynolds numbers, the cost of computing the inner layer exceeds by several order of magnitudes the cost of simulating the outer layer. In this case, the cost of a LES is driven by the inner layer resolution requirement, making the computational cost of LES similar to DNS (Jarrin [37]). Hybrid RANS-LES methods exist, aiming to overcome the empirical default of the RANS models while making LES less computationally demanding.

Another issue of great importance is the specification of realistic boundary conditions, and, especially, inlet boundary conditions. The prescribed inflow data at the inlet should be consistent with the turbulence model chosen for the simulation. Except for the RANS, where only mean profiles are needed, for LES and DNS simulations the specification of inflow data at the inlet plane requires as specific care: in order to simulate turbulence, turbulence has to be prescribed at the inlet plane. In the context of my thesis, a thorough overview of the literature on this subject has been conducted and it is depicted in what follows.

3.2.1 Generation of inflow boundary conditions for a turbulent flow

The numerical simulation of a spatially developing turbulent flow is not straightforward. The simplest way is to simulate the developement of the boundary layer from the laminar to the turbulent regime. For example, Wu and Moin [107] propose a DNS of a nominally zero-pressure-gradient flat-plate boundary layer with heat transfer, starting from the Blasius theory solution at $Re_\theta = 80$ continuously to a turbulent state of $Re_\theta = 1950$. The computational domain size is $12750\theta_0$, $2250\theta_0$ and $562.5\theta_0$ in the streamwise, wall-normal , and spanwise directions, respectively, where θ_0 is the inlet boundary layer momentum thickness. The number of grid points along these three directions is $8192 \times 500 \times 256$, respectively. The same strategy is used by Zhao *et al.* in [111]. The laminar Blasius profile is specified at the inflow boundary, and the laminar inlet is located downstream of the leading edge of the flat plate where $Re_\theta = 80$. At the inlet station, periodically migrating isotropic turbulent blocks that were obtained from a precursor DNS of homogeneous decay turbulence were introduced to trigger the laminar boundary layer to transition.

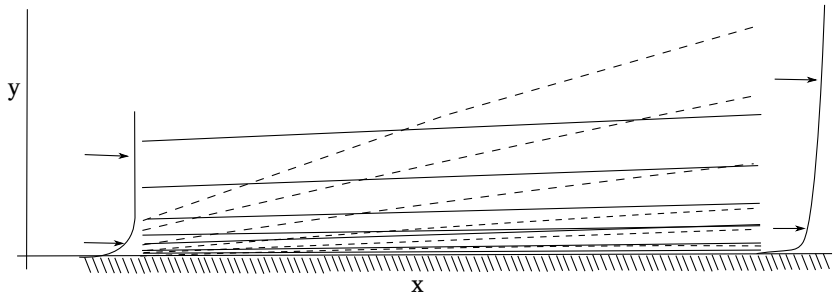

Figure 3.9: Sketch of the Spalart's approach to simulate a spatially developing boundary layer using periodic boundary conditions. The graph is extracted from Spalart [95]. (solid lines) - streamlines; (dashed lines) - coordinate lines.

The computational domain in each direction ($L_x \times L_y \times L_z$) is $6375\theta_0 \times 1500\theta_0 \times 375\theta_0$ and the corresponding numbers of grid points N_x, N_y, and N_z are 4096, 512, and 128. As noted, this kind of approach demands a high computational cost. Additionally, even if some strategies are used to trigger the transition to turbulence, the physical time needed for the simulation to converge is very long. To avoid these drawbacks, an inflow boundary condition can be imposed at the inlet; the corresponding inflow has to be as close as possible to a turbulent flow.

All the existing inflow generation methods are based on the decomposition of the flow fields into a mean component and a fluctuating component. Thus, the flow problem resumes to the generation of turbulent fluctuations of zero mean. Depending upon the used approach, in principle, it is possible to match the first and second moments of the fluctuations. However, imposing the spectra or the appropriate phase information between the modes is found to be more difficult and in some cases very costly. Nevertheless, without this structural information, inflow conditions are not accurate and the flow is far from beeing realistic. It must therefore undergo an adjustment distance, as the turbulent eddies are generated and evolve until the correct phase information is established. This adjustment distance is one of the criteria for judging an inflow generation method. Ultimately, the most efficient methods are those that allow giving as much structural information as possible for a reasonable computationally cost.

A recent review proposed by Wu [106] summarizes the research activities on inflow turbulence generation methods for computations of spatially developing turbulent flows, such as the synthetic Fourier method [53], recycling/rescaling method [62], synthetic eddy method [38], and digital filtering method [108], among others. Keating *et al.* [45] carried out comparisons of inflow conditions for simulations of turbulent, wall-bounded flows. Inter alia, they give a plain survey of the existing methods for generating inflow conditions for the simulation of spatially evolving wall-bounded flows. According to their paper, the latter can be divided into three major categories: the recycling methods, the use of a precursor calculation and the synthetic turbulence methods.

3.2.1.1 The recycling methods

The difficulty to impose realistic turbulent inflow at the inlet plane made that early simulations were often dedicated to temporally developing flows (homogeneous isotropic decay, shear layers, mixing layers and plane channels) where one could use periodic boundary conditions in the flow direction. This approach was then extended to simulations of spatially developing turbulent flows. Spalart [95], for instance, performed DNS of flat-plate boundary layers using periodic boundary conditions. In order to account for the thickening of the boundary layer he added source terms to the Navier-Stokes equations. In this way, the equations are transformed into a self-similar

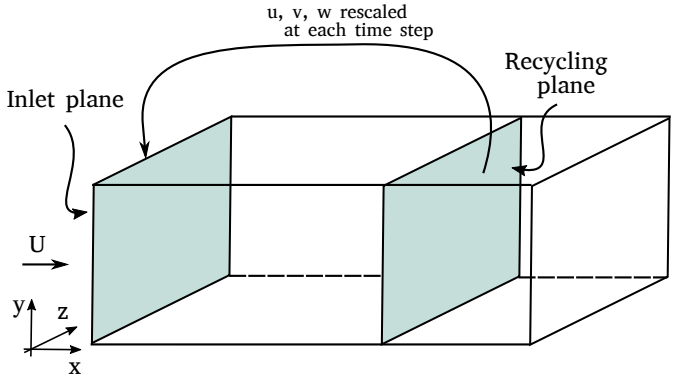

Figure 3.10: Schematics of the recycling method.

coordinate frame, in which the flow is periodic. A schematic of this approach is shown in figure 3.9. Spalart's method allows producing an equilibrium spatially evolving boundary layer and a direct control of the skin friction and momentum thickness is possible. The phrase 'equilibrium layer' was used by Townsend [104] to mean a region of a boundary layer where the local rates of energy production and dissipation are equal. DeGraaff and Eaton [20] gave a more applicable definition: an equilibrium boundary layer is a wall-bounded flow where the shear stress distribution is in equilibrium with the shear stress at the wall.

Returning to the recycling technique of Spalart, despite its robustness, it is complicated to understand and to program. Additionally, it requires a special purpose flow solver as well as external inputs for the streamwise gradients of mean flow variables.

Lund *et al.* [62] were the first to propose a more flexible version of the Spalart's approach. The modification is achieved by choosing to transform only the boundary conditions in the flow direction, as opposed to the entire solution domain. The method consists of taking a plane of data from a location several boundary-layer thicknesses δ_{99} downstream of the inflow, and rescaling the inner and the outer layers of the velocity profiles separately, to account for the different similarity laws that are observed in these two regions. The rescaled velocity profiles are then reintroduced at the inlet (see figure 3.10). The exponents *inner* and *outer* are used to designate the inner and the outer zone. The quantities extracted from the recycling station will be denoted by the subscript *recy* and the ones imposed to the inlet plane will be marked with the subscript *inlt*. The technique proposed by Lund *et al.* assumes the specification at the inlet plane of a velocity field decomposed into a mean and a fluctuating part

$$u_i(x_{inlt}, y, z, t) = U_i(x_{inlt}, y) + u_i'(x_{inlt}, y, z, t). \tag{3.24}$$

The flow is decomposed according to the inner and the outer zone of the boundary layer,

$$u_i = \left((U_i)^{inner} + \left(u_i'\right)^{inner}\right)(1 - W(\eta)) + \left((U_i)^{outer} + \left(u_i'\right)^{outer}\right) W(\eta), \tag{3.25}$$

where the weighting function $W(\eta)$ is defined as

$$W(\eta) = \frac{1}{2}\left(1 + \tanh\left(\frac{\alpha(\eta - b)}{(1-2b)\eta + b}\right) / \tanh(\alpha)\right), \tag{3.26}$$

The parameters $\alpha = 4$ and $b = 0.2$ ensure that the function is zero at 0, equals to 0.5 for $\eta = b$ and equals to 1 when $\eta = 1$. The choice for $b = 0.2$ corresponds to the limit of validity of the logarithmic law.

The mean flow is rescaled according to the law of the wall in the inner region

$$U_i^{inner}(y^+) = u_\tau(x) f_1\left(y^+\right), \tag{3.27}$$

and the defect law in the outer region

$$U_i^{outer}(\eta) = U_\infty - u_\tau(x) f_2\left(\eta\right). \tag{3.28}$$

The functions $f_1(y^+)$ and $f_2(\eta)$ are supposed to be universal, which allows obtaining

$$U_{inlt}^{inner} = \gamma U_{recy}(y_{inlt}^+), \tag{3.29}$$

and

$$U_{inlt}^{outer} = \gamma U_{recy}(\eta_{inlt}) + (1-\gamma) U_\infty, \tag{3.30}$$

where

$$\gamma = \frac{u_{\tau,inlt}}{u_{\tau,recy}}. \tag{3.31}$$

The mean velocity at the recycle station $U_{recy}\left(y_{inlt}^+\right)$ is expressed as a function of y^+ and evaluated at the inner coordinate of the mesh at the inlet. The same goes for the outer region. The scaling for the vertical velocity writes

$$V_{inlt}^{inner} = V_{recy}(y_{inlt}^+), \tag{3.32}$$

and

$$V_{inlt}^{outer} = V_{recy}(\eta_{inlt}). \tag{3.33}$$

The velocity fluctuations are decomposed using a similar reasoning, obtaining

$$\left(u_i'\right)_{inlt}^{inner} = \gamma u_{i,recy}'\left(y_{inlt}^+, z, t\right) \tag{3.34}$$

and

$$\left(u_i'\right)_{inlt}^{outer} = \gamma u_{i,recy}'\left(\eta_{inlt}, z, t\right). \tag{3.35}$$

This set of equations allows the reconstruction of the velocity field at the inlet plane of the domain, using the velocity field from the recycling station. However, this technique requires knowing δ_{99} and u_τ for both stations, inlet and recycling. These two parameters are needed to compute y_{inlt}^+, y_{recy}^+, η_{inlt} and η_{recy}. Additionally, Lund *et al.* [62] propose to estimate the ratio of the friction velocities γ using the momentum thicknesses,

$$\gamma = \frac{u_{\tau,inlt}}{u_{\tau,recy}} = \left(\frac{\theta_{recy}}{\theta_{inlt}}\right)^{1/(2(n-1))}, \tag{3.36}$$

with $n = 5$. This expression is obtained using the standard power-law approximations for the friction coefficient and the momentum boundary layer thickness (Schlichting [92]).

As often claimed in the turbulence literature (Pamies *et al.* [72], Spalart *et al.* [97], Ferrante and Elghobashi [24]), the initial condition for simulations using this technique is of great importance. If, for instance, the flow is initialized with random noise, without the adequate frequency content, the fluctuations can be rapidly dissipated which will lead to the laminarization of the flow. Spalart *et al.* [97] propose to first position the recycling station far away from the inlet plane. This allows the turbulence to establish. Once the statistical quantities are converged, the recycling plane can be located closer to the inlet plane in order to reduce the numerical costs. Liu and Pletcher [60] propose a modification to the Lund's method in order to overcome this drawback. The recycling plane is dynamically positioned according to the downstream instantaneous field, using

$$X(t) = X(0) + \min\left(X_\infty - X(0), \alpha U_\infty \max\left(0, (t - t_0)\right)\right), \tag{3.37}$$

where X is the position of the recycling plane, X_∞ is its final desired position, αU_∞ is the plane convection velocity, and t_0 is the time at which the turbulent flow generated at the inlet plane arrives to the coordinate $X(0)$. This procedure allows having the recycling station in the region where the turbulent structures are well developed.

At the moment, the recycling/rescaling methods represent the most reliable and robust solution for the turbulent inflow generation problem. They allow a good control of the friction coefficient and the boundary layer thickness. However, their use demands that the flow is at equilibrium in order to apply the universality of the wall laws. This condition often translates by the use of an auxiliary simulation, whose utility is only to generate the inlet conditions. Ferrante and Elghobashi [24] used an auxiliary simulation, denoted as Code-A in their work, in which the method of Lund *et al.* [62] is implemented. The rescaling process is repeated until a satisfactory solution is obtained. At each time step, the velocity components on a vertical plane in the middle of the domain of Code-A are stored and are used later as inflow boundary conditions for the main simulation, denoted as Code-B. Although the recycling/rescaling method [62] is a powerful technique, Ferrante and Elghobashi were not able to obtain satisfactory development of the turbulent velocity correlations in Code-A for the DNS of a spatially developing boundary layer over a flat plate (in [62], the method was tested using LES). They corrected this by initializing the flow in the rescaling region using the method of Le *et al.* [53], which prescribes the Reynolds-stress tensor and the energy spectra. Their technique is essential for sustaining the production rate of turbulent kinetic energy near the wall throughout the domain. Additionaly, the recycling station is taken much closer to the inflow so that the computational cost of generating the inflow data is reduced. The recycling station is positioned at δ_{99} downstream of the inlet compared to $8\delta_{99}$ in the original method. Their results for a Reynolds number $Re_\theta = 1430$ are in good agreement with the experimental data of DeGraaff and Eaton [20].

A second drawback of this type of methods is the introduced spurious periodicity, as remarked by Keating *et al.* [45], among others. The presence of this periodicity can be problematic if the corresponding frequency is close to the one of a physical phenomenon that we want to study (see Pamies [71]).

3.2.1.2 The use of a precursor calculation

The use of a precursor calculation, prior stored in a database, allows the specification of turbulent data providing a reasonable degree of realism. The idea is to rescale a time-dependent set of data in order to reproduce a velocity profile and turbulent fluctuations (see the work of Schlüter *et al.* [93]). Usually, the data can be obtained using a RANS simulation.

This method is particularly attractive when the flow we want to simulate does not contain an equilibrium zone where a recycling/rescaling procedure could be applied. From this point of view, this technique can be adaptabted to any flow, independently of the Reynolds number value. However, the acces to important storage capacities as well as the costly reading operations during the simulation make this approach unappealing.

3.2.1.3 Synthetic turbulence methods

The last group of inflow generation methods is represented by the synthetic turbulence techniques. They are based on the assumption that a turbulent flow can be approximated by reproducing a set of low order statistics, such as the mean velocity, the turbulent kinetic energy, the Reynolds stresses. However, higher order statistics such as the terms in the turbulent kinetic energy balance equation (the rate of dissipation, the turbulent transport or the pressure-strain term) are not

usually reproduced. Therefore, the synthetic turbulence represents only a crude approximation of real turbulence. Additionaly, the synthetic turbulence might have a structure sensibly different from the one of the real flow. If the structure of the turbulent eddies and their dynamics is not accurately reproduced, then it is expected that the synthetic turbulence undergoes a transition process before it redevelops towards a more physical state. The distance for the transition process is called *adaptation or adjustement distance* and determines the performance of the method because it fixes the streamwise length of the computational box devoted to the generation of realistic turbulence.

The synthetic turbulence generation methods are numerous, in what follows we will discuss only a few of them. For more details, the recent review of Wu [106] is recommended.

Lund *et al.* [62] propose a random fluctuation method designed to match a prescribed mean flow and Reynolds stress tensor. Their idea is similar to the one proposed by Le *et al.* [53]. Three sequences of random numbers $\tilde{u}_j$ are generated. They are conditioned so that each distribution has zero mean, unit variance, and zero covariance with the other two distributions. The corresponding fluctuations are computed using the Reynolds stress tensor via

$$u_i' = \sum_j a_{ij}\tilde{u}_j, \tag{3.38}$$

where the amplitude tensor a_{ij} has the expression

$$a_{ij} = \begin{bmatrix} \sqrt{R_{11}} & 0 & 0 \\ \dfrac{R_{21}}{a_{11}} & \sqrt{R_{22}-a_{21}^2} & 0 \\ \dfrac{R_{31}}{a_{11}} & \dfrac{\sqrt{R_{32}-a_{21}a_{31}}}{a_{22}} & \sqrt{R_{33}-a_{31}^2-a_{32}^2} \end{bmatrix}. \tag{3.39}$$

where $R_{ij} =< u_i'u_j' >$.

In [62] it is shown that inflow conditions for a spatially developing boundary layer generated using this technique lead to a laminarization of the flow up to a point where transition takes place and realistic turbulence starts to develop. However, in their study, the boundary layer thickness never grew at the correct rate (the domain length was $48\delta_{99}$, and the friction coefficient never reached a fully developed value).

To go further, Klein *et al.* [46] introduced a new approach for the generation of artificial velocity data, based on digital filtering of random data. The objective was to remedy the lack of large-scale dominance in the inflow data generated by the random data described above. In one dimension, the velocity signal is defined by a convolution or a digital linear non-recursive filter

$$u'(j) = \sum_{n=-N}^{N} b_n r(j+n), \tag{3.40}$$

where b_n are the filter coefficients, N is connected to the support of the filter and $r(j+n)$ is the random number generated at point $(j+n)$ with $< r_j >= 0$ and $< r_j r_j >= 1$. It follows easily that the two-point correlations between points j and $(j+m)$ depend on the filter choice and read

$$< u'(j)u'(j+m) >= \sum_{n=-N+m}^{N} b_n b_{n-m}. \tag{3.41}$$

Jarrin *et al.* [38, 37] proposed a method, whose originality lies in the use of coherent structures, with a random position in space and in time. The signal is then coupled to a prescribed second

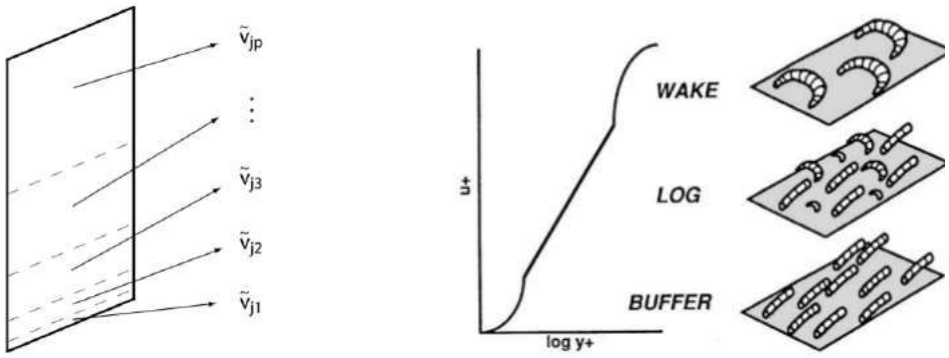

(a) (b)

Figure 3.11: (a) Schematics of the partitioning of the inlet plane into P zones, proposed by Pamies [71]. (b) Schematics of the distribution of different turbulent structures in a boundary layer in fonction of the distance to the wall, extracted from Robinson [86].

order moments using the technique of Lund *et al.* [62], described above. The velocity fluctuations are expressed by

$$u_i'(\mathbf{x},t) = \sum_{j=1}^{3} a_{ij} \frac{1}{N_E} \sum_{k=1}^{N_E} \epsilon_{jk} f_j \left(\mathbf{x} - \mathbf{x}_k(t)\right), \tag{3.42}$$

where N_E is the number of coherent structures, ϵ_{jk} are the random independent variables equal to 1 or -1 and f_j is a normalized function accounting for the velocity distribution of the turbulent eddy. $x_k(t)$ is the position of the center of the structure k, convected through the flow using Taylor hypothesis. The authors used this approach for a spatially decaying homogeneous isotropic turbulence and a fully developed turbulent channel. Rawat *et al.* [81] used this method in an auxiliary simulation of a spatially developing turbulent boundary layer meant to obtain inflow data. Next, the stored planes were used as inflow data for the main simulation of a turbulent boundary layer with bubbles.

Jarrin's method was later modified by Pamies [71, 72] for the use on a LES of a spatially developing turbulent boundary layer on a plate. They propose that the stochastic signal be modified so that it can be split into several modes (see figure 3.11, with different time, length and velocity scales and also with different vorticity contents. In particular, the random signal $\tilde{u}_j$ needed for the Cholesky decomposition (3.38) is computed as a sum over the P zones of the inlet plane,

$$\tilde{u}_j = \sum_{p=1}^{P} \tilde{v}_{jp}, \tag{3.43}$$

where $\tilde{v}_{jp}$ corresponds to a normalized random sequence that has a compact support on the pth zone. To each structure, time scale l_p^t, as well as wall-normal l_p^y and transverse l_p^z length scales are assigned. The velocity signal is therefore obtained by

$$\tilde{u}_j(t,y,z) = \sum_{p=1}^{N} \frac{1}{\sqrt{N(p)}} \sum_{k=1}^{N(p)} \epsilon_k \Lambda_{jp} \left(\frac{t - t_k - l_p^t}{l_p^t}\right) \Phi_{jp} \left(\frac{y - y_k}{l_p^y}\right) \Psi_{jp} \left(\frac{z - z_k}{l_p^z}\right). \tag{3.44}$$

The modified method is also able to generate randomly located turbulent structures, of customizable sizes, celerity and geometrical shape. The boundary layer is populated with several types of coherent structures: elongated streamwise vortices in the near-wall region and hairpinlike vortices in the logarithmic layer. Pamies *et al.* [71] extracted information from the work of Jeong *et al.* [39]

that they used for the prescription of the geometrical shape of the structures at the inlet plane. They found that their technique allows obtaining more realistically the distribution of scales in the wall-normal direction. Also, they show that the specification of realistic modes for the buffer and the logarithmic layers helps to reduce the spatial transient undergone by the synthetic inflow data.

	Lund *et al.* [62]	Ferrante & Elghobashi [24]	Pamies *et al.* [71]
Re_θ	$1400 - 1640$	$800 - 1500$	3535
Grid points	$100 \times 45 \times 64$	$256 \times 96 \times 256$	-
Domain dimensions	$(10 \times 3 \times \pi/2)\delta_{inlt}$	$(10 \times 3.6 \times 5)\delta_{inlt}$	$\sim (7.5 \times 4 \times 2)\delta_{inlt}$
	$L_x^+ = 6400$	-	-
	$L_y^+ = -$	-	-
	$L_z^+ = 960$	-	-
Grid resolution	$\Delta x^+ \simeq 64$	$\Delta x^+ \simeq 14$	$\Delta x^+ \simeq 44$
	$\Delta z^+ \simeq 15$	$\Delta z^+ \simeq 7$	$\Delta z^+ \simeq 14$
	$\Delta y^+_{min} \simeq 1.2$	$\Delta y^+_{min} \simeq 0.58$	$\Delta y^+_{min} \simeq 1$
	-	$\Delta y^+_{min} \simeq 34$	-
Time step Δt	$2\nu/u_\tau^2$	$0.15\nu/u_\tau^2$	$0.00096\delta_{inlt}/U_\infty$
Time of turbulence statistics	$1400\theta_{inlt}/U_\infty$	$2600\theta_{inlt}/U_\infty$	$3000\theta_{inlt}/U_\infty$

Table 3.1: Description of numerical cases overviewed above for a turbulent boundary layer.

All in all, the synthetic turbulence generation methods allows imposing a distribution of time and space scales with a good degree of realism. In addition, this kind of techniques can be implemented directly as an inflow condition, at a certain distance upstream the region of study, without the need for a careful flow initialization. This distance translates the capacity of the approach to produce a turbulence containing realistic statistical and temporal informations. Unfortunately, as stated by Keating *et al.* [45], even the most complex procedures for synthetized turbulence can involve large adaptation distances, superior to the ones demanded by the recycling/rescaling techniques. Nevertheless, these methods do not induce spurious periodicity, making them more appealing. In table 3.1 the reader can find a description of some of the numerical cases overviewed above. Especially, the domain dimensions as well as the grid resolution are given.

3.2.2 Selection criteria

The choice of the method used for the generation of inflow data can be made taking into account the following parameters:

- the adaptation distance which drives directly the computational domain streamwise length. It depends, on one hand, on the capacity of the technique to generate a turbulence fairly realistic and on the other hand, on the level of realism the user expects.
- the integrability of the inflow condition represented by the need of a careful flow initialization, the compatibility of the method with the physical frequencies in study etc.
- the degree of empiricism which indicates the quantity of informations the user has to provide.

- the computational cost.
- the complexity of the implementation.

An assessment of the methods described in the previous section is given in table 3.2, in accordance to the selection criteria presented above. The symbol $'+'$ signifies that the method is particularly performing for the concerned criterion. On the contrary, the symbol $'-'$ translates that the criterion represents a drawback for the corresponding method.

Recycling/rescaling methods

	Spalart [95]	Lund *et al.* [62]	Liu and Pletcher [60]
Adaptation distance	+ ($12\delta_{99}$)	+ ($8\delta_{99}$)	+
Integrability	-	-	+
Degree of empiricism	+	+	-
CPU cost	-	+	-
Complexity	-	-	-

Synthetic methods

	Lund *et al.* [62]	Klein *et al.* [46]	Jarrin *et al.* [38]	Pamies *et al.* [72]
Adaptation distance	- ($20\delta_{99}$)	-	- ($24\delta_{99}$)	+ ($7.5\delta_{99}$)
Integrability	+	+	+	+
Degree of empiricism	+	+	-	-
CPU cost	+	-	-	-
Complexity	+	+	+	+

Hybrid methods

	Keating *et al.* [45]	Ferrante and Elghobashi [24]
Adaptation distance	- ($20\delta_{99}$)	+ ($8.25\delta_{99}$)
Integrability	+	-
Degree of empiricism	+	+
CPU cost	-	-
Complexity	+	-

Table 3.2: Comparison between the overviewed methods for generating turbulent inflow data (Pamies [72]).

As already stated, the synthetic methods demand a fairly long adaptation distance. For the method of Pamies [71], the information is misleading, note that the outlet of the domain is located at the end of an additional box placed after the main box. In this box, mesh cells are stretched in the

streamwise direction so that turbulent fluctuations are progressively damped. On the other hand, this type of method is straightforward to implement, does not need a careful flow initialization and does not create nonphysical frequencies. However, the prescription of turbulent information is needed and can be a constraint.

The recycling methods demand a lower CPU cost and the adjustment distance is more reasonable. Nevertheless, their integrability and their complexity represent major drawbacks in comparison with the synthetic turbulence techniques.

Last but not least, the configuration under study (boundary layer blown by a vertical velocity induced by the liquid/vapor phase change) will not be at equilibrium. Therefore, the use of a recycling/rescaling approach will be possible only if an auxiliary simulation is considered for the generation of the turbulent inflow data.

After thoroughly analyzing all of these arguments we decided to use the synthetic eddy method of Jarrin [38] to generate the inflow condition for the simulation of the spatially developing boundary layer on a flat plate. Additionally, Rawat *et al.* [81] showed an excellent adjustment of this method for a turbulent boundary layer simulation.

3.2.3 Generation of inflow boundary conditions for a turbulent boundary layer with heat transfer

In what follows, we will give a survey of the existing techniques for the simulation of turbulent boundary layer flows with heat transfer. The thermal field can be treated as a passive scalar field. The concept of passive scalars and thermal fields is equivalent only under the following assumptions [2]: the temperature difference in the thermal boundary layer is assumed small, the buoyancy effects and temperature dependence of material properties are negligible.

As seen for the dynamic turbulent boundary layer, performing simulations requires time-varying realistic thermal turbulent data at the inlet of the computational domain. The first DNS study of turbulent boundary layers was performed by Bell and Ferziger [6]. They use the fringe concept of Spalart and Watmuff [96] to convert the nonperiodic inflow/outflow boundary conditions to periodic ones. In their study, they use isothermal wall condition for an extent of momentum thickness Reynolds number from 300 to 700 and values of the Prandtl number equal to 0.1, 0.71, and 2.

The recycling/rescaling method of Lund *et al.* [62] was extended to thermal inflow by Kong *et al.* [49]. As in the original method [62], the authors use a single scale along the entire boundary layer for the rescaling processes of the thermal field: the friction temperature Θ_τ. They show that the behavior of the wall-normal heat-flux is similar to that of the Reynolds shear stress indicating close correlation between the streamwise velocity and temperature.

Hattori *et al.* [31] employ the inflow generation method ([62], [49]) to investigate the effects of buoyancy on the near-wall region of stable and unstable turbulent thermal boundary layers. Their computational domain was composed of two parts: the driver part and the main part. In the driver part, a zero-pressure-gradient flow with an isothermal wall and without buoyancy effect is generated and used as the inflow boundary condition for the main simulation. In the main part, stable boundary layer and unstable boundary layer are simulated. They concluded that the structure of near-wall turbulence was significantly altered by thermal stratifications caused by the weak buoyant force.

Araya and Castillo [2] propose a modification to the recycling/rescaling method [62, 49] for an adverse-pressure gradient turbulent boundary layer with heat transfer. Their modification consists in using scaling laws obtained by performing a similarity analysis over the governing equations

in the inner and outer regions of the boundary layer. This allows the assimilation of streamwise pressure gradients. Additionally, the auxiliary domain that generates inflow turbulent information in [62] is eliminated and the principal domain produces its own inflow conditions at every time step by rescaling the solution downstream.

	Kong *et al.* [49]	Araya and Castillo [2]	Li *et al.* [58]
Re_θ	$300 - 430$	$1940 - 2300$	$1100 - 1940$
Grid points	$352 \times 64 \times 128$	$400 \times 150 \times 125$	$4096 \times 512 \times 128$
Domain dimensions	$(22 \times 3.4 \times 4.5)\delta_{inlt}$	$(11 \times 3.3 \times 1.75)\delta_{inlt}$	$(464 \times 109 \times 27)\theta_{inlt}$
	$L_x^+ = 3203$	$L_x^+ = 8800$	-
	$L_y^+ = 608$	$L_y^+ = 2640$	-
	$L_z^+ = 666$	$L_z^+ = 1375$	-
Grid resolution	$\Delta x^+ \simeq 9.1$	$\Delta x^+ \simeq 22$	$\Delta x^+ \simeq 5.36$
	$\Delta z^+ \simeq 5.2$	$\Delta z^+ \simeq 11$	$\Delta z^+ \simeq 9.98$
	$\Delta y^+_{min} \simeq 0.19$	$\Delta y^+_{min} \simeq 0.5$	$\Delta y^+_{min} \simeq 0.62$
	$\Delta y^+_{min} \simeq 25$	$\Delta y^+_{min} \simeq 12$	$\Delta y^+_{min} \simeq 26.1$
Time step Δt	$0.38\nu/u_\tau^2$	$0.44\nu/u_\tau^2$	$0.057\theta_{inlt}/U_\infty$
Time of turbulence statistics	$1700\theta_{inlt}/U_\infty$	$1460\theta_{inlt}/U_\infty$	$3420\theta_{inlt}/U_\infty$

Table 3.3: Description of numerical cases overviewed above for a turbulent boundary layer with heat transfer.

Li *et al.* [58] run an auxiliary computation to obtain the inlet flow; instantaneous fluid velocity and temperature fields were extracted at the location $Re_\theta = 1100$. The precursor data was then used to perform DNS of turbulent thermal boundary layer for a momentum thickness Reynolds number = 1100−1940 with $Pr = 0.71$. They have observed a strong correlation between streamwise velocity and temperature fluctuations near the wall.

Simulation of turbulent boundary layer with heat transfer has been done either with methods based on the recycling/rescaling method [62, 49] or in a domain were the transition from laminar to turbulence is triggered in some way [107, 59, 111]. In table 3.3 the corresponding parameters (when avalaible) of some of the overviewed works are shown. Attention is drawn to the values of the mesh resolution in the wall-normal direction; the minimum value of the Δy^+ is around 0.5, or smaller, in order to solve the viscous sublayer.

Given the order in which the present work was conducted, some preliminary simulations have been conducted only for the dynamic boundary layer. To this extent, as mentioned in the previous section, the synthetic eddy method of Jarrin [38] has been used and therefore implemented in the code DIVA. The implementation of a new method of inflow generation would have been undue. For this reason, an extension of the synthetic eddy method for the thermal boundary layer has been proposed during this thesis. The mentioned method as well as the proposed extension are further described in detail.

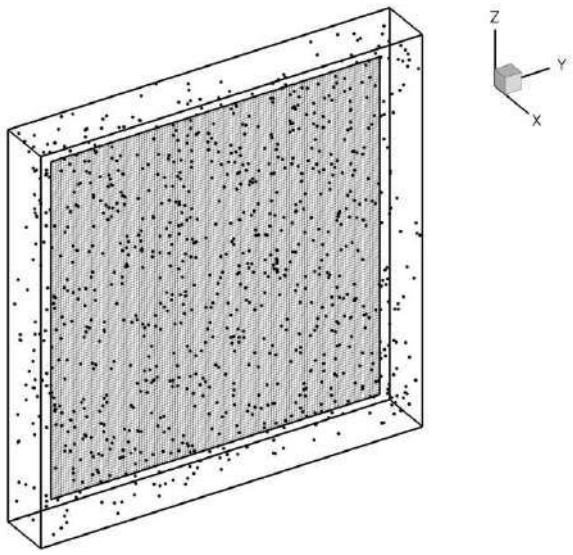

Figure 3.12: Box of edies around the inlet plane. The figure is extracted from Jarrin [37].

3.3 Synthetic Eddy Method (SEM)

3.3.1 Basic equations of the SEM

The synthetic eddy method (SEM) allows to generate a velocity signal with prescribed first- and second-order moments in a three-dimensional virtual box. This operation, already proposed in [62], uses the Cholesky decomposition $a_{ij}(y)$ of a prescribed Reynolds stress tensor $R_{ij}(y)$ to assign second-order moments to a normalized stochastic signal $\widetilde{u}_j(x,y,z,t)$ superimposed to a mean velocity $\overline{u}_i(y)$,

$$u_i(x,y,z,t) = U_i(y) + \sum_j a_{ij}\tilde{u}_j(x,y,z,t), \tag{3.45}$$

with: $\tilde{u}_j(x,y,z,t)$ - a centered random sequence with unit variance ($\mathrm{var}(\tilde{u}_j(x,y,z,t)) =< \tilde{u}_j^2 >= 1$) and zero covariance ($\mathrm{covar}(\tilde{u}_j(x,y,z,t)) = \sqrt{< \tilde{u}_j^2 >} = 0$).

The inlet plane $x = 0$ is defined by a finite set of points $S = \{\mathbf{x}_1, \mathbf{x}_2, ..., \mathbf{x}_s; \mathbf{x} = (0,y,z)\}$ on which the synthetic velocity fluctuations will be generated with the SEM. We assume that the mean velocity U_i, the Reynolds stresses R_{ij} and a characteristic length scale of the flow σ are avalaible for the set of points considered.

The first step is to create a box B which contains the synthetic eddies. The dimensions of the box are chosen in such a way that all the points in S are surrounded by eddies,

$$B = \left\{ x_i^E = (x^E, y^E, z^E) \in \mathbb{R}^3 : x_{i,min}^E \leqslant x_i^E \leqslant x_{i,max}^E \right\}, \tag{3.46}$$

where $x_{i,min}^E = \min\left(x_i^E - \sigma(\mathbf{x}_S)\right)$ and $x_{i,max}^E = \max\left(x_i^E + \sigma(\mathbf{x}_S)\right)$. Figure 3.12 shows the inlet plane surrounded by the virtual box of eddies B, of volume V_B.

The velocity signal generated by the N eddies is expressed by

$$\tilde{u}_i(y,z) = \frac{1}{N}\sum_{k=1}^{N} \epsilon_{i,k} f_{\sigma(\mathbf{x})}\left(\mathbf{x} - \mathbf{x}_k^E\right), \tag{3.47}$$

where $\mathbf{x}_k^E$ are the locations of the N eddies, $\epsilon_{i,k}$ are independent variables taken from any distribution with zero mean and unit variance. We choose $\epsilon_{i,k} \in \{-1, 1\}$ with equal probability to take

one value or the other. The velocity distribution of the eddy located at $\mathbf{x}_k^E$ is represented by the function f_σ. It is assumed that the differences in the distributions between the eddies depend only on the length scale σ,

$$f_\sigma = \sqrt{V_B \sigma^{-3}} f\left(\frac{x_k^E}{\sigma}\right) f\left(\frac{y - y_k^E}{\sigma}\right) f\left(\frac{z - z_k^E}{\sigma}\right). \tag{3.48}$$

The shape function f is common to all eddies. The latter has the compact support $[-\sigma, \sigma]$ and has the normalization $\int_{-\sigma}^{+\sigma} f^2(x)dx = 1$. The multiplying factor $\sqrt{\sigma^{-3}}$ assures the normalization condition.

The position of the eddies $\mathbf{x}_k^E$ before the first time step are independent from each other and taken from a uniform distribution.

Finally, the different steps in the generation of a velocity signal with the SEM are as it follows:

1. Estimate all the necessary input data (U_i, R_{ij} and σ) on the set of points S.
2. Define the virtual box B where the eddies will be generated using (3.46).
3. Generate for each eddy k two random vectors $\mathbf{x}_k^E$ and $\epsilon_{i,k}$ for its location and its intensity, respectively.
4. Compute the velocity signal on the set of points S by the use of (3.48). In all simulations carried out in this thesis a tent function has been used for the shape of the velocity distribution,
$$f(x) = \begin{cases} \sqrt{\frac{3}{2}}\left(1 - |x|\right), & |x| < 1 \\ 0, & \text{otherwise} \end{cases}. \tag{3.49}$$
5. Compute, at each time step, the velocity field using (3.45).
6. Convect the eddies though B with the characteristic velocity $\mathbf{U}_c = \int_S \mathbf{U}(\mathbf{x})d\mathbf{x}$,
$$\mathbf{x}_k^E(t + dt) = \mathbf{x}_k^E(t) + \mathbf{U}_c \mathrm{d}t, \tag{3.50}$$
with dt - the time step.
7. Generate new locations and intensities for eddies which were convected outside B. Advance to next time step and go back to step 4.

3.3.2 Preliminary validation of the SEM

3.3.2.1 Simulation of instantaneous signals

After implementing the SEM following the steps described in the previous section, a preliminary validation was conducted by first simulating instantaneous signals of synthetic isotropic turbulence. This validation configuration is extracted from the thesis of Jarrin [37].

Isotropic synthetic fluctuations are generated on a two-dimensional plane with the SEM. The dimensions of the (Oyz) plane are $2\pi \times 2\pi$. A mean velocity in the streamwise direction $U = 10$ m/s and fluctuating velocities $u_i' = 1$ m/s are imposed. The length scale defining the radius of each eddy is constant and has the value $\sigma = 0.5$ m. The number of eddies generated in the virtual box is $N = 1000$. The mesh grid employed for the two-dimensional domain is 128×128.

Figure 3.13 shows the temporal evolution of u, v and w recorded at point $(y, z) = (\pi, \pi)$ and instantaneous contours of u, v and w on the two-dimensional plane. The obtained signal is stationary in time and homogeneous and isotropic in space, as expected.

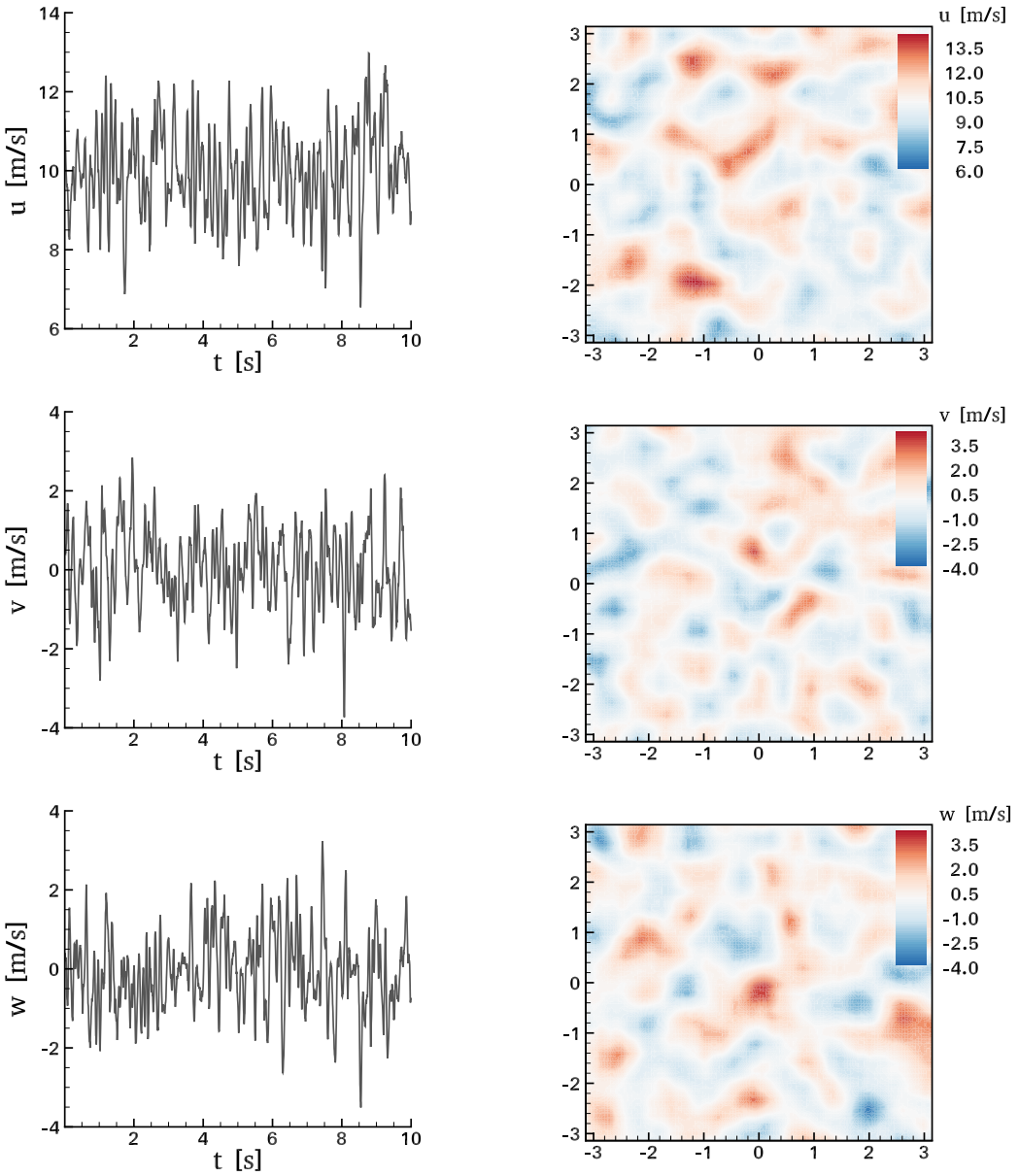

Figure 3.13: Simulation of instantaneous signals for a THI. Time evolution and velocity field of u, v, and w from top to bottom.

Figure 3.14 shows the time convergence of the time averaged mean velocity, the Reynolds stresses, the skewness and the flatness of the SEM simulated signal at a point $(y, z) = (\pi, \pi)$. The velocity derivatives skewness S and kurtosis or flatness F represent the normalized velocity-derivative moments of order 3 and 4, respectively:

$$S_{ij} = \frac{\langle (\partial u_i/\partial x_j)^3 \rangle}{\langle (\partial u_i/\partial x_j)^2 \rangle^{3/2}}, \tag{3.51}$$

and

$$F_{ij} = \frac{\langle (\partial u_i/\partial x_j)^4 \rangle}{\langle (\partial u_i/\partial x_j)^2 \rangle^2}. \tag{3.52}$$

The skewness allows to have a measure of the symmetry of the velocity distribution while the

flatness defines the "spreading" of the distribution field. For example, for a Gauss distribution, the flatness equals to 3 while the skewness is zero.

The obtained statistics converge towards the imposed values,

$$< u >= U_0, \quad < u_i' u_j' >= u_{rms}^2 \delta_{ij}, \tag{3.53}$$

where δ_{ij} is the Dirac distribution and $u_{rms} = \sqrt{< u_i' u_j' >}$ is the rms velocity. Jarrin demonstrates in [37] that for the present configuration, the target values of the skewness and flatness are

$$S_{u_i} = 0, \quad F_{u_i} = 4.1. \tag{3.54}$$

The skewness and the flatness demand further averaging to be fully converged.

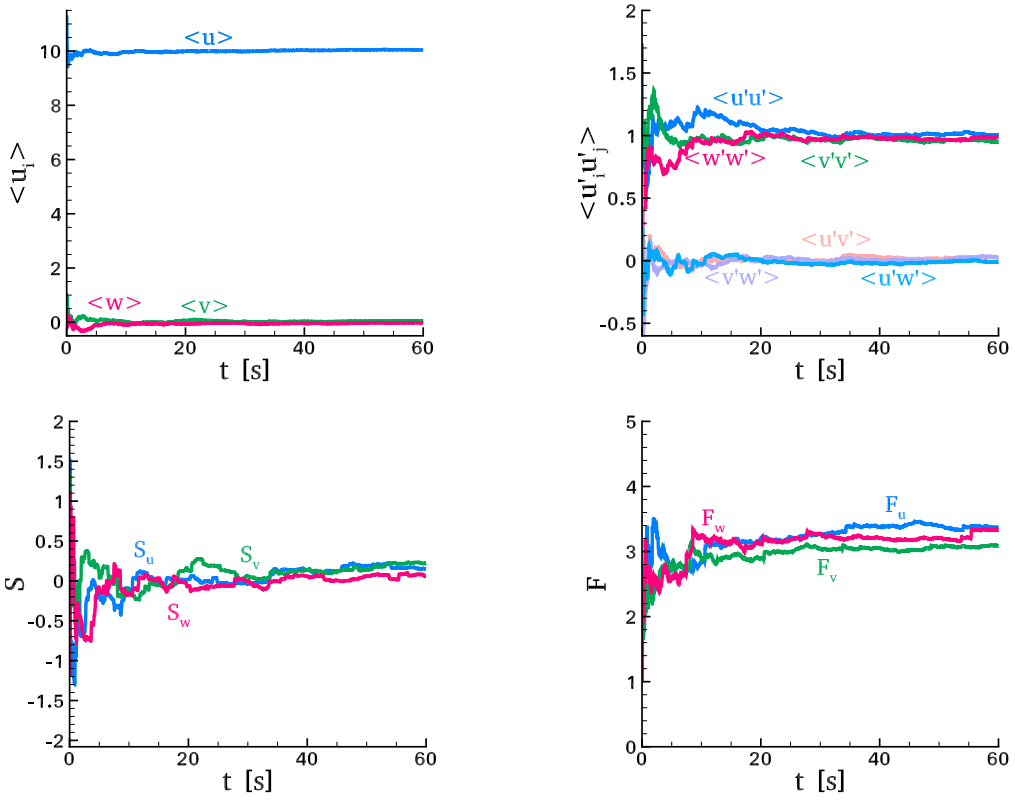

Figure 3.14: Time evolution of the time averaged velocity $< u_i >$ (top left), the Reynolds stresses $< u_i' u_j' >$ (top right), skewness (bottom left) and flatness (bottom right) at a point $(y, z) = (\pi, \pi)$ for the simulated SEM signal.

The time-averaged two-point correlations in the y-direction of the three velocity components are illustrated in figure 3.15. The expression of the two-point correlations of the velocity fluctuations writes

$$R_{ij}(\mathbf{x}, \mathbf{r}) =< u_i'(\mathbf{x}, t) u_j'(\mathbf{x} + \mathbf{r}, t) >, \tag{3.55}$$

where $\mathbf{r} = (r_1, r_2, r_3)$ is a vector defining the relative positions between the two-points at which the velocity correlations are computed. In [37], Jarrin demonstrates that given the formulation of the SEM, and for $\mathbf{x} = 0$, the following expression can be found for $R_{ij}(0, r, 0)$,

$$R_{ij}(\mathbf{r}) = R_{ij} \prod_{l=1}^{3} [f \star f] \left(\frac{r_l}{\sigma} \right), \tag{3.56}$$

where '⋆' denotes the convolution product. The obtained evolutions for the three time-averaged two-point correlations are therefore coherent; a maximum value of 1 for $r = 0$ and a decreasing evolution towards zero, attained at $\sim r = 1$.

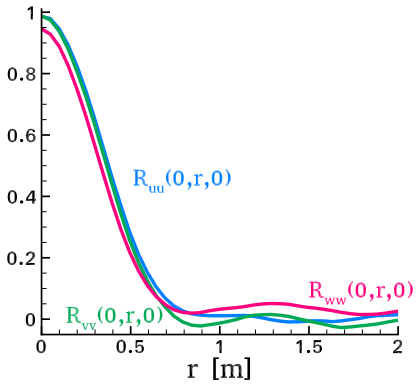

Figure 3.15: Two point correlations in the y direction for the velocity components of the simulated SEM signal.

3.3.2.2 Homogeneous isotropic turbulence

A second validation study for the implemented SEM was conducted for the simulation of spatially decaying homogeneous isotropic turbulence (HIT). This configuration allows to verify that the coherent structures generated using the SEM evolve towards a turbulent flow. Most works involve temporal decaying HIT ([46], [1]), where the computational domain is filled with turbulent fluctuations and their evolution in time is recorded. The spatially decaying HIT assumes a rough initialization of the field. The turbulence is imposed as an inflow boundary condition at the inlet plane. Synthetic turbulent fluctuations are superimposed on the mean velocity, non-zero only in the streamwise direction. The spatially evolution of the coherent structures is studied.

The computational domain has the dimensions $l_x \times l_y \times l_z$, with $l_x = l_y = l_z = 1\ m$. Periodic boundary conditions are imposed in the normal y and spanwise z directions. At the inlet plane, we prescribe turbulent fluctuations obtained with the SEM superimposed to the streamwise mean velocity $U = 0.2\ m/s$. At $x = l_x$, an outflow boundary condition is imposed for the velocity field. For the pressure, the boundary conditions in the streamwise directions are: a Neumann condition $\partial p/\partial x = 0$ at $x = 0$ and a Dirichlet condition $p = 0$ at $x = l_x$. The velocity field is initialized by superimposing on the mean field of random fluctuations of maximum value $0.1\mathbf{U}$.

The turbulent Reynolds number $Re_{t,max} = u_{rms}\sigma/\nu$ one can simulate depends on the used mesh grid, as will be further explained. The minimum value for the Kolmogorov scale l_k corresponds to the grid dimension $\Delta x = l_x/(n_x - 1)$. On the other hand, the first Kolmogorov hypothesis states that for a HIT the dissipative structures are entirely described by the kinematic viscosity ν and the dissipation rate ϵ. This leads to the following relation between the length scale σ and the Kolmogorov scale l_k,

$$\epsilon = \frac{u_{rms}^3}{\sigma} = \frac{u_k^3}{l_k}, \tag{3.57}$$

where u_k is the Kolmogorov characteristic velocity. Furthermore, the Reynolds number based on the Kolmogorov scales has to be 1, which leads to

$$u_k = \frac{\nu}{l_k}. \tag{3.58}$$

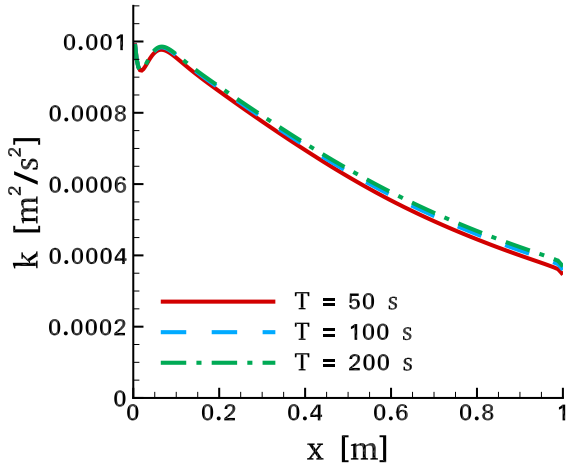

Figure 3.16: Spatial evolution of the turbulent kinetic energy in the x direction for a spatially decaying HIT at a turbulent Reynolds number $Re_t = 43.7$.

Injecting this expression in the dissipation rate relation we obtain

$$\frac{\sigma}{l_k} = Re_t^{3/4}. \tag{3.59}$$

For this study, the value for the length scale is $\sigma = l_x/15$. The argument for this choice is that it allows to generate enough vortices in order to have converged statistics (see Alis [1]).

The Kolmogorov and the length scales being fixed, the equation (3.59) gives the maximum turbulent Reynolds number not to be exceeded for a certain mesh grid. The rms velocity u_{rms} can then be computed.

In the present study we have used the mesh grid $256 \times 256 \times 256$. This implies a turbulent Reynolds number of $Re_t = 43.7$ with the characteristic length scales $\sigma = 0.067\ m$ and $l_k = 3.91 \cdot 10^{-5}\ m$ and a rms velocity $u_{rms} = 0.0262\ m/s$.

All the necessary parameters have now been defined. For the study of the spatially decaying HIT at $Re_t = 43.7$ we have investigated three criteria: the spatially decrease of the turbulent kinetic energy, the skewness and the flatness coefficients of the turbulent fluctuations. The statistics are computed using a space (in the y and z directions) average and a time average. For each quantity, a time convergence study has been conducted.

Figure 3.16 shows the evolution of the turbulent kinetic energy k' for different times of simulation. The time convergence is acquired for $T = 200\ s$. At the inlet plane, the turbulent kinetic energy converge towards the imposed value $k' = \frac{3}{2}u_{rms}^2 = 0.00102\ m^2/s^2$. The kink on all k' profiles from $x = 0$ to $x = 0.1$ is most certainly a numerical artifact.

For a HIT, the skewness and the flatness are calculated as the one-third of the trace of the corresponding tensors defined in the previous section (equations (3.51) and (3.52)),

$$S = \frac{1}{3}Tr(\mathbf{S}), \quad F = \frac{1}{3}Tr(\mathbf{F}). \tag{3.60}$$

In the textbook of Pope [76] it is shown that S and F are not constant, but increase with Reynolds number. Measurements of the flatness increase from $F \simeq 4$ in low-Reynolds-number grid turbulence to $F \simeq 40$ at the highest Reynolds numbers measured. For a Reynolds number $Re_t < 50$, the flatness is in the interval $3 < F < 4$. For this range of flatness values, the skewness

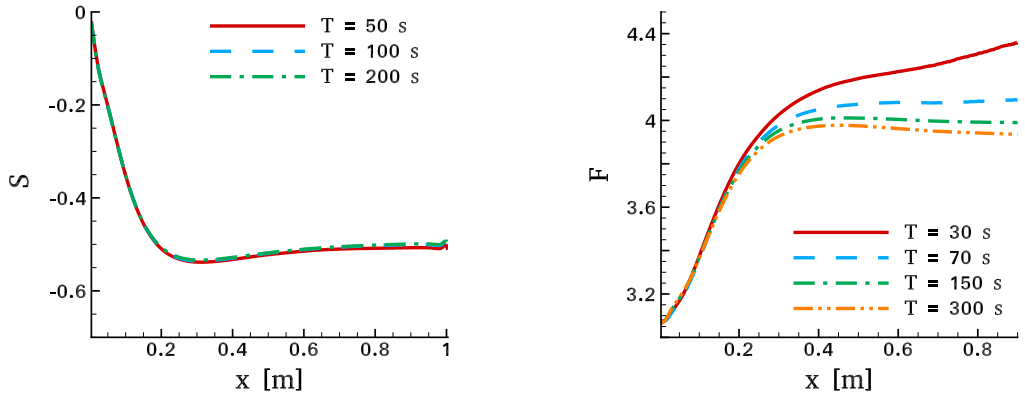

Figure 3.17: Spatial evolution of the skewness and the flatness for a spatially decaying THI at a turbulent Reynolds number $Re_t = 43.7$.

is $-0.5 < S < -0.4$. The spatial evolutions of these quantities are plotted in figure 3.17. It can be observed that the flatness demands further averaging to be fully converged.

The skewness and the flatness reach values that are at the limit of their corresponding range interval. Better results could certainly be obtained if the length in the streamwise direction was increased. Indeed, in comparison to the temporal decaying HIT, the spatial decrease demands a greater length in the streamwise direction. In the left of figure 3.18, the vorticity field obtained with the configuration presented above is plotted. The picture from the right of figure 3.18 corresponds to a length two times higher in the streamwise direction and using a coarser mesh grid $256 \times 128 \times 128$. For this second case, the decrease of the turbulence is unequivocal. Nevertheless, the computational cost to simulate this configuration for the correct mesh grid $512 \times 256 \times 256$ are fairly important. Additionally, the results obtained for the computation domain $1 \times 1 \times 1$ are in very good agreement with the reference values. It has therefore been shown that the SEM allows the simulation of a spatially decaying HIT. We will further describe its configuration for a turbulent boundary layer flow.

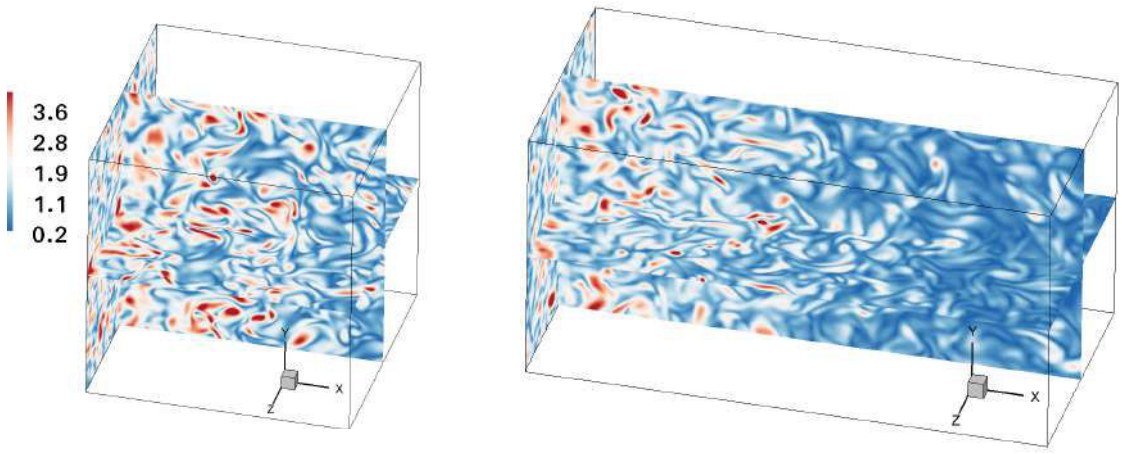

Figure 3.18: Vorticity magnitude field for a spatially decaying HIT at a turbulent Reynolds number of $Re_t = 43.7$ for two computational configurations: left - a box $1 \times 1 \times 1$ and $256 \times 256 \times 256$; right - a box $2 \times 1 \times 1$ and $256 \times 128 \times 128$.

3.3.3 Configuration of the SEM for a turbulent boundary layer flow

The SEM was originally used in [38] for the simulation of a spatially decaying homogeneous isotropic turbulence and of a fully developed turbulent channel flow. In this section the configuration of the SEM for the simulation of a spatially developing turbulent boundary layer flow on a flat plate is presented.

The use of the SEM demands first of all the knowledge of the input data $\overline{u}_i$, R_{ij} and σ. Furthermore, the friction velocity u_τ and the boundary layer thickness δ_{99} are also necessary for the processes of dimensionalization of the inflow data and the nondimensionalization of the obtained results.

Jimenez *et al.* [40] propose a full database for three momentum thickness Reynolds numbers: $Re_\theta = 1100, 1551$, and 1968. In the context of my thesis, only the database for $Re_\theta = 1100$ was used for computational cost reasons.

In addition to the dimensionless averaged statistics, Jimenez *et al.* also give the values for the friction velocity $u_\tau = 0.0462\ m/s$, the boundary layer thickness $\delta_{99} = 2.7568\ m$, the displacement thickness $\delta^* = 0.45\ m$, the momentum thickness $\theta = 0.3143\ m$ and the Reynolds number computed for the friction velocity $Re_\tau = \dfrac{u_\tau \delta_{99}}{\nu} = 445$. The information that can be extracted from this data are

- the kinematic viscosity, $\nu = 2.85911 \cdot 10^{-4}\ m^2/s$ from $\nu = \dfrac{u_\tau \delta_{99}}{Re_\tau}$,
- the free-stream velocity, $U_\infty = 1\ m/s$ from $U_\infty = \dfrac{\nu Re_\theta}{\theta}$,
- from $u_\tau = \left(\dfrac{\tau_0}{\rho}\right)^{1/2}$, if $\rho = 0.426\ kg/m^3$ then one can deduce the wall friction shear $\tau_0 = u_\tau^2 = 2.13444 \cdot 10^{-3}\ kg/m/s^2$.

The length scales $\sigma = (\sigma_x, \sigma_y, \sigma_z)$ define the size of the generated eddies. As outlined in section 3.2.1.3, the specification of length scales close to the ones found in real turbulent flows is of great importance (Pamies *et al.* [71]). In this work, we considered isotropic length scales, $\sigma_x = \sigma_y = \sigma_z = \sigma(y)$, that varies with the wall-normal direction y based on Prandtl's mixing-length hypothesis (Bejan [5]), i.e. $\sigma(y) = \kappa y$, where κ is the von Karman constant. However, due to the grid stretching in the wall-normal direction, close to the wall, the eddy becomes too small to be discretized in spanwise and streamwise directions. Therefore, the size of the eddies is calculated using

$$\sigma(y) = \max\left(\kappa y, \Delta\right), \tag{3.61}$$

where $\Delta = \max\left(\Delta x, \Delta y, \Delta z\right)$. The generated eddies are convected throughout the box B using the mean of the averaged velocity at the inlet plane $U_c = \left(\int_S \overline{u}(y)\mathrm{d}y\mathrm{d}z\right)/(l_y l_z)$.

3.3.4 Extension of the SEM for a thermal boundary layer

We describe here the proposed extension of this method for a thermal boundary layer inflow generation. The approach for generating a temperature signal $\tilde{\Theta}$ follows exactly the same steps detailed in section 3.3.1. The temperature imposed at the inlet plane writes

$$T(y, z, t) = T(y) + \theta_{rms}(y)\tilde{\Theta}(y, z, t), \tag{3.62}$$

where $\theta_{rms} = \sqrt{< \theta'^2 >}$ is the rms temperature.

The mean temperature T and the rms temperature θ_{rms} have to be specified at the inlet plane. To avoid an increase of the computational cost due to a change in the computational domain

dimensions ($Pr < 1$) or a more refined grid ($Pr > 1$), during all the simulations for this study, the Prandtl number was taken to be $Pr = 1$. This means that the thermal and dynamic boundary layers have the same thickness.

The survey of the literature on turbulent boundary layer flow with heat transfer presented in section 3.2.3 showed that the existing works were in general for momentum thickness Reynolds numbers of less than $Re_\theta = 1100$. Additionally, no database with all the necessary information was found.

Much attention has been paid on the similarity between the temperature and streamwise velocity. Perry and Hoffman [74] carried out experiments of a turbulent boundary layer developing on a heated uniform-temperature plate. They showed that the characteristics of momentum and heat fluxes are very similar to each other. Iritani *et al.* [36] showed that the feature of the temperature field near the wall is very similar to that of the velocity in the viscous wall region.

For these reasons, we decided to use the same database proposed by Jimenez *et al.* [40], making the assumption on the equivalence between the streamwise velocity and the temperature field. For this reason, the temperature equation (1.13) is transformed using a reduced temperature field defined by

$$\tilde{T} = \frac{T - T_\infty}{T_0 - T_\infty}, \tag{3.63}$$

where $\tilde{T} \in [0, 1]$.

The dimensionalization of the input data obtained from [40] is done using

$$\tilde{T}^+ = \frac{\tilde{T}}{\Theta_\tau}, \tag{3.64}$$

and

$$\theta'^+ = \frac{\theta'}{\Theta_\tau}. \tag{3.65}$$

In the context of this thesis, $Pr \simeq 1$ and $\epsilon_M = \epsilon_H$ ($\equiv Pr_t = 1$), which leads to (Bejan [5])

$$\Theta_\tau = \frac{\tau}{U_\infty}, \tag{3.66}$$

given that $\tilde{T}_\infty - \tilde{T}_0 = 1$.

For simplification reasons, hereinafter, the reduced temperature will be noted without the tilde, $T \equiv \tilde{T}$.

3.4 Inlet plane statistics obtained using the SEM

The implemented SEM was validated for the simulation of instantaneous signals of synthetic isotropic turbulence as well as for a spatially decaying HIT in section 3.3.2. After configuring the SEM for a turbulent boundary layer, we have first made some verifications on the inlet inflow data calculated using this approach. The objective is to make sure that the mean and rms fields of the SEM inflow is equal to the prescribed Jimenez data [40]. Different parameters can influence the performance of the SEM at the inlet plane: the number of eddies N, the length scale σ, the mesh resolution in the wall-normal direction and the physical time over which the statistics are averaged. All these will be discussed in what follows.

3.4.1 Computational configuration

For this preliminary study, we have considered a box of dimensions $(3.6 \times 3.6 \times 3.6)\delta_{inlt}$, where δ_{inlt} is the boundary layer thickness at the inlet plane equal to 2.7568 m. Different mesh grids as

well as different values for the number of eddies N are used in order to study their corresponding influence, as further explained. These configurations are described in table 3.5.

Periodic boundary conditions are imposed in the spanwise y-direction for the velocity components and the temperature. The no-slip boundary condition for the velocity components and Neumann condition for the pressure, as well as a Dirichlet condition for the reduced temperature, are imposed at the wall boundary,

$$u = v = w = 0, \quad \frac{\partial p}{\partial y} = 0, \quad T = 0 \quad \text{at} \quad y = 0. \tag{3.67}$$

Neumann conditions for the velocity components, the pressure and the reduced temperature field were imposed at the free-stream boundary,

$$\frac{\partial u}{\partial y} = \frac{\partial w}{\partial y} = 0, \quad v = 0, \quad \frac{\partial p}{\partial y} = 0, \quad \frac{\partial T}{\partial y} = 0 \quad \text{at} \quad y = l_y. \tag{3.68}$$

At the outflow plane $x = l_x$ the following conditions were prescribed for the velocity components

$$\frac{\partial u}{\partial x} + \frac{\partial v}{\partial y} + \frac{\partial w}{\partial z} = 0, \quad \frac{\partial v}{\partial x} + \frac{\partial u}{\partial y} = 0, \quad \text{and} \quad \frac{\partial w}{\partial x} + \frac{\partial u}{\partial z} = 0. \tag{3.69}$$

A zero value for the pressure $p = 0$ and a Neumann condition for the temperature $\partial T/\partial x = 0$ are also imposed at the outflow $x = l_x$.

At the inflow plane, the described SEM is used to impose the velocity and temperature profiles. A zero-gradient $\partial p/\partial x = 0$ is prescribed at $x = 0$.

The velocity and the temperature fields are initialized with the mean profile obtained from Jimenez *et al.* [40]. Random fluctuations are superimposed, with a maximum amplitude of 10% of the mean profile.

Note that the post-processing is done at the inlet plane $x = 0$. The statistics are averaged in time and in the z direction. For each configuration, former time convergence studies have been conducted in order to determine the time of simulation at which the averaged statistics are converged (see Appendix B.1).

3.4.2 Computational constraints

Before discussing the results obtained at the inlet plane, we consider of great importance to detail the different computational constraints encountered during this work.

The in-house code DIVA has been described in section 1.3. The resolution of the pressure equation as well as the temperature field is done using a Black Box MultiGrid method. This solver performance has greatly been demonstrated for configurations where uniform grids and computational domains of equal dimensions l^3 are used [22, 63]. Nevertheless, during my thesis, it has been found that the solver performances are deteriorated for simulations using non uniform grids and/or high aspect ratio for the domain or the grid dimensions. This represents a limitation of the current solver to investigate thoroughly the DNS of turbulent boundary layer.

We will further show these limitations by investigating the BBMG solver performances on configurations with different aspect ratio, for the simulation of a turbulent boundary layer flow on a flat plate.

Let it be $\xi_l = \max(l_x/l_y, l_x/l_z, l_y/l_z)$ the maximum aspect ratio for the computational domain dimensions and $\xi_g = \max(\Delta x/\Delta y, \Delta x/\Delta z, \Delta y/\Delta z)$ the maximum aspect ratio for the mesh grid. In table 3.4 the number of iterations needed to solve the pressure equation is given, for different configurations. The configuration $\xi_l = 4$ or $\xi_l = 8$ is representative of a computational box 4 or 8

times longer in the streamwise direction. The value $\xi_g = 1$ corresponds to an uniform mesh grid while $\xi_g \sim 8$ or $\xi_g \sim 17$ represents a non-uniform mesh grid in the y direction.

It can be observed that, when the aspect ratio, ξ_l or ξ_g, is increased, the number of iterations in the BBMG solver is also considerably increased. The use of a computational domain 8 times longer than a $l_x = l_y = l_z$ domain, implies a time cost multiplied by 8 for a non-uniform grid. Additionally, if one wants to refine the mesh in the y direction in order to capture the smaller eddies as well as go further in the viscous sublayer, the limit value for the aspect ratio is around 8. For higher values, the number of iterations increases drastically. Additionally, a reduction of the time step is needed to ensure the stability of our simulation.

These computational constraints due to the used solver will impact our work and results, by limiting the resolution of the boundary layer.

	$\xi_l = 1$			$\xi_l = 4$		$\xi_l = 8$	
	$\xi_g = 1$	$\xi_g \sim 8$	$\xi_g \sim 17$	$\xi_g = 1$	$\xi_g \sim 8$	$\xi_g = 1$	$\xi_g \sim 8$
BBMG nb. of iterations	10	45	204 ($\Delta t/2$)	45	65	310	370

Table 3.4: Computational constraints due to the BBMG solver used for the resolution of the Poisson equation for the pressure. The number of iterations needed for the resolution of the Poisson equation for the pressure for different configurations. The configuration ($\xi_l = 1$, $\xi_g = 1$) is representative of the box $(3.6 \times 3.6 \times 3.6)\delta_{inlt}$ and the uniform mesh grid $128 \times 128 \times 128$.

3.4.3 Mesh grid and number of eddies influence onto the inlet statistics

The structural information of the boundary layer is varying in the wall-normal direction. In tables 3.1 and 3.3, it has been shown that the minimum size of grid close to the wall should be around $\Delta y^+_{min} = 0.5$ for a DNS. Nevertheless, given the computational constraints explained in section 3.4.2, we only went to $\Delta y^+_{min} = 1.55$.

Table 3.5 exposes the different configurations used for the discussion on the mesh grid and number of eddies influence onto the inlet plane obtained statistics. The key parameters in this discussion are the time cost per 8 s simulation t_{cost} and the convergence time of the turbulent statistics T_{cv}.

Some trends emerge from table 3.5. Increasing the mesh refinement induces an increase of the time cost while lowering the convergence time. Eddies multiplication in the virtual box does not entail the same increase in the time of simulation for each mesh grid. For a coarse mesh (C.1), an increase of 10 times in the number of eddies induce an increase of 6 times in the time cost, while for a more refined mesh (C.2), the ratio is only of 2. The time of convergence is highly influenced by the number of eddies and the mesh grid. Indeed, if the virtual box is poorly populated, then the averaged statistics need a much longer time to attain convergence. Last but not least, when increasing the number of eddies N, for a refined mesh grid (C.2), a reduction of the time step is needed in order to ensure the stability.

First, we have conducted a study allowing to determine the number of eddies N needed to obtained the expected statistics at the inlet plane. The obtained evolutions are plotted in figure 3.19. For the coarse grid $64 \times 64 \times 64$, the value of $N = 4000$ is sufficient. When the mesh grid is refined to $128 \times 128 \times 128$, besides enabling a deeper resolution into the viscous sublayer, we observe that some of the statistics are under- or overevaluated.

	Mesh	Nb. eddies (N)	t_{cost} $[h]$ (for 8 s job)	T_{cv} $[s]$
C.1.1	$64 \times 64 \times 64$ $\Delta x^+ = \Delta z^+ \sim 25$ $\Delta y^+_{min} = 3.1$ $\Delta y^+_{max} \sim 40$ $\sigma^+_{min} \sim 25$	4000	~ 0.09	~ 960
C.1.2		8000	~ 0.1	~ 480
C.1.3		16000	~ 0.15	~ 240
C.1.4		40000	~ 0.55	~ 240
C.2.1	$128 \times 128 \times 128$ $\Delta x^+ = \Delta z^+ \sim 12.6$ $\Delta y^+_{min} = 1.55$ $\sigma^+_{min} \sim 12.6$	4000	~ 3	~ 480
C.2.2		8000	~ 5 $(\Delta t/2)$	~ 240
C.2.3		16000	~ 5.2 $(\Delta t/2)$	~ 120
C.2.4		40000	~ 6 $(\Delta t/2)$	~ 120
C.3.1	$128 \times 64 \times 128$ $\Delta x^+ = \Delta z^+ \sim 12.6$ $\Delta y^+_{min} = 3.1$ $\Delta y^+_{max} \sim 40$ $\sigma^+_{min} \sim 12.6$	4000	~ 0.8	~ 480
C.3.2		40000	~ 1.4	~ 120

Table 3.5: Configurations used for the discussion on the mesh grid and the number of eddies influence onto the inlet statistics. $l^+_{s,min}$ is the smaller length scale captured with the corresponding configuration. t_{cost} $[h]$ is the time cost for a simulation of 8 s. T_{cv} $[s]$ is the time of convergence for the turbulent statistics. Each simulation has been conducted using 8 processus.

The number of eddies has to be increased 10 times in order to obtain the prescribed statistics, except for the rms velocity in the spanwise direction, w^+_{rms}. Indeed, the mesh refinement used here does not suffice to obtain the prescribed w^+_{rms}. Nonetheless, an improvement can be observed when the mesh is refined, as it can be observed in figure 3.20.

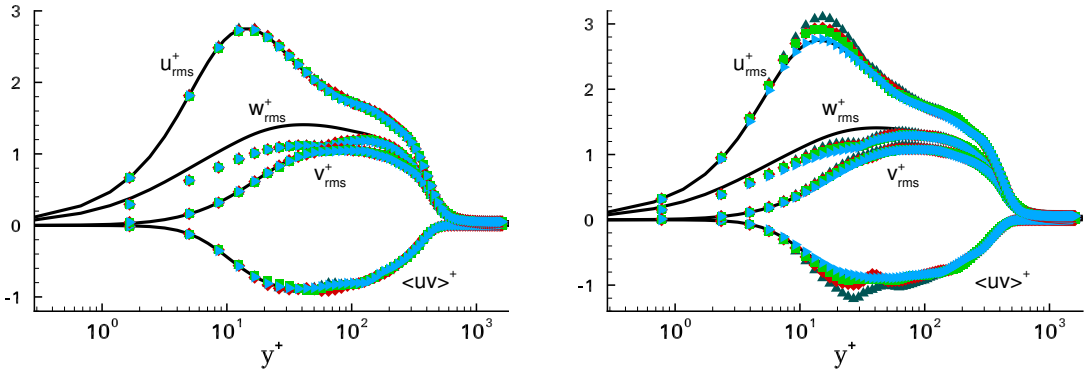

(a) 64 × 64 × 64

(b) 128 × 128 × 128

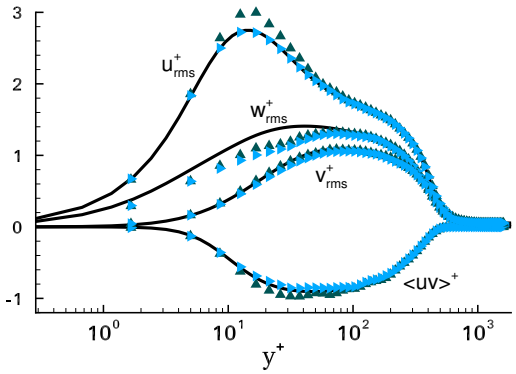

(c) 128 × 64 × 128

Figure 3.19: Inlet plane statistics evolution with the wall coordinate, for different values of number of eddies N. Each curve is plotted after the corresponding T_{cv}. (black line) - Jimenez data [40]; (▲) - $N = 4000$; (♦) - $N = 8000$; (■) - $N = 16000$; (▶) - $N = 40000$;

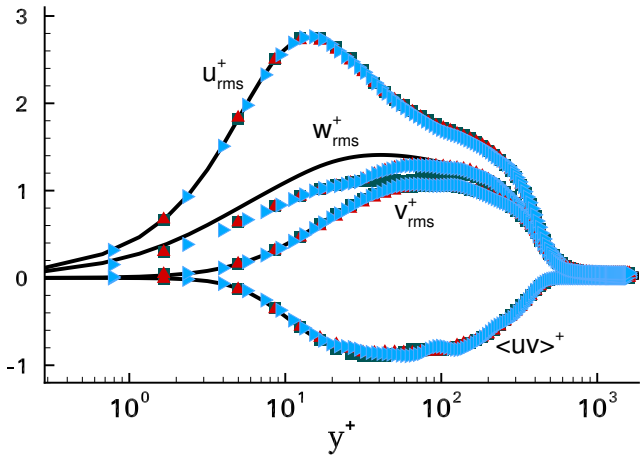

Figure 3.20: Inlet plane statistics evolution with the wall coordinate, for different mesh grids. Each curve is plotted after the corresponding T_{cv}. (black line) - Jimenez data [40]; (■) - $64 \times 64 \times 64$, $N = 4000$; (▲) - $128 \times 128 \times 128$, $N = 40000$; (▶) - $128 \times 64 \times 128$, $N = 40000$.

It is interesting that the mesh refinement in the three directions $128 \times 128 \times 128$ or in the x and z directions $128 \times 64 \times 128$, have the same influence. Indeed, the number of eddies has to be increased for both cases and, as it can be remarked from figure 3.20, the obtained curves overlap. As seen from the definition of the length scale σ, equation (3.61), the smallest length scale captured does not depend on the Δy_{min}, when a non-uniform mesh is used. So, when the length scale is smaller due to smaller dimensions of the mesh in the x and z directions, the compact support of the velocity distribution f_σ, equation (3.48), is diminished. Thus, more eddies are needed for the convergence of the ensemble mean (3.47). This also follows from the illustration of the velocity field u in figure 3.21. The velocity field plotted in 3.21c is much more closer to a boundary layer flow snapshot than 3.21b, where fewer eddies spots can be observed.

Considering the maximum ratio of the mesh dimensions at the wall, the inner zone is populated with eddies of larger length scales, regardless of the Δy_{min} (see values of σ in table 3.5). This implies a structural information of the turbulence fairly different from the real one.

During my thesis, an attemp to adress this point was conducted by implementing the method of Pamies *et al.* [72]. Their approach to impose dimensions and velocity distributions allows to dispose of the definition of the length scale (3.61). Nevertheless, as it can be observed in Appendix B.2, we were not able to obtained satisfactory results for our DNS (their work was on a LES of spatially developing boundary layer).

3.4.3.1 Closing remarks

The analysis on the inlet plane statistics presented in the previous section was first of all a validation of the SEM for a boundary layer inflow data. Second, the purpose of this study was to allow choosing the most suitable computational configuration for the forthcoming work on the spatial evolution of a boundary layer. The analysis showed a strong link between the mesh grid, the consequent length scale and the number of eddies.

Considering the informations on the domain dimensions (tables 3.1 and 3.3) and on the adaptation distance (table 3.2), the ideal computational domain should mesure $(28.8 \times 3.6 \times 3.6)\delta_{inlt}$. The corresponding mesh grid should write $2048 \times 128 \times 256$, with $N = 40000$ at least. This ideal configuration is considerably out of reach, considering the computing constraints explained in sec-

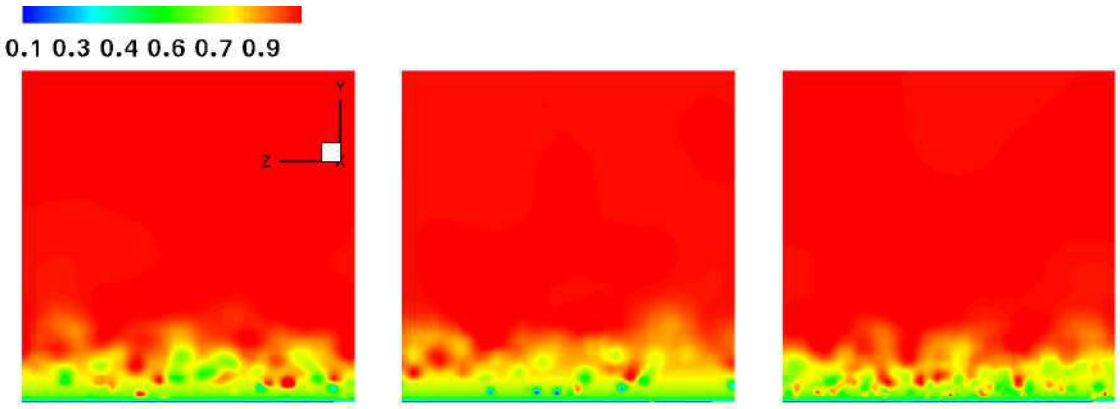

(a) $64 \times 64 \times 64$, $N = 4000$ (b) $128 \times 64 \times 128$, $N = 4000$ (c) $128 \times 64 \times 128$, $N = 40000$

Figure 3.21: Streamwise velocity field u $[m/s]$ at the inlet plane for different configurations.

tion 3.4.2. Additionally, the time step should undoubtedly be diminished to ensure the stability of the numerical solver.

Therefore, for the forthcoming study on the spatial development of a turbulent boundary layer on a flat plate, the following configuration has been used: a computational domain of dimensions $(14.4 \times 3.6 \times 3.6)\delta_{inlt}$, a mesh grid $512 \times 128 \times 128$ and a number of eddies of $N = 4000$. The imposed statistics are satisfactory and the computational cost in term of physical time needed for the simulations as well as the number of hours used on a supercomputer is reasonably. The specifics will be detailed in the next section.

3.5 Numerical simulation of a turbulent boundary layer flow with heat transfer at $Re_\theta = 1100$

In the following section we will describe the work on the numerical simulation of a turbulent layer flow over a flat plate with heat transfer, for a momentum thickness number of Re_θ. First, the computational configuration is described. Only small differences exist in comparison with the computational configuration described in the previous section 3.4. Next, the results obtained are presented and discussed.

3.5.1 Computational configuration

As already stated, for the present study we use a computational domain of dimensions $(14.4 \times 3.6 \times 3.6)\delta_{inlt}$ and a mesh grid $512 \times 128 \times 128$. The number of eddies is fixed at $N = 4000$.

The boundary conditions employed for this study are a slight different from the one described in section 3.4. At the free-stream boundary $y = l_y$, outflow boundary conditions are imposed,

$$\frac{\partial u}{\partial x} + \frac{\partial v}{\partial y} + \frac{\partial w}{\partial z} = 0, \quad \frac{\partial v}{\partial x} + \frac{\partial u}{\partial y} = 0, \quad \text{and} \quad \frac{\partial w}{\partial y} + \frac{\partial v}{\partial z} = 0. \tag{3.70}$$

and a Dirichlet condition for the pressure $p = 0$. The Neumann boundary condition on the temperature field has been conserved. The choice of an outflow boundary condition instead of a Neumann condition is related to the fact that later on the boundary layer will be blown by the liquid/vapor phase change. This would have not been coherent with a symmetrical condition on the velocity.

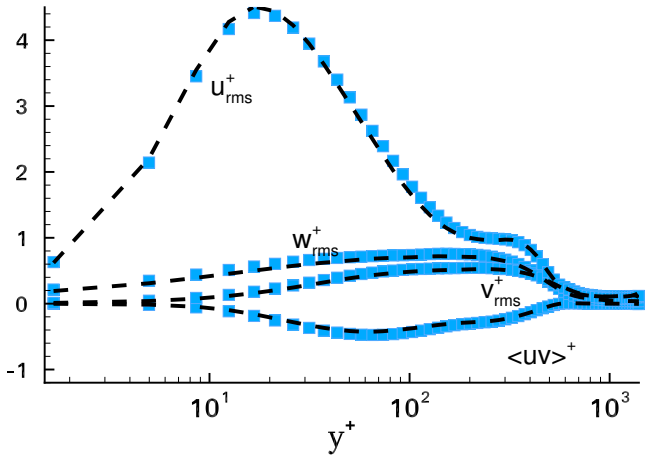

Figure 3.22: The influence of the outflow boundary condition on the computed statistics at the post-processing plane x_{pp}. Each curve is plotted after the corresponding T_{cv}. (■) - $256 \times 64 \times 64$; (dashed line) - $384 \times 64 \times 64$. For both configurations, the the post-processing plane is positioned at the same distance relative to the inlet plane.

The other boundary conditions, as well as the initialization have been done as described in section 3.4. Note that verifications have been made to show that the specified changes did not influence the inlet plane statistics (see Appendix B.3).

The post-processing for the evolution of the turbulent quantities with the wall coordinate y^+ is done on a normal to the streamwise plane, located at $x_{pp} = x(i = 5N_x/6)$, where N_x is the number of grids in the x direction. Considering the spatial development of the boundary layer and the constraint of the adaptation distance for the SEM, the choice of this position was done in order to be as far as possible from the inlet plane. On the other hand, too close to the outflow boundary can also have repercussions on the results. A verification has been made in order to ensure that the outflow boundary condition at $x = l_x$ does not influence the wall coordinate evolution of the obtained statistics. A coarse mesh has been employed, $256 \times 64 \times 64$, given the computational costs when $\xi_l >> 1$ (see table 3.4). For both configurations, the post-processing plane is positioned at the same distance relative to the inlet plane. The obtained evolutions are shown in figure 3.22 and demonstrates that the post processing plane located at x_{pp} is not influenced by the outflow boundary conditions.

For the fixed x_{pp}, the average is done in time and in the z direction. Note that the average in time has been done after a certain time of simulation in order to remove all spurious influence of the initialization of the velocity and the temperature fields.

The simulations have been conducted using the supercomputer from Idris, ADA. Note that a simulation of $1528\theta_{inlt}/U_\infty = 480\ s$, done using $512 \times 128 \times 128$, lasted 25 days.

3.5.2 Results

We will further present the results obtained for the numerical simulation of the spatial development of a boundary layer flow on a flat plate with heat transfer, for a momentum thickness $Re_\theta = 1100$. Figure 3.23 shows a capture of the vorticity magnitude field for the developed boundary layer. Qualitatively, the synthetic vortices generated at the inlet plane evolve towards a boundary layer flow.

In figure 3.24 the reduced temperature field and the streamwise velocity field are represented.

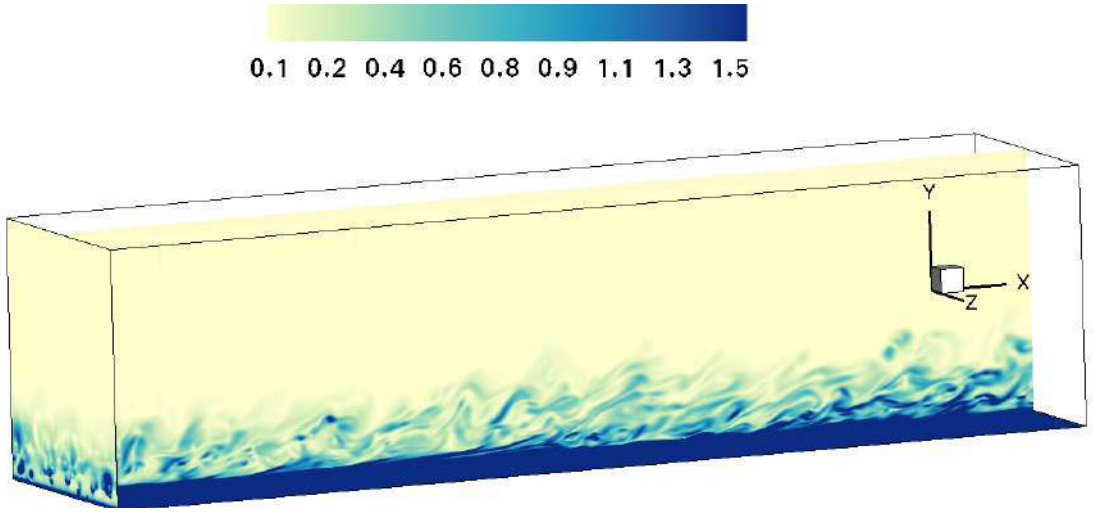

Figure 3.23: Vorticity magnitude field for a spatially developing boundary layer over a flat plate. The caption is taken after a simulation of $1528\theta_{inlt}/U_\infty = 480\ s$.

Some differences can be found between the two captions, but primarly the hypothesis used on the equivalence between the temperature and the streamwise velocity can be considered reasonable.

3.5.2.1 Evolution of the mean and rms quantities with the wall coordinate

In this section we will present the results obtained for the mean and the rms quantities (for velocity and temperature).

The mesh grids employed in this study are $256 \times 64 \times 64$ and $512 \times 128 \times 128$. As seen previously, the time of convergence of the turbulent statistics is not the same when using different mesh grid resolutions. The evolution of the mean and rms quantities is plotted, for the mesh grid $256 \times 64 \times 64$, in figure 3.25, and for the mesh grid $512 \times 128 \times 128$, in figure 3.26. The time needed for the averages to achieve convergence is $T_{cv} = 1528U_\infty/\theta_{inlt} = 480\ s$ for $256 \times 64 \times 64$ and $T_{cv} = 764U_\infty/\theta_{inlt} = 240\ s$ for $512 \times 128 \times 128$.

The influence of the mesh grid has already been studied in consideration to the inlet plane statistics. It has been shown that, for the inlet plane, refining the mesh grid to go further into the viscous sublayer demanded a larger number of eddies in order to achieve convergence to the prescribed statistics. Aside from the poor resolution of the viscous sublayer, the coarse mesh was sufficient to obtain the prescribed statistics. These tendencies are not expected for the post-processing plane. Indeed, as already stated in the literature (section 3.2.3), the inlet synthetic turbulence will first encounter a decline and then, after a certain adaptation distance, it will start to redevelop into real turbulence. This trend can be observed in figure 3.27, where we plotted the isosurfaces 0.25 of the Q criterion. Q represents the local balance between shear strain rate and vorticity magnitude, defining vortices as areas where the vorticity magnitude is greater than the magnitude of rate-of-strain. The inlet imposed vortices, lacking energy spectra, are rapidly dissipated, to finally redevelop into real turbulence.

For the chosen computational configuration, the influence of the mesh grid onto the evolution of the mean and rms quantities, as well as a comparaison with the Jimenez [40] prescribed statistics and the actual statistics calculated for the imposed inlet inflow are plotted in figure 3.28. The first observation is that the mesh refinement greatly improve the obtained results. This can be seen for all the turbulent quantities. However, some differences can be observed in the logarithmic layer

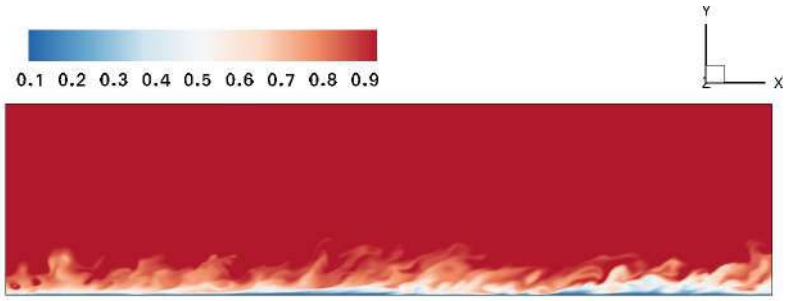

(a) T

(b) u $[m/s]$

Figure 3.24: Reduced temperature and streamwise velocity fields for a spatially developing boundary layer over a flat plate. The caption is taken after $1528\theta_{inlt}/U_\infty = 480$ s.

for the rms quantities. The mean fields are not entirely recovered in the buffer layer.

These illustrations show that mesh refinement is still needed to obtain the correct statistics. Indeed, smaller scales would be captured and the energy cascade from the large to small eddies would be better reproduced. This observation agree with what we have seen in the literature (see tables 3.1 and 3.3) where a more refined mesh grid is often used.

The evolution obtained for the rms temperature is slightly different from the streamwise rms velocity. This was also visible when the temperature and the velocity fields have been represented in a x-y plane (figure 3.24). These differences can be related inter alia, to the use of the scattered mesh, where the temperature and the velocity are not computed on the same grid. Or else, the use of different boundary conditions could also induce some discrepancies between the resolutions of the two fields.

3.5.2.2 Evolution of the heat fluxes quantities with the wall coordinate

To analyze the characteristics of the correlations between the velocity and the temperature fluctuations, the turbulent heat fluxes are defined by:

$$< u'\theta' >^+ = \frac{< u'\theta' >}{u_\tau \theta_\tau}, \tag{3.71}$$

$$< v'\theta' >^+ = \frac{< v'\theta' >}{u_\tau \theta_\tau}. \tag{3.72}$$

Their evolutions in wall units are illustrated in figure 3.29, for the two mesh grids used in this study. Additionally, the heat fluxes calculated for the inlet inflow is also plotted. It can be observed that the mesh grid influence is even more important than for the rms velocity and temperature. The profiles obtained with the more refined mesh $512 \times 128 \times 128$ are close to the ones calculated at the inlet plane.

Figure 3.30 shows the streamwise and wall-normal turbulent heat fluxes here obtained for a momentum thickness Reynolds number $Re_\theta = 1100$, together with the numerical results of Wu and

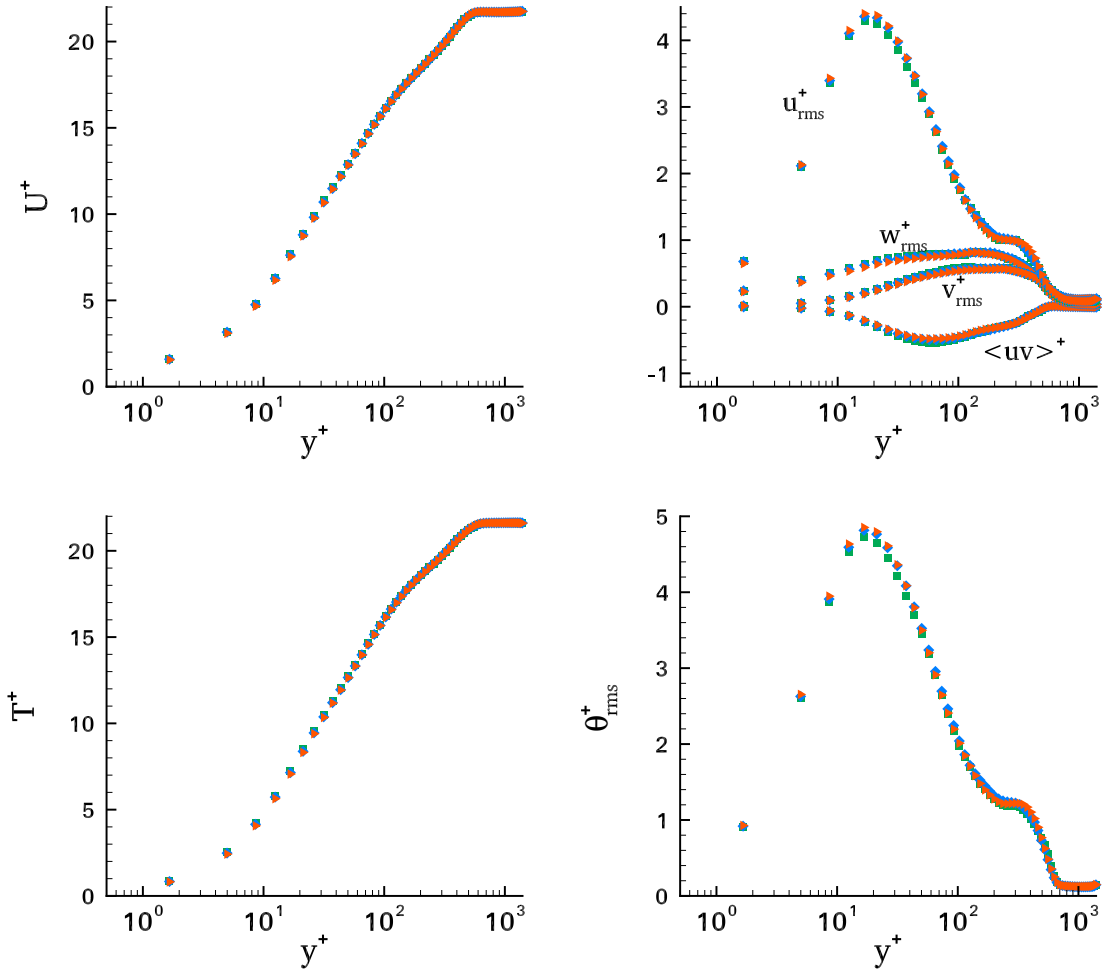

Figure 3.25: Turbulent statistics evolution with the wall coordinate, for the mesh grid $256 \times 64 \times 64$. Different values of times of simulation for the average processus (after eliminating 240 s of simulation) are considered: (■) - $T_{cv} = 120$ s; (◆) - $T_{cv} = 240$ s; (▶) - $T_{cv} = 480$ s.

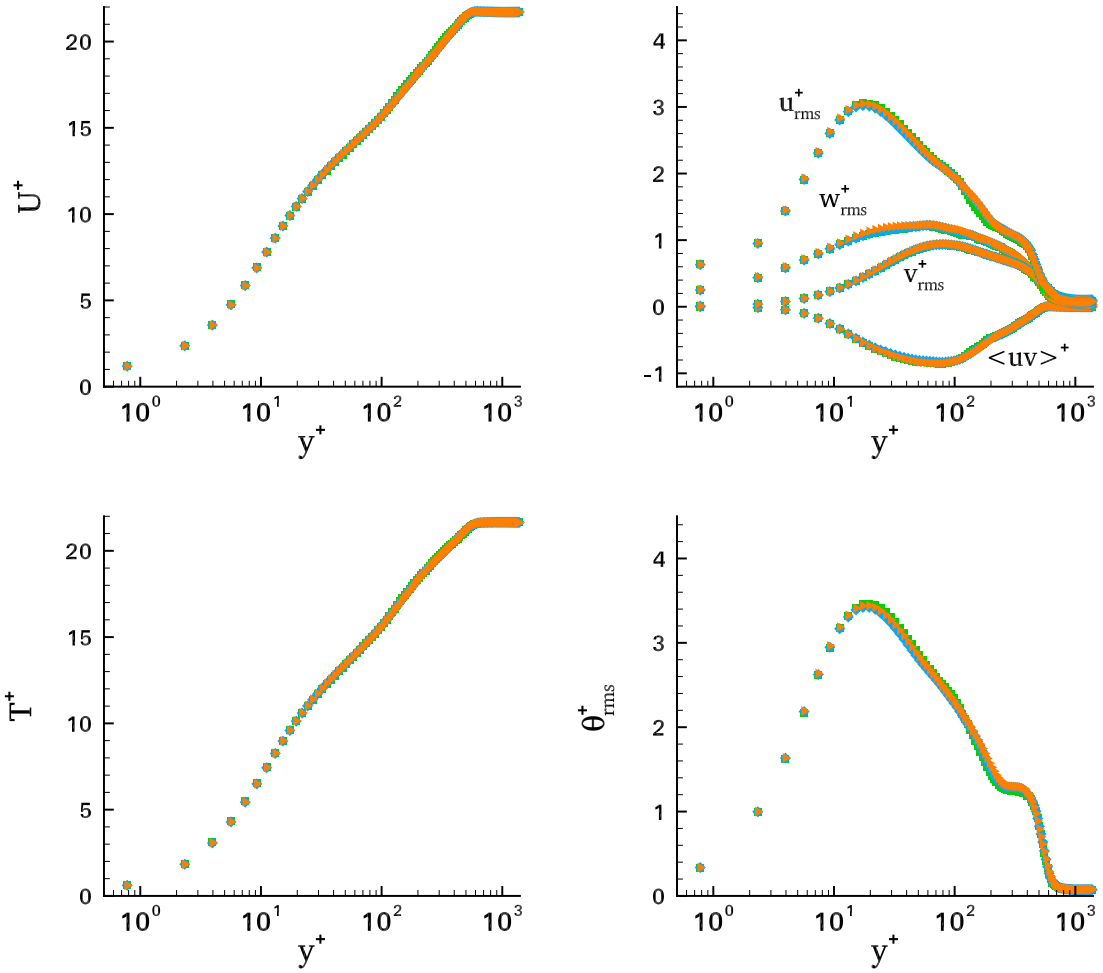

Figure 3.26: Turbulent statistics evolution with the wall coordinate, for the mesh grid $512 \times 128 \times 128$. Different values of times of simulation for the average processus (after eliminating 480 s of simulation) are considered: (■) - $T_{cv} = 60$ s; (◆) - $T_{cv} = 120$ s; (▶) - $T_{cv} = 240$ s.

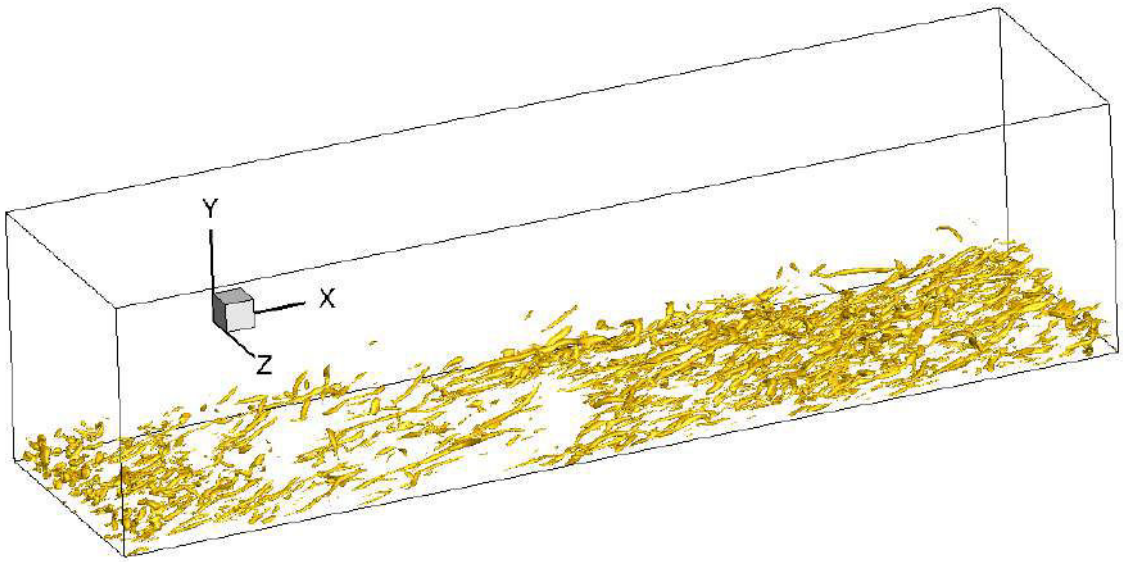

Figure 3.27: Isosurfaces of the Q criterion of value $Q = 0.25$ for a spatially developing boundary layer over a flat plate. The caption is taken after $T = 1528\theta_{inlt}/U_\infty = 480\ s$.

Moin [107] at $Re_\theta = 1840$ and $Re_\theta = 300$, for a Prandtl number of $Pr = 1$. Despite the different values of the Reynolds number, strong similarities are observed between the obtained profiles and the ones from [107]. The wall-normal heat flux $< v'\theta' >^+$ is in good agreement with the data from [107] in the near-wall region. Good agreement is also observed in the profile of the streamwise heat flux $< u'\theta' >^+$ except in the vicinity of the peak location. This difference can be related to the lack of mesh convergence.

In the outer region, the profiles are slighty different from the reference data. This difference can be explained by the difference in Reynolds number. Indeed, in this region, the curves obtained for a $Re_\theta = 1100$ are situated between the $Re_\theta = 300$ and $Re_\theta = 1840$ Wu and Moin x profiles.

Kong *et al.* [49] have also shown that the wall-normal heat fluxes for different Reynolds numbers coincide up to $y^+ = 50$. In the outer region, the wall-normal flux becomes larger with increasing Reynolds number. The profile of the streamwise heat flux also shows a similar behavior as the wall-normal heat flux as the Reynolds number increases.

Figure 3.31 illustrates the evolution of the turbulent Prandtl number with the wall coordinate. Pr_t tends to remain constant along the wall-normal direction except in the very near-wall region where a maximum value is obtained at the wall, with $Pr_t = 1.09$. Similar wall values have also been reported in other previous studies, [49, 59, 2], in which Pr_t approaches a value of 1.1 at the wall. In the $y^+ < 40$ region, the turbulent Prandtl number is in very good agreement with the reference data. For higher values of the wall coordinate, some slight differences can be observed.

3.5.2.3 Streamwise evolution of the turbulent quantities

Figure 3.32 shows the variations of the mean skin-friction coefficient C_f and the Stanton number St with the momentum thickness Reynolds number Re_θ. The definitions of these parameters are given in section 3.1.1, equations (3.6) and (3.7). The turbulent correlations for the skin-friction coefficient, $C_f = 0.024 Re_\theta^{-1/4}$, and for the Stanton number, $St = 0.0125 Pr^{-2/5} Re_\theta^{-1/4}$, proposed by Kays and Crawford [44], are also included for comparison. In addition, the evolutions obtained in the DNS of Wu and Moin [107] and Li *et al.* [58] are also plotted.

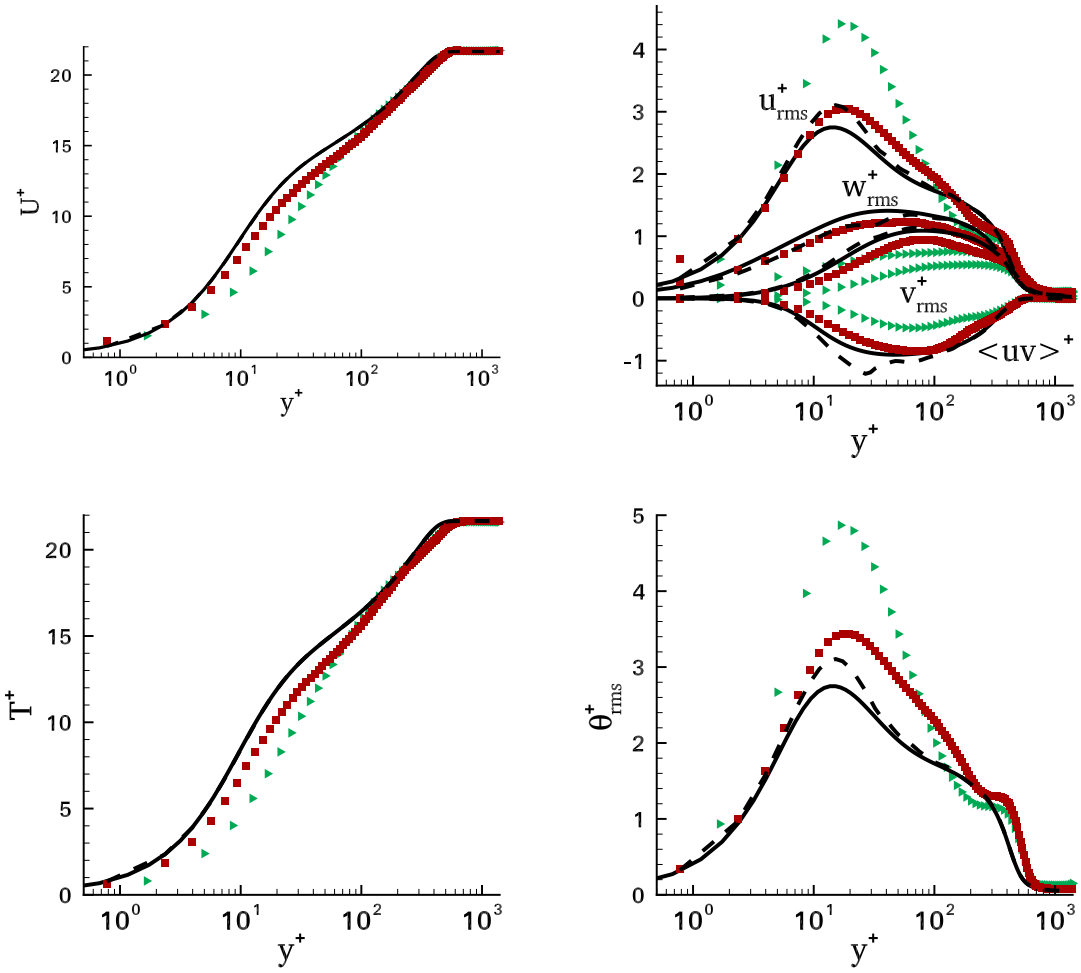

Figure 3.28: The influence of the mesh grid onto the wall coordinate evolution of the turbulent statistics. Each curve is plotted after the corresponding T_{cv}. (black line) - Jimenez data [40]; (dashed line) - the statistics of the imposed inlet inflow; (▶) - $256 \times 64 \times 64$; (■) - $512 \times 128 \times 128$.

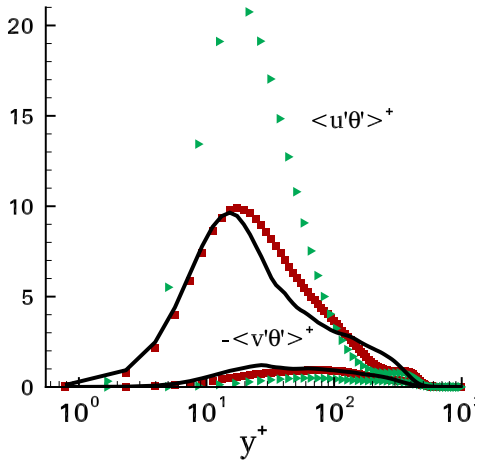

Figure 3.29: Turbulent heat fluxes in the streamwise $< u'\theta' >^+$ and wall-normal $< v'\theta' >^+$ directions. Each curve is plotted after the corresponding T_{cv}. (black line) - the statistics of the imposed inlet inflow; (▶) - $256 \times 64 \times 64$; (■) - $512 \times 128 \times 128$.

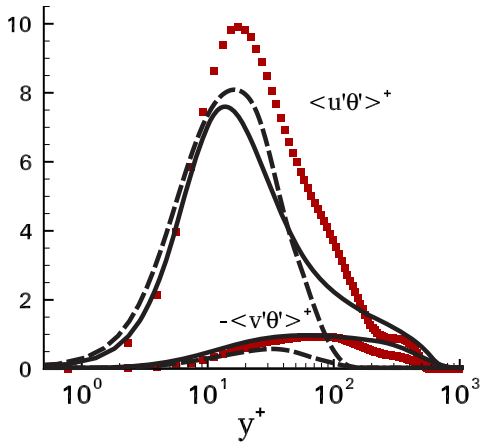

Figure 3.30: Turbulent heat fluxes in the streamwise $< u'\theta' >^+$ and wall-normal $< v'\theta' >^+$ directions. Comparison with the data extracted from Wu and Moin [107] for a $Pr = 1$; (solid lines) - $Re_\theta = 1840$ and (dashed lines) - $Re_\theta = 300$. (■) - present results obtained with $512 \times 128 \times 128$.

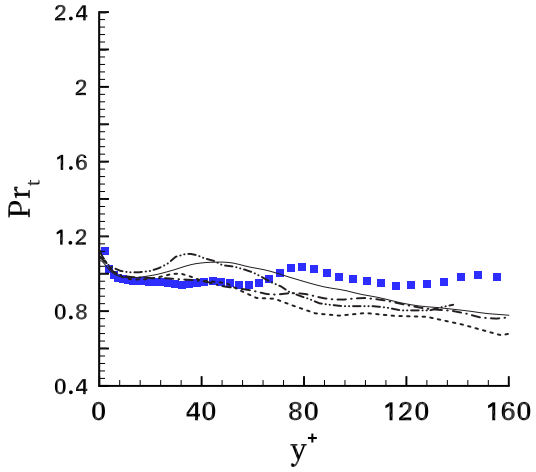

Figure 3.31: Turbulent Prandtl number Pr_t in wall units. Comparison with the data extracted from the literature; (solid line) - DNS of Li *et al.* [59] for $Re_\theta = 800$, (dashed lines) - DNS of Araya and Castillo [2] for $Re_\theta = 400$; (dashed dot lines) - DNS of Araya and Castillo [2] for $Re_\theta = 2290$; (dashed dot dot lines) - DNS of Kong *et al.* [49] for $Re_\theta = 376$; (■) - present results obtained with $512 \times 128 \times 128$, for $Re_\theta = 1100$.

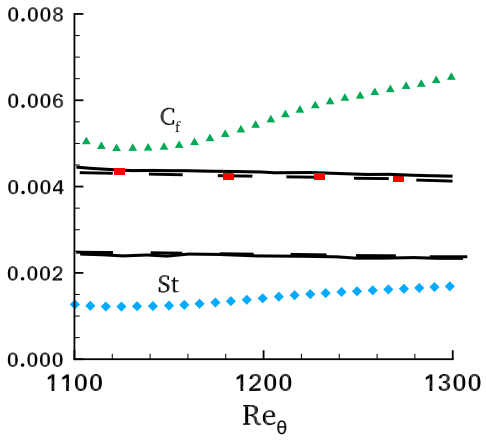

Figure 3.32: Streamwise variation of the skin friction coefficient C_f and the Stanton number St with Re_θ. (solid lines) - Li *et al.* [58]; (dashed lines) - turbulent correlations from Kays and Crawdord [44];(■) - Wu and Moin [107]; (▲) - present C_f; (♦) - present St, obtained with $512 \times 128 \times 128$.

The results obtained in the present study are overvalued, for the C_f, and underestimated, for the St. The friction coefficient decreases close to the inlet plane, for $Re_\theta < 1150$, followed by an increase with the Reynolds number, whereas its evolution should be the opposite. The Stanton number evolution is on the right path. One can assume that if the length in the streamwise dimension l_x was higher, the St curve would reach the reference curves, and maybe attain the correct slope.

These behaviour patterns are often found in the numerical simulation of turbulent boundary layer flow on a flat plate. For example, in the random fluctuation method proposed by Lund *et al.* [62], the friction coefficient exhibits a sharp drop between the inlet plane at $Re_\theta = 1500$ until $Re_\theta = 1850$, the maximum error being 70%, followed by an increase once the flow develops realistic turbulent structure. The same trend is observed by Keating *et al.* in [45], where precursor time series are used for the inlet inflow. The coefficient of friction decreases immediately downstream of the inflow plane, but then recovers after $6 - 10\delta_{inlt}$, as can be seen in figure 3.33. Pamies *et al.* [72] obtain also a similar behavior, when using the modified SEM of Jarrin *et al.* [38]. In their case, the friction coefficient increases drastically downstream the inlet plane but recover quickly, after $3 - 6\delta_{inlt}$.

This information implies that, in order to obtain better profiles for the friction coefficient and Stanton number, we should increase the length dimension in the streamwise direction. This would allow the development of the generated turbulence towards a more realistic one. Given the already stated computational constraints, in the present study, the increase of the streamwise direction was not possible.

In the next chapter we will present our work on the interaction between the phase change induced velocity and the boundary layer flow. To this extent, a second simulation will be used. This will allow, firstly, to consider an extension of the spatial development of the boundary layer and to investigate the influence of the dimension l_x onto the evolutions of the turbulent quantities.

3.6 Conclusions

This chapter was devoted to the numerical simulation of the spatial development of a turbulent boundary layer flow on a flat plate, with heat transfer. A thorough overview of the literature on

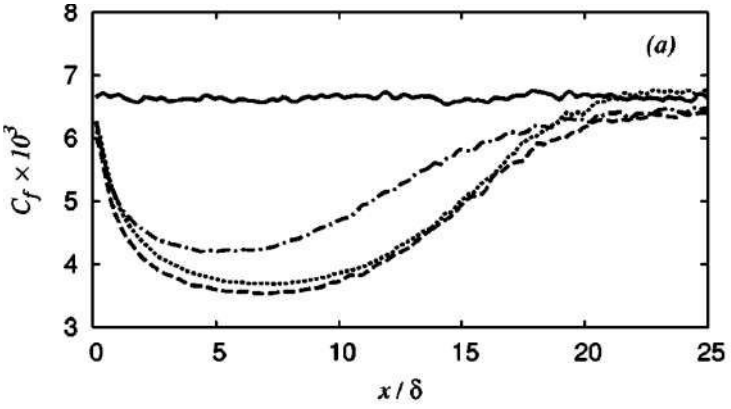

Figure 3.33: Streamwise variation of the skin friction coefficient C_f. The graph has been extracted from Keating *et al.* [45]. (solid line) - precursor simulation; (dashed line) - synthetic turbulence using standard scales; (dashed dot line) - "suboptimal" synthetic turbulence; (dotted line) - synthetic turbulence using corrected scales ("optimal").

the existing numerical methods to generate inflow data for turbulent flows simulation allowed us to choose the SEM for the present study.

The implemented method was validated for the simulation of instantaneous turbulent signals as well as for the spatially decaying HIT. Additionally, the influence of the mesh grid, the length scale value, the number of eddies and a time convergence study were conducted. It allowed, on one hand, to validate our implementation, and on the other hand, to choose the computational configuration to use for this work. It was shown that for the inlet plane inflow, the obtained statistics outside the viscous sublayer were correct for a coarse mesh of dimensions $\Delta x = \Delta z \sim 25$, $\Delta y^+_{min} = 3.1$, $\Delta y^+_{max} \sim 40$. For a more refined mesh grid, the number of eddies had to be increased in order to obtain the correct evolutions. This was explained using the definition of the length scale σ, which depends on the spanwise and streamwise mesh dimensions in the close-to-the-wall region.

Finally, the numerical simulation of a turbulent boundary layer flow with heat transfer at a momentum thickness Reynolds number $Re_\theta = 1100$ was described. It was shown via snapshots of the streamwise velocity and temperature fields that the hypothesis of the equivalence between the two can be considered reasonable. The evolutions of the turbulent statistics, mean and rms velocities and temperature profiles, with the wall coordinate were plotted. It is shown that the mesh refinement greatly improve their corresponding evolutions. The same is found for the turbulent heat fluxes, in the streamwise and the wall-normal directions. A comparaison with data extracted from the literature shows a good agreement of the obtained evolutions. The same goes for the turbulent Prandtl number, which reaches a maximum value of 1.09 close to the wall, while similar values have also been reported in other previous studies, in which Pr_t approaches a value of 1.1 at the wall.

The streamwise evolutions of the friction coefficient and the Stanton number, allowing for the characterization of the local boundary layer flow, showed significant differences in comparison with the existing empirical (Kays and Crawford [44]) and numerical or experimental evolutions. In the vicinity of the inlet plane, it has already been reported that, when using a synthetic method, these parameters have incorrect evolutions. Often, their evolution regain the correct path, but only after some distance in the streamwise direction. This matter will be tackled with in the next chapter.

The next chapter is dedicated to the numerical simulation of the interaction between a spatially evolving boundary layer flow with heat transfer and the normal velocity induced by liquid/vapor

phase change.

Chapter 4

Interaction between liquid/vapor phase change and a spatially developing turbulent boundary layer flow

Contents

In what follows, we investigate the interaction between a spatially developing turbulent boundary layer flow and a normal velocity field induced by liquid/vapor phase change. This has been conducted first qualitatively, by analysing the normal velocity field, the vorticity magnitude field and the isosurfaces of the Q criterion. Next, a study on the influence of the phase change onto the turbulent quantities is presented. Several Jakob numbers are studied and a preliminar physical analysis is proposed for the obtained profiles. Additionally, we take interest on the impact of the phase change onto the Nusselt number evolution. This is given in the continuity of the work on the laminar regime where correlations on the Nusselt number were proposed.

4.1 Introduction

In practical applications, most flows which occur are turbulent. To this extent, the previous chapter was dedicated to the spatial development of a turbulent boundary layer flow. The next step, taken in this chapter, is to investigate the interaction between liquid/vapor phase change and a spatially developing turbulent boundary layer flow. More precisely, we focus on the influence of a normal velocity field induced by liquid/vapor phase change onto the evolution of turbulent quantities: mean and rms fields, turbulent heat fluxes, friction coefficient, Stanton number. Additionally, an analysis on the Nusselt number evolutions with and without phase change, for different values of the Jakob number is proposed.

The present chapter is structured as it follows. First, we describe the computational configuration used for this study, where two simulations are used: an auxiliary and a main simulations. The main simulation is used to study the blowing effects of the phase change onto the turbulent boundary layer. The auxiliary simulation serves to generate input data for the main simulation.

We first use this numerical configuration for the case without phase change, for which the main simulation serves as a spatial extension of the computational domain in the x direction. This allows studying whether and how the length in the streamwise direction influences the development of the turbulent boundary layer flow.

Next, we address the configuration involving liquid/vapor phase change. The approach for this study has been of varying the Jakob number and analyzing its influence onto the spatial development of the turbulent boundary layer flow. First, a qualitative analysis of the obtained results is proposed. The normal velocity field, the vorticity magnitude and the isosurfaces of the Q criterion are plotted for the configurations with and without phase change. Comparisons and physical interpretations are given for the observed influences of the phase change onto these fields.

Last but not least, we propose a quantitative study on the influence of the Jakob number onto the turbulent quantities, namely onto the mean and the rms fields, the turbulent heat fluxes in the streamwise and normal directions, the friction coefficient and onto the Stanton number. Additionally, a preliminary analysis on the influence of the Jakob number onto the Nusselt number is also given, in the continuity of the work on the laminar boundary layer presented in chapter 2.

Finally, the chapter ends with conclusions and perspectives on this work.

4.2 Computational configuration

For the study of the influence of liquid/vapor phase change onto an external turbulent flow, the corresponding turbulent flow had first to be simulated. To this extent, in the previous chapter, the focus was on the implementation of a turbulent inflow generator. The next step is to consider a configuration allowing to investigate the influence of liquid/vapor phase change onto the spatial development of the turbulent boundary layer. The most straightforward approach would be to expand the computational domain. This configuration would strongly resemble to the laminar boundary layer configuration illustrated in figure 2.1 in chapter 2. However, for the turbulent flow, in comparison with the laminar boundary layer, an upstream additional length would have to be added in order to simulate the spatial development of the turbulent boundary layer flow. This approach is not conceivable given the computational constraints involved by the simulation of a 3D turbulent flow.

In order to alleviate the involved computational costs, two aspects had to be tackled with. First, the addition of the upstream length was avoided by splitting the simulation into two parts, an auxiliary and a main simulation. The configuration and the results of the auxiliary simulation,

hereinafter denoted as Code-1, were the subject of the previous chapter. The inflow is generated using the SEM and the post processing is done at x_{pp}. After a certain computation time, allowing to achieve the average convergence, the simulation advances while storing, at each time step, the velocity components and the temperature on a vertical plane located at x_{pp}. These planes are later used as inflow boundary condition for the second simulation, hereinafter denoted as Code-2 (figure 4.1). The coupling between Code-1 and Code-2 involves writing/reading operations in the MPIIO environment. Therefore, during my thesis, development of MPIIO communicators in the zy post-processing and inlet planes was realized.

The second simulation uses the same computational configuration as Code-1, except for the inflow boundary condition where we impose the planes generated using Code-1. This allows to have a continuity in the spatial development of the turbulent boundary layer flow. The simulation of the spatial development of the turbulent boundary layer flow on a flat plate is conducted until the obtained averaged statistics attain temporal convergence (about 480 s), and then the phase change is plugged in. No difference exists between Code-1 and Code-2, regarding the initialization, mesh grid or domain dimensions. For more details on these aspects refer to section 3.5.1 of the previous chapter.

The second aspect is related to the simulation of the liquid/vapor phase change. In order to avoid the computational costs induced by the simulation of the static liquid pool at saturation, the phase change is imposed as a boundary condition. Once the turbulent boundary layer is well developed, the liquid/vapor phase change is activated, as illustrated in the lower part of figure 4.1. The same Code-2 is used to this end, with the only difference concerning the boundary condition imposed at $y = 0$. The specifics on how the liquid/vapor phase change is treated are given in the upcoming section.

4.2.1 Treatment of the liquid/vapor phase change

In chapter 2 we have described our study on the influence of liquid/vapor phase change onto an external laminar boundary layer flow of vapor. The 2D computational configuration, shown in figure 2.1, contains a liquid pool at saturation overflown by a boundary layer flow overheated or subcooled. The Navier-Stokes equations, as well as the energy equation, are solved in both domains, by the use of the Ghost Fluid Thermal Solver for Boiling, described in section 1.3.5 of chapter 1.

The present 3D configuration has already a high computational cost. Avoiding the simulation of the liquid pool and the use of the Ghost Fluid Thermal Solver for Boiling is therefore mandatory. For the laminar 2D configuration, it was shown that the liquid velocity field induced by the shearing of the external vapor flow is negligible. This observation allows to consider simulating only the vapor flow and imposing the liquid/vapor phase change as a boundary condition on the velocity field.

As already explained in chapter 1, through the liquid/vapor interface, the continuity of the mass flux has to be satisfied. This induces a jump on the velocity field across the interface, written as

$$[\mathbf{V}]_\Gamma = \dot{m} \left[\frac{1}{\rho}\right]_\Gamma \mathbf{n}, \tag{4.1}$$

where, we recall, that $\dot{m}$ is the mass flow rate, proportional to the interface thermal flux,

$$\dot{m} = \frac{1}{L_v} \left[k \frac{\partial T}{\partial y}\right]_\Gamma. \tag{4.2}$$

We take the assumption of a plane interface, with $\mathbf{n} = \mathbf{e}_y$, between the vapor and the static liquid

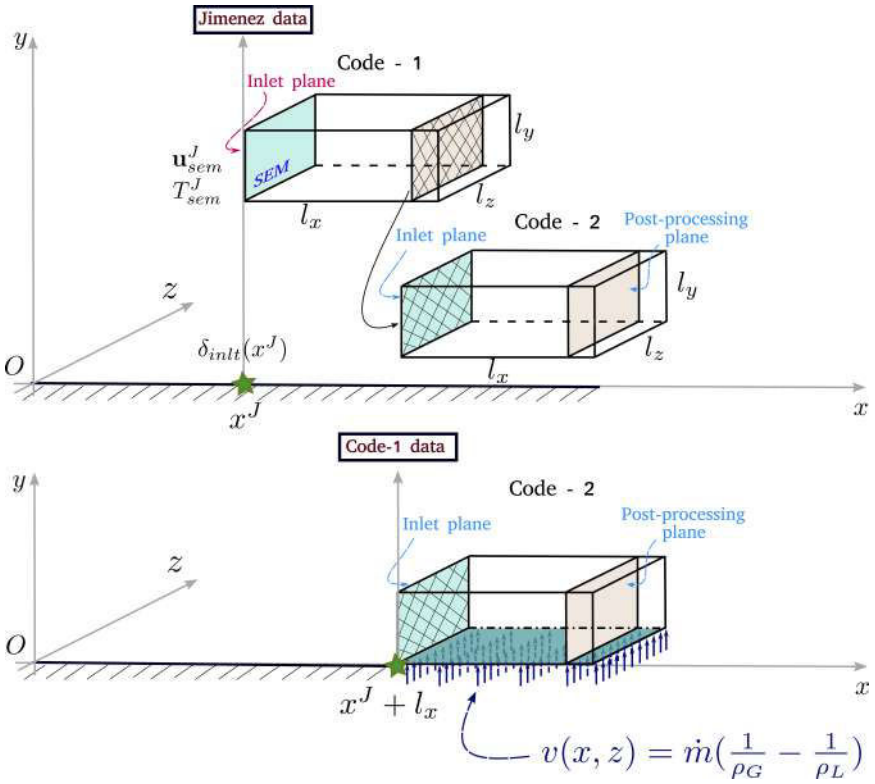

Figure 4.1: Schematic drawing of the computational domains of the auxiliary simulation (Code-1) and the main simulation (Code-2).

pool at saturation. The velocity field in the liquid is therefore zero $\mathbf{u}_l = 0$ and the liquid is at saturation temperature $T_l(x, y, z) = T_{sat}$. Consequently, equations 4.1 and 4.2 write

$$[v]_\Gamma = \dot{m}\left(\frac{1}{\rho_v} - \frac{1}{\rho_l}\right), \quad \text{with} \quad \dot{m} = \frac{1}{L_v}\left(k_v \frac{\partial T}{\partial y}\Big|_{y=0}\right). \tag{4.3}$$

The liquid/vapor phase change is therefore imposed as an inflow boundary condition at $y = 0$, with $u = 0$ and $v = \dot{m}\,(1/\rho_v - 1/\rho_l)$. The mass flow rate $\dot{m}$ is obtained at each time step, using the vapor temperature gradient at $y = 0$. We recall that, for methodology reasons, we simulate the reduced temperature field $\tilde{T} = (T - T_\infty)/(T_0 - T_\infty)$. This implies that the mass flow rate, computed using the reduced temperature, writes $\dot{m} = \dfrac{(T_0 - T_\infty)}{L_v}\left(k_v \dfrac{\partial \tilde{T}}{\partial y}\Big|_{y=0}\right)$.

4.2.2 Validation of the proposed treatment of liquid/vapor phase change on the 2D laminar configuration

Before presenting the results obtained for the turbulent boundary layer flow, we first validate the proposed treatment of liquid/vapor phase change on the 2D laminar configuration, whose results are described in chapter 2.

We consider the same 2D computational domain described in figure 2.1, chapter 2, with the difference that the liquid domain is not simulated. The liquid/vapor phase change is imposed through the boundary condition at $y = 0$, as described in the previous section. Therefore, the dimensions of the computational domain are (l_x, l_y) with $l_x = 0.007$ and $l_y = 0.014$. The used mesh grid is 512×1024. For the sake of simplicity, we consider here only the case of vaporization,

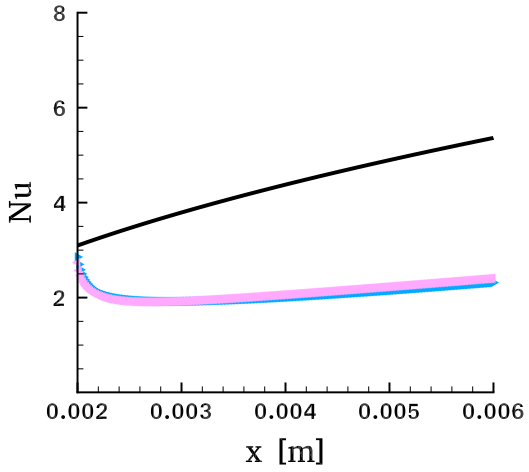

Figure 4.2: Evolution of the Nusselt number for the laminar flow, for the dimensionless numbers: $Re_{x_L} = 85.726$, $Pr = 1.022$, $\frac{\rho_l}{\rho_v} = 17.746$ and $Ja = 3.69$. The influence of the liquid/vapor phase change treatment; (black line) - Blasius theory; (▶) - simulation of both phases; (◀) - liquid/vapor phase change imposed as a boundary condition at $y = 0$.

described by the dimensionless numbers $Pr = 1.022$, $Re_{x_L} = 85.726$, $\frac{\rho_l}{\rho_v} = 17.746$, and $Ja_{vap} = 3.69$.

In figure 4.2 the evolution of the Nusselt number is plotted, for the two configurations, with the simulation of the liquid/vapor phase change and when the liquid/vapor phase change is imposed as a boundary condition at $y = 0$. Very little difference can be observed. We show therefore that the two approaches can be considered equivalent.

4.3 Influence of the spatial extension in the streamwise direction onto the development of the turbulent boundary layer flow

In this section, the scope is to see whether and how an extension in the streamwise direction improves the turbulent quantities obtained in our simulation. The simulations described in the previous chapter showed that the inlet synthetic turbulence will first encounter a decline and then, after a certain adaptation distance, it will start to redevelop into real turbulence. This has been illustrated, inter alia, by plotting the isosurfaces 0.25 of the Q criterion (figure 3.27). When using Code-2, the turbulent fluctuations imposed at the inlet plane are closer to real turbulence and no adaptation distance is needed. This is shown in figure 4.3 where the isosurfaces of the Q criterion of value $Q = 0.25$ are plotted. In comparison with figure 3.27, it can be observed here a larger population of vortices and a continuity in the spatial development of the boundary layer.

Figure 4.4 shows a comparison between the rms velocities profiles obtained at the post processing plane in Code-1 and the ones obtained at the post processing plane in Code-2. For the coarse mesh grid $256 \times 64 \times 64$, the influence of the extension in the streamwise direction, via the use of Code-2, is significant, while, for the more refined grid, slight differences can be observed only in the outer zone. When using the coarse mesh grid, the generated synthetic turbulence contains mostly large scales in the logarithmic layer. The development into more realistic turbulence with a correct variation in the normal-wall direction of the length scales demands therefore a larger distance in

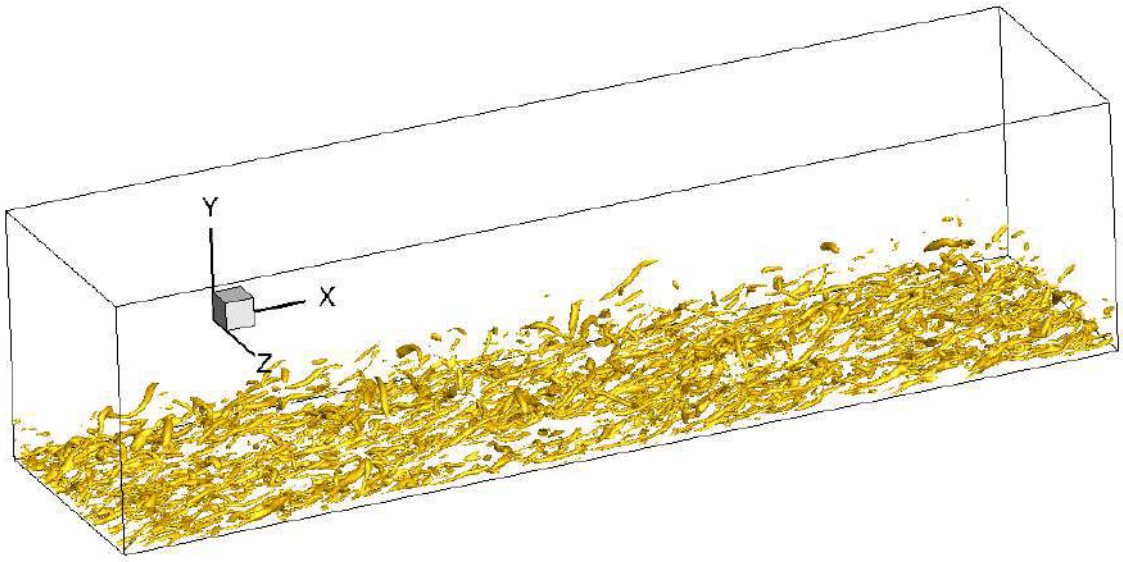

Figure 4.3: Isosurfaces of the Q criterion of value $Q = 0.25$ for a spatially developing boundary layer over a flat plate, obtained using Code-2. The caption is taken after $T = 1528\theta_{inlt}/U_\infty = 240$ s.

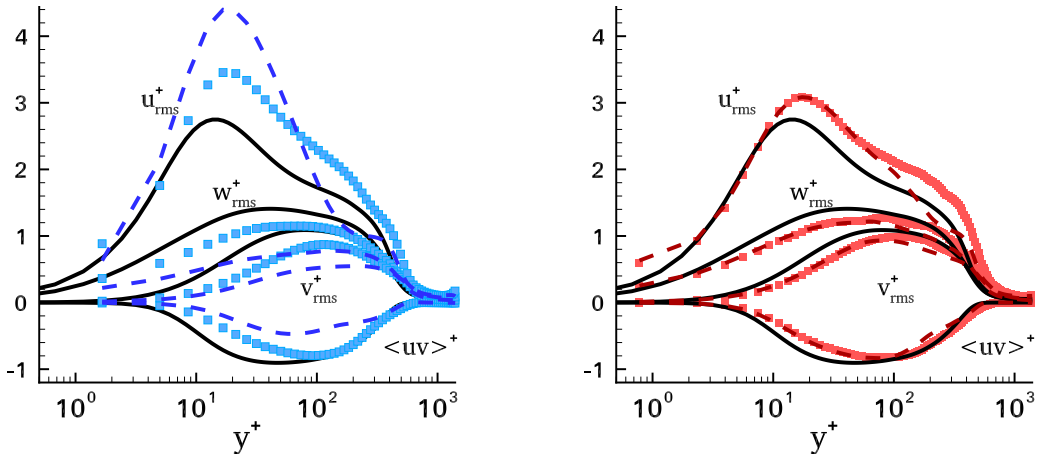

(a) 256 × 64 × 64

(b) 512 × 128 × 128

Figure 4.4: Evolution of the rms velocity with the wall coordinate, using Code-1 and Code-2. The influence of the extension in the streamwise direction. Each curve is plotted after the corresponding T_{cv}. (black line) - Jimenez data [40]; (dashed line) - the statistics obtained in Code-1; (symbols) - the statistics obtained in Code-2.

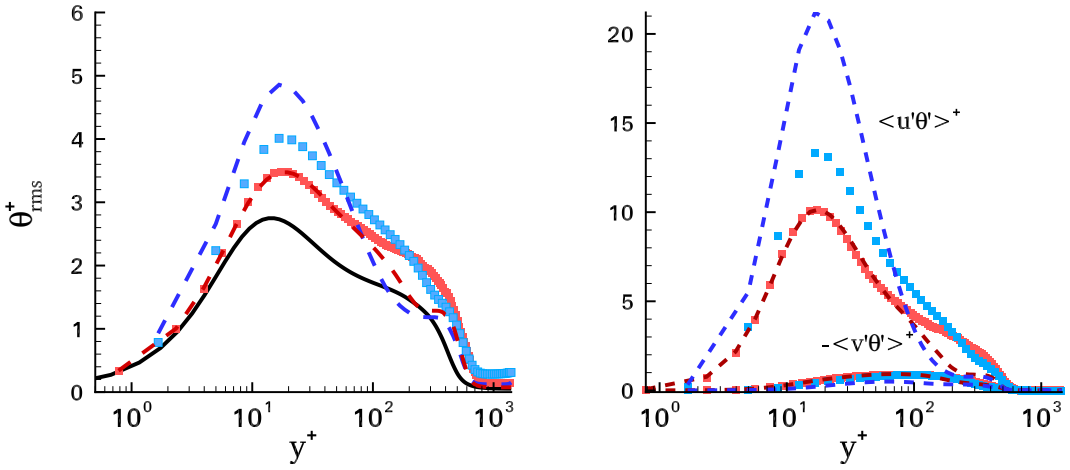

Figure 4.5: Evolution of the rms temperature and the turbulent heat fluxes with the wall coordinate, using Code-1 and Code-2. The influence of the extension in the streamwise direction. Each curve is plotted after the corresponding T_{cv}. (black line) - Jimenez data [40]; (dashed line) - the statistics obtained in Code-1; (symbols) - the statistics obtained in Code-2; (blue color) - $256 \times 64 \times 64$; (red color) - $512 \times 128 \times 128$

the streamwise direction. Meanwhile, for the more refined grid, the observed differences can be explained by the increase in the Reynolds number. Indeed, as already discussed, it has been largely shown that, even in wall units, there is an influence of the Reynolds number onto the evolution of the turbulent quantities (see for example Degraaff *et al.* [20]).

Note that the same tendencies are observed for the rms temperature and the turbulent heat fluxes profiles, in figure 4.5.

The influence of the extension in the streamwise direction, via the use of Code-2, on the friction coefficient and Stanton number evolutions is shown in figure 4.6. The curves obtained with Code-2 overlap with the profiles obtained with Code-1, showing the continuity in the turbulence development. This supports the hypothesis of equivalence between an extension of the length in the streamwise direction and the use of a second simulation. Additionally, the friction coefficient stops increasing and starts decreasing at almost the same slope as the reference profile from Li *et al.* [58]. The same behaviour is encountered for the Stanton number. A more refined grid would allow, inter alia, to have a better resolution of the viscous sublayer and therefore to obtain more realistic profiles for the friction coefficient and the Stanton number.

4.4 Results

In this section we will present our preliminary results on the influence of the liquid/vapor phase change onto the spatial evolution of the turbulent boundary layer flow. We will first show some tendencies when increasing the Jakob number Ja and extract a physical understanding of the effects of a blowing velocity field onto the spatial development of the turbulent boundary layer flow. Next, a more quantitive analysis is proposed by focusing on the different turbulent quantities characterizing the turbulent boundary layer flow.

As previously, the post processing parameters studied here are the mean and rms velocity and temperature fields, the turbulent heat fluxes in the streamwise and normal directions, the friction coefficient and the Stanton number. Additionally, we take interest in the evolution of the

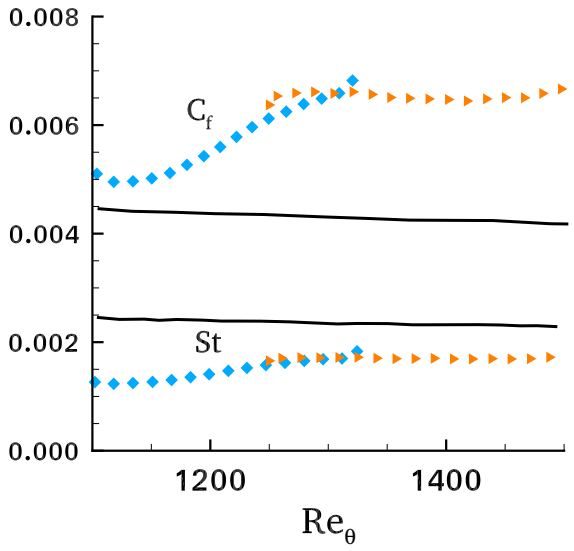

Figure 4.6: Streamwise variation of the skin friction coefficient C_f and the Stanton number St with Re_θ, using Code-1 and Code-2. The influence of the extension in the streamwise direction. (solid lines) - Li *et al.* [58]; (♦) - Code-1, (▶) - Code-2.

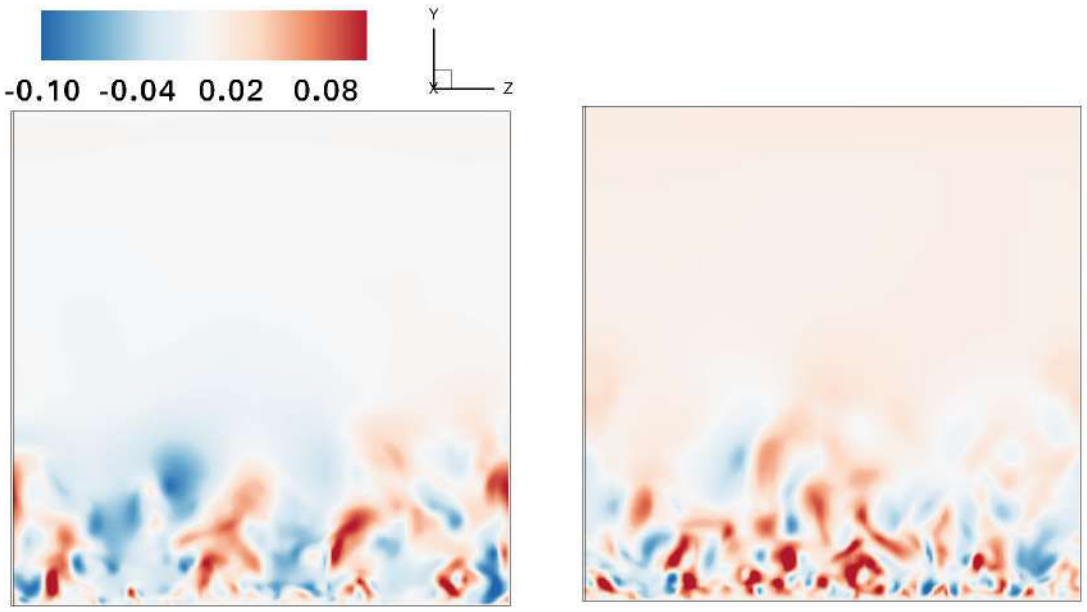

(a) Without phase change ($Ja = 0$). (b) With phase change ($Ja = 14$).

Figure 4.7: Snapshots of the normal to the wall velocity v $[m/s]$ in a Oyz plane situated at $x = l_x/2$. Influence of the liquid/vapor phase change induced velocity on the normal to the wall velocity.

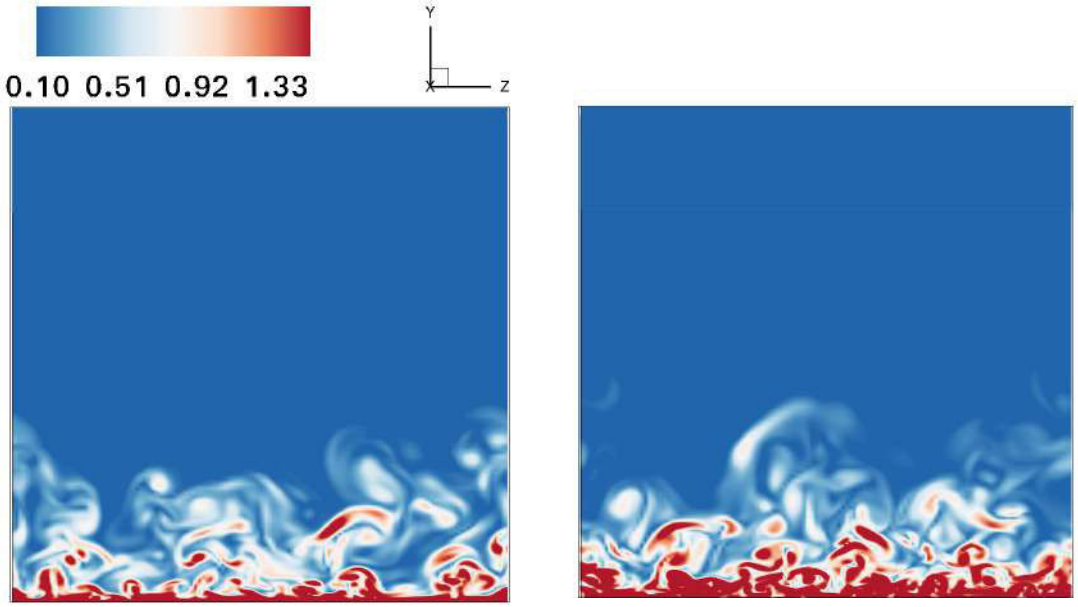

(a) Without phase change ($Ja = 0$).

(b) With phase change ($Ja = 14$).

Figure 4.8: Snapshots of the vorticity magnitude field in a Oyz plane situated at $x = l_x/2$. Influence of the liquid/vapor phase change induced velocity on the vorticity magnitude.

Nusselt number in the streamwise direction. Some comparisons will be done in regard to the results obtained for the 2D laminar configuration studied in chapter 2.

Note that the time average is done after eliminating 120 s of simulation. The time convergence study is shown in Appendix C.1. The mesh grids used are $256 \times 64 \times 64$ and $512 \times 128 \times 128$. Only the results obtained with the more refined mesh resolution are shown in what follows. The influence of the mesh grid is shown in Appendix C.2.

At present, only four Jakob numbers have been investigated, $Ja = [0.088;\ 0.88;\ 8.8;\ 14]$, while keeping constant the other three dimensionless numbers, the Prandtl number $Pr = 1.022$, the Reynolds number $Re_\theta = 1100$ and the density ratio $\rho_l/\rho_v = 17.746$. We recall the expression of the Jakob number, $Ja = \frac{C_p \Delta T}{L_v}$, where $\Delta T = T_\infty - T_0 = 100^o$.

4.4.1 Qualitative study

Before discussing the influence of the Jakob number onto the evolution of the turbulent quantities, we first show the blowing effects onto the normal velocity component, the vorticity magnitude and the Q criterion.

In figure 4.7 is plotted the normal velocity component v in a Oyz plane located at $x = l_x/2$ for two configurations: without phase change ($Ja = 0$) and with phase change ($Ja = 14$). Differences can be observed between the two illustrated fields. The length scales of the spots are highly diminished when the boundary layer is blown by the velocity induced by liquid/vapor phase change. This is prominent in the region close to the wall, where numerous small spots can be observed. Additionally, when comparing the two pictures, the free stream normal velocity value is higher when liquid/vapor phase change occurs. On the other hand, no conclusion can be made on whether the phase change increases the boundary layer thickness.

The vorticity magnitude field is shown in figure 4.8 for the same two configurations. The spots with higher vorticity magnitude value are more abundant when liquid/vapor phase change is

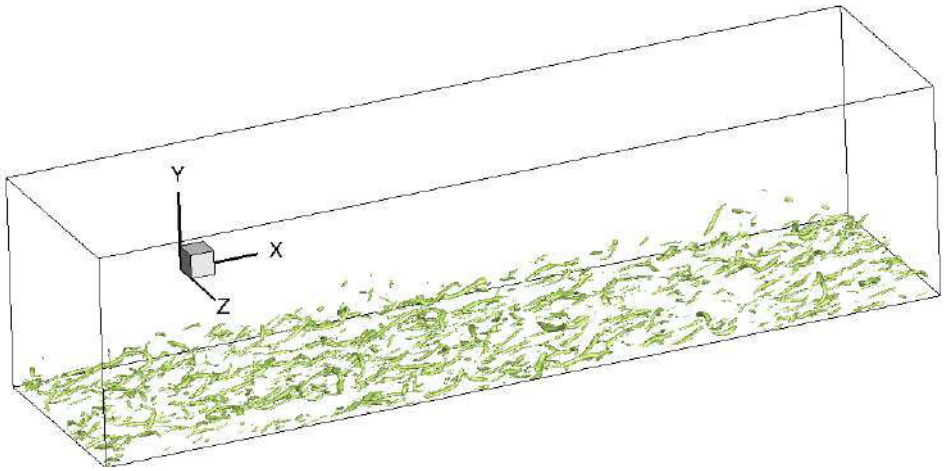

(a) Without phase change ($Ja = 0$).

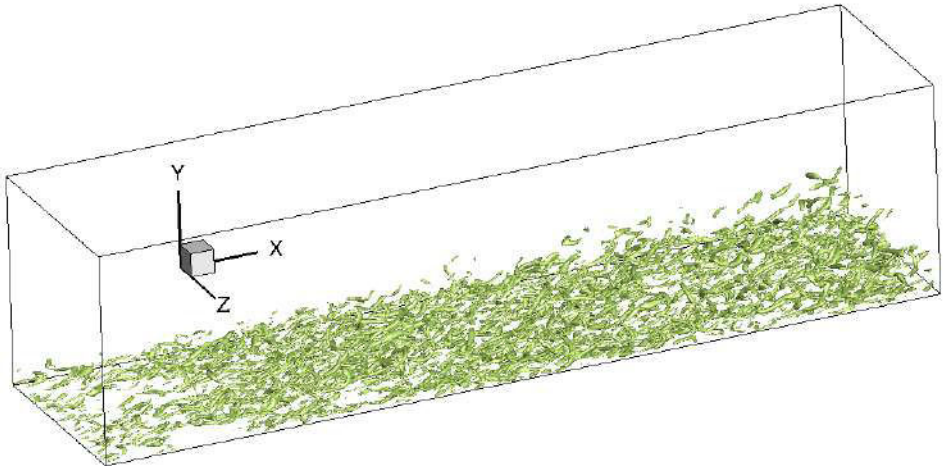

(b) With phase change ($Ja = 14$).

Figure 4.9: Isosurfaces of the Q criterion of value $Q = 0.5$. Influence of the liquid/vapor phase change induced velocity on the spatial development of the turbulent boundary layer flow.

involved. This implies that the vertical velocity aids the energy transfer from large eddies to small eddies. Furthermore, it would seem that the quantity of small eddies is highly increased.

A verification of the latter statements is done by using the Q criterion. In figure 4.9 the isosurfaces of value $Q = 0.5$ are plotted. Note that we have chosen here a higher value of Q than in the previous cases. Figure 4.9b shows an important increase in the population of vortices when the boundary layer is blown by the liquid/vapor phase change. This increase begins at a certain length from the inlet plane and this behaviour would certainly be noticeable when showing the streamwise evolution of the friction coefficient and the Stanton number.

Qualitatively, we have observed until now, that the vertical velocity imposed at the $y = 0$ boundary modifies the structure of the turbulent boundary layer. It would seem that a fragmentation of large eddies into small eddies is enhanced. The liquid/vapor phase change brings through the imposed normal velocity energy that is then used for the creation of eddies of high vorticity.

Further on we will focus on the influence of the Jakob number onto the evolution of the turbulent quantities and try to explain the tendencies observed in this section. Even if we were not strictly able to demonstrate the spatial convergence of our simulations, we will nevertheless consider that

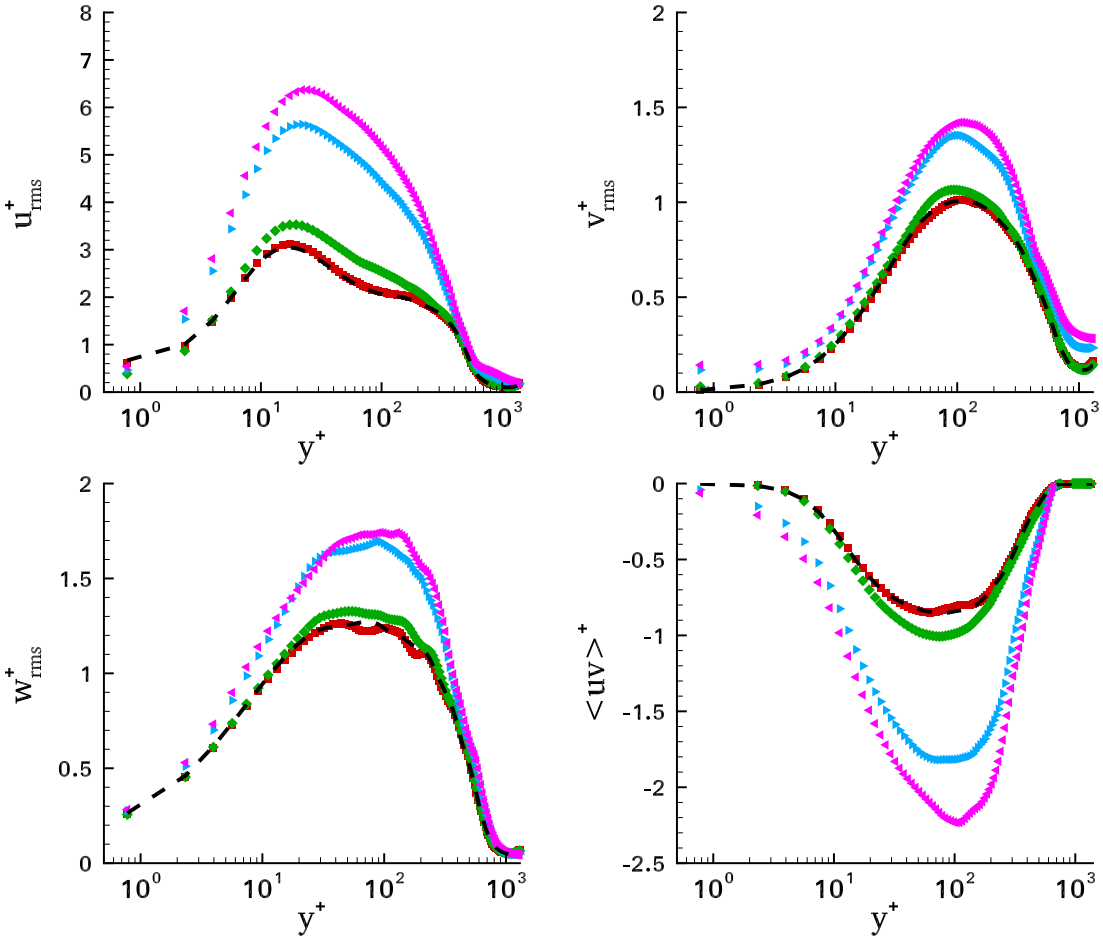

Figure 4.10: Influence of the Jakob number onto the evolution of the rms velocity fields. The dimensionless numbers are $Re_\theta = 1100$, $Pr = 1.022$, $\rho_l/\rho_v = 17.746$ and different values of the Jakob number: (dashed line) - $Ja = 0$; (■) - $Ja = 0.088$; (◆) - $Ja = 0.88$; (▶) - $Ja = 8.8$; (◀) - $Ja = 14$.

we are not far from its achievement, as the graphs from Appendix C.2 indicate it.

4.4.2 Quantitative study

Figure 4.10 shows the evolution of the rms velocities with the wall coordinate for different values of the Jakob number. Its influence onto the rms temperature and the turbulent heat fluxes is plotted in figure 4.11. The mean fields are also concerned and their evolutions for different rates of phase change are illustrated in figure 4.12.

Increasing the Jakob number leads to an increase of the rms fields and of the turbulent heat fluxes. The turbulent kinetic energy k' is therefore increased. This is coherent with the previous qualitative observations on the increase of the small eddies population. Indeed, small eddies possess higher turbulent kinetic energy than large eddies.

The region on which the phase change impacts the profiles of these quantities expands with the Jakob number. The buffer and the logarithmic zones are the most impacted. For the quantities containing the normal velocity component, v^+_{rms}, $< uv >^+$ and $< v\theta >^+$, the influence can be observed for all y^+.

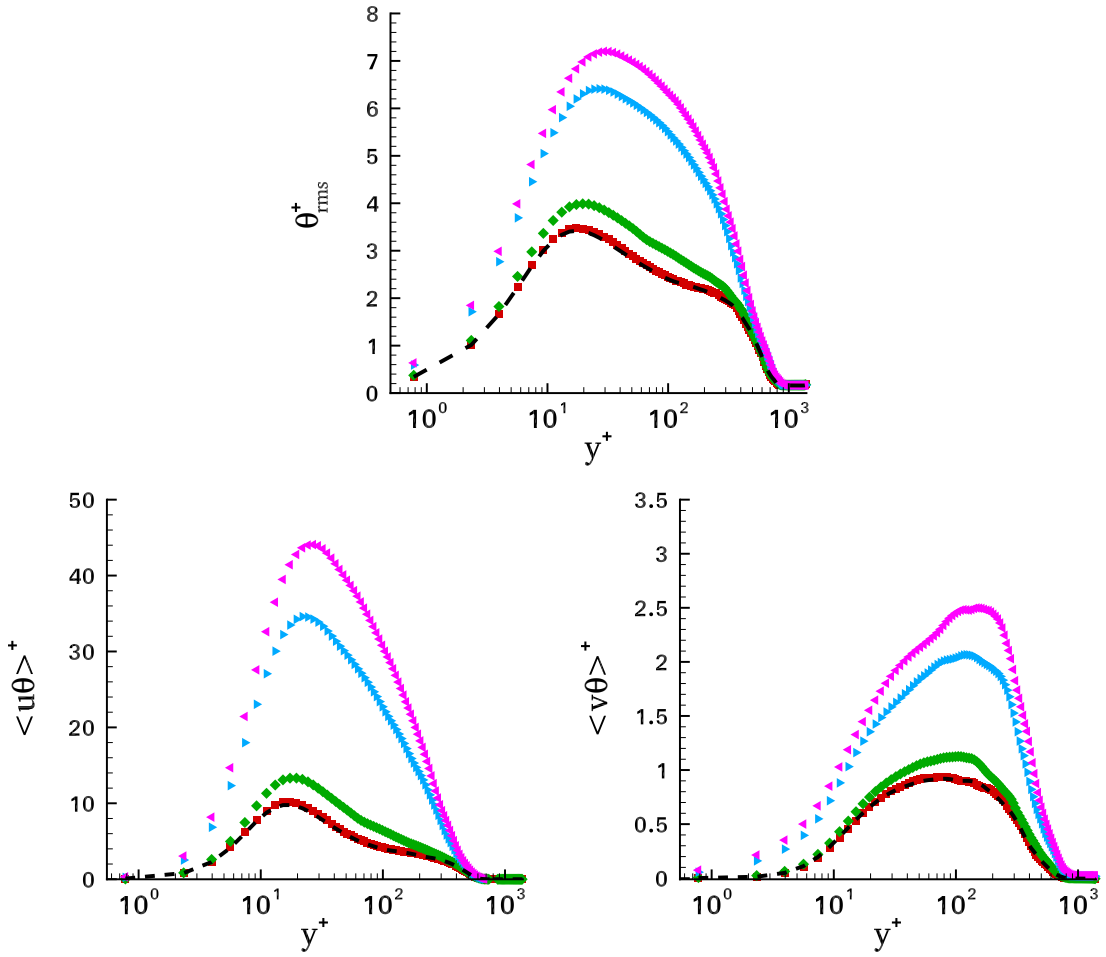

Figure 4.11: Influence of the Jakob number onto the evolution of the rms temperature and the heat fluxes. The dimensionless numbers are $Re_\theta = 1100$, $Pr = 1.022$, $\rho_l/\rho_v = 17.746$ and different values of the Jakob number: (dashed line) - $Ja = 0$; (■) - $Ja = 0.088$; (♦) - $Ja = 0.88$; (▶) - $Ja = 8.8$; (◀) - $Ja = 14$.

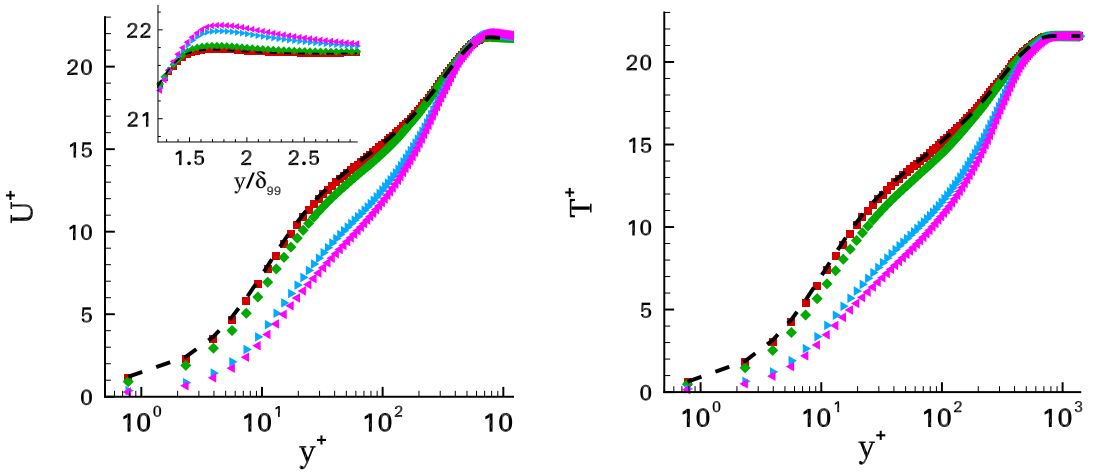

Figure 4.12: Influence of the Jakob number onto the evolution of the mean velocity and mean temperature. The dimensionless numbers are $Re_\theta = 1100$, $Pr = 1.022$, $\rho_l/\rho_v = 17.746$ and different values of the Jakob number: (dashed line) - $Ja = 0$; (■) - $Ja = 0.088$; (◆) - $Ja = 0.88$; (▶) - $Ja = 8.8$; (◀) - $Ja = 14$.

The turbulent heat flux in the streamwise direction, $< u\theta >^+$, is enhanced by the liquid/vapor phase change, its evolution with the wall coordinate beeing highly influenced by the liquid/vapor phase change(figure 4.11). The peak of the heat flux in the normal direction $< v\theta >^+$ is shifted to the right when increasing the Jakob number. This can be explained by the fact that the maximum of the turbulent heat flux in the normal direction is displaced further from the wall when increasing the vertical velocity induced by the phase change.

Figure 4.12 illustrates the mean profiles of velocity and temperature for different values of the Jakob number. The phase change induced velocity decreases the mean fields gradient close to the wall while increasing it in the logarithmic zone. Outside the boundary layer, $y/d_{99} > 1$, the velocity profile presents the same kind of growth as for the laminar regime velocity profile, plotted in figure 2.19. As until now, the nondimensionalization of the turbulent quantities is achieved using the reference friction velocity $u_\tau = 0.0462$, from Jimenez *et al.* [40]. As for flows at different Reynolds number, it would be interesting to see if the curves overlap in the inner region, when using the corresponding computed friction velocity. However, the employed mesh grid allows to have only 3 points in the viscous sublayer, the friction velocity computed at $y = 0$ is therefore not yet converged. Its use will undoubtedly introduce errors.

The analysis of the influence of the phase chnage onto the evolutions of the mean velocity and the crossed rms velocity $< u'v' >$ can also be done by plotting the total shear stress τ and its two components, the Reynolds shear stress $-\rho < u'v' >$ and the viscous shear stress $\mu\dfrac{\partial U}{\partial y}$. This is done for the case without phase change and for a Jakob number $Ja = 0.88$ in figure 4.13. It can be seen that the viscous shear stress is influenced by the phase change only in the viscous sublayer, for $y^+ < 5$. The Reynolds shear stress follows the same evolution in the close to the wall zone ($y^+ < 10$), regarless of the Jakob number. In the logarithmic zone, its profile is increased when phase change occurs.

In figure 4.14 we have plotted the evolution of the friction coefficient and the Stanton number with the x-axis. As expected, an increase in the Jakob number generates a decrease of these parameters. Indeed, the blowing velocity imposed at the $y = 0$ boundary will decrease the mean velocity and temperature variation in the normal wall direction.

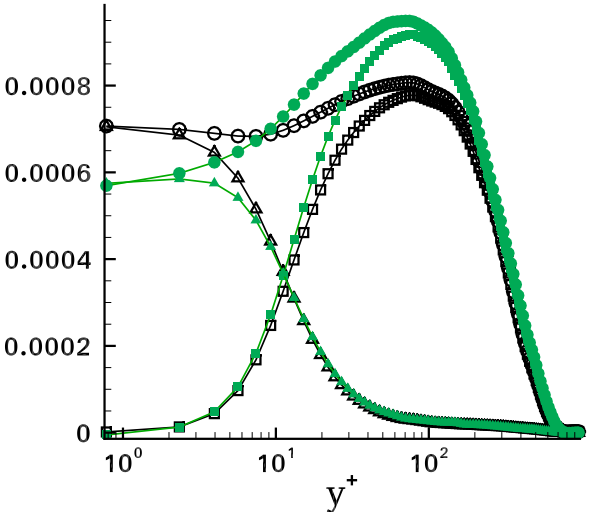

Figure 4.13: Shear stress distribution with the wall coordinate. The dimensionless numbers are $Re_\theta = 1100$, $Pr = 1.022$, $\rho_l/\rho_v = 17.746$ and two values of the Jakob number: (black colour) - $Ja = 0$; (green colour) - $Ja = 0.88$; (circle) - total shear stress; (square) - Reynolds shear stress; (triangle) - viscous shear stress.

For the laminar configuration, very little influence of the phase change onto the evolution of the friction coefficient has been observed. Given that for a turbulent regime, close to the wall there is a viscous sublayer where the flow is considered laminar, we could expect to obtain the same tendency on the evolution of the friction coefficient. However, the behaviour of the mean velocity when phase change occurs is not the same as for the laminar. We recall that for the laminar boundary layer configuration, the evolution of the tangential velocity profilewas almost identical to the Blasius boundary layer velocity profile, despite the vapor blowing in the normal direction due to phase change.

An additional observation in regard to the friction coeffient and the Stanton number evolutions can be made. Close to the inlet plane, the profiles present a very steep slope, whose length increases with the Jakob number. We can link this behaviour with what we have observed when plotting the isosurfaces of the Q criterion. Indeed, an increase of the small eddies population could be observed only at a certain distance from the inlet plane. This could perhaps explain the presence of the steep slope on the obtained profiles. After this region, both the friction coefficient and the Stanton number follow a power low evolution, close to the ones proposed by Kays ans Crawford [44], $Cf \sim Re_\theta^{-1/4}$ and $St \sim Pr^{-2/5} Re_\theta^{-1/4}$. Very little influence of the Jakob number can be observed on the slope of these power law curves. Further studies could be conducted in order to establish an evolution law with the Jakob number for these parameters.

4.4.3 Nusselt number

We now take interest into the Nusselt number evolution when phase change occurs. We recall its expression that writes $Nu = hx/k$, where the heat transfer coefficient is expressed using the reduced temperature field,

$$h = \frac{k}{\Delta T}\frac{\partial T}{\partial y} = k\frac{\partial \tilde{T}}{\partial y}. \tag{4.4}$$

For the laminar regime, the Blasius theory allows to calculate the analytical solutions for

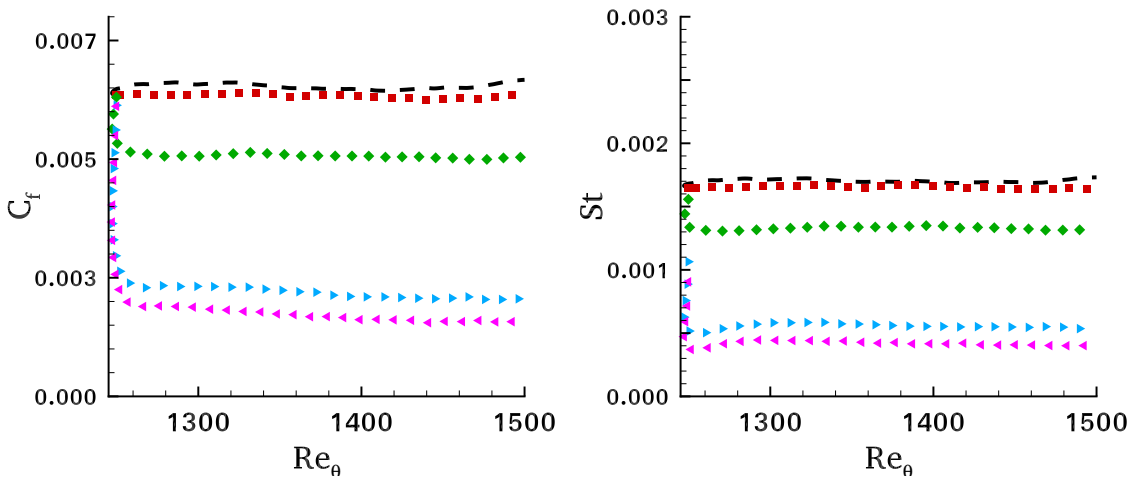

Figure 4.14: Influence of the Jakob number onto the evolution of the friction coefficient and Stanton number. The dimensionless numbers are $Re_\theta = 1100$, $Pr = 1.022$, $\rho_l/\rho_v = 17.746$ and different values of the Jakob number: (dashed line) - $Ja = 0$; (■) - $Ja = 0.088$; (◆) - $Ja = 0.88$; (▶) - $Ja = 8.8$; (◀) - $Ja = 14$.

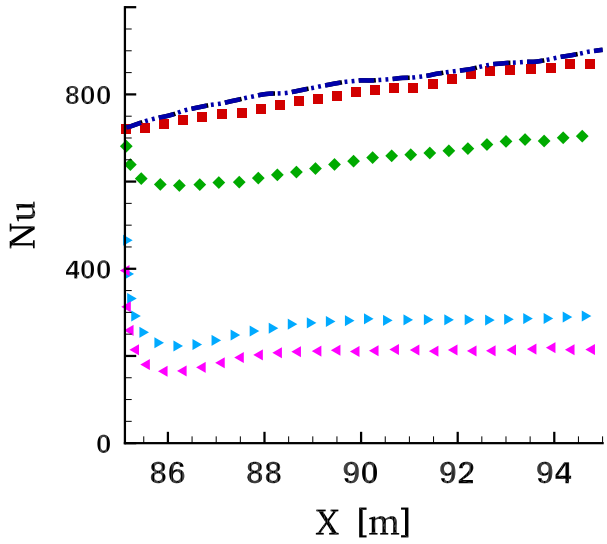

Figure 4.15: Spatial evolution of the Nusselt number for the dimensionless numbers: $Re_\theta = 1100$, $Pr = 1.022$, $\rho_l/\rho_v = 17.746$ and different values of the Jakob number: (dash dot dot line) - $Ja = 0$; (■) - $Ja = 0.088$; (◆) - $Ja = 0.88$; (▶) - $Ja = 8.8$; (◀) - $Ja = 14$. Note that $X = x_L + x$, with $x \in [0, l_x]$ and $\delta_{x_L} = 2.7568\ m$.

the boundary layer problem. Here, in the absence of such a theory, we take as reference the Nusselt number profile computed when no phase change occurs. Note that only a mean value of the Nusselt number, computed over a length L, can be found in the literature, where $Nu_L = 0.036(Re_L)^{0.8}(Pr)^{0.6}$.

In the continuity of the work conducted for the laminar boundary layer, one would want to plot the Nusselt number evolution from the position x_L, where $\delta_{99}(x = x_L) = \delta_{inlt}$. To this extent, this specific position has to be calculated. For this we use Prandtl's 1/7th power law (see Bejan [5])

$$\frac{\delta_{99}}{x} = 0.37 \left(\frac{U_\infty x}{\nu} \right)^{-1/5} . \tag{4.5}$$

where $\delta_{99} = 2.7568\ m$ is given by Jimenez and we add to the obtained distance the length of the Code-1 domain, $l_x = 14.4\delta_{99}$, allowing to obtain $x_L = 82.02\ m$.

The evolution of the Nusselt number is plotted in figure 4.15, for different values of the Jakob number. We see that increasing the phase change has the same impact on the Nusselt number for the turbulent boundary layer as for the laminar regime. The Nusselt number decreases when increasing the Jakob number. In the same way, a transition zone is observed near the inlet plane, with the presence of a minimum followed by a positive slope of the Nusselt curve evolution. This result is very promising in our intent to find a similarity between the turbulent and the laminar regime. However, further study is needed in order to conduct a parametric study by simulating several intermediate Jakob numbers. It is possible that the values 8 and 14 are too high. We recall that for the laminar regime, the highest value was 8 and it was at the limit of the validity range of the proposed correlation. The change in the slope observed on the Nusselt number profiles in figure 4.15, for the high Jakob numbers, could therefore be linked to a too important phase change rate.

4.5 Conclusions and perspectives

In this chapter we have presented our results obtained for the study on the interaction between a turbulent boundary layer flow of vapor and a normal velocity field induced by liquid/vapor phase change.

The illustrations of the normal velocity and of the vorticity magnitude fields in a vertical plane Oyz showed an increase of vortices in the inner zone of the boundary layer, possesing a high vorticity. When plotting the isosurfaces of $Q = 0.5$, an increase in the population of small eddies was observed. These tendencies have been explained by considering that the energy cascade from large to small eddies is higly enhanced by the blowing velocity induced by liquid/vapor phase change.

A quantitative study has been conducted in order to determine the influence of liquid/vapor phase change onto the evolution of the turbulent quantities. The rms fields showed a considerable increase with the Jakob number. This is coherent with the observation on the increase of small eddies number, considering that the energy goes from large to small turbulent scales. The turbulent heat fluxes are also impacted by the phase change. The turbulent heat flux in the streamwise direction is highly increased when increasing the Jakob number. The peak of the heat flux in the normal direction is shifted towards higher values of the wall coordinate y^+ when increasing the Jakob number. This can be explain by the blowing effect of the liquid/vapor phase change.

The mean profiles of the temperature and the velocity are also modified when phase change occurs. The velocity gradient is decreased in the viscous sublayer and increased in the logarithmic zone when increasing the Jakob number. It would be interesting, when obtaining the spatial

convergence for our simulations, to use the computed friction velocity for the nondimensionalization of the mean profiles in order to see whether the profiles overlap in the inner region. The evolutions of the shear stressed show some interesting trends. The viscous shear stress is influenced by the phase change only in the viscous sublayer, for $y^+ < 5$. The Reynolds shear stress follows the same evolution in the close to the wall zone ($y^+ < 10$), regarless of the Jakob number while in the logarithmic zone, its profile is increased when phase change occurs.

The friction coefficient and the Stanton number show little influence of the Jakob number onto the slope of their profiles. Nevertheless, the corresponding curves are shifted towards smaller values when increasing the phase change.

The evolution of the Nusselt number shows similar tendencies that the one obtained for the laminar regime: first a region where the Nusselt number decreases towards a minimum followed by a curve of positive slope.

The present work is in progress and opens to many perspectives. Simulations for intermediate values for the Jakob number are ongoing. This will allow to get a better understanding from the observed trends. For example, for all the turbulent quantities, a certain saturation effect could be predicted, especially for v_{rms}, w_{rms}, C_f and St, where a constriction between the curves of $Ja = 8$ and $Ja = 14$ can be observed. Additionally, studying several values of the Jakob number would allow to determine a behaviour law and compare it with the correlation obtained for the laminar regime.

It would be valuable to investigate the terms from the turbulent kinetic energy balance. A study on the influence of phase change onto the terms of production, diffusion and dissipation is planned for the near future. This will allow to go further in the comprehension of the obtained tendencies, comprehend what turbulent processus is most influenced by the liquid/vapor phase change. Additionally, investigations on the energy spectra could allow to determine to what scales the energy from the phase change is distributed.

Finally, simulations with a more refined mesh grid, $1024 \times 256 \times 256$, would surely allow to obtain better profiles for the friction coefficient and the Stanton number. This would enable a parametric study for different Jakob numbers with the objective to determine behaviour laws for the heat flux and the friction coefficient.

Chapter 5

Interaction between liquid/vapor phase change and natural convection induced flow

Contents

In the previous chapter, the focus was on the microgravity regime, in which the liquid propellant is pressurized by a superheated vapor. In this chapter, the objective is to characterize the configuration where the cryogenic tank is subjected to gravitational accelerations. In this framework, natural convection motions develop in the liquid while the walls of the tank are heated through solar radiation or residual thermal diffusion. This leads to an interaction between the convective mouvements and the phase change taking place at the liquid/vapor interface. For this study, a 2D computational configuration has been considered, where the density variations in the liquid phase are treated using the low-Mach approximation while the vapor phase is incompressible. The influence of the Grashof number, characterizing the natural convection, onto the evolution of the interface thermal flux is investigated.

5.1 Introduction

In this chapter we present the work conducted on the natural convection motion driven by the thermal stratification in a cryogenic tank.

The industrial context of this study is related to a cryogenic tank of a satellite, where the subcooled liquid phase is pressurized by a superheated gas. During the launching phase or the orbit insertion, convective mouvements develop in the ergol. The origine of these motions is twofold. First, the subcooled liquid is heated in the vicinity of the tank wall. This can be due to the thermal diffusion of the engines, or as a result of the solar radiation, depending on whether the launching phase or the orbit insertion is considered. Second, the cryogenic tank is subjected to a hypergravity acceleration, during the launching phase, or to a residual gravity acceleration, during the orbit insertion, which leads to a thermal stratification in the ergol. The coupling of these two phenomena produces the convective motions which will interact with the liquid/vapor phase change.

The physical and the thermodynamical properties of the cryogenic fluids, the tank wall heat flux and the tank dimensions make that the flow regime in the tank is turbulent ($Gr \sim 10^{10}$). The direct numerical simulation of such a configuration is out of reach, in terms of computation cost. Indeed, the simulation of turbulence has proved to be very complex and costly. Additionally, the characteristic time of natural convection flow is very long while the tank dimensions are of order of meters which would demand a very large number of points for the mesh resolution.

Our approach was to consider a 2D computational configuration, where natural convection mouvements interact with liquid/vapor phase change, while being in a laminar regime ($Gr \sim 10^6$). Even if the configuration studied in the present work is fairly different from the industrial configuration, it allows to have a better understanding of the involved physical phenomena. This first step can also open to many perspectives and generate ideas on how to treat more complex configurations.

The objective of this study is therefore to simulate the interaction between the natural convection motions and the liquid/vapor phase change. To this extent, a variable density solver had to be implemented into the code DIVA.

In what follows we will give a short review of the literature on the numerical simulation of natural convection. The chosen numerical approach for the implementation of a variable density solver is then described. The validation of the implemented solver is done on a natural convection configuration in a closed domain.

The second part of this chapter is dedicated to the core of this study, the numerical simulation in a 2D configuration of a two phase flow, where the vapor is incompressible while the density variations in the liquid are accounted for using the low Mach number approximation. The vapor is initially at saturation temperature and the liquid is subcooled. Wall conduction is considered for the boundary conditions on the vertical walls. A natural convection flow is induced in the liquid and its interaction with the liquid/vapor phase is investigated. Three values for the Grashof number are studied and a discussion on its influence on the thermal flux is given. The chapter ends with the conclusions and the perspectives. Note that the present study is in progress and that the obtained results are preliminary.

5.2 Short overview on the numerical simulation of natural convection

Batchelor [4] was one of the firsts to study two-dimensional convective motion generated by buoyancy forces on the fluid. Its configuration was represented by a long rectangle, of which the two long sides are held at different temperatures. Since then, many authors have investigated free convection in many different geometries.

For the numerical simulation of variable pressure for confined flows, where the variations of the pressure is non negligible, a fully compressible treatment of all fluid phases has often been considered, as for example in the work of Saurel and Abgrall [90]. Two major drawbacks exist when applying this approach to a natural convection configuration, where the velocity in the gas is very small. First, the variation of the dynamic pressure is of order ρV^2. This can be an issue for the numerical representation of the pressure given that the mean pressure is of order 10^5 Pa. Additionally, it involves a poor conditioning of the Jacobian matrix. The second and major drawback is the severe limitation of the time step induced by the large value of the sound velocity in the liquid, much larger than the convection velocity. Considering that for a natural convection configuration, the equations are integrated on the order of a viscous or diffusion time scale, this renders impossible to attain the asymptotic flow regime.

All-Mach or Mach-uniform methods are aimed to remedy this second drawback. These techniques are categorized into: density based methods and pressure based methods. The second ones are derived from the projection methods. The implicit treatment of the pressure allows avoiding the limitation of the time step and can be used both for incompressible and compressible flows. This was demonstrated by Kadioglu *et al.* [41], who proposed a new second order primitive preconditioner technique for solving all speed multi-phase flow problems. Their technique allows to compute both compressible and incompressible flows with Mach-uniform accuracy and efficiency. Kwatra *et al.* [50] propose a method for the simulation of inviscid compressible flow with shocks, contacts and rarefactions. Their method allows to alleviate the severe CFL condition imposed by the sound speed. It is based on the pressure equation and leads to a standard Helmholtz equation similar to a diffusion equation. In the limit as the sound speed goes to infinity one obtains the Poisson equation for incompresible flows. This makes the methods suitable for two-way coupling between compressible and incompressible flows.

Ida [35] proposes an improved numerical solver for the unified solution of flows involving an interface between either compressible or incompressible fluids. In their method, each of convection and acoustic parts of the Euler equations are treated individually by a splitting manner. In their work, Ida [35] and Kwatra *et al.* [50] show that for unsteady calculations where one wants to capture the acoustic waves, the time step still has a value of order of the acoustic time step for accuracy reasons.

Huber *et al.* presents in [34] a numerical simulation of the interaction of an ultrasound wave with a bubble. Their interest is to develop a fully compressible solver in the two phases and to account for surface tension effects.

For configuration involving small velocity values and liquid/vapor phase change, low Mach number approach seems more adapted considering that the acoustic part is removed beforehand from the equations. The use of this technique was already proposed by Dellacherie [21] in the context of multicomponent gaseous flows. The proposed model allows the simulation of non-stationary deformations on an interface separating two immiscible fluids induced by large temperature differences at low Mach number. The model system is obtained through an asymptotic expansion applied to

the two-phase compressible Navier-Stokes system which filters out the acoustic waves. In [54], Le Quéré *et al.* develop a Chebyshev collocation algorithm to integrate the time-dependent Navier-Stokes equations for natural convection flow with large temperature differences. The working fluid is assumed to be a perfect gas and its thermophysical properties vary with temperature according to Sutherland laws.

In low-Mach number approaches, the pressure is split into a mean pressure evolving in time and an additional component responsible for the continuity equation. This procedure removes the local coupling between pressure and density. The simulation of acoustic waves is therefore avoided and the corresponding stability criteria is lessen. Paillère *et al.* [70] and Le Quéré *et al.* [55] show that the low-Mach number techniques are much more efficient than fully compressible models when treating natural convection flows in closed cavities. In their papers, they give benchmarks for low Mach number solvers for natural convection flows with large temperature differences.

Daru *et al.* [19] propose a model dedicated for the simulation of low speed non isothermal two-phase flows in closed vessels. In their model, both liquid and gaseous phases are described by the Navier-Stokes equations and the energy equation. The liquid is treated as fully incompressible while the gas follows a low-Mach number approximation. Their proposed numerical model is validated on air bubbles embedded in a closed cavity filled with liquid water.

For more details, a detailed summary of numerical and experimental studies related to laminar natural convection in enclosures can be found in the work of Pandey *et al.* [73]. Miroshnichenko and Sheremet [66] present a review of the research on turbulent natural convection in rectangular cavities using numerical and experimental techniques. In the present work only laminar regime is considered.

5.3 Numerical method for the simulation of low Mach number liquid/vapor flows

The numerical simulation of natural convection demands a specific solver where the variation of the density is taken into account. During my thesis, I have implemented in the code DIVA a low Mach number solver for the liquid phase, based on the numerical approach proposed by Daru *et al.* [19].

The configuration described in [19] consists in a multiphase flow involving a strictly incompressible liquid phase and a compressible gaseous phase, the latter being considered under the low-Mach number assumption. In what follows, we will first describe the different steps of implementation of the variable density numerical solver for a gas phase and second, the corresponding modifications when the method is used for a liquid phase.

5.3.1 Gas phase treated using the low-Mach number approximation

The system of equations governing a configuration involving two-phase flows, containing an incompressible liquid and a compressible gas phase treated with a low-Mach number approximation,

writes

$$\frac{\partial \rho}{\partial t} + \nabla \cdot (\rho \mathbf{u}) = 0, \tag{5.1}$$

$$\rho(\frac{\partial \mathbf{u}}{\partial t} + \mathbf{u} \cdot \nabla \mathbf{u}) = -\nabla \tilde{p} + \nabla \cdot \tau + \rho \mathbf{g}, \tag{5.2}$$

$$\rho C_p \left(\frac{\partial T}{\partial t} + \mathbf{u} \cdot \nabla T \right) = \nabla \cdot (k \nabla T) - P \nabla \cdot \mathbf{u}, \tag{5.3}$$

$$\rho(\mathbf{x}, t) = \frac{P(t)}{rT(\mathbf{x}, t)}, \tag{5.4}$$

where $\tilde{p}(\mathbf{x}, t) \simeq p(\mathbf{x}, t) - P(t)$, $P(t)$ is the thermodynamic pressure and r is the ideal gas constant. The viscous tensor τ is equal to $\lambda \nabla \cdot \mathbf{u}\mathbf{I} + 2\mu\mathbf{D}$ with Lamé coefficients λ and μ, $\mathbf{D}$ the strain rate tensor and $\mathbf{I}$ the identity tensor.

Using the ideal gas law (5.4), the continuity equation (5.1) can also be expressed as

$$\nabla \cdot \mathbf{u} = -\frac{1}{\rho}\frac{D\rho}{Dt} = \frac{1}{T}\frac{DT}{Dt} - \frac{1}{P}\frac{DP}{Dt}. \tag{5.5}$$

The thermodynamic pressure is calculated using an integral relation derived from (5.5),

$$\frac{1}{P}\frac{dP}{dt} = \frac{1}{\Omega_g}\left(\int_{\Omega_g} \frac{1}{T}\frac{DT}{Dt} d\mathbf{x} - \int_{\partial\Omega_g} \mathbf{u} \cdot \mathbf{n} ds \right), \tag{5.6}$$

where Ω_g is the volume of the gas domain and $\partial\Omega_g$ is its bounding surface. Equation (5.6) allows for the calculation of the source term

$$P(t) = P(t_0) \exp\left(\int_{t_0}^{t} \left(\frac{1}{P}\frac{dP}{dt} \right) dt' \right). \tag{5.7}$$

where t_0 is some reference time.

Note that in the original method of Daru *et al.* [19], the temperature field was determined using the enthalpy formulation

$$\rho C_p \frac{DT}{Dt} = \nabla \cdot (k \nabla T) - \frac{T}{\rho}\left(\frac{\partial \rho}{\partial T} \right)_p \frac{Dp}{Dt}. \tag{5.8}$$

Finally, the different steps of the numerical procedure are

(1) initialization of the velocity, the temperature and the density field (via equation (5.4)),

$$\mathbf{u}^n; \quad T^n; \quad \rho^n. \tag{5.9}$$

(2) solve the Navier-Stokes equations using the projection method,

$$\mathbf{u}^{n+1}. \tag{5.10}$$

(3) solve the temperature equation (5.3),

$$T^{n+1}. \tag{5.11}$$

(4) calculate the temporal derivative of the thermodynamic pressure with equation (5.6),

$$\left(\frac{1}{P}\frac{dP}{dt} \right)^{n+1} = \frac{1}{\Omega_g}\left(\int_{\Omega_g} \frac{1}{T^{n+1}} \left(\frac{T^{n+1} - T^n}{\Delta t} + (\mathbf{u} \cdot \nabla T)^{n+1} \right) d\mathbf{x} \right). \tag{5.12}$$

(5) determine the thermodynamic pressure P using equation (5.7).

$$P^{n+1} = P(t_0)\exp\left(\int_{t_0}^{t^{n+1}} \left(\frac{1}{P}\frac{dP}{dt}\right) dt'\right). \tag{5.13}$$

(6) compute the density ρ with the relation (5.4),

$$\rho^{n+1} = \frac{P^{n+1}}{rT^{n+1}}. \tag{5.14}$$

(7) calculate the continuity equation (5.5),

$$(\nabla \cdot \mathbf{u})^{n+1} = \frac{1}{T^{n+1}}\left(\frac{T^{n+1}-T^n}{\Delta t} + (\mathbf{u}\cdot\nabla T)^{n+1}\right) - \left(\frac{1}{P}\frac{dP}{dt}\right)^{n+1}. \tag{5.15}$$

Note that steps (4-7) are done only for the phase treated under the low-Mach number approximation, in this case the gas phase.

5.3.2 Liquid phase treated using the low-Mach number approximation

For the simulation of variable density in the liquid phase, some modifications are made to the above described method. First of all, the equation of state for a perfect gas can no longer be used. The density is written using

$$\rho(\mathbf{x},t) = \rho_0\left(1-\beta\left(T-T_0\right)\right), \tag{5.16}$$

with ρ_0 the density at temperature of reference T_0 and β the thermal dilatation coefficient.

The continuity equation is then expressed with

$$\nabla\cdot\mathbf{u} = -\frac{1}{\rho}\frac{D\rho}{Dt} = -\beta\rho_0\frac{DT}{Dt}. \tag{5.17}$$

The algorithm for the liquid phase maintains steps (1-3), followed by

(4) compute the density ρ with the relation (5.16),

$$\rho^{n+1} = \rho_0\left(1-\beta\left(T^{n+1}-T_0\right)\right). \tag{5.18}$$

(5) calculate the continuity equation (5.17),

$$(\nabla\cdot\mathbf{u})^{n+1} = -\beta\rho_0\left(\frac{T^{n+1}-T^n}{\Delta t} + (\mathbf{u}\cdot\nabla T)^{n+1}\right). \tag{5.19}$$

Note that, for the liquid phase, we no longer have acces to the thermodynamic pressure P. Nevertheless, its variations are negligible for an open computational configuration, and one can use the value of an external thermodynamic pressure in equation (5.3).

5.4 Validation test case

The implemented variable density solver is now validated on a 2D configuration. The test case, taken from [55], consists in a differentially heated square cavity problem illustrated in figure 5.1.

On all walls, the no-slip condition is imposed for the velocity. On the horizontal walls, Neumann conditions, $\partial T/\partial y = 0$, are applied for the temperature. The wall at $x = 0$ is heated, $T(x = 0, y) = T_h$, while the wall at $x = l_x$ is cooled, $T(x = l_x, y) = T_c$. The imposed initial conditions are: $T(x, y) = T_0$, $\rho(x, y) = \rho_0$, $u(x, y) = v(x, y) = 0$ and $P(t = 0) = P_0$.

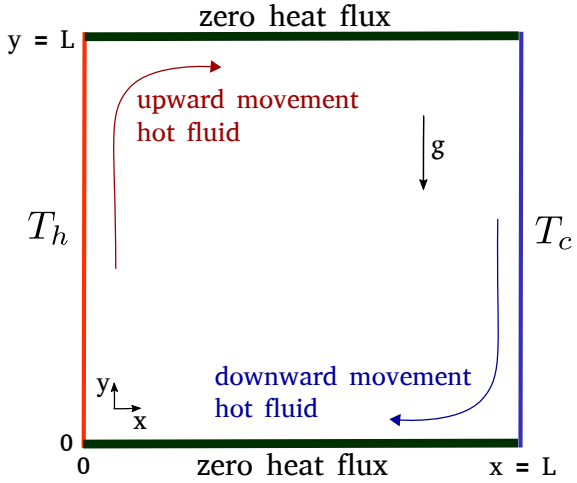

Figure 5.1: Differentially heated square cavity problem.

The dimensions of the computational domain are $[0, L] \times [0, L]$ and their determination is further given. The configuration is defined by a Rayleigh number of 10^6. For a perfect gas, the Rayleigh number is defined as

$$Ra = Pr \frac{g\rho_0^2 \left(T_h - T_c\right) L^3}{T_0 \mu_0^2}, \tag{5.20}$$

where g is the gravitational acceleration, L is the height of the cavity, T_0 is a reference temperature equal to $\left(T_h + T_c\right)/2$, ρ_0 the reference density corresponding to T_0, and μ_0 is the dynamic viscosity at T_0.

We introduce a non-dimensional parameter $\epsilon = \left(T_h - T_c\right) / \left(T_h + T_c\right)$ characterizing the compressibility effects. For small enough ϵ, incompressible flow models with the Boussinesq approximation are valid, meanwhile for high values of ϵ the Boussinesq assumptions break down and one needs to resort to a compressible flow model, or since the Mach numbers remain small, to a low-Mach number approximation model.

The problem is completely defined by the Rayleigh number, the value of ϵ and the following parameters:

$$P_0 = 101325\ Pa; \quad T_0 = 600\ K; \quad r = 287\ J/kg/K; \quad \rho_0 = \frac{P_0}{rT_0};$$

$$Pr = 0.71; \quad \gamma = 1.4; \quad g = 9.81\ m/s^2; \quad \epsilon = 0.6.$$

The heat transfer to the walls is characterized by the local Nusselt number,

$$Nu(y) = \frac{L}{\left(T_h - T_c\right)} \left(\frac{\partial T}{\partial x}\right)_w. \tag{5.21}$$

In figure 5.2 are illustrated the temperature field and the streamlines obtained in the heated square cavity. As expected, each side wall is coated with a conduction layer. The heated layer tends to rise along the heated wall while the cooled layer falls along the cooled wall. A steady state characterized by en energy balance between conduction and convection is reached by the thermal layers (Bejan [5]).

Different mesh grids were used for the convergence study. Additionally, verifications were carried out to evaluate whether the energy formulation or the enthalpy formulation gives the same results. All the results are shown in Tables 5.1 and 5.2. The convergence is achieved with the mesh

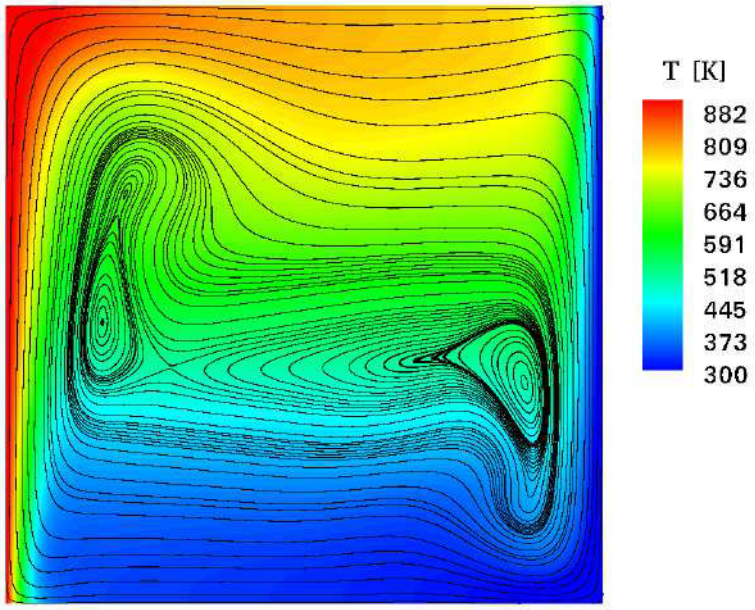

Figure 5.2: Temperature field and streamlines in the heated square cavity configuration.

Table 5.1: Results obtained with the internal energy formulation (equation 5.3).

	Nu_h	Nu_c	P/P_0	m/m_0
128 × 128	8.87755	8.811519	0.82640	0.9682
256 × 256	8.83592	8.844706	0.848147	0.99129
512 × 512	8.851341	8.853514	0.853832	0.99729
1024 × 1024	8.856285	8.856827	0.85547	0.99904
Reference Solution [55]	**8.859777**	**8.859777**	**0.8563380**	

grid 512×512 and, as expected, the formulation for the temperature equation does not influence the results. In addition to the Nusselt number and the variation of the thermodynamic pressure, the conservation of mass is also computed. For both formulations, the simulations converge towards 0.1% of mass loss, which is negligible.

5.5 Present work

In this section we present the work conducted on the numerical simulation of a 2D configuration describing the interaction between natural convection mouvements in the liquid and the liquid/vapor phase change.

In what follows we first describe the computational configuration. For the present study, in addition to variable density, wall conduction was also implemented into the code DIVA. The latter is validated for a classic test case of pure conduction. Finally, our preliminary results are presented; the influence of the natural convection, through the Grashof number, onto the thermal flux is shown and discussed. Conclusions and perspectives on the present study are given at the end of the chapter.

Table 5.2: Results obtained with the enthalpy formulation (equation (5.8).

	Nu_h	Nu_c	P/P_0	m/m_0
128×128	8.77279	8.823986	0.82712	0.96743
256×256	8.83685	8.84917	0.8486	0.991244
512×512	8.852247	8.855293	0.85407	0.997318
Reference Solution [55]	**8.859777**	**8.859777**	**0.8563380**	

5.5.1 Computational configuration

In the present study, as a first approach, the cryogenic tank has been represented by a 2D configuration, illustrated in figure 5.3. The liquid is located in the lower part of the domain and the vapor is found above the liquid. The two sub-domains are separated by a plane interface Γ, the contact angle being imposed at 90^o. The dimensions of the computational domain are $l_x \times l_y$, the interface being situated at $2l_y/3$, with $l_y = 0.05\ m$ and $l_x = l_y$.

The velocity is initialized with a static field, both for the liquid and vapor phases, $\mathbf{u}_l = \mathbf{u}_v = 0$. The liquid temperature is initialized with a thermal gradient, with $T_l(x, y_\Gamma) = T_{sat}$ and $T_l(x, 0) = T_{sat} - \Delta T$. The temperature in the vapor phase is initially uniform and equal to the saturation temperature, $T_v = T_{sat}$. The configuration is under gravitational acceleration $\mathbf{g} = -g\mathbf{e}_y$.

The no-slip condition is imposed for the horizontal wall $y = 0$ and for the two vertical walls $x = 0$ and $x = l_x$. A free outflow is applied at the $y = l_y$ boundary, using the relations presented in section 3.4.1 of chapter 3. For the pressure, Neumann conditions are imposed for the walls, $(\partial p/\partial x)_{x=0,x=l_x} = 0$ and $(\partial p/\partial y)_{y=0} = 0$, and a Dirichlet condition for the outflow condition, $p(x, y = l_y) = 0$.

For the temperature, a Dirichlet condition is imposed at $y = 0$, equal to $T(x, y = l_y) = T_{sat} - \Delta T$. At the top of the computational domain, an adiabatic condition is applied, $(\partial T/\partial y)_{y=l_y} = 0$. In the x direction, the vertical walls are heated through conduction, where the imposed temperature at $x_w = 0$ is $T_w(x_w = 0, y) = T_{sat} + \Delta T/2$. More on the wall conduction is found in the next section.

Considering the symmetry of the proposed computational configuration, we choose to simulate only the half of the domain by applying a symmetrical boundary condition at $x = l_x/2$. This will alleviate the computational cost of our simulations.

At present, only two uniform mesh grids $N_x \times N_y$ were employed, 64×128 and 128×256.

The liquid is treated under the low-Mach number approximation while the vapor phase is incompressible.

5.5.2 Wall conduction

For the 2D computational configuration described above, we have considered that the vertical walls are heated through wall conduction. The wall dimensions are $[l_{x,wall} \times l_y]$, with $l_{x,wall} = l_x/4 = 62.5 \cdot 10^{-4}\ m$.

The Dirichlet condition imposed on the temperature at $x = 0$ is calculated solving the wall conduction, described by the equation

$$\rho_S C_{p,S} \frac{\partial T_{wall}}{\partial t} = \nabla \cdot (k_S \nabla T_{wall}) \,. \tag{5.22}$$

with T_{wall} the temperature field in the wall domain, k_S the wall conductivity, ρ_S the wall density and $C_{p,S}$ the heat capacity of the wall.

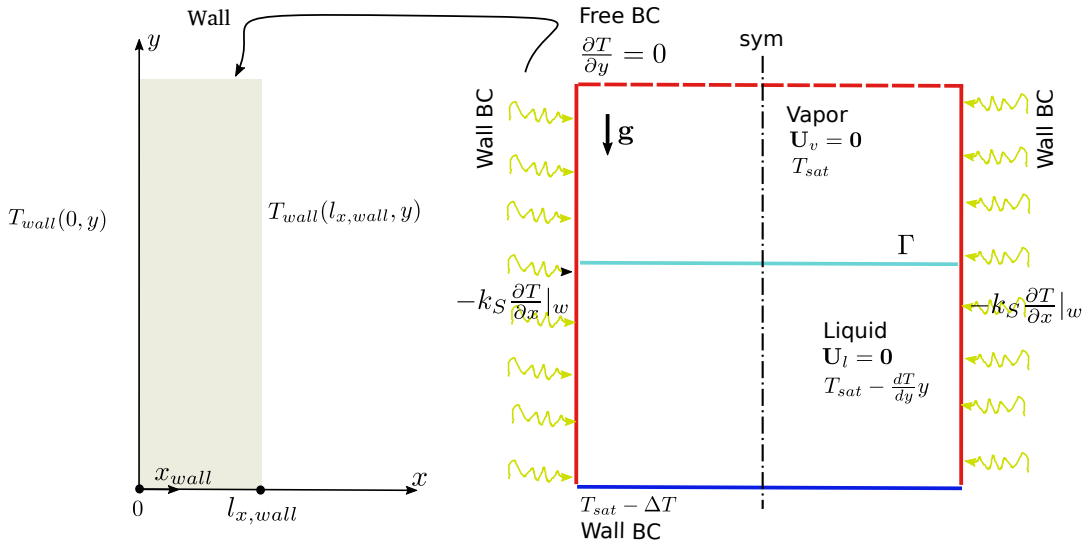

Figure 5.3: Schematics of the computational configuration.

The temperature field in the wall is initialized with the profile

$$T_{wall}(\mathbf{x}, t=0) = Ax_{wall} + B, \tag{5.23}$$

with

$$A = \frac{T(x=0,y) - T_{wall}(x_w=0,y)}{l_{x,wall}} \quad \text{and} \quad B = T_{wall}(x_w=0,y), \tag{5.24}$$

where $x_{wall} \in [0, l_{x,wall}]$.

Dirichlet boundary conditions are imposed in the x direction, $T_{wall}(x_w=0,y) = T_{sat} + \Delta T/2$ and $T_{wall}(x_w=l_{x,wall},y) = T(x=0,y)$. Zero flux Neumann boundary conditions are applied at $y=0$ and $y=l_y$.

The wall conduction equation is solved using a Gauss-Seidel algorithm. The mesh grid employed depends upon the resolution of the fluid domain. The number of grids in the y direction is the same as for the fluid while in the x direction we use $N_x/4$ points.

The wall conduction solver is validated on a pure conduction test case. Three layers are considered, the solid wall, the liquid and the vapor, as can be seen in figure 5.4a. An analytical solution is avalaible for this configuration, which give access to the temperature profile and therefore to the temperature at the interface between each layer: $T_{s/l} = 382.995\ K$ and $T_{l/v} = 381.468\ K$.

In figure 5.4a we have plotted the initial temperature field, constant in the liquid and the vapor phases and equal to $T = 373\ K$. In the solid, we impose a linear evolution. Dirichlet boundary conditions are imposed in the y direction: $T_{wall}(x, y_w=0) = 383\ K$ and $T(x, y=l_y) = 363\ K$.

Figure 5.4b illustrates the established temperature field, obtained after a certain time of simulation. The values of temperature obtained at the solid-liquid and liquid-vapor interfaces are in very good agreement with the theory.

5.5.3 Preliminary results

In what follows we present some preliminary results obtained for the described configuration. Even though the present study is under development and not finalized, this initial analysis is an opening to a more thorough study and allows for a first physical understanding of the involved phenomena. Additionally, this step allows to determine the different perspectives for this study.

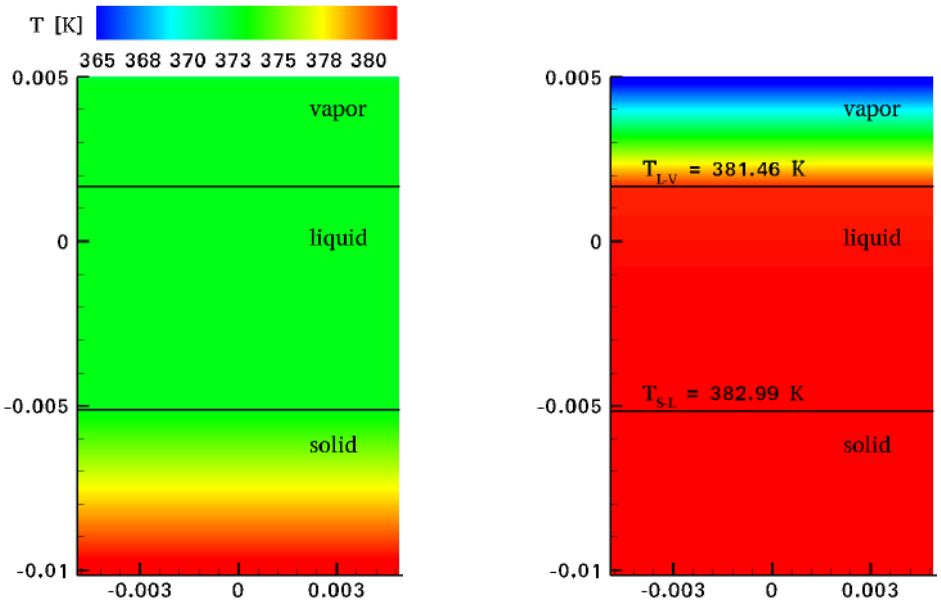

(a) Inital temperature field

(b) Final temperature field

Figure 5.4: Validation of the wall conduction solver for a pure conduction test case. Temperature field.

5.5.3.1 Dimensionless numbers

The present problem is characterized by several dimensionless numbers:

- Prandtl number,

$$Pr = \frac{\mu C_p}{k} = \begin{cases} 3.93, & \text{for the liquid phase} \\ 0.98, & \text{for the vapor phase} \end{cases}.$$

- Jakob number,

$$Ja = \frac{C_p \Delta T}{L_v} = \begin{cases} 0.1481, & \text{for the liquid phase} \\ 0.035, & \text{for the vapor phase} \end{cases}.$$

- density ratio,

$$r = \frac{\rho_l}{\rho_v} = 1623.$$

- effusivity ratio,

$$K = \frac{(\rho C_p k)_S}{(\rho C_p k)} = \begin{cases} 4.7518 & \text{for the liquid phase} \\ 3.85 \cdot 10^5, & \text{for the vapor phase} \end{cases}.$$

  where $(\rho C_p k)_S$ are respectively, the density, the heat capacity and the thermal conductivity of the solid wall. The effusivity ratio characterizes the thermal contact between the fluid and the solid wall.

- Grashof number,

$$Gr = \frac{g\beta \Delta T L^3}{\nu^2} = \begin{cases} [4.71;\ 9.93;\ 18.8] \cdot 10^5, & \text{for the liquid phase} \\ 1168, & \text{for the vapor phase} \end{cases}.$$

where g is the gravitational acceleration, β is the coefficient of thermal expansion, ΔT is the thermal gradient described previously and L is the vertical length.

The Grashof number Gr is described as the ratio between the buoyancy and the viscous force and is analogous to the Reynolds number Re, where the velocity scale is related to buoyancy effects.

Several observations can be made concerning this configuration. First, in comparison with the 2D configuration of a laminar boundary layer, described in chapter 2, here, the jump velocity is in the liquid phase and not in the vapor phase. Second, both the liquid and the vapor are in contact with the heated wall. Therefore, two Grashof numbers could be calculated, one for the liquid and one for the vapor phase. However, for the present study, the vapor is considered incompressible. Treating the vapor with a low-Mach number approximation can be one of the perspectives for this study. For the liquid phase, we have considered three values for the Grashof number, showed above. Note that for a laminar regime of the flow, the Grashof number has to be in the range $10^3 < Gr < 10^6$.

The product between the Grashof number and the Prandtl number gives the Rayleigh number, $Ra = Pr \cdot Gr$. The latter is often used in relation to natural convection problems, characterizing the thermal flux.

5.5.3.2 Convergence study

In this work, we first investigate the influence of the natural convection onto the thermal flux induced at the liquid/vapor interface. Note that only the thermal flux calculated in the liquid phase is considered here.

The natural convection motions, governed by the Grashof number value, influence the thermal flux evolution at the liquid/vapor interface. This thermal flux, computed with

$$\Phi_I = k_l \frac{\partial T}{\partial y}\Big|_{\Gamma,l} \tag{5.25}$$

is, inter alia, induced by the liquid/vapor phase change, governed by the Jakob number value.

As already said, three values for the Grashof number are studied, $Gr = [4.71;\ 9.93;\ 18.8] \cdot 10^5$, by varying the coefficient of thermal expansion β. For each simulation, a convergence study is required. The simulation of the natural convection being fairly long, $T \sim 1600\ s$ to obtain an established regime, only two mesh grids were here used: 64×128 and 128×256. The simulations done with the more refined mesh 256×512 are ongoing. Note that for the simulation of 128×256, the computation lasted 14 days while for the simulation of 256×512, we expect a duration of 60 days (using 32 processors).

Figure 5.5 illustrates the spatial evolution of the liquid thermal flux Φ_I at the liquid/vapor interface, for the two used mesh grids. We observe that the mesh convergence is influenced by the Grashof number value. Indeed, increasing the latter induces an increase in the velocity, which, in turn, decreases the thermal boundary layer thickness. Therefore, a better resolution of the zone close to the interface is needed in order to capture the induced high thermal gradient. On the other hand, the lack of convergence can be observed only for $x < 0.01\ m$, for $Gr = 9.93 \cdot 10^5$ and $Gr = 1.88 \cdot 10^6$, and close to the wall, $x \sim 0$, for $Gr = 4.71 \cdot 10^5$.

Even if, at present, our computations are not entirely converged, we will nevertheless try to go further in the understanding of the evolution of the thermal flux at the liquid/vapor interface.

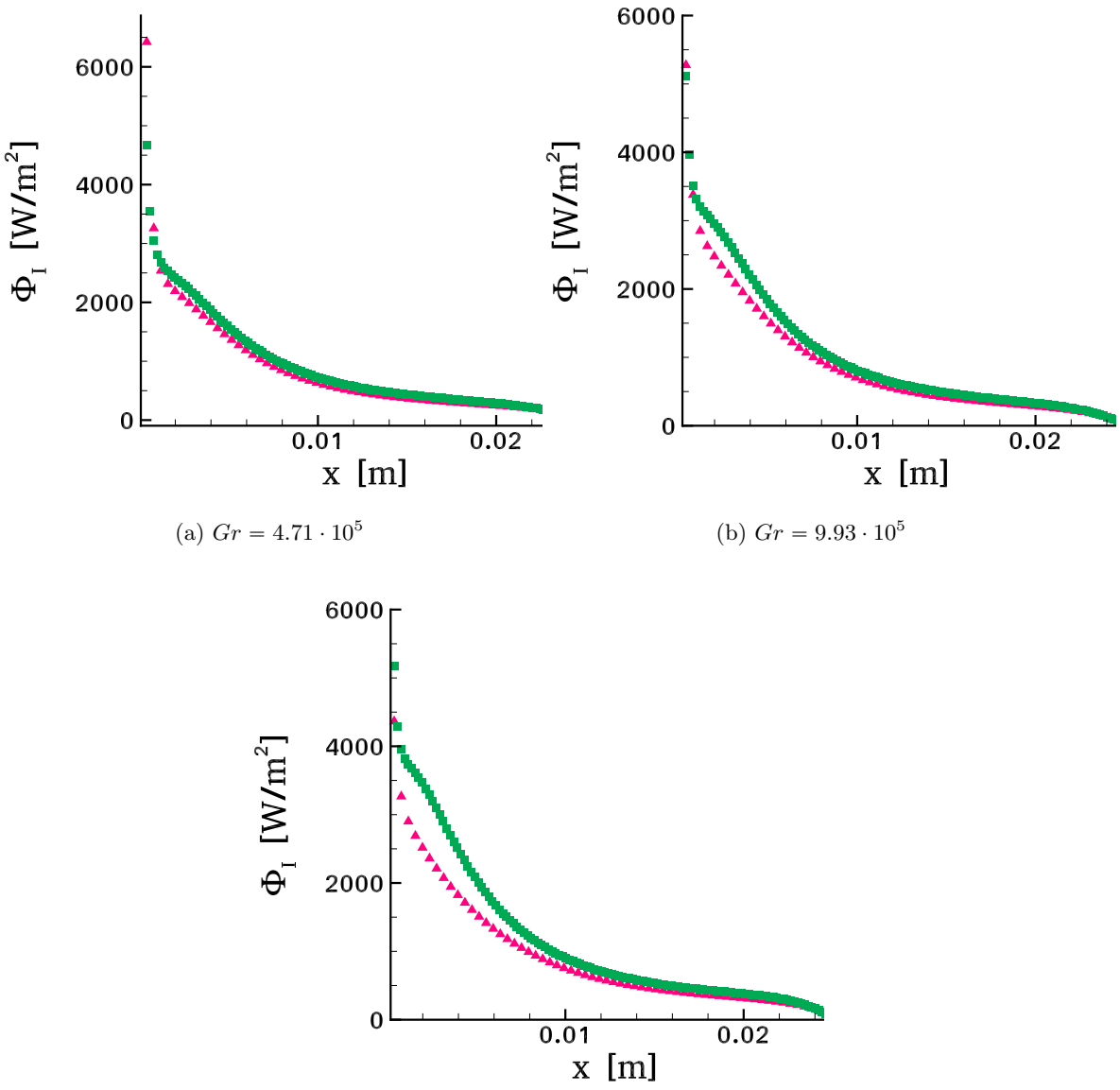

(a) $Gr = 4.71 \cdot 10^5$

(b) $Gr = 9.93 \cdot 10^5$

(c) $Gr = 1.88 \cdot 10^6$

Figure 5.5: Spatial evolution of the liquid thermal flux at the liquid/vapor interface. Mesh convergence. (▲) - 64×128 ; (■) - 128×256.

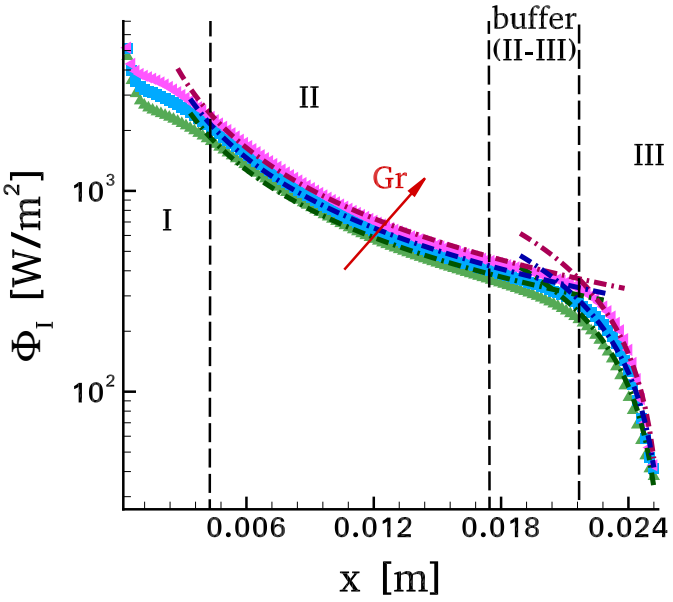

Figure 5.6: Influence of the Grashof number Gr onto the evolution of the liquid thermal flux at the liquid/vapor interface. Mesh grid employed 128×256. (▲) - $Gr = 4.71 \cdot 10^5$; (■) - $Gr = 9.93 \cdot 10^5$; (▶) - $Gr = 1.88 \cdot 10^6$. Zone II, (dash dot lines) - power laws ax^n; Zone III, (dash dot lines) - linear laws $ax + b$. Each dash dot lines color is calculated for the corresponding Grashof number.

5.5.3.3 Grashof influence onto the evolution of the thermal flux

We have plotted in figure 5.6 the spatial evolution of the liquid thermal flux at the interface, for three values of Grashof number. Note that the y axis is in logarithmic scale. Increasing the Grashof number increases the interface thermal flux. Additionally, figure 5.7 shows the temperature field and the streamtraces for the three configurations. Three principal zones can be distinguished.

Zone I is represented by the region in the vicinity of the solid wall, where the thermal flux is considerably high. The proximity to the triple line renders this region difficult to converge. Unfortunately, we will have to wait for a more refined simulation, such as the 256×512, in order to make an analysis on this zone.

A second region, denoted as zone II, is delimited by $0.0065 < x < 0.018$ m and represents the region where the convection mouvements shear the liquid/vapor interface. In this region, the spatial evolutions of the thermal flux can be fitted with power laws ax^n, where a and n could depend on the dimensionless numbers governing the problem.

Finally, the third zone, denoted as zone III, is located in the region where the convective mouvements stop shearing the interface and have already moved away from the interface. In this region, the interfacial flux can be fitted with a linear law, $ax + b$. This fit demonstrates the lack of interaction between the natural convection and the interface.

Further investigations can be made on this matter. The dependence of the coefficients a and b with the dimensionless numbers, for each zone, could be determined by conducting a parametric study. More on this will be discussed in the perspectives of the present work.

The streamtraces plotted in figure 5.7 show also a dependence on the value of the Grashof number. For a low Grashof number, we have a discrepancy between the scale of the two circulations. When increasing its value, the situation tends to inverse, the small circulation increases its scale while the large circulation tends to decrease its scale. Another observation one can made is on

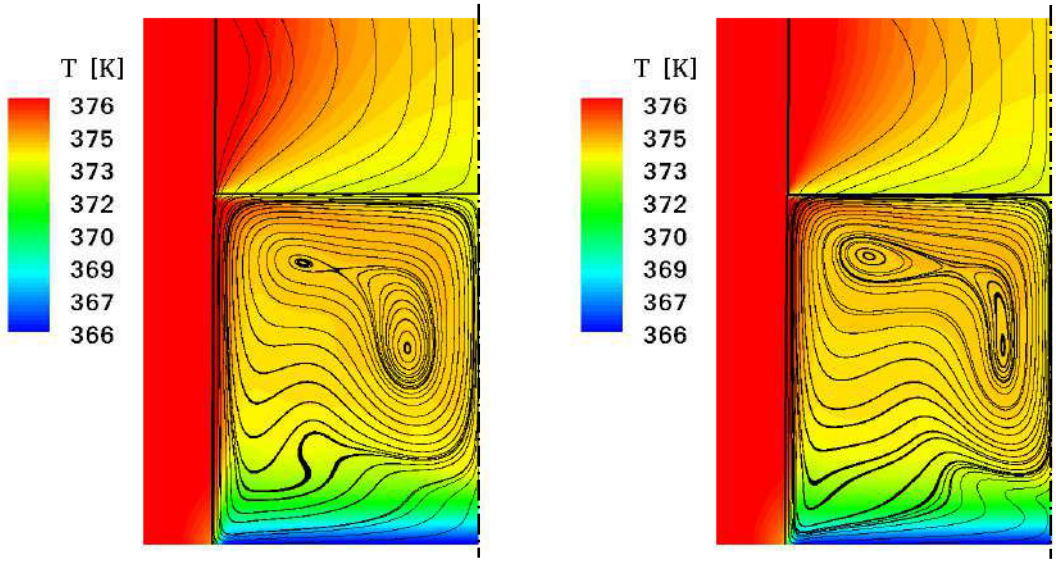

(a) $Gr = 4.71 \cdot 10^5$ (b) $Gr = 9.93 \cdot 10^5$

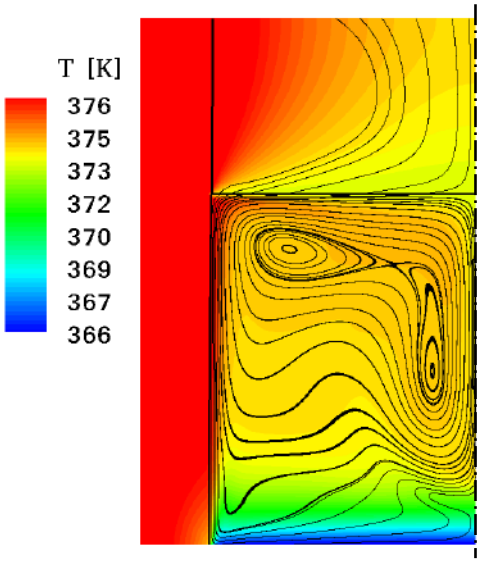

(c) $Gr = 1.88 \cdot 10^6$

Figure 5.7: Captions of the simulations for different values of the Grashof number. Temperature field and streamtraces. The entire computational domain is illustrated, the solid wall at the left, the liquid phase at the lower part of the domain and the vapor phase at the upper part of the domain. Note that only half of the 2D configuration has been simulated.

the thermal boundary layer located at $y = 0$, above the cooled wall. The increase on the Grashof number decreases its thickness. A more detailed analysis on these matters could also be considered among the perspectives of the present work.

5.6 Conclusions and perspectives

In this chapter we have described our preliminary work on the interaction between natural convection and liquid/vapor phase change. For computational cost reasons, we have considered the laminar regime ($Gr \sim 10^6$) while the industrial configuration is characterized by a turbulent regime ($Gr \sim 10^{10}$). Nevertheless, this first approach employed to study this type of configuration is not without value.

The work was first on the implementation and validation of a variable density solver in the liquid phase. The wall conduction solver was also validated for a pure conduction test case.

Next, we have configurated our simulation in order to begin the study on the interaction between natural convection and liquid/vapor phase change in a 2D domain. Several values of the Grashof number were simulated and a preliminary spatial convergence study was carried out for each one of them. It was shown that for some of this simulations, a more refined mesh grid was needed. However, the obtained results allowed a first discussion on the influence of the natural convection onto the interface thermal flux, which increases when Gr increases. Additionally, we have proposed a decomposition of the interface region into three zones: the close to the solid wall zone, the sheared interface zone and the no-interaction-with-the-natural-convection zone. For the last two zones, a power law and a linear evolution were proposed, respectively, for the spatial evolution of the thermal flux at the liquid/vapor interface.

The present work is ongoing and opens to many perspectives. Simulations allowing for a complete convergence study are in progress. We plan next to conduct a parametric study to investigate the influence of the dimensionless numbers onto the thermal flux, particularly the Grashof number Gr and the effusivity ratio K. In addition, we would want to investigate how the mass flow rate at the liquid/vapor interface behaves for these configuration. A dimensional analysis of the evolution of the observed circulations in fonction of the dimensionless numbers could also be relevant.

In the distant future, a 2D axisymmetric configuration could be considered. This would allow a deeper investigation of the region close to the contact line. Additionally, for both 2D and 2D axisymmetric configurations, the contact angle could be variated and its influence studied. For the cryogenic tank application, when the liquid hydrogen is emplyed as cyrogenic propellant, its pressurization is done using a non-condensable gas. Therefore, studying the configuration involving a multi species gas could be one of the perspectives. This will increase the complexity of the study by adding the Marangoni convection at the liquid/gas interface.

And finally, a reflexion on how to simulate a turbulent natural flow convection is mandatory. An approach could consist of injecting turbulent fluctuations close to the wall, at $x = 0$, and see how they evolve when advected via the natural convection flow.

Conclusions and future directions

Conclusions

This thesis has described the numerical study conducted on the interaction between liquid/vapor phase change and an external flow.

This research was motivated by the need of a better understanding of the physical phenomena generated in a cryogenic tank, during the various phases of the flight mission of a satellite. More precisely, the objective was to find behaviour laws for the heat transfer at the liquid/vapor interface, laws that can further be used in industrial codes to model the interface.

The numerical study presented in this thesis was conducted using the in house code DIVA, stating for Interfacial Dynamics for Atomization and Vaporization. The solver implemented in the code DIVA was first described, together with all the corresponding numerical methods for the simulation of two phase flows with phase change.

The chapters that follow were dedicated to the work realized during the present thesis. Two configurations were studied, in microgravity and under gravitational acceleration.

First, the focus was on the interaction between liquid/vapor phase change and an external boundary layer flow. This configuration characterizes the microgravity regime, when the satellite is in orbit and the subcooled liquid contained in the cryogenic tank is pressurized by a superheated vapor. Even if, for most of the industrial applications, the flows are turbulent, we have considered of scientific and theoretical importance to tackle first the laminar regime. Therefore, the computational configuration implemented was a 2D laminar boundary layer flow of vapor shearing a static and plane liquid. Both condensation and vaporization were studied, by considering, respectively, a subcooled or a superheated vapor, while the liquid phase is at saturation temperature. A parametric study was conducted by varying the dimensionless numbers characterizing this problem, the Reynolds number, the Prandtl number, the density ratio and the Jakob number. Correlations were obtained on the Nusselt number when phase change occurs. It was showed that the local flow, induced by the phase change, decreases or increases, respectively, the local heat flux, depending upon vaporization or condensation is considered. For the vaporization configuration it was found that the Nusselt number, and therefore the heat transfer, decreases exponentially with the Jakob number until reaching a saturation value. The opposite trend was observed for the condensation, for which the Nusselt number increases as an exponential function of the Jakob number. Based on the obtained correlations for the Nusselt number, we were able to determine expressions for the integrated heat flux at the liquid/vapor interface. Another noteworthy result was about the viscous friction on the interface, or the tangential component of the viscous tensor, which was found to be weakly affected by the phase change in the case of a plane interface.

The obtained correlations are difficult to be used for a cryogenic tank application, considering the existing turbulent regime flow. It was only natural to further study the interaction between a spatial developing turbulent boundary layer flow and liquid/vapor phase change. In comparison

with the laminar regime, no exact theory exists for the resolution of the turbulent boundary layer flow. For this reason, our work was first dedicated to the numerical simulation of the spatial development of a turbulent boundary layer flow on a flat plate, with heat transfer. A thorough overview of the literature on the existing numerical methods to generate inflow data for turbulent flows simulation allowed us to choose the SEM for the present study. The implemented method was first validated for the simulation of instantaneous turbulent signals as well as for a spatially decaying HIT.

The numerical simulation of a turbulent boundary layer flow with heat transfer at a momentum thickness Reynolds number $Re_\theta = 1100$ was next described. For the thermal turbulent boundary layer simulation, an extension of the initial method of Jarrin *et al.* [38] was proposed. The assumption of the equivalence between the thermal and the dynamic boundary layer has therefore been taken, for a Prandtl number $Pr = 1$. Studies on the influence of the mesh grid, the length scale value, the number of eddies and a time convergence study on the generated turbulent fluctuations at the inlet plane were conducted. It allowed, on one hand, to validate our implementation, and on the other hand, to choose the computational configuration used for this work. Additionally, a study on the performance of the employed pressure solver was conducted and a detailed description of the involved computational constraints was given.

Finally, the results obtained were presented. We have shown via snapshots of the streamwise velocity and temperature fields that the hypothesis of the equivalence between the two can be considered reasonable. The evolutions of the turbulent statistics, mean and rms velocities and temperature profiles, with the wall coordinate were illustrated. The mesh refinement greatly improve their corresponding evolutions. The same was found for the turbulent heat fluxes, in the streamwise and the wall-normal directions. A comparaison with data extracted from the literature showed a good agreement of the latter evolutions. The same was found for the turbulent Prandtl number, which reaches a maximum value of 1.09 close to the wall, while similar values were also reported in other previous studies, in which Pr_t approaches a value of 1.1 at the wall. The streamwise evolutions of the friction coefficient and the Stanton number, allowing for the characterization of the local boundary layer flow, showed significant differences in comparison with the existing empirical (Kays and Crawford [44]) and numerical or experimental evolutions. In the vicinity of the inlet plane, it has already been reported that, when using a synthetic method, these parameters have incorrect evolutions. Often, their evolutions regain the correct path, but only after some distance in the streamwise direction.

Further on, the focus has been on the simulation of the interaction between the spatially developing turbulent boundary layer flow and liquid/vapor phase change. The procedure employed was to use two simulations. The auxiliary simulation allows the development of the boundary layer from a synthetic turbulence imposed at the inlet plane. After a certain time of simulation allowing to achieve the average convergence, the auxiliary simulation advances while storing, at each time step, the velocity components and the temperature on a vertical plane. These planes are later used as inflow boundary condition for the second simulation, where the phase change is plugged in. The liquid/vapor phase change was imposed as a boundary condition, for computational costs reason. The results obtained were analyzed qualitatively and quantitatively. The illustrations of the normal velocity and of the vorticity magnitude fields in a vertical plane Oyz showed an increase of vortices in the inner zone of the boundary layer, possesing a high vorticity. When plotting the isosurfaces of $Q = 0.5$, an increase in the population of small eddies was observed. These tendencies were explained by considering that the energy cascade from large to small eddies is higly enhanced by the blowing velocity induced by liquid/vapor phase change. A quantitative study allowed to investigate the influence of liquid/vapor phase change onto the evolution of the turbulent quantities.

The rms fields showed a considerable increase with the Jakob number. This is coherent with the observation on the increase of small eddies number, considering that the maximum of turbulent energy is contained by small turbulent scales. The heat fluxes were also impacted by the phase change. The turbulent heat flux in the streamwise direction was highly increased when increasing the Jakob number. The peak of the heat flux in the normal direction was shifted towards higher values of the wall coordinate y^+ when increasing the Jakob number. This was explained by the blowing effect of the liquid/vapor phase change. The mean profiles of the temperature and the velocity were also modified when phase change occurs. The velocity gradient was decreased in the viscous sublayer and increased in the logarithmic zone when increasing the Jakob number. The evolutions of the shear stressed showed some interesting trends. The viscous shear stress was influenced by the phase change only in the viscous sublayer, for $y^+ < 5$. The Reynolds shear stress followed the same evolution in the close to the wall zone ($y^+ < 10$), regarless of the Jakob number while in the logarithmic zone, its profile was increased when phase change occurs. The friction coefficient and the Stanton number have shown little influence of the Jakob number onto the slope of their profiles. Nevertheless, the corresponding curves were shifted towards smaller values when increasing the phase change. The evolution of the Nusselt number showed similar tendencies that the one obtained for the laminar regime. The curves presented a first region where the Nusselt number decreases towards a minimum and followed by a curve of positive slope.

The second configuration involved natural convection. As explained in the **??**, during the launching phase or for the space manoeuvres, the satellite is in a gravitational acceleration field. This induces convective motions in the liquid that will influence onto the liquid/vapor phase change. The last part of this thesis was dedicated to the interaction between natural convection and liquid/vapor phase change. More precisely, an investigation on how the Grashof number, governing the natural convection, will influence the spatial evolution of the liquid thermal flux at the liquid/vapor interface. To this extent, a variable density solver using the low-Mach number approximation was implemented into the code DIVA. Its validation was conducted on the simulation of a heated square cavity. Additionally, a wall conduction solver was used to impose the boundary conditions on the vertical walls of the tank. This solver was validated on a pure conduction test case for which the temperature profile can be determined analytically. Preliminary results were shown. We have first investigated the mesh convergence and as was showed, for some of the Grashof number values, the convergence was not achieved. More refined simulations are in progress. However, the obtained results allowed a first discussion on the influence of the natural convection onto the interface thermal flux, which increased when Gr increased. Additionally, we have proposed a decomposition of the interface region into three zones: the close to the solid wall zone, the sheared interface zone and the no-interaction-with-the-natural-convection zone. For the last two zones, a power law and a linear evolution were proposed, respectively, for the spatial evolution of the thermal flux at the liquid/vapor interface.

Both turbulent and natural convection configurations open to many perspectives that will be further detailed.

Future Directions

The following research could be considered as direct extensions of the present work. We will first consider the turbulent configuration.

Simulations for intermediate values for the Jakob number are ongoing. This will allow to get a better understanding from the observed trends. For example, for all the turbulent quantities,

a certain saturation effect could be predicted, especially for v_{rms}, w_{rms}, C_f and St, where a constriction between the curves of $Ja = 8$ and $Ja = 14$ can be observed. Additionally, studying several values of the Jakob number would allow to determine a behaviour law and compare it with the correlation obtained for the laminar regime.

It would be valuable to investigate the terms from the turbulent kinetic energy balance. A study on the influence of phase change onto the terms of production, diffusion and dissipation is planned for the near future. This will allow to go further in the comprehension of the obtained tendencies, comprehend what turbulent processus is most influenced by the liquid/vapor phase change. Additionally, investigations on the energy spectra could allow to determine to what scales the energy from the phase change is distributed.

Finally, simulations with a more refined mesh grid, $1024 \times 256 \times 256$, would surely allow to obtain better profiles for the friction coefficient and the Stanton number. This would enable a parametric study for different Jakob numbers with the objective to determine behaviour laws for the heat flux and the friction coefficient.

The work on the natural convection is at its early stages and many perspective can be foreseen. For the near future, a complete convergence study is intended, the corresponding simulations are ongoing. We plan next to conduct a parametric study to investigate the influence of the dimensionless numbers onto the thermal flux, particularly the Grashof number Gr and the effusivity ratio K. In addition, we would want to investigate how the mass flow rate at the liquid/vapor interface behaves for these configuration. A dimensional analysis of the evolution of the observed circulations in fonction of the dimensionless numbers could also be relevant.

In the distant future, a 2D axisymmetric configuration could be considered. This would allow a deeper investigation of the region close to the contact line. Additionally, for both 2D and 2D axisymmetric configurations, the contact angle could be variated and its influence studied. For the cryogenic tank application, when the liquid hydrogen is used as cryogenic propellant, its pressurization is done using a non-condensable gas. Therefore, studying the configuration involving a multi species gas could be one of the perspectives. This will increase the complexity of the study by adding the Marangoni convection at the liquid/gas interface. Finally, a reflexion on how to simulate a turbulent natural flow convection is mandatory. An approach could consist of injecting turbulent fluctuations close to the wall, at $x = 0$, and see how they evolve when advected via the natural convection flow.

Last but not least, a discussion with the industry sector in order to determine how the obtained behaviour laws could be employed in their industrial codes seems important.

Appendix A

Parametric study fo the laminar boundary layer

The purpose of the present work was to investigate the influence of liquid/vapor phase change on the Blasius theory results, particularly on the Nusselt number evolution. At first, the correction

$$Nu_x^{Bl} - Nu_x^{vap} = F\left(Re_x, Pr, Ja, \frac{\rho_l}{\rho_v}, x_L\right), \tag{A.1}$$

has been plotted. As it can be seen in Fig. A.1, for $x = x_L$, the correction $Nu_x^{Bl} - Nu_x^{vap} \neq 0$ and

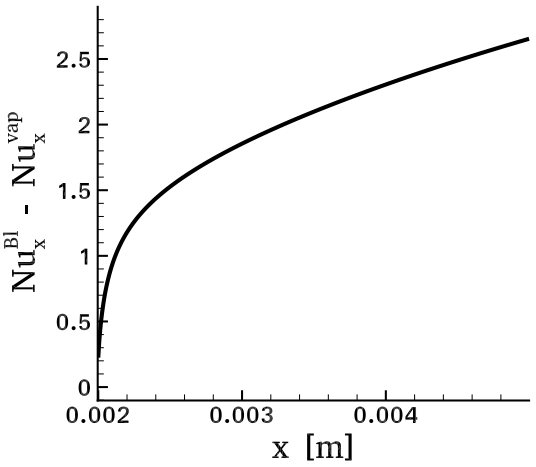

Figure A.1: The correction on the Nusselt number from the Blasius theory with the x-axis - Vaporization configuration - dimensionless numbers: $Pr = 1.022$, $Re_{x_L} = 85.726$, $Ja = 3.69$ and $\frac{\rho_l}{\rho_v} = 17.746$.

it increases with x as a power function. Therefore, the Nusselt number with vaporization can be written as

$$Nu_x^{vap} = Nu_x^{Bl} - \left(\alpha\left(\frac{x}{x_L} - 1\right)^n + \beta\right) H(x - x_L), \tag{A.2}$$

where the Heaviside function $H(x - x_L)$ enables locating the phase change only for $x > x_L$.

The next step in our inquiry was to determine the evolution of the parameters α, β and n with the dimensionless numbers characterizing the configuration of interest: Reynolds number Re_{x_L}, Prandtl number Pr, Jakob number Ja and the density ratio $\frac{\rho_l}{\rho_v}$. It is noteworthy that, given the

dimensionless form of the Eq. A.2, the choice of an inlet Reynolds number Re_{x_L} instead of a general Reynolds number Re_x is straighforward.

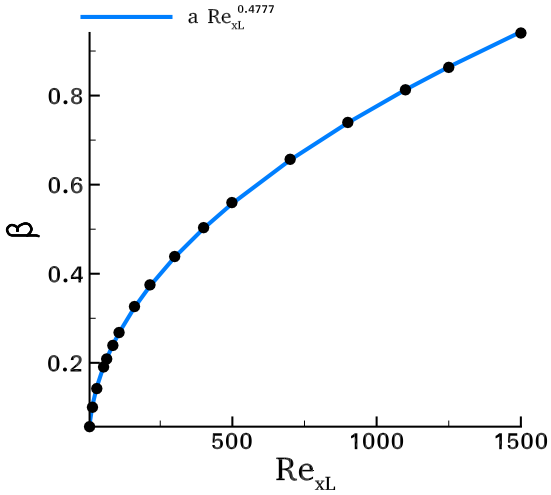

(a) Evolution with the Reynolds number and keeping fixed the dimensionless numbers: $Pr = 1.022$, $Ja = 3.69$ and $\frac{\rho_L}{\rho_v} = 17.746$. // $a(Pr, Ja, \frac{\rho_L}{\rho_v}) = 0.02866$.

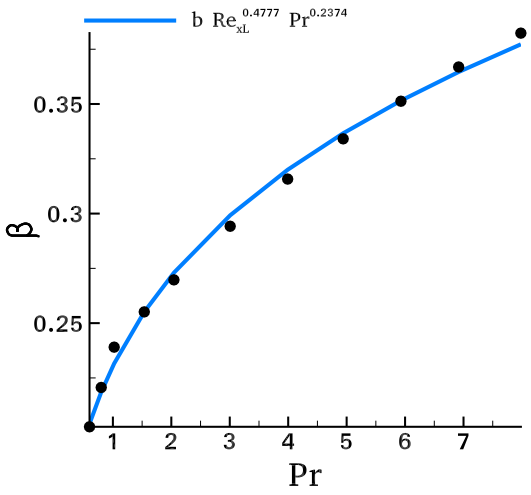

(b) Evolution with the Prandtl number and keeping fixed the dimensionless numbers: $Re_{x_L} = 85.7226$, $Ja = 3.69$ and $\frac{\rho_L}{\rho_v} = 17.746$. // $b(Ja, \frac{\rho_L}{\rho_v}) = 0.0748$.

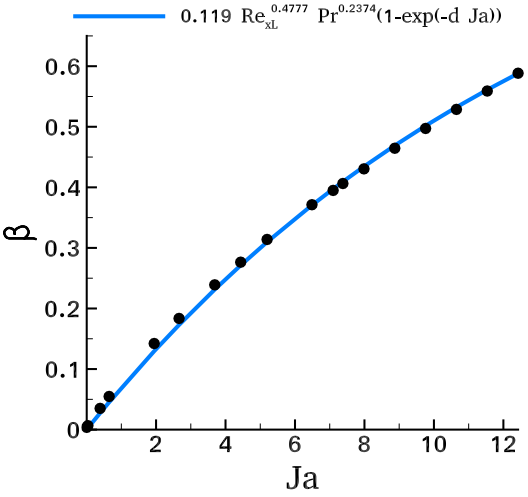

(c) Evolution with the Jakob number and keeping fixed the dimensionless numbers: $Pr = 1.022$, $Re_{x_L} = 85.7226$ and $\frac{\rho_L}{\rho_v} = 17.746$. // $d(\frac{\rho_L}{\rho_v}) = 0.07108$.

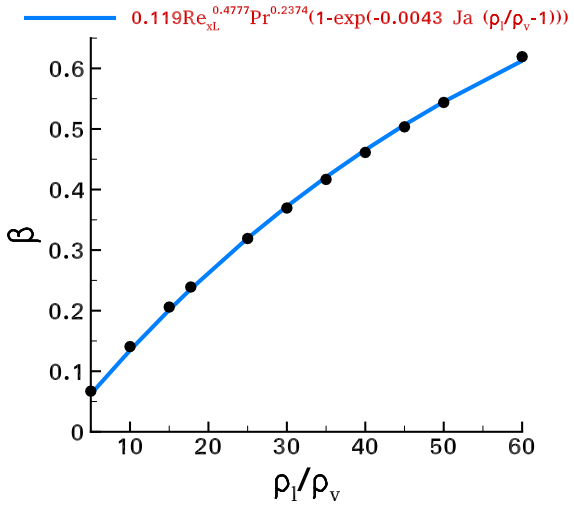

(d) Evolution with the density ratio and keeping fixed the dimensionless numbers: $Pr = 1.022$, $Re_{x_L} = 85.7226$ and $Ja = 3.69$.

Figure A.2: Evolution of the jump $\beta(Re_{x_L}, Pr, Ja, \frac{\rho_L}{\rho_v})$ for $x = x_L$ - Vaporization configuration.

The adressed approach to determine the parameters α, β and n is developed as it follows. First, the jump β for $x = x_L$ has been examined. Its evolution with the Reynolds number Re_{x_L} (Fig. A.2a), the Prandtl number (Fig. A.2b), the Jakob number (Fig. A.2c) and finally with the density ratio (Fig. A.2d) have been plotted.

By means of a Matlab library, CFTool, one was able to obtain its evolution with the dimen-

sionless numbers,

$$\beta = 0.119 Re_{x_L}^{0.4777} Pr^{0.2374} \left(1 - exp\left(-0.0043 Ja \left(\frac{\rho_l}{\rho_v} - 1\right)\right)\right).$$

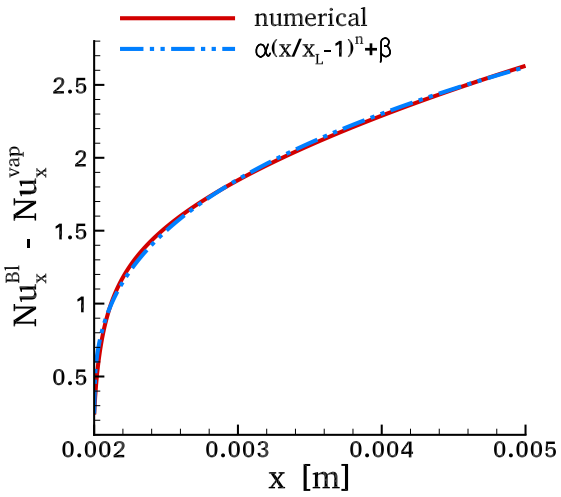

Figure A.3: Spatial evolution of the correction on the Nusselt number from the Blasius theory obtained from the numerical simulation and the function fitting its evolution: $\alpha = 2.062$ and $n = 0.3561$; β known for the corresponding couple of dimensionless numbers.

In the interest of finding the expressions of the parameters α and n from Eq. A.2, the relation $Nu_x^{Bl} - Nu_x^{vap}$ has been plotted with the x axis for each value of dimensionless number. For exemple, in Fig. A.3 the evolution of $Nu_x^{Bl} - Nu_x^{vap}$ is plotted for $Re_{x_L} = 85.7226$, $Pr = 1.022$, $Ja = 3.689$, and $\frac{\rho_l}{\rho_v} = 17.746$. Conducting a full set of simulations sweeping a large range of values for the dimensionless numbers enabled us to determine the expressions of parameters α and n,

$$\alpha = 0.294 Re_{x_L}^{0.495} Pr^{0.333} \left(1 - exp\left(-0.0248 Ja \left(\frac{\rho_l}{\rho_v} - 1\right)\right)\right),$$

and

$$n = 0.9351 Re_{x_L}^{-0.11} Pr^{-0.07} Ja^{-0.1} \left(\frac{\rho_l}{\rho_v}\right)^{-0.12}.$$

Their evolution with each dimensionless number is plotted in Fig. A.4 and Fig.A.5.

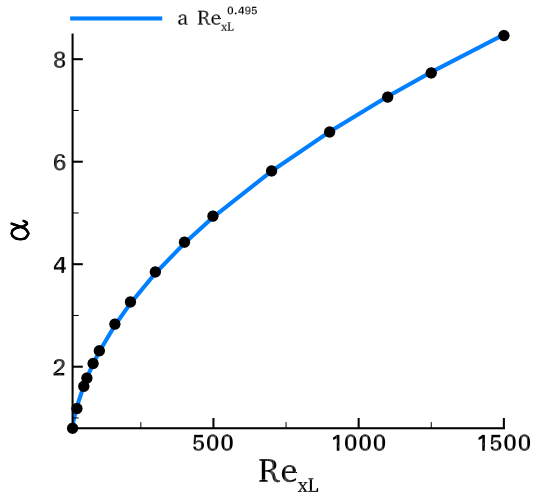

(a) Evolution with the Reynolds number and keeping fixed the dimensionless numbers: $Pr = 1.022$, $Ja = 3.69$ and $\frac{\rho_l}{\rho_v} = 17.746$. // $a(Pr, Ja, \frac{\rho_l}{\rho_v}) = 0.2271$.

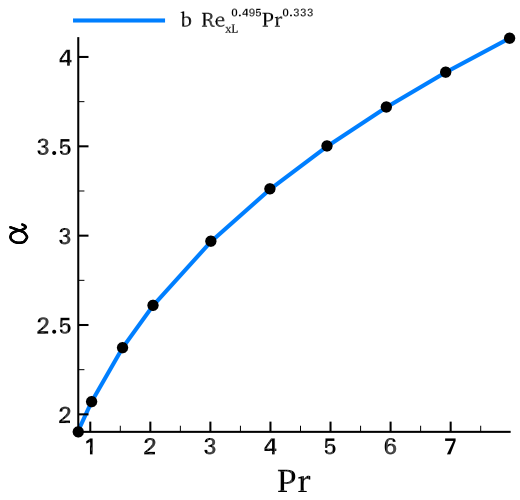

(b) Evolution with the Prandtl number and keeping fixed the dimensionless numbers: $Re_{x_L} = 85.7226$, $Ja = 3.69$ and $\frac{\rho_l}{\rho_v} = 17.746$. // $b(Ja, \frac{\rho_l}{\rho_v}) = 0.227$.

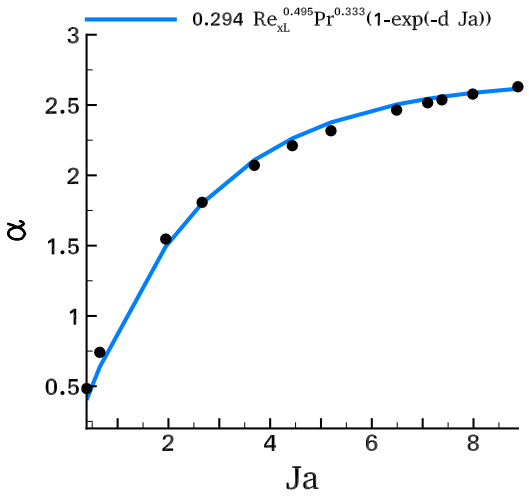

(c) Evolution with the Jakob number and keeping fixed the dimensionless numbers: $Pr = 1.022$, $Re_{x_L} = 85.7226$ and $\frac{\rho_l}{\rho_v} = 17.746$. // $d(\frac{\rho_l}{\rho_v}) = 0.4185$.

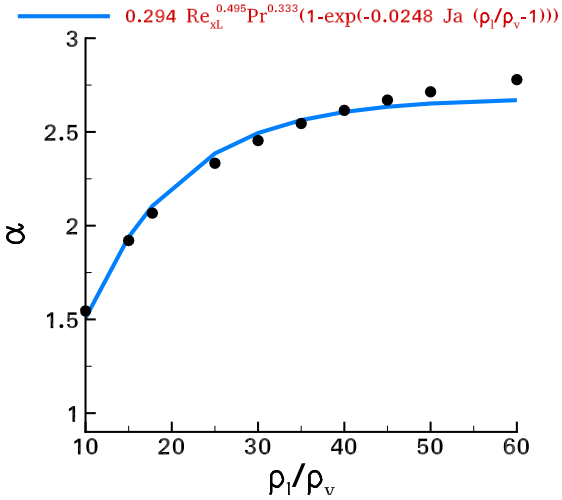

(d) Evolution with the density ratio and keeping fixed the dimensionless numbers: $Pr = 1.022$, $Re_{x_L} = 85.7226$ and $Ja = 3.69$.

Figure A.4: Evolution of the coefficient $\alpha(Re_{x_L}, Pr, Ja, \frac{\rho_l}{\rho_v})$ for $x > x_L$ - Vaporization configuration.

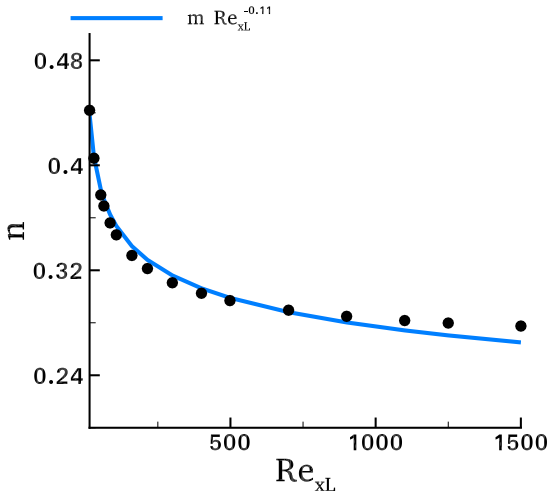

(a) Evolution with the Reynolds number and keeping fixed the dimensionless numbers: $Pr = 1.022$, $Ja = 3.69$ and $\frac{\rho_l}{\rho_v} = 17.746$. // $m(Pr, Ja, \frac{\rho_l}{\rho_v}) = 0.5879$.

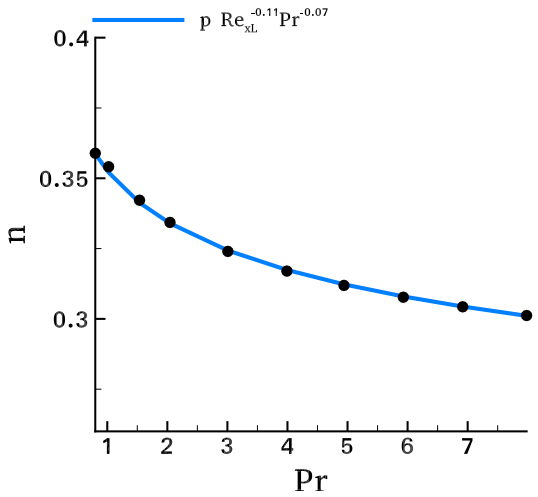

(b) Evolution with the Prandtl number and keeping fixed the dimensionless numbers: $Re_{x_L} = 85.7226$, $Ja = 3.69$ and $\frac{\rho_l}{\rho_v} = 17.746$. // $p(Ja, \frac{\rho_l}{\rho_v}) = 0.5739$.

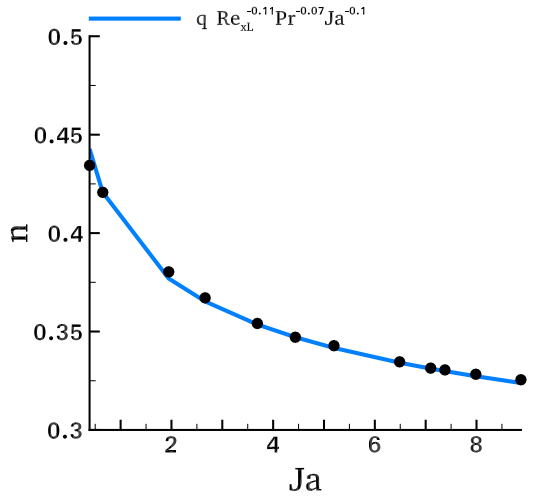

(c) Evolution with the Jakob number and keeping fixed the dimensionless numbers: $Pr = 1.022$, $Re_{x_L} = 85.7226$ and $\frac{\rho_l}{\rho_v} = 17.746$. // $q(\frac{\rho_l}{\rho_v}) = 0.6567$.

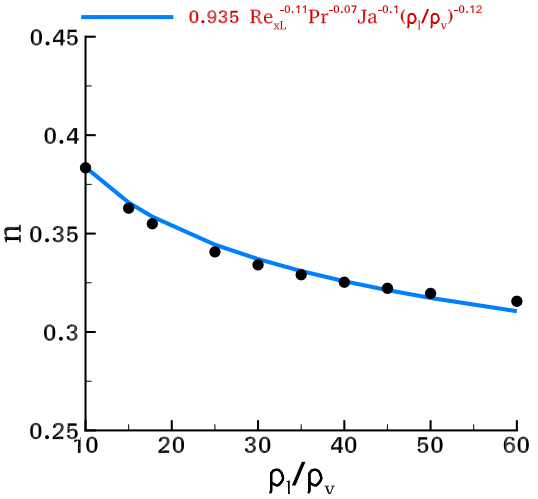

(d) Evolution with the density ratio and keeping fixed the dimensionless numbers: $Pr = 1.022$, $Re_{x_L} = 85.7226$ and $Ja = 3.69$.

Figure A.5: Evolution of the parameter $n(Re_{x_L}, Pr, Ja, \frac{\rho_l}{\rho_v})$ for $x > x_L$ - Vaporization configuration.

Appendix B

Inlet plane statistics obtained using the SEM

B.1 Time convergence

We present here the study of temporal convergence for the turbulent statistics, for each configuration presented in table 3.5, section 3.4. Figure B.1 shows the evolution of the inlet plane statistics with the wall coordinate y^+ for a mesh grid $64 \times 64 \times 64$ and different values of the number of eddies in the virtual box, an this for different times of simulation. The same is done for the mesh grid $128 \times 128 \times 128$ (figure B.2) and $128 \times 64 \times 128$ (figure B.3).

For all mesh grids, depending upon the number of eddies employed in the virtual box, the time of convergence is not the same.

B.2 Modified SEM

Figure B.4 shows the evolution of the inlet plane statistics with the wall coordinate, obtained using the modified SEM, proposed by Pamies *et al.* [72]. The computational domain is $(3.6 \times 3.6 \times 3.6\times)\delta_{inlt}$ and the mesh grid is $256 \times 256 \times 256$. As can be observed, we were not able to obtain the corect profiles in the inner zone of the boundary layer.

B.3 Comparaison on the obtained inlet statistics when different boundary conditions are used

In figure B.5 we have plotted the evolution of the inlet plane statistics with the wall coordinate y^+ for two configurations: the one used for the study on the inlet plane statistics, presented in table 3.5 as (C.1.1) and the one used for the numerical simulation of a spatially evolving boundary layer flow presented in section 3.5. It can be observed that the modification on the free-stream boundary conditions (from Neumann condition to an outflow condition) and the modification on the pressure condition at the outflow plane (from a Dirichlet condition to a Neumann condition) does not influence the evolution of the statistics at the inlet plane.

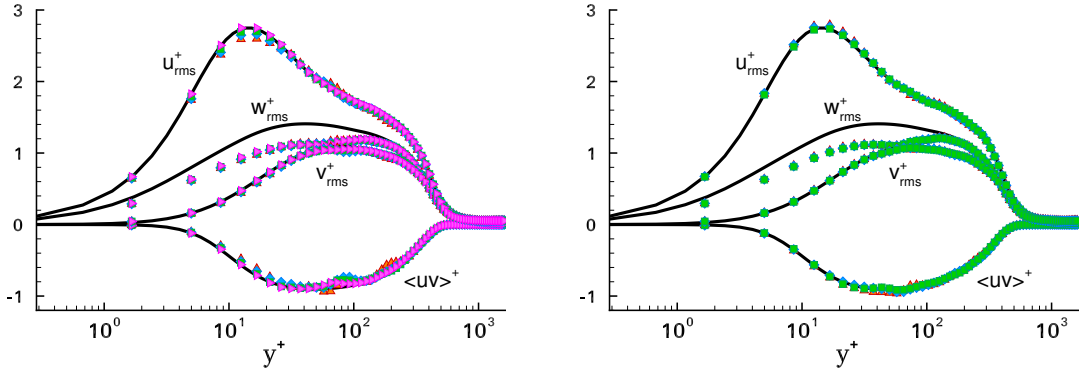

(a) $N = 4000$

(b) $N = 8000$

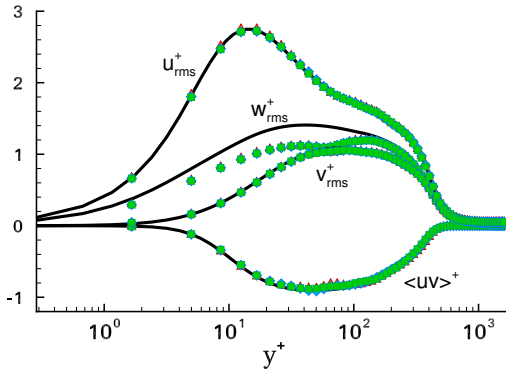

(c) $N = 16000$

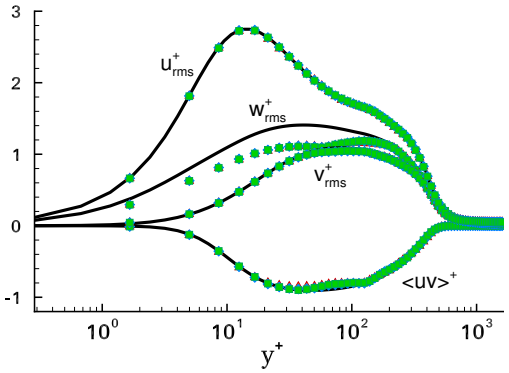

(d) $N = 40000$

Figure B.1: Time convergence for the turbulent statistics at the inlet plane $x = 0$, for a mesh grid $64 \times 64 \times 64$ (configuration (C.1) from table 3.5, section 3.4). (black line) - Jimenez data [40]; (▲) - $T_{cv} = 120\ s$; (◆) - $T_{cv} = 240\ s$; (■) - $T_{cv} = 480\ s$; (▶) - $T_{cv} = 960\ s$.

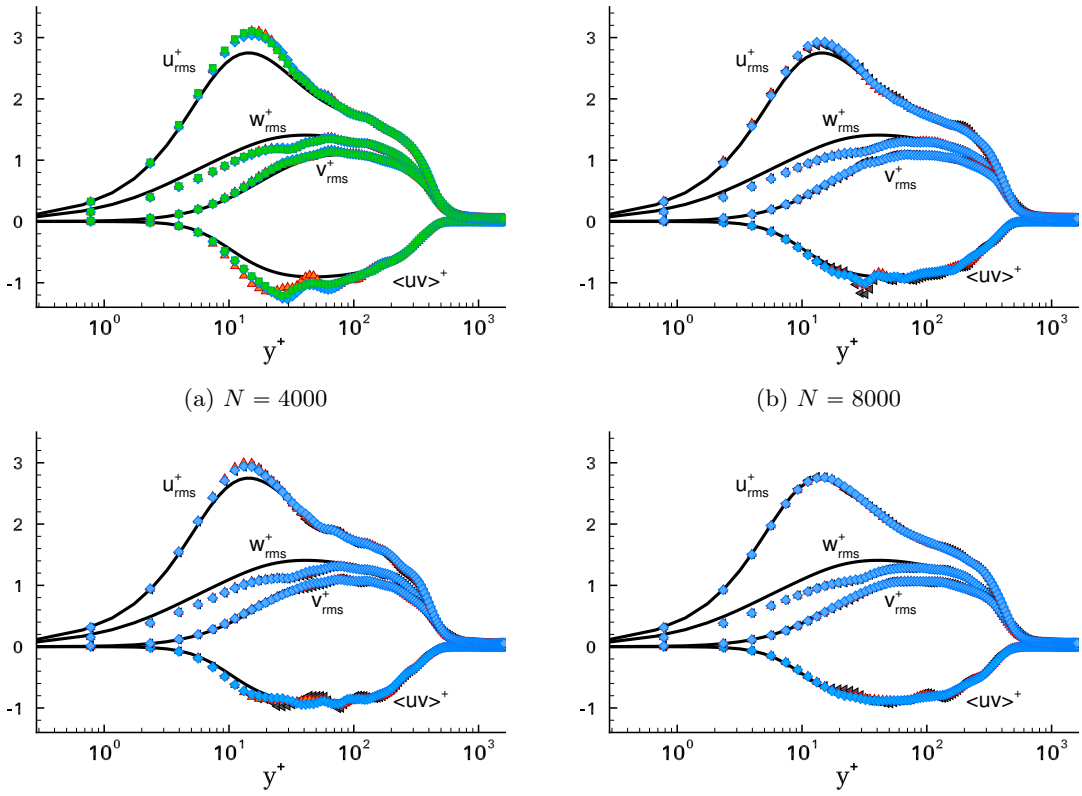

(a) $N = 4000$ (b) $N = 8000$

(c) $N = 16000$ (d) $N = 40000$

Figure B.2: Time convergence for the turbulent statistics at the inlet plane $x = 0$, for a mesh grid $128 \times 128 \times 128$ (configuration (C.2) from table 3.5, section 3.4). (black line) - Jimenez data [40]; (◀) - $T_{cv} = 60\ s$; (▲) - $T_{cv} = 120\ s$; (◆) - $T_{cv} = 240\ s$; (■) - $T_{cv} = 480\ s$;

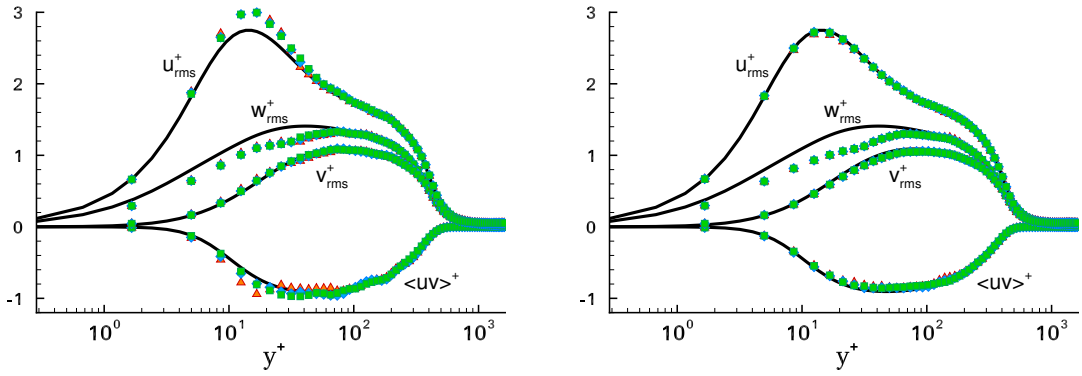

(a) $N = 4000$ (b) $N = 40000$

Figure B.3: Time convergence for the turbulent statistics at the inlet plane $x = 0$, for a mesh grid $128 \times 64 \times 128$ (configuration (C.3) from table 3.5, section 3.4). (black line) - Jimenez data [40]; (▲) - $T_{cv} = 120\ s$; (◆) - $T_{cv} = 240\ s$; (■) - $T_{cv} = 480\ s$;

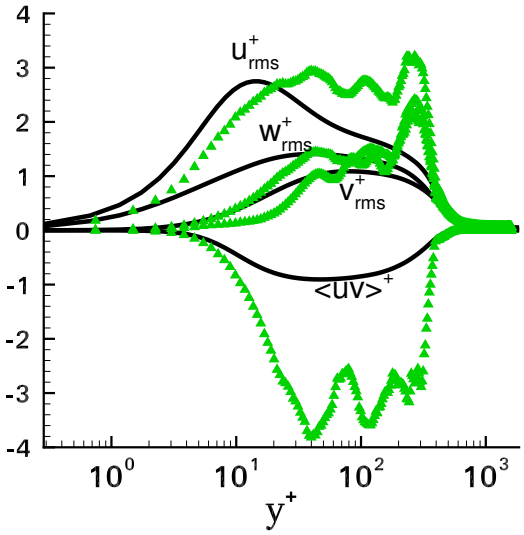

Figure B.4: Inlet plane statistics evolution with the wall coordinate obtained using the modified SEM, proposed by Pamies *et al.* [72]. (black line) - Jimenez data [40]; (▲) - the obtained profiles.

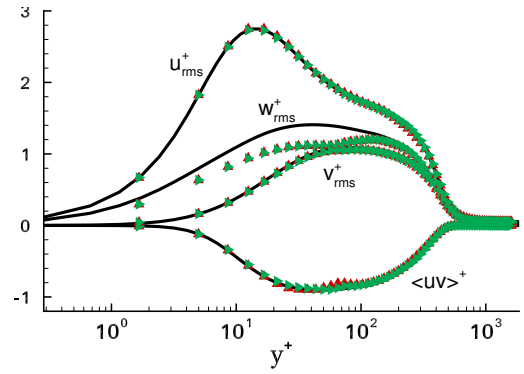

Figure B.5: Inlet plane statistics evolution with the wall coordinate. Comparaison between the computational configuration (C.1.1) from table3.5 and the present configuration, in regard to the changes in the employed boundary conditions. Each curve is plotted after the corresponding T_{cv}. (black line) - Jimenez data [40]; (▲) - (C.1.1); (▶) - present configuration.

Appendix C

Turbulent boundary layer interaction with liquid/vapor phase change

C.1 Time convergence

In figure C.1 are plotted the evolutions of the rms quantities for different time of simulation. Note that we have excluded $T = 120\ s$ of simulation before begining the time convergence. Two configurations are shown here, for $Ja = 0.08$ and $Ja = 14$, with the mesh grid $512 \times 128 \times 128$.

It can be seen that we obtain convergence after $T = 120\ s$.

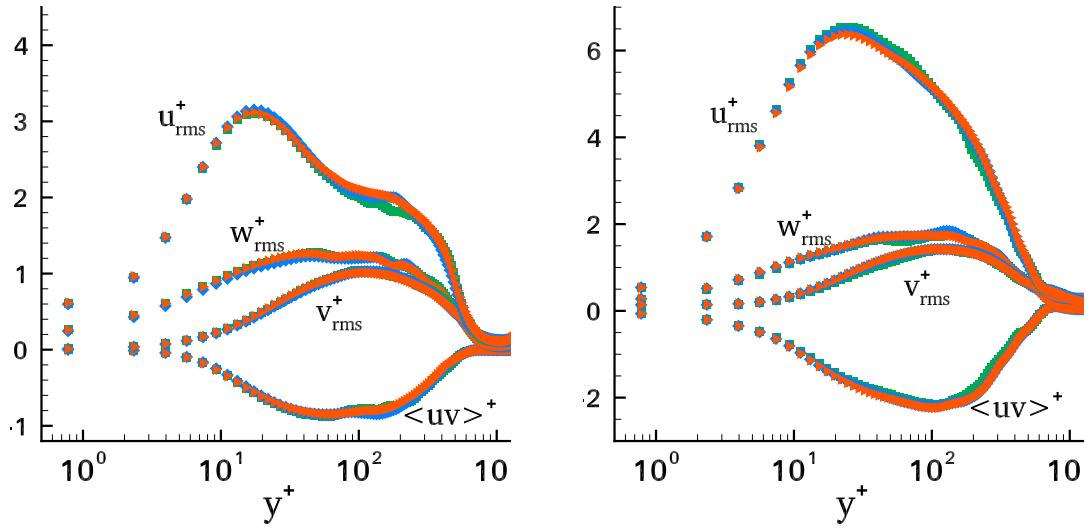

(a) $Ja = 0.088$ (b) $Ja = 14$

Figure C.1: Time convergence for the turbulent statistics, for a mesh grid $512 \times 128 \times 128$. (■) - $T_{cv} = 30\ s$; (◆) - $T_{cv} = 60\ s$; (▶) - $T_{cv} = 120\ s$;

C.2 Mesh grid influence

We show here the influence of the mesh grid onto the obtained turbulent quantities. Two mesh grids are employed, $256 \times 64 \times 64$ and $512 \times 128 \times 128$. Only the two extreme values of the Jakob

number are here shown, $Ja = 0.08$ and $Ja = 14$.

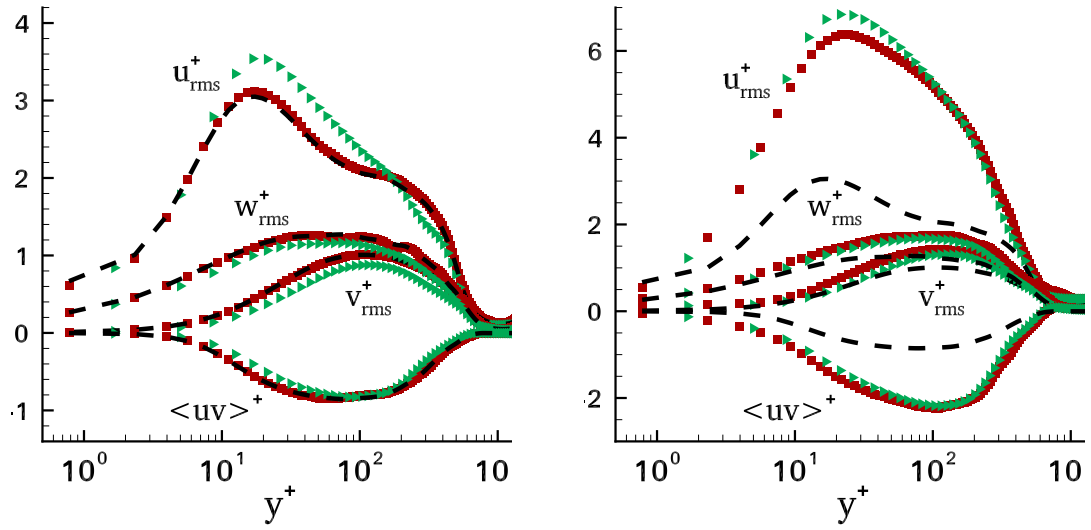

(a) $Ja = 0.088$ (b) $Ja = 14$

Figure C.2: Influence of the mesh grid onto the evolution of the rms quantities. (▶) - $256 \times 64 \times 64$; (■) $512 \times 128 \times 128$; (dashed line) - without phase change with the mesh $512 \times 128 \times 128$.

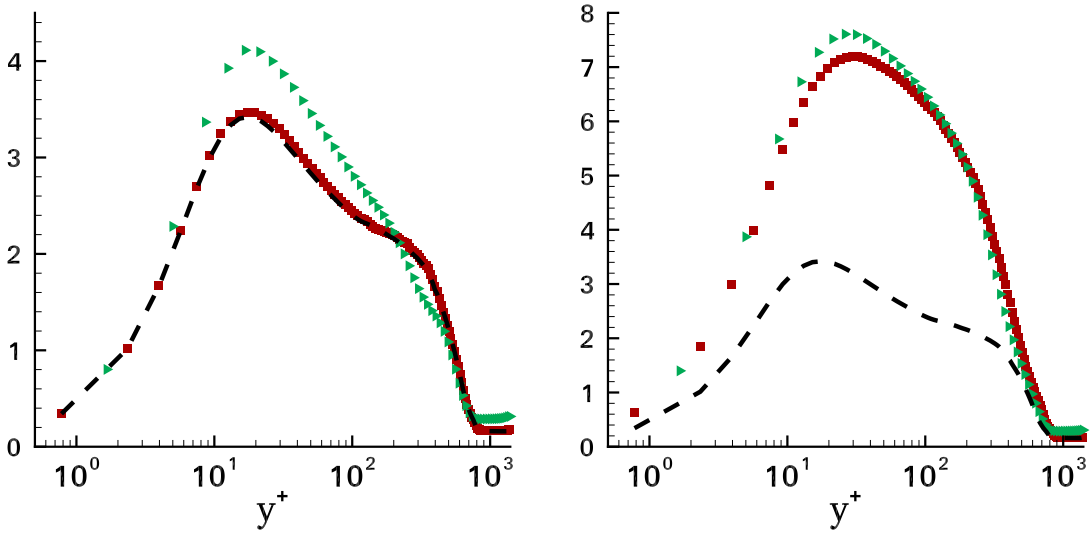

(a) $Ja = 0.088$ (b) $Ja = 14$

Figure C.3: Influence of the mesh grid onto the evolution of the rms temperature. (▶) - $256 \times 64 \times 64$; (■) $512 \times 128 \times 128$; (dashed line) - without phase change with the mesh $512 \times 128 \times 128$.

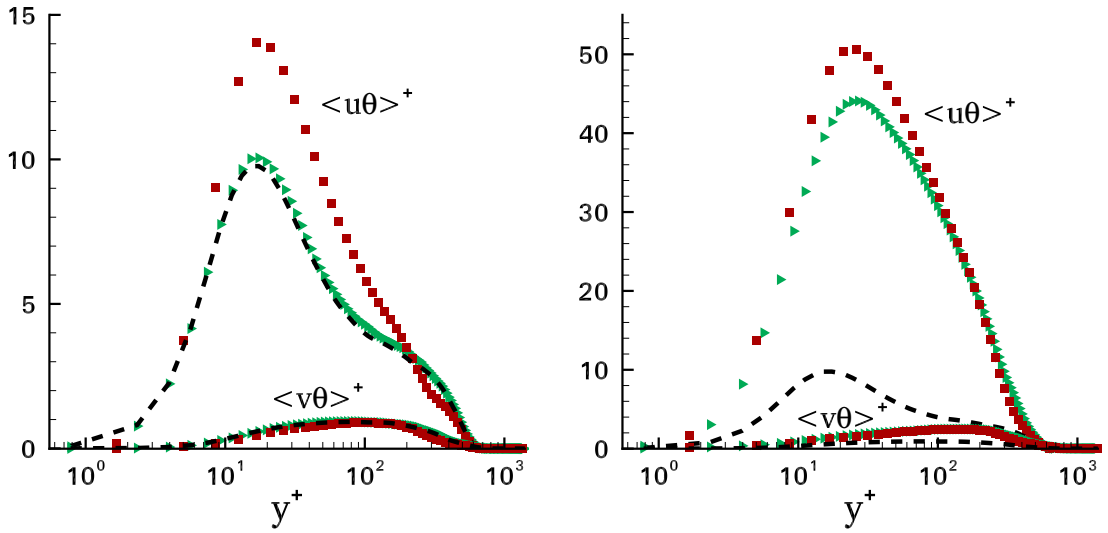

(a) $Ja = 0.088$ (b) $Ja = 14$

Figure C.4: Influence of the mesh grid onto the evolution of the heat fluxes. (▶) - $256 \times 64 \times 64$; (■) $512 \times 128 \times 128$; (dashed line) - without phase change with the mesh $512 \times 128 \times 128$.

Appendix D

Research paper: On the influence of liquid/vapor phase change onto the Nusselt number of a laminar superheated or subcooled vapor flow

International Journal of Thermal Sciences 140 (2019) 397–412

Contents lists available at ScienceDirect

International Journal of Thermal Sciences

journal homepage: www.elsevier.com/locate/ijts

On the influence of liquid/vapor phase change onto the Nusselt number of a laminar superheated or subcooled vapor flow

Elena-Roxana Popescu*, Sébastien Tanguy**, Catherine Colin

Institut de Mécanique des Fluides de Toulouse (IMFT), Université de Toulouse, CNRS, Toulouse, France

ARTICLE INFO

Keywords:
Film vaporization/condensation
Heat transfer
Boundary layer flow
Nusselt number
Friction coefficient

ABSTRACT

Based on a numerical approach, we propose in this study to characterize the interaction between a laminar boundary layer of a superheated or subcooled vapor flow and a static liquid pool at saturation temperature. For the purpose of this study, we define a canonical configuration that will help to improve our physical understanding of the interaction between a laminar flow and vaporization or condensation. By performing a full set of simulations sweeping the parameters space, correlations are proposed for the first time on the Nusselt number depending on the dimensionless numbers (the Reynolds number, the Prandtl number, the Jakob number and the density ratio) that characterize both vaporization and condensation. As attended, the Nusselt number decreases or increases in the configurations involving vaporization or condensation respectively. For high Jakob number, opposite trends are observed depending whether if vaporization or condensation is considered. Indeed a saturation of the heat flux happens in the first case, whereas a self-amplification of the heat flux occurs in the second one. Since the Nusselt number expressions are known, analytical expressions for the integrated heat flux exchanged at the liquid/vapor interface can be determined. Our study also takes interest to the behaviour of the viscous friction of the vapor flow on the liquid pool, which is weakly affected by the phase change, despite the important variation of the local flow structure due to evaporation or condensation. The physical mechanisms inducing all these phenomena are here discussed and clarified.

1. Introduction

There is currently little information on how an external flow will modify evaporation or condensation of a liquid plane surface in spite of its significant interest in various fields, such as processes in thermal engineering, in combustion applications, weather forecasting or climate modeling. Most applications cited above involve turbulent flows and gas mixture. Nevertheless, the simpler configuration where a laminar superheated or subcooled vapor flow is shearing a saturated liquid interface has still never been solved whether theoretical, numerical or experimental approaches are considered. This would be a significant step forward before considering more complex configurations. The theory of an expanding laminar boundary layer of a fluid above a solid plate, known as the Blasius theory [1], has been generalized to account for heat transfer between the fluid and an isothermal plate by Pohlhausen in Ref. [21]. Both theories are based on a boundary layer hypothesis assuming that the velocity component in the streamwise direction is much higher than the one in the normal direction to the plate. However, when one considers an expanding boundary layer of a superheated or subcooled vapor flow over a saturated liquid, the latter assumption is no longer valid due to the phase change vapor flow that will respectively blow or aspirate the boundary layer, depending on whether vaporization or condensation occurs. The mathematical complexity of this problem being strongly increased, the resulting flow will exhibit a fully two-dimensional rotational structure for which a classical theoretical analysis can hardly be practiced. Consequently, using fully resolved numerical simulation is a promising alternative for tackling such a problem in order to improve our knowledge in the field of heat transfer in liquid-vapor flow with phase change. Phase change heat transfer, treated using the so-called conception of the two-phase boundary layer, has been a subject of study in several papers. For example, Koh et al. made an analysis of a saturated vapor in a forced-convection flow over a flat plate in Ref. [12] and a vertical plate in Ref. [13]. The configuration with film boiling was studied for a forced-convection flow by Cess and Sparrow in Ref. [4] and for a free-convection flow by Kaneyasu and Takehiro in Ref. [11]. Turkyilmazoglu in Ref. [32] studies the traditional Stefan problems concerning solidification or liquidisation phenomena of a phase changing bar. Regarding

* Corresponding author.
** Corresponding author.
E-mail addresses: epopescu@imft.fr (E.-R. Popescu), tanguy@imft.fr (S. Tanguy).

https://doi.org/10.1016/j.ijthermalsci.2019.02.046
Received 26 September 2018; Received in revised form 5 February 2019; Accepted 28 February 2019

the interaction between liquid-vapor phase change and two-phase flows, since the seminal works of Renksizbulut and Yuen [23,24], where correlations on Nusselt number and drag coefficient of evaporating droplets have been designed, a few studies have been dedicated to fully characterize other configurations.

Scriven [27] has proposed 1D theory of bubble growth involving an induced phase change flow motion (radial and irrotational flow). In the context of bubble growth, Ruckenstein and Davis [25] have developed a theoretical study where the external flow is approximated by a potential flow. Nevertheless, rotational effects can have influence both on the viscous friction and the heat flux as it is the case in the present study.

In this paper, we present a numerical study to characterize the interaction between a superheated or subcooled external laminar vapor flow shearing a static and plane liquid pool at saturation temperature. The Blasius-Pohlhausen theory of an expanding laminar boundary layer over an isothermal plate can be considered as a reference solution. Our purpose was to find, for this configuration, a correlation on the Nusselt number accounting for the modification of the local thermal gradient on the interface due to the vaporization or condensation induced flow. As the local structure of the flow is also modified in the vicinity of the liquid-vapor interface, our study includes an analysis on the interfacial viscous friction when phase change occurs.

To the best of our knowledge, the study on the interaction between an external vapor flow and the liquid/vapor phase change of a liquid pool has never been conducted before in the proposed configuration. In addition to its academic interest, this study could also be relevant in more industrial configurations, as for example in space applications. In launchers fuel tanks, the pressure regularization is done by injecting vapor jets above a liquid plane. It is of utmost importance to predict the vaporization or condensation mass flow rate in such a configuration. A solution is to solve the flow only on a small region close to the liquid/vapor interface and obtain local laws on the heat flux that could be used as a closure model in larger scale approaches.

2. Numerical methods for the direct numerical simulation

2.1. Mathematical formulation

The model used to compute the process of heat transfer with phase change is identical to one described in Refs. [10,31], where the liquid and the vapor phases are supposed incompressible and monocomponent. It is assumed that the fluid densities and the thermophysical properties in each phase are spatially uniform. Therefore, the mathematical formulation of the two-phase incompressible flow is:

$$\nabla\cdot\mathbf{V} = 0, \tag{1}$$

$$\rho\frac{D\mathbf{V}}{Dt} = -\nabla p + \nabla\cdot(2\mu\mathbf{D}) + \rho\mathbf{g}. \tag{2}$$

where $\mathbf{V}$ is the velocity field, p is the pression field, ρ is the density, μ is the dynamic viscosity, $\mathbf{D}$ is the deformation tensor and $\mathbf{g}$ is the gravity acceleration.

The thermal field is computed by solving a simplified conservation energy equation, formulated using the enthalpy primitive variable:

$$\rho C_p\left(\frac{DT}{Dt}\right) = \nabla\cdot(k\nabla T), \tag{3}$$

where T is the thermal field, C_p is the specific heat at constant pressure and k is the thermal conductivity.

The governing equations are formulated in a “Jump Condition Form”, meaning that the field equations are written in each phase separately and additional jump conditions have to be imposed at the interface to maintain the conservation of mass (Eq. (4)), momentum (Eq. (5)) and energy (Eq. (6)). The movement of expansion or suction in the vapor, depending on whether vaporization or condensation occurs, is directly related to the phase change mass flow rate,

$$[\mathbf{V}]_\Gamma = \dot{m}\left[\frac{1}{\rho}\right]_\Gamma\mathbf{n}. \tag{4}$$

Because of the interface motion, momentum in the direction of the unit normal vector $\mathbf{n}$ is convected at the relative velocity of the fluid with respect to the interface. Including the effects of the pressure and surface tension forces, the momentum balance normal to the interface writes

$$[p]_\Gamma = \sigma\kappa + 2\left[\mu\frac{\partial V_n}{\partial n}\right]_\Gamma - \dot{m}^2\left[\frac{1}{\rho}\right]_\Gamma. \tag{5}$$

Finally, the balance of energy at the interface translates that the thermal flux exchanged at the interface depends on the energy released or absorbed in the process of phase change,

$$[-k\nabla T\cdot\mathbf{n}]_\Gamma = \dot{m}L, \tag{6}$$

with σ the surface tension, κ the local interface curvature, $\mathbf{n}$ the normal vector at the interface pointing towards the liquid phase, L the latent heat of vaporization, $\dot{m}$ the phase change rate and $\frac{\partial V_n}{\partial n}$ the normal derivative of the normal velocity component. The operator $[\cdot]_\Gamma$ accounts for the jump across the interface Γ and it is defined by: $[f]_\Gamma = f_{vap} - f_{liq}$.

The formalism to deduce the jump equations (4)–(6) is described in Appendix A (see Refs. [7,8,19]).

As in this paper we consider a plane interface, simulations results do not depend on surface tension due to zero interface curvature. Moreover, according to the second law of thermodynamics and assuming that the local equilibrium hypothesis is still valid, the interface temperature is imposed at the saturation temperature. This assumption is thermodynamically consistent with a pure liquid/vapor system, see for instance the following reference [3].

2.2. Numerical methods

In this section, the methods used in our numerical study are presented. The dimensional Navier Stokes equations (1)–(6) are solved for a steady incompressible two-phase flow in a two-dimensional domain.

Thermal field is computed by solving the simplified conservation energy Eq. (3). As the liquid-gas interface is not boundary fitted with computational grid, the suitable jump conditions can be imposed across the interface following the general guidelines of the Ghost Fluid Method [6] to maintain the conservation of mass [19,30] and energy [7,8,31]. That is made possible by using the subgrid location of the interface with a static Level Set function whose zero level curve represents the interface [20]. Spatial derivatives are computed with fifth order WENO-Z schemes [2]. A Black-Box MultiGrid solver [5] is used to solve the pressure Poisson equation and we perform an implicit temporal discretization of the viscous terms as presented in Refs. [15,16]. The system of unsteady equations is solved until reaching a steady state by using a second order TVD Runge-Kutta scheme for the temporal integration.

As the interface temperature is constant and continuous across the interface, the following algorithm, named GFTSB (Ghost Fluid Thermal Solver for Boiling) in Refs. [31,34], has been designed in Ref. [7] to solve the heat transfer around the interface when phase change occurs. The scheme used for solving the energy equation is given by

$$\frac{T^{n+1}-T^n}{\Delta t} + \mathbf{u}^n\cdot\nabla T^n = \nabla\cdot(k\nabla T^{n+1}) \tag{7}$$

First, solve the temperature field in the liquid domain with a prescribed Dirichlet boundary condition at the interface

$$\begin{aligned}&\rho_l C_{p_l} T_l^{n+1} - \Delta t\nabla\cdot(k_l\nabla T_l^{n+1}) = \rho_l C_{p_l}(T_l^n - \Delta t\mathbf{u}_l^n\cdot\nabla T_l^n), \text{ if } \phi > 0\\ &T|_\Gamma = T_{sat}\end{aligned} \tag{8}$$

with ϕ the Level Set function. Next, solve the temperature field in the vapor domain with the same prescribed Dirichlet boundary condition at

the interface

$$\rho_v C_{p_v} T_v^{n+1} - \Delta t \nabla\cdot(k_v \nabla T_v^{n+1}) = \rho_v C_{p_v} (T_v^n - \Delta t \mathbf{u}_v^n \cdot \nabla T_v^n), \text{ if } \phi < 0$$
$$T|_\Gamma = T_{sat} \quad (9)$$

Once the temperature field has been computed, the local mass flow rate can be easily deduced from

$$\dot{m} = \frac{[-k\nabla T\cdot\mathbf{n}]_\Gamma}{L_{vap}} \quad (10)$$

Given that the temperature field in the liquid is uniform and equal to the saturation temperature, the thermal flux in the liquid phase is zero. The local mass flow rate depends therefore only on the thermal flux in the vapor phase. This formalism allows switching naturally from vaporization to condensation depending only on the sign of the thermal gradient. Indeed, if the vapor is superheated $\dot{m}$ is positive and this leads to a blowing effect in the vapor phase. On the other hand, if the vapor is subcooled, $\dot{m}$ becomes negative which generates an aspirating flow towards the interface.

Our in house code, *DIVA*, has been extensively validated with theoretical solutions [9,31,34] and with experimental data whether Nucleate Boiling [10,33] or Leidenfrost Droplet [26] is considered. Successful comparisons between numerical simulations and experimental data in Ref. [29] for droplets collisions or in Ref. [14] for oscillations of rising bubbles or droplets have also been reported.

3. Computational configuration of numerical simulations

3.1. Initialization and boundary conditions

We consider here the canonical configuration of an expanding Blasius-Pohlhausen boundary layer interacting with a saturated and static liquid pool. Our aim is to investigate the influence of the external flow on the local heat flux, for an improved knowledge on the interaction between liquid/vapor phase change and fluid mechanics. Even though each different industrial system would require a specific quantitative study, there is a strong interest in understanding local mechanisms in academic configurations. A possible experimental set-up representative of our computations is illustrated in Fig. 1.

The actual computational domain implemented in our simulations is the liquid/vapor domain (for $x \geq x_L$). The interface has a plane shape, which corresponds to the asymptotic case of a high Weber number (high surface tension value). The vapor stream is flowing in the upper part of the domain over a static saturated liquid pool located in the lower part of the computational domain. An inflow boundary condition is used on the left of the domain for the injection of the superheated or subcooled vapor flow. Given that the purpose of this work is to study the influence of the liquid/vapor phase change on an expanding Blasius-Pohlhausen boundary layer, a boundary layer thickness δ_{x_L} has to be imposed at the inlet of the domain. This boundary layer thickness depends on the length of the solid plate, defined as x_L on the schematics in Fig. 1. It should be emphasized that the results of the present study will directly depend on the inlet boundary layer thickness δ_{x_L}. Such a

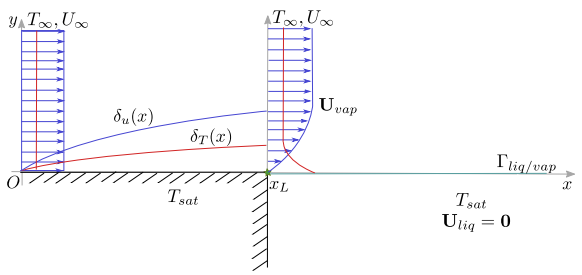

Fig. 1. Schematics of the expanding Blasius-Pohlhausen boundary layer interacting with a saturated and static liquid pool.

dependence on the boundary layer thickness is classical in Fluid Mechanics and has been observed for various type of flows as reported in Refs. [17,18] in the framework of primary atomization, for instance.

Velocity and temperature inflow profiles are computed by solving respectively the Prandtl [22] and the Pohlhausen [21] boundary layer equations:

$$f'''(\eta) + \frac{1}{2} f(\eta) f'(\eta) = 0, \quad (11)$$

and

$$\theta''(\eta) + \frac{Pr}{2} f(\eta)\theta'(\eta) = 0 \quad (12)$$

where $f = \frac{u}{U_\infty}$ and $\theta = \frac{T - T_{sat}}{\Delta T}$ are the normalized stream function and the non-dimensional temperature, respectively; ΔT is the thermal gradient. The boundary conditions are: $\eta = 0$: $f = 0, f' = 0$; $\eta \to \infty$: $f' = 1$ for Eq. (11) and $\eta = 0$: $\theta = 0$; $\eta \to \infty$: $\theta = 1$ for Eq. (12). We recall that $\eta \sim \frac{y}{\delta}$ is the dimensionless variable, $\delta \sim \sqrt{\frac{\nu x}{U_\infty}}$ is the boundary layer thickness, $Pr = \frac{\mu C_p}{k}$ is the Prandtl number.

Free-boundary condition is used on top and on the right of the computational domain, in order to avoid containment effects and to maintain isobaric conditions.

As the aim of this work is to characterize a steady solution of the interaction between an external flow and a static liquid pool, it is considered that the interface position is fixed in time in order to maintain a constant liquid height in the computational domain. This assumption is fitting with the schematics of a possible experimental set-up proposed in Fig. 1, if one considers an additional device that allows maintaining a constant liquid level in the liquid pool. Unlike boiling, stationary hypothesis is a classical approximation [28] when considering the evaporation of a liquid (as droplet evaporation for instance) interacting with a superheated vapor since the velocity of the vapor flow is much higher than the interface speed regression.

Moreover, it has been verified that for viscosity ratios $\frac{\mu_{liq}}{\mu_{vap}} \in [2,56]$ the liquid motion due to the shear stress of the vapor flow on the interface can be neglected in our configurations. Consequently, only the velocity jump condition due to phase change will interact with the external flow. However, such a configuration is consistent with the static liquid hypothesis only if one assumes a sufficiently high density ratio, since the ratio between the interface velocity and the vapor velocity on the interface is close to the density ratio.

The velocity and thermal field are initialized, in the whole domain, with the Blasius-Pohlhausen dynamic and thermal boundary layer profiles, respectively.

3.2. Computational domain and mesh grid

To avoid the thermal singularity on the phase change mass flow rate at the inlet plane, we assume that the vapor flow has traveled a distance x_L over an isothermal solid plate before contacting the liquid pool (Fig. 2 and Fig. 3). Consequently, the boundary layer thickness of the vapor inlet flow depends on this distance x_L that can be accounted for in our dimensionless analysis by defining an inlet Reynolds number Re_{x_L}, such as $Re_{x_L} = \frac{\rho_v U_\infty x_L}{\mu_v}$. The dimensions of the computational domain are (l_x, l_y) with $l_x = 6.7\delta_{x_L}$, $\delta_{x_L} = min(\delta_u, \delta_T)$ where $\delta_u = 4.92\frac{x_L}{\sqrt{Re_{x_L}}}$ and $\delta_T = \delta_u Pr^{-\frac{1}{3}}$ are the dynamic and the thermal boundary layers, respectively. Our interest is to compute the spatial development of the thermal and dynamical boundary layers over the saturated liquid pool. A study on containment effects allowed showing that, for the vaporization configuration, the dimension in the normal direction has to be $l_y = 2l_x$, while, in the condensation configuration, $l_y = l_x$ is sufficient to ensure that the numerical solutions do not depend on the computational domain size. That can be explained considering that the vaporization has a "blowing" effect on the boundary layer and so a larger

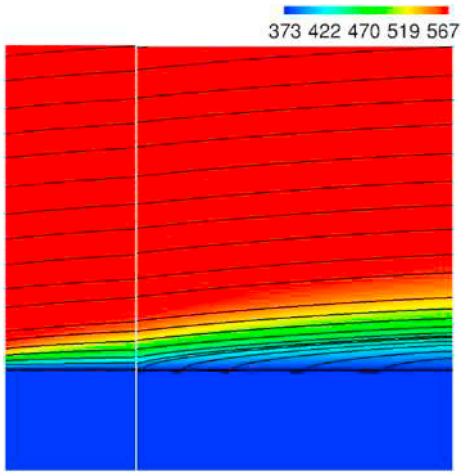

Fig. 2. Streamlines and temperature profile [K] of a liquid pool evaporating in an superheated gas flow for $Pr = 0.98$, $Re_{x_L} = 211$, $\frac{\rho_l}{\rho_v} = 1623$, $Ja_{vap} = 7.38$; left - classic Blasius boundary layer, right - the boundary layer blown by the vaporization.

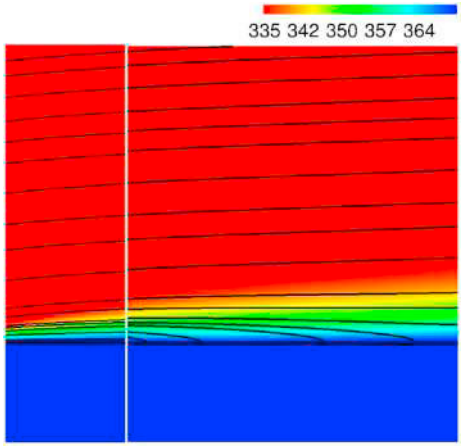

Fig. 3. Streamlines and temperature profile [K] of a subcooled gas flow condensating in the liquid pool. for $Pr = 0.98$, $Re_{x_L} = 211$, $\frac{\rho_l}{\rho_v} = 1623$, $Ja_{cond} = 0.74$; left - classic Blasius boundary layer, right - the boundary layer "aspirated" by the condensation.

domain in the y-direction is needed to assure that the development of the boundary layer is not affected by the upper boundary condition. Unlike vaporization, condensation aspirates the boundary layer, so containement effects have smaller influence on its spatial development.

Even though the present parametric study has been conducted using the computation configuration presented in Section 3.1., some additional verifications have been done to ensure that the upstream containment effects do not have a significant influence on the Nusselt number evolution (Fig. B.16 in B).

A convergence study with different mesh grids has been carried out for both configurations, for a couple of liquid/vapor defined by the following dimensionless numbers: $Pr = 1.022$, $Re_{x_L} = 85.726$, $\frac{\rho_l}{\rho_v} = 17.746$, and two different values for the Jakob number: $Ja_{vap} = 3.69$ and $Ja_{vap} = 8.87$ for the vaporization and $Ja_{cond} = 0.37$ and $Ja_{cond} = 1.15$ for the condensation. The dimensionless numbers are defined as it follows: $Re_x = \frac{\rho_v U_\infty x}{\mu_v}$, , $Ja_{vap} = \frac{C_{p_v}(T_\infty - T_{sat})}{L}$ and $Ja_{cond} = \frac{C_{p_v}(T_{sat} - T_\infty)}{L}$. The subscript '$v$' is for vapor and '$l$' is for liquid, μ is the viscosity, C_{p_v} is the specific heat, k is the thermal conductivity, $T_v - T_{sat}$ is the thermal gradient and U_∞ is the velocity in the uniform zone outside the boundary layer.

The local dimensionless coefficient of heat transfer, known also as the local Nusselt number, is defined as

$$Nu_x = \frac{hx}{k} = \frac{\phi_I x}{k(T_I - T_\infty)}, \tag{13}$$

where h is the convective heat transfer coefficient, ϕ_I is the local heat flux at the liquid/vapor interface and T_I is the liquid/vapor interface temperature, equal to the saturation temperature T_{sat}.

At first glance, the evolution of the Nusselt number seems to be converged with the grid 256×256, for the vaporization (Fig. 4) and with the grid 128×128 for the condensation configuration (Fig. 5). Nevertheless, the velocity jump at $x = x_L$ from a single-phase boundary layer flow to a phase change boundary layer flow has to be captured and well resolved. As one of the objectives of this numerical study is to define correlations on the Nusselt number, high accuracy is required. Consequently, the mesh grid 2048×1024 - for the vaporization, and 1024×1024 - for the condensation have been chosen to run the present numerical study. At the inlet, this mesh grid allows to have ~ 150 points in the boundary layer.

Since all the simulations are 2D and reach a steady state, the overall computational cost of one simulation remains moderate even if a very refined grid is considered. This has permitted to perform a full parametric study by varying the four dimensionless numbers characterizing

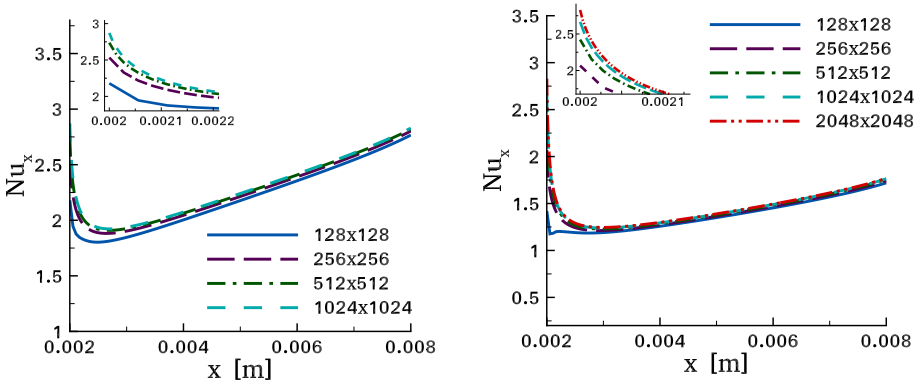

(a) $Ja = 3.69$ (b) $Ja = 8.87$

Fig. 4. Convergence study for the evolution of the Nusselt number for the vaporization configuration, for the dimensionless numbers: $Re_{x_L} = 85.726$, $Pr = 1.022$, $\frac{\rho_l}{\rho_v} = 17.746$.

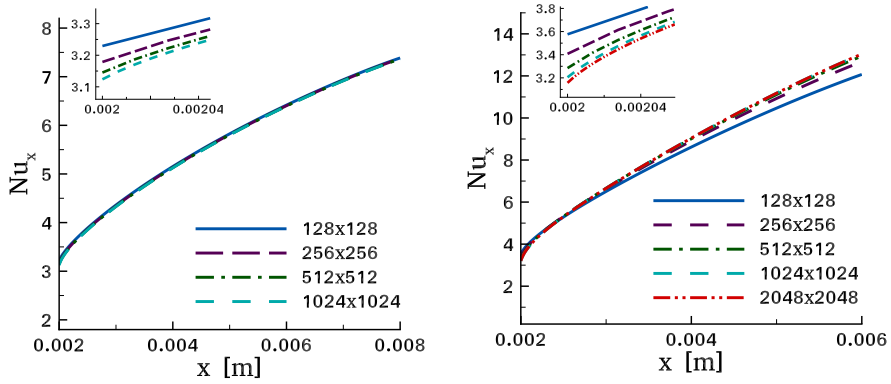

(a) $Ja = 0.37$ (b) $Ja = 1.15$

Fig. 5. Convergence study for the evolution of the Nusselt number for the condensation configuration, for the dimensionless numbers: $Re_{x_L} = 85.726$, $Pr = 1.022$, $\frac{\rho_l}{\rho_v} = 17.746$.

our configuration in a wide range of values. Moreover, solving mass and momentum conservation equations in the liquid field enabled us to assess that neglecting the liquid motion was a correct assumption, for high viscosity ratio.

4. Results and discussion

4.1. Parametric study

A parametric study has been conducted to determine how the Nusselt number is varying with the dimensionless numbers characterizing our configuration. These dimensionless numbers can be extracted from the physical model as: the Reynolds number Re_x from the momentum balance Eq. (2), the Prandtl number Pr from the energy conservation equation Eq. (3), the Jakob number Ja from the balance of energy at the interface Eq. (6) and the density ratio $\frac{\rho_l}{\rho_v}$ from the jump condition on the mass conservation Eq. (4).

The physical variables varied in this parametric study are the velocity U_∞ for the Reynolds number, the thermal conductivity of the vapor k for the Prandtl number, the latent heat L for the Jakob number and the liquid density ρ_l for the density ratio.

The range of values for our parametric study was: $Re_{x_L} = (15; 1250)$, $Pr = (0.6; 8)$, $Ja = (0.00037; 8.87)$ and $\frac{\rho_l}{\rho_v} = (10; 5000)$, with approximately fifty simulations in both configurations.

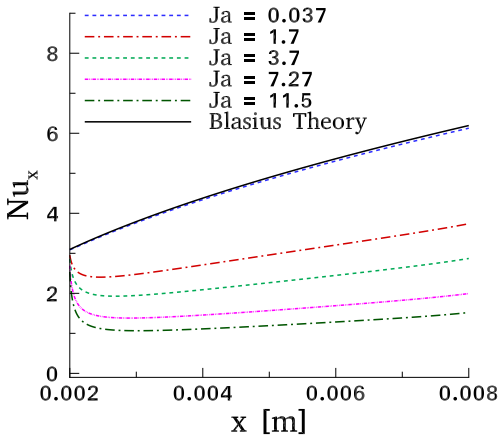

Fig. 6. Spatial evolution of the Nusselt number for different Jakob number for the vaporization configuration; $Pr = 1.022$, $Re_{x_L} = 85.726$, $\frac{\rho_l}{\rho_v} = 17.746$.

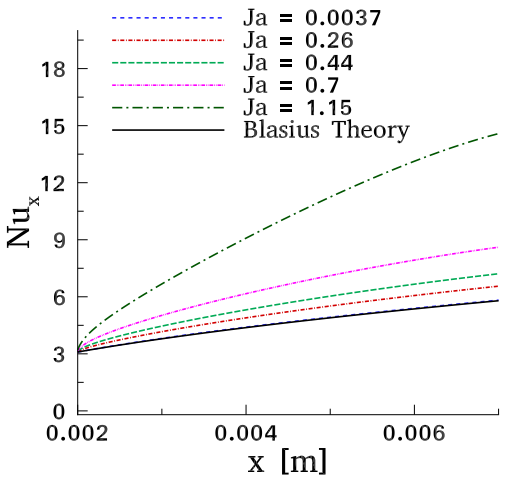

Fig. 7. Spatial evolution of the Nusselt number for different Jakob number for the condensation configuration; $Pr = 1.022$, $Re_{x_L} = 85.726$, $\frac{\rho_l}{\rho_v} = 17.746$.

4.2. The spatial evolution of the Nusselt number

The spatial evolution of the Nusselt number along the longitudinal coordinate x is showed in Fig. 6 for vaporization, and in Fig. 7 for condensation, with a couple of liquid/vapor defined by the following dimensionless numbers: $Pr = 1.022$, $Re_{x_L} = 85.726$, $\frac{\rho_l}{\rho_v} = 17.746$, and different values of Jakob number. One can see that the Nusselt number is lower for vaporization and higher for condensation than the Nusselt number obtained from the Blasius theory. Indeed, as observed in Fig. 2, when vaporization occurs, the thermal boundary layer being thickened due to the expansion flow of vapor, the heat transfer coefficient decreases. The same trend has been observed by Yan and Soong in Ref. [35], where the convective heat and mass transfer along an inclined heated plate with film evaporation have been studied. On the other hand, the condensation involves an aspirating flow towards the liquid/vapor interface, as it can be visualized in Fig. 3. As this flow decreases the thermal boundary layer thickness, the heat transfer coefficient is increased.

For the vaporization, the minimum value observed on the Nusselt number can be related to the rapid decrease of the heat flux in the vicinity of the inlet flow (see Fig. 8). This can be explained by the connecting zone between the Blasius-Pohlhausen expanding boundary layer (for $x < x_L$) and the established flow in interaction with the phase change (for $x >> x_L$).

The influence of the Jakob number on the spatial evolution of the Nusselt number can also be visualized in Figs. 6 and 7. The increase of

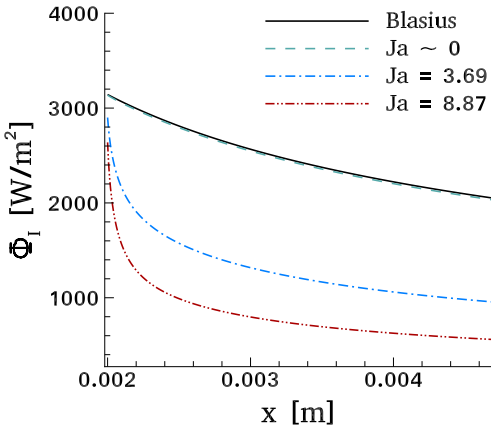

Fig. 8. Vaporization Configuration - Evolution of the local heat flux ϕ_I with the x-axis for the dimensionless numbers: $Pr = 1.022$, $Re_{x_L} = 85.726$, $\frac{\rho_l}{\rho_v} = 17.746$ and different values of Jakob number.

the Jakob number implies an increase of the vapor/liquid phase change and therefore the Nusselt number decreases or increases if vaporization or condensation is respectively concerned, as expected. Figs. 6 and 7 are now compared in regard to the influence of the Jakob number on the Nusselt number evolution. If the Jakob number is doubled and then tripled, in the case of the boundary layer "blown" by the liquid pool vaporization, a decrease of the intervals between the succesives curves is observed, while if the boundary layer is "aspirated" by the condensation, the intervals between the succesives curves increase. These unanticipated results will be further explained, but first, the correlations on the Nusselt number will be presented.

4.3. Correlations on the Nusselt number

By fitting the numerical Nusselt number evolution obtained in all of our simulations, we have found, general correlations that depend on the dimensionless numbers characterizing this configuration. In what follows, the resulting correlations are presented separately for the vaporization and for the condensation. For the sake of simplicity, the approach to find these correlations is described in the Appendix C. Both correlations have been designed by adding correction terms to the Nusselt number from the Blasius theory which is defined as $Nu_x^{Bl} = 0.332 Pr^{0.333} Re_x^{0.5}$.

4.3.1. Vaporization

The correlation for the Nusselt number with vaporization has the following expression

$$Nu_x^{vap} = Nu_x^{Bl} - \left(\alpha\left(\frac{x}{x_L} - 1\right)^n + \beta\right) H(x - x_L), \tag{14}$$

where $H(x - x_L)$ is the Heaviside function who has a non-zero value only for $x > x_L$, α, β and n have the following expressions

$$\alpha = 0.294 Re_{x_L}^{0.495} Pr^{0.333}\left(1 - e^{-0.0248\left(Ja\left(\frac{\rho_l}{\rho_v} - 1\right)\right)}\right),$$

$$n = 0.935 Re_{x_L}^{-0.11} Pr^{-0.07} Ja^{-0.1} \frac{\rho_l}{\rho_v}^{-0.12},$$

$$\beta = 0.119 Re_{x_L}^{0.477} Pr^{0.237}\left(1 - e^{-0.0043 Ja\left(\frac{\rho_l}{\rho_v} - 1\right)}\right),$$

4.3.2. Condensation

In the configuration involving condensation, the correlation on the Nusselt number writes as

Table 1
The average relative error and the maximum relative error for the Nusselt number for different couples of dimensionless numbers.

	Condensation	$\bar{\epsilon}$[%]	ϵ_{max}[%]
C.1	$Pr = 8$, $Re_{x_L} = 85.726$	1.028	1.171
	$Ja = 0.37$, $\frac{\rho_l}{\rho_v} = 17.6$		
C.2	$Pr = 0.98$, $Re_{x_L} = 1250$	0.58	0.75
	$Ja = 0.179$, $\frac{\rho_l}{\rho_v} = 1623$		
C.3	$Pr = 1.022$, $Re_{x_L} = 85.726$	0.65	1.34
	$Ja = 0.7$, $\frac{\rho_l}{\rho_v} = 17.6$		
C.4	$Pr = 0.98$, $Re_{x_L} = 105.51$	0.28	0.32
	$Ja = 0.179$, $\frac{\rho_l}{\rho_v} = 5000$		
C.5	$Pr = 0.98$, $Re_{x_L} = 30$	1.38	1.6
	$Ja = 0.179$, $\frac{\rho_l}{\rho_v} = 1623$		
C.6	$Pr = 6$, $Re_{x_L} = 105.51$	1.69	1.8
	$Ja = 0.179$, $\frac{\rho_l}{\rho_v} = 1623$		
C.7	$Pr = 0.98$, $Re_{x_L} = 105.51$	0.57	0.703
	$Ja = 0.29$, $\frac{\rho_l}{\rho_v} = 1623$		
	Vaporization	$\bar{\epsilon}$[%]	ϵ_{max}[%]
V.1	$Pr = 8$, $Re_{x_L} = 85.726$	1.56	7
	$Ja = 3.69$, $\frac{\rho_l}{\rho_v} = 17.6$		
V.2	$Pr = 0.98$, $Re_{x_L} = 1250$	1.09	1.45
	$Ja = 0.179$, $\frac{\rho_l}{\rho_v} = 1623$		
V.3	$Pr = 1.022$, $Re_{x_L} = 85.726$	2.13	9.4
	$Ja = 8.87$, $\frac{\rho_l}{\rho_v} = 17.6$		
V.4	$Pr = 0.98$, $Re_{x_L} = 105.51$	2.4	2.8
	$Ja = 0.179$, $\frac{\rho_l}{\rho_v} = 3500$		
V.5	$Pr = 1.022$, $Re_{x_L} = 30$	4.8	6
	$Ja = 3.69$, $\frac{\rho_l}{\rho_v} = 17.6$		
V.6	$Pr = 1.022$, $Re_{x_L} = 85.726$	1.8	2.69
	$Ja = 3.69$, $\frac{\rho_l}{\rho_v} = 5$		
V.7	$Pr = 0.98$, $Re_{x_L} = 105.51$	2.17	2.64
	$Ja = 0.3598$, $\frac{\rho_l}{\rho_v} = 1623$		

$$Nu_x^{cond} = Nu_x^{Bl} + \left(\gamma\left(\frac{x}{x_L} - 1\right)^m + \eta\right) H(x - x_L), \tag{15}$$

where γ, η and m have the following expressions

$$\gamma = 0.0854 Re_{x_L}^{0.483} Pr^{0.356}\left(e^{0.1018 Ja\left(\frac{\rho_l}{\rho_v} - 1\right)} - 1\right),$$

$$m = 0.519 Re_{x_L}^{-0.045} Pr^{-0.042} e^{0.02985 Ja \frac{\rho_l}{\rho_v}},$$

$$\eta = 0.00042 Re_{x_L}^{0.426} Pr^{0.55}\left(Ja\left(\frac{\rho_l}{\rho_v} - 1\right)\right)^{1.25}.$$

4.3.3. Validation of the proposed correlations

For the sake of validation of the proposed correlations, we present for various configurations in Table 1, the average relative error $\bar{\epsilon}$ and the maximum relative error ϵ_{max}, between the computed Nusselt number and the correlations, with the relative error defined as: $\epsilon = \frac{Nu_x^{correl} - Nu_x^{num}}{Nu_x^{num}} 100\%$. One can see that the average relative error between the Nusselt number from DNS and the correlation is less than 2% for condensation and less than 5% for vaporization. Comparisons between the proposed correlations and numerical results are also plotted in Fig. 9 for the vaporization and in Fig. 10 for the condensation for different configurations from Table 1.

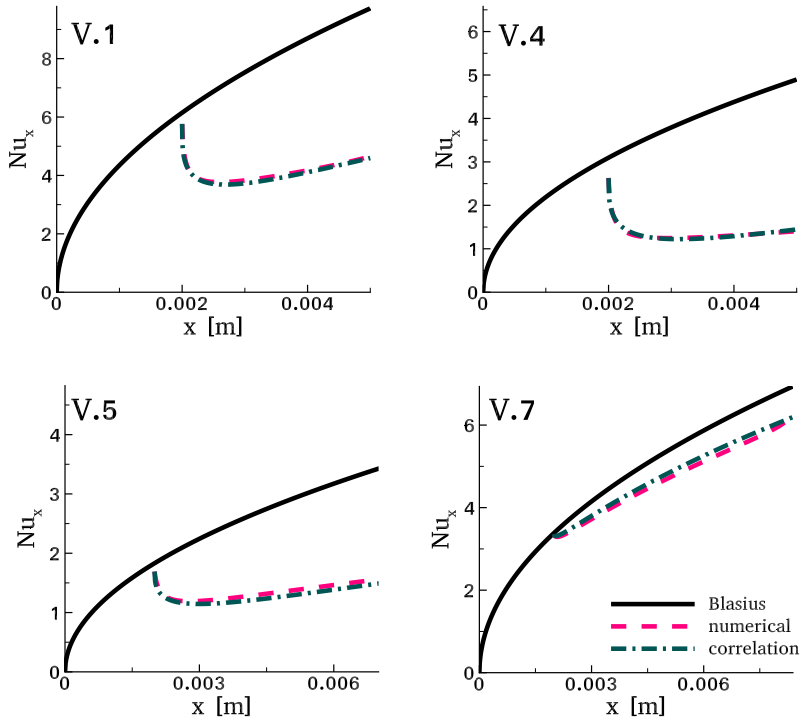

Fig. 9. Spatial evolution of the Nusselt number for different configurations extracted from Table 1 for the case involving vaporization.

4.4. Asymptotic cases

The correlations on the Nusselt number can be simplified when considering asymptotic cases, as it will be shown in the following paragraphs.

4.4.1. Asymptotic cases for the vaporization Nusselt number correlation

If $Ja \rightarrow 0$, the approximation of the terms depending on the Jakob number yields simpler expressions for the parameters α and β from Eq. (14):

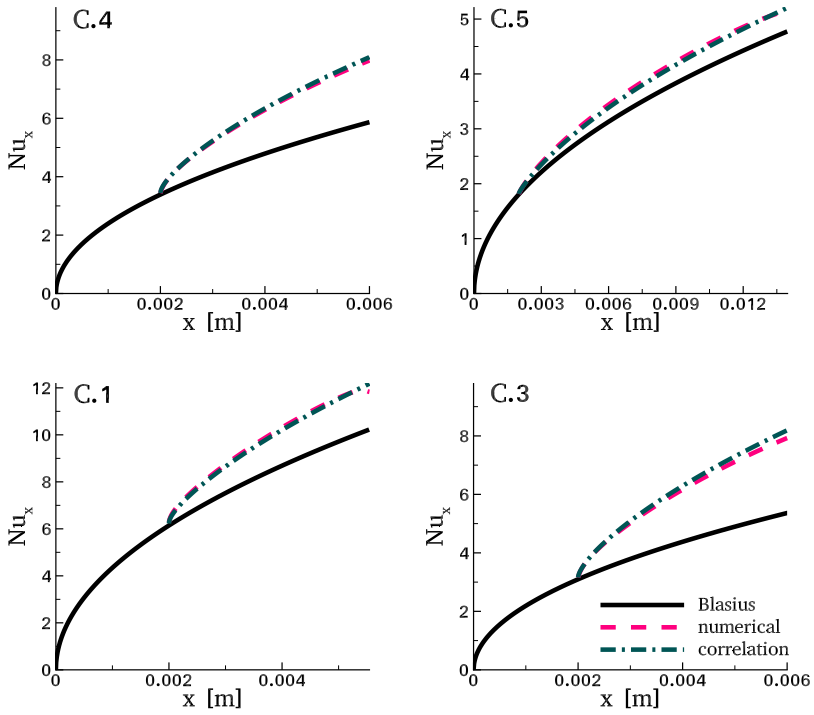

Fig. 10. Spatial evolution of the Nusselt number for different configurations extracted from Table 1 for the case involving condensation.

$$\alpha(Ja \to 0) = 0.0073Ja\left(\frac{\rho_l}{\rho_v} - 1\right)Re_{x_L}^{0.495}Pr^{0.333}$$

and

$$\beta(Ja \to 0) = 0.0005Ja\left(\frac{\rho_l}{\rho_v} - 1\right)Re_{x_L}^{0.477}Pr^{0.237}.$$

This asymptotic case brings out a linear evolution of the Nusselt number, both with the Jakob number and the density ratio, for low vaporization rate.

When $Ja = 0$, the correction terms equal to 0 as the jump condition on the velocity field is zero. Hence, the boundary layers are not modified and the expression of the Nusselt number fits simply with the one obtained with the Blasius theory.

Considering the asymptotic cases $Ja \to \infty$ or $\frac{\rho_l}{\rho_v} \to \infty$, it can be shown that in the vaporization case, the expression of the Nusselt number tends towards a saturation value:

$$Nu_x^{vap}(Ja \to \infty) \to Nu_x^{Bl} - \left(0.294Re_{x_L}^{0.495}Pr^{0.333} + 0.119Re_{x_L}^{0.4777}Pr^{0.2374}\right).$$

It can be explained by remarking that an increase of the vapor superheat tends to increase the local heat flux on the interface, and thus, the jump on the normal velocity. As this jump condition tends to thicken the thermal boundary layer and thus to decrease the local heat flux, the saturation effect results from an equilibrium state between these two antagonistic effects.

4.4.2. Asymptotic cases for the condensation Nusselt number correlation

The expression of the Nusselt number in the condensation case is now presented for a low Jakob number.

If $Ja \to 0$, Eq. (15) becomes:

$$Nu_x^{cond} \simeq Nu_x^{Bl} + \gamma\left(\frac{x}{x_L} - 1\right)^m H(x - x_L),$$

with

$$\gamma(Ja \to 0) = 0.0087Ja\left(\frac{\rho_l}{\rho_v} - 1\right)Re_{x_L}^{0.483}Pr^{0.356}$$

and

$$m(Ja \to 0) = 0.519Re_{x_L}^{-0.045}Pr^{-0.042},$$

considering

$$\eta(Ja \to 0) = 0.$$

As for the vaporization, when $Ja = 0$, the Nusselt number simply fits with the Blasius theory.

Moreover, if $Ja \to \infty$ or $\frac{\rho_l}{\rho_v} \to \infty$, an opposite trend to the one observed for vaporization is reported. In the case of condensation, the oncoming subcooled flow being aspirated towards the interface, the thickness of the thermal boundary layer is reduced. This leads to an increase of the local heat transfer as it can be visualized in Fig. 7. It is found that in the case of condensation, no saturation effect on the Nusselt number is observed neither in the numerical simulations, nor in the expression of the proposed correlation 15. This can be understood by remarking that, compared to vaporization, in the case of condensation, the jump condition on the normal velocity is of opposite direction, favoring the local heat transfer. These trends have also been observed when Figs. 6 and 7 were compared regarding to the influence of the Jakob number on the evolution of the Nusselt number.

4.5. The integrated heat flux

From the correlations on the Nusselt number one can calculate the expression of the integrated heat flux exchanged at the liquid/vapor interface.

4.5.1. Vaporization

Given the expression (eq. (14)) of the Nusselt number when vaporization happens, the heat flux per unit of width, integrated between x_L and x is defined as

$$\begin{aligned}\Phi^{vap}(x, x_L) &= \int_{x_L}^{x} \phi^{vap}(x)dx = k(T_\infty - T_{sat})\int_{x_L}^{x} \frac{Nu^{vap}(x)}{x}dx \\ &= k(T_\infty - T_{sat})\left(\int_{x_L}^{x} \frac{Nu^{Bl}(x)}{x}dx - \alpha\int_{x_L}^{x} \frac{\left(\frac{x}{x_L} - 1\right)^n}{x}dx - \beta\int_{x_L}^{x} \frac{1}{x}dx\right)\end{aligned} \tag{16}$$

The different components of eq. (16) are calculated as it follows

$$\int_{x_L}^{x} \frac{Nu^{Bl}(x)}{x}dx = 2(Nu^{Bl}(x) - Nu^{Bl}(x_L)), \tag{17}$$

$$\int_{x_L}^{x} \frac{\left(\frac{x}{x_L} - 1\right)^n}{x}dx = \frac{\left(\frac{x}{x_L}\right)^n {}_2F_1\left(-n, -n; 1 - n, \frac{x_L}{x}\right)}{n} - \pi\csc(\pi n), \tag{18}$$

where $\csc(\pi n) = \frac{1}{\sin(\pi n)}$ is the cosecant function and ${}_2F_1\left(-n, -n; 1 - n; \frac{x_L}{x}\right)$ is the Gauss hypergeometric function, defined as

$${}_2F_1(a, b; c; z) = \frac{\Gamma(c)}{\Gamma(a)\Gamma(b)}\sum_{k=0}^{\infty}\left(\frac{\Gamma(a + k)\Gamma(b + k)}{\Gamma(c + k)}\frac{z^k}{k!}\right)$$

with $\Gamma(a) = (a - 1)!$ the gamma function.

If one considers also the region $x \in (0, x_L)$ where the boundary layer is evolving without interacting with the vaporization, one will find the following expression for the heat flux per unit of width

$$\begin{aligned}\Phi(x, x_L) = \int_0^{x_L} \phi^{Bl}(x)dx + \int_{x_L}^{x} \phi^{vap}(x)dx = k(T_\infty - T_{sat})\Bigg\{2Nu^{Bl}(x) - \\ - \left[\alpha\left(\frac{\left(\frac{x}{x_L}\right)^n {}_2F_1\left(-n, -n; 1 - n, \frac{x_L}{x}\right)}{n} - \pi\csc(\pi n)\right) + \beta\ln\left(\frac{x}{x_L}\right)\right]H(x - x_L)\Bigg\}\end{aligned} \tag{19}$$

The expression (eq. (19)) of the integrated heat flux is plotted in Fig. 11. The black curve represents the integrated flux exchanged if the boundary layer evolved without interacting with the liquid vaporization. The dotted lines depict the x-evolution of the thermal flux exchanged at the liquid/vapor interface from x_L to L_x for different values of the Jakob number. As expected, the vaporization reduces the exchanged heat flux.

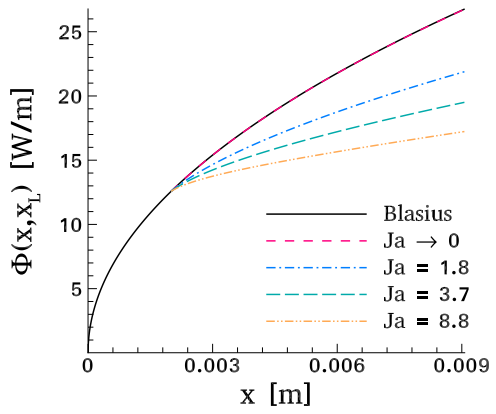

Fig. 11. The x-evolution of the integrated exchanged thermal flux at the interface for $Pr = 1.022$, $Re_{x_L} = 85.726$, $\frac{\rho_l}{\rho_v} = 17.746$ and different values of the Jakob number - vaporization configuration.

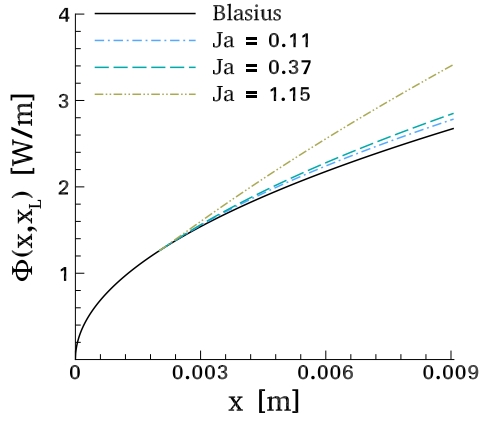

Fig. 12. The x-evolution of the integrated exchanged thermal flux at the interface for $Pr = 1.022$, $Re_{x_L} = 85.726$, $\frac{\rho_l}{\rho_v} = 17.746$ and different values of the Jakob number - condensation configuration.

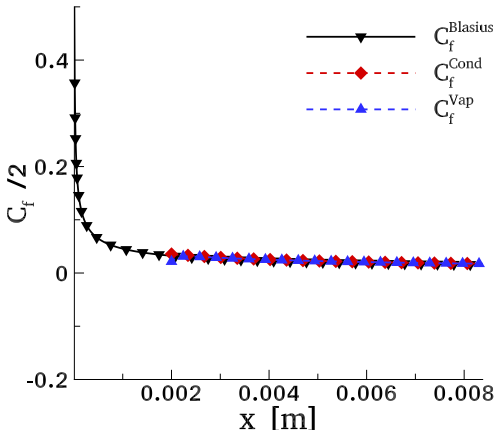

Fig. 13. Evolution of the friction coefficient for: $Pr = 1.022$, $Re_{x_L} = 85.726$, $\frac{\rho_l}{\rho_v} = 17.746$, $Ja_{vap} = 3.69$ and $Ja_{cond} = 0.369$.

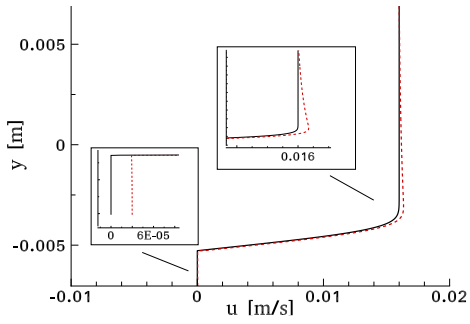

Fig. 14. Evolution of the tangential velocity u for the vaporization study case for $Pr = 1.022$, $Re_{x_L} = 85.726$, $\frac{\rho_l}{\rho_v} = 17.746$, $Ja_{vap} = 3.69$: black line - Blasius theory, red dashed line - vaporization configuration. Zoom on the liquid region (the bottom left) and on the zone close to the interface (middle right).

4.5.2. Condensation

For the configuration with condensation, the approach to calculate the exchanged heat flux is the same as for the vaporization. Considering the expression (eq. (15)) of the Nusslet number, the exchanged heat flux per unit of width is expressed as

$$\Phi(x, x_L) = \int_0^{x_L} \phi^{Bl}(x)dx + \int_{x_L}^{x} \phi^{cond}(x)dx = k(T_\infty - T_{sat})\Bigg\{2Nu^{Bl}(x)+ \\ + \left[\gamma\left(\frac{\left(\frac{x}{x_L}\right)^m {}_2F_1\left(-m,-m;1-m,\frac{x_L}{x}\right)}{m} - \pi\csc(\pi m)\right) + \eta\ln\left(\frac{x}{x_L}\right)\right]H(x - x_L)\Bigg\} \tag{20}$$

The evolution of the integrated heat flux is plotted in Fig. 12. The black curve represents the integrated flux exchanged if the boundary layer evolved without interacting with the condensation. The dotted lines depict the x-evolution of the exchanged heat flux at the liquid/vapor interface from x_L to L_x for different values of the Jakob number. The exchanged heat flux is increased by the condensation.

4.6. The influence of the phase change on the viscous friction

We now examine the influence of the liquid/vapor phase change on the viscous friction. Given the expression of the viscous tensor:

$$\bar{\bar{\tau}} = \begin{pmatrix} 2\mu\frac{\partial u}{\partial x} & \mu\left(\frac{\partial u}{\partial y} + \frac{\partial v}{\partial x}\right) \\ \mu\left(\frac{\partial u}{\partial y} + \frac{\partial v}{\partial x}\right) & 2\mu\frac{\partial v}{\partial y} \end{pmatrix}$$

we know that at the interface of normal vector $\mathbf{e}_y$, the stress vector $\mathbf{T} = \bar{\bar{\tau}}\cdot\mathbf{e}_y$ has the following normal and shear components: $\mathbf{T}\cdot\mathbf{e}_y = \mu\frac{\partial v}{\partial y}$ and $\mathbf{T}\cdot\mathbf{e}_x = \mu\left(\frac{\partial u}{\partial y} + \frac{\partial v}{\partial x}\right)$.

The friction coefficient can be determined by: $\frac{C_f}{2} = \frac{\tau_I}{\rho U_\infty^2}$ with the expression of the interfacial friction: $\tau_I = \mathbf{T}\cdot\mathbf{e}_x|_{y_I}$. We recall that for the Blasius theory the friction coefficient is $\frac{C_f^{Bl}}{2} = \frac{0.332}{\sqrt{Re_x}}$. Plotted in Fig. 13 is the evolution of the friction coefficient for the three configurations, i.e. Blasius theory, vaporization and condensation. One can see that, surprisingly, the phase change does not influence the viscous friction at the liquid/vapor interface, despite the modification of the velocity field in the vicinity of the interface.

In order to justify the relevance of this result we will further take a look at the tangential and the normal velocities at the liquid/vapor interface. For the sake of simplicity we will take only the example of the vaporization. In Fig. 14, the evolution of the tangential velocity with the Y-axis is plotted for $x = \frac{l_x}{2}$. It is noteworthy that the evolution of the tangential velocity profile in the vaporization configuration is almost identical to the Blasius boundary layer velocity profile, despite the vapor blowing in the normal direction due to phase change. The liquid motion due to the shear stress of the vapor flow on the interface is negligible (see the zoom at the bottom left of the figure). Moreover, there is little modification of the tangential velocity profile at the liquid/vapor interface (for $y = -0.005$ m) (see the zoom situated in the middle right of the graphics). As simulations showed that we can still make the assuption $\frac{\partial u}{\partial y} \gg \frac{\partial v}{\partial x}$, this explains why only marginal modifications of the interfacial friction coefficient are observed.

Plotted in Fig. 15 is the evolution of the normal velocity v and the thermal flux $\Phi = k_v\frac{\partial T}{\partial y}$ with the Y-axis for a fixed value of x. An important difference can be observed between the normal velocity from the Blasius theory and the normal velocity when the vaporization phenomenon occurs. Unlike the classical Blasius theory, where the thermal flux is induced only by conduction, in the phase change configuration there is a significant influence of the thermal convection in the transverse direction. Thereby, it can be understood that the discontinuity on the Nusselt number is induced by the jump condition on the normal velocity field.

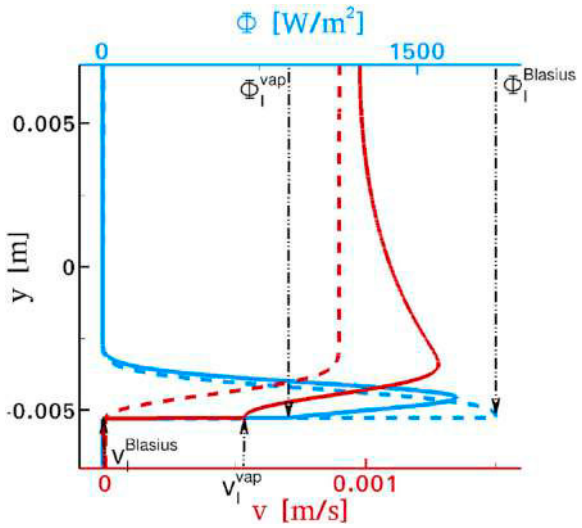

Fig. 15. Evolution of the normal velocity v and the thermal flux Φ for the vaporization study case for $Pr = 1.022$, $Re_{x_L} = 85.726$, $\frac{\rho_l}{\rho_v} = 17.746$, $Ja_{vap} = 3.69$: dashed line - Blasius theory, solid line - vaporization configuration.

5. Conclusions

Based on numerical simulations, in this paper we propose correlations on the influence of an external flow on the vaporization or condensation of a static liquid pool. It is shown that the local flow, induced by the phase change, decreases or increases, respectively, the local heat flux, depending upon vaporization or condensation is considered. For the vaporization configuration it was found that the Nusselt number, and therefore the heat transfer, decreases exponentially with the Jakob number until reaching a saturation value. The opposite trend is observed for the condensation, for which the Nusselt number increases as an exponential function of the Jakob number. Another noteworthy result is about the viscous friction on the interface, or the tangential component of the viscous tensor, which is weakly affected by the phase change in the case of a plane interface. Additionally, given the evolution of the normal velocity v with y, the influence of the phase change on the normal component of the viscous tensor is still very weak in comparison to the tangential one, as it is the case for the classical Blasius boundary layer. Moreover, even if the profiles are not superimposed, it can be qualitatively observed that the derivative $\frac{\partial v}{\partial y}$ is in the same order of magnitude with or without phase change. This is why we can conclude that the liquid vapor phase change has little influence on the components of the viscous stress vector.

Acknowledgements

The authors gratefully acknowledge the CNES and Air Liquid Advanced Technologies for the financial support of the present doctoral study. The authors gratefully acknowledge the French National Research Agency in the frame of the COALA (COndensation And Liquid Atomization) project ANR-15-CE06-0013. The authors gratefully acknowledge the CNRS (Centre National pour la Recherche Scientifique) for funding delegation to Sebastien Tanguy during the year 2017–2018.

Appendix A. Jump conditions

The liquid and the vapor phases are separated by an interface across which the phase change occurs (i.e. the liquid vaporizes into vapor or the vapor condenses into the liquid). The subscripts l and v are used to refer to the liquid and vapor phases, respectively. The interface velocity is denoted by $\mathbf{V}_\Gamma$ and $\mathbf{n}$ is the local unit vector pointing towards the liquid phase. The interface mass flux, $\dot{m}$ is obtained by using the mass conservation across the interface:

$$\dot{m} = \rho_l(\mathbf{V}_l - \mathbf{V}_\Gamma)\cdot\mathbf{n} = \rho_v(\mathbf{V}_v - \mathbf{V}_\Gamma)\cdot\mathbf{n}. \tag{A.1}$$

The jump on the velocity field across the interface can therefore be written as:

$$[\mathbf{V}]_\Gamma = \dot{m}\left[\frac{1}{\rho}\right]_\Gamma \mathbf{n}. \tag{A.2}$$

According to the second law of thermodynamics and assuming that the local equilibrium hypothesis is still valid, the interface temperature is imposed at the saturation temperature: $T_l = T_v = T_{sat}$ at the interface. Integrating Eq. (3) across the interface along with Eq. (A.1) gives the following jump condition for the energy conservation

$$[\rho h(\mathbf{V}_l - \mathbf{V}_\Gamma)\cdot\mathbf{n}]_\Gamma = [-k\nabla T\cdot\mathbf{n}]_\Gamma, \tag{A.3}$$

where the operator $[\cdot]_\Gamma$ accounts for the jump across the interface Γ and it is defined by: $[f]_\Gamma = f_v - f_l$ and h defines the enthalpy. It is assumed that h depends only on the temperature. By using Eq. (A.1), the jump condition for the energy conservation rewrites

$$\dot{m}L = [-k\nabla T\cdot\mathbf{n}]_\Gamma, \tag{A.4}$$

with $L = [h]_\Gamma$ the latent heat of phase change. Finally, integrating Eq. (2) across the interface and including the effects of surface tension leads to:

$$\left[p - \mu\frac{\partial V_n}{\partial n} + \rho(\mathbf{V}\cdot\mathbf{n} - \mathbf{V}_\Gamma\cdot\mathbf{n})^2\right]_\Gamma = \sigma\kappa, \tag{A.5}$$

which, by using Eq. (A.2), is rewritten as

$$[p]_\Gamma = \sigma\kappa + 2\left[\mu\frac{\partial V_n}{\partial n}\right]_\Gamma - \dot{m}^2\left[\frac{1}{\rho}\right]_\Gamma, \tag{A.6}$$

Appendix B. The influence of a conditioning section within the simulation domain

We have included here a graph demonstrating the validity of the inflow boundary condition. A conditioning section has been added, where the

boundary layer is spatially developing from a certain point $x = x_{L_0}$ to $x = x_L$. The phase change is plugged at x_L and we want to investigate the differences between imposing a Blasius profile at the inlet plane and simulating its development upstream. Even if the computation domain starts before the point $x = x_L$, the evolution of the Nusselt number is not affected at all in the far field and only weakly affected in the inlet vicinity, as demonstrated on the figure below.

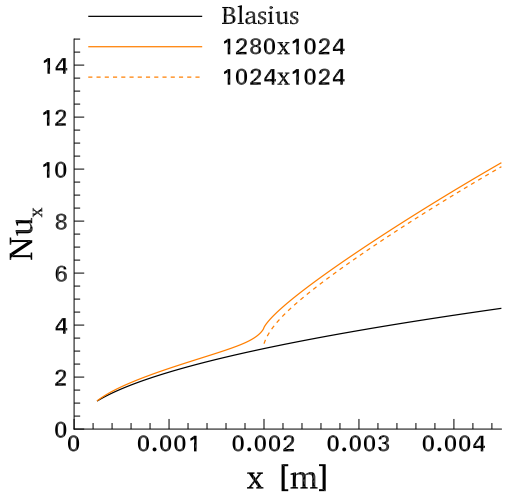

Figure B.16. Spatial evolution of the Nusselt number. Condensation configuration for: $Pr = 1.022$, $Re_{x_L} = 85.726$, $Ja = 1.15$ and $\frac{\rho_l}{\rho_v} = 17.746$.

Appendix C. Parametrical study

The purpose of the present work was to investigate the influence of liquid/vapor phase change on the Blasius theory results, particularly on the Nusselt number evolution. At first, the correction

$$Nu_x^{Bl} - Nu_x^{vap} = F\left(Re_x, Pr, Ja, \frac{\rho_l}{\rho_v}, x_L\right), \tag{C.1}$$

has been plotted.

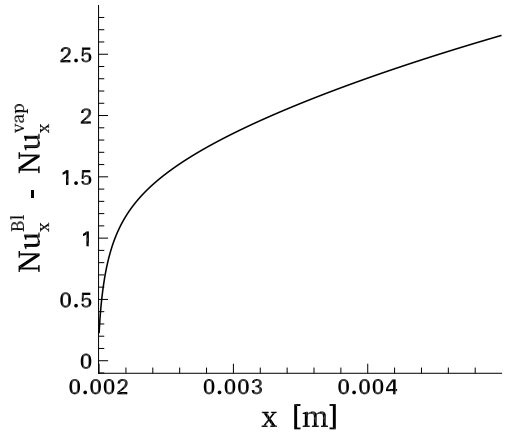

Fig. C.16. The correction on the Nusselt number from the Blasius theory with the x-axis - Vaporization configuration - dimensionless numbers: $Pr = 1.022$, $Re_{x_L} = 85.726$, $Ja = 3.69$ and $\frac{\rho_l}{\rho_v} = 17.746$.

As it can be seen in Fig. C.17, for $x = x_L$, the correction $Nu_x^{Bl} - Nu_x^{vap} \neq 0$ and it increases with x as a power function. Therefore, the Nusselt number with vaporization can be written as

$$Nu_x^{vap} = Nu_x^{Bl} - \left(\alpha\left(\frac{x}{x_L} - 1\right)^n + \beta\right)H(x - x_L), \tag{C.2}$$

where the Heaviside function $H(x - x_L)$ enables locating the phase change only for $x > x_L$.

The next step in our inquiry was to determine the evolution of the parameters α, β and n with the dimensionless numbers characterizing the configuration of interest: Reynolds number Re_{x_L}, Prandtl number Pr, Jakob number Ja and the density ratio $\frac{\rho_l}{\rho_v}$. It is noteworthy that, given the dimensionless form of Eq. (C.2), the choice of an inlet Reynolds number Re_{x_L} instead of a general Reynolds number Re_x is straightforward.

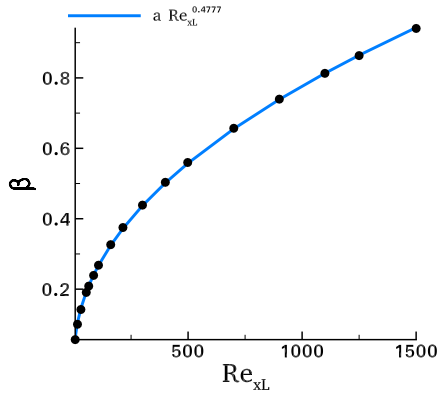

(a) Evolution with the Reynolds number and keeping fixed the dimensionless numbers: $Pr = 1.022$, $Ja = 3.69$ and $\frac{\rho_l}{\rho_v} = 17.746$. // $a(Pr, Ja, \frac{\rho_l}{\rho_v}) = 0.02866$.

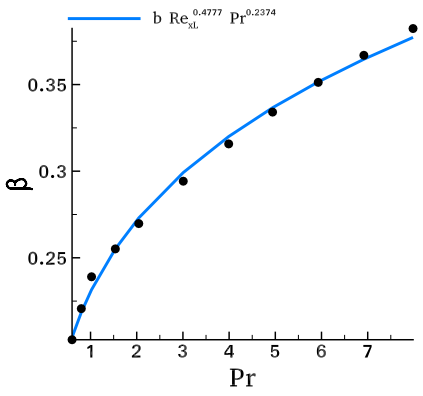

(b) Evolution with the Prandtl number and keeping fixed the dimensionless numbers: $Re_{x_L} = 85.7226$, $Ja = 3.69$ and $\frac{\rho_l}{\rho_v} = 17.746$. // $b(Ja, \frac{\rho_l}{\rho_v}) = 0.0748$.

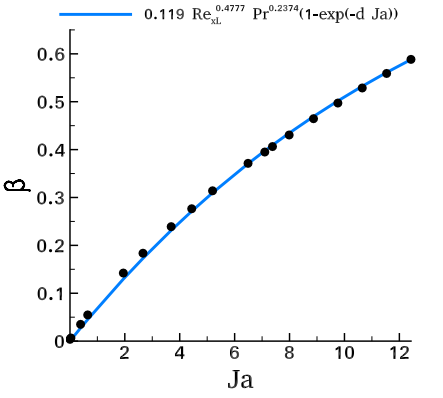

(c) Evolution with the Jakob number and keeping fixed the dimensionless numbers: $Pr = 1.022$, $Re_{x_L} = 85.7226$ and $\frac{\rho_l}{\rho_v} = 17.746$. // $d(\frac{\rho_l}{\rho_v}) = 0.07108$.

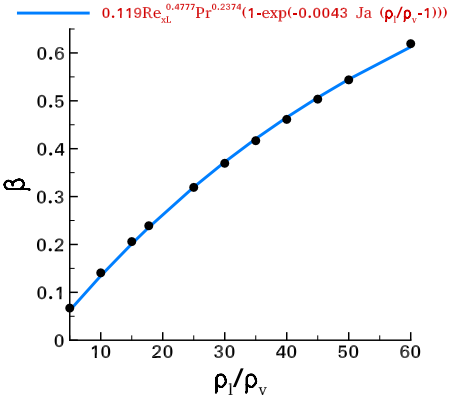

(d) Evolution with the density ratio and keeping fixed the dimensionless numbers: $Pr = 1.022$, $Re_{x_L} = 85.7226$ and $Ja = 3.69$.

Figure C.18. Evolution of the jump $\beta\left(Re_{x_L}, Pr, Ja, \frac{\rho_l}{\rho_v}\right)$ for $x = x_L$ - Vaporization configuration.

The addressed approach to determine the parameters α, β and n is developed as it follows. First, the jump β for $x = x_L$ has been examined. Its evolution with the Reynolds number Re_{x_L} (Fig. C.18a), the Prandtl number (Fig. C.18b), the Jakob number (Fig. C.18c) and finally with the density ratio (Fig. C.18d) have been plotted.

By means of a Matlab library, CFTool, one was able to obtain its evolution with the dimensionless numbers,

$$\beta = 0.119 Re_{x_L}^{0.4777} Pr^{0.2374} \left(1 - exp\left(-0.0043 Ja \left(\frac{\rho_l}{\rho_v} - 1\right)\right)\right).$$

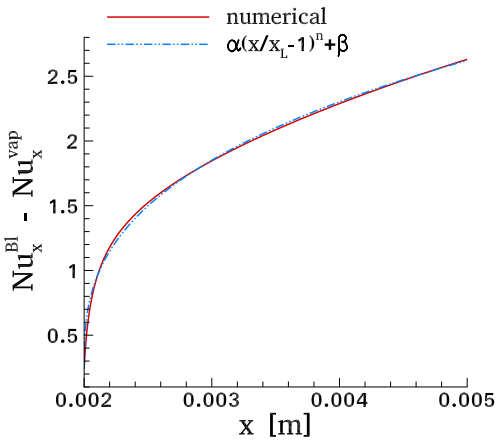

Figure C.19. Spatial evolution of the correction on the Nusselt number from the Blasius theory obtained from the numerical simulation and the function fitting its evolution: $\alpha = 2.062$ and $n = 0.3561$; β known for the corresponding couple of dimensionless numbers.

In the interest of finding the expressions of the parameters α and n from Eq. (C.2), the relation $Nu_x^{Bl} - Nu_x^{vap}$ has been plotted with the x axis for each value of dimensionless number. For example, in Fig. C.19 the evolution of $Nu_x^{Bl} - Nu_x^{vap}$ is plotted for $Re_{x_L} = 85.7226$, $Pr = 1.022$, $Ja = 3.689$, and $\frac{\rho_l}{\rho_v} = 17.746$. Conducting a full set of simulations sweeping a large range of values for the dimensionless numbers enabled us to determine the expressions of parameters α and n,

$$\alpha = 0.294 Re_{x_L}^{0.495} Pr^{0.333} \left(1 - exp\left(-0.0248 Ja \left(\frac{\rho_l}{\rho_v} - 1\right)\right)\right),$$

and

$$n = 0.9351 Re_{x_L}^{-0.11} Pr^{-0.07} Ja^{-0.1} \left(\frac{\rho_l}{\rho_v}\right)^{-0.12}.$$

Their evolution with each dimensionless number is plotted in Fig. C.20 and Fig.C.21.

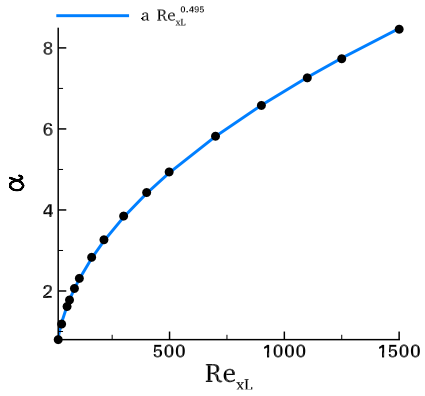

(a) Evolution with the Reynolds number and keeping fixed the dimensionless numbers: $Pr = 1.022$, $Ja = 3.69$ and $\frac{\rho_l}{\rho_v} = 17.746$. // $a(Pr, Ja, \frac{\rho_l}{\rho_v}) = 0.2271$.

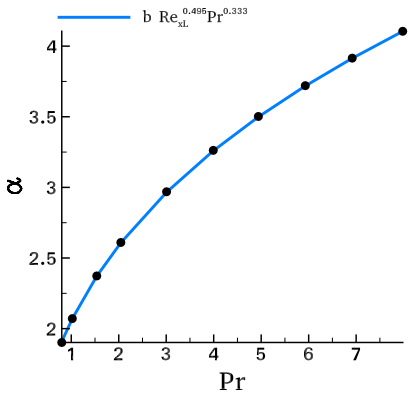

(b) Evolution with the Prandtl number and keeping fixed the dimensionless numbers: $Re_{x_L} = 85.7226$, $Ja = 3.69$ and $\frac{\rho_l}{\rho_v} = 17.746$. // $b(Ja, \frac{\rho_l}{\rho_v}) = 0.227$.

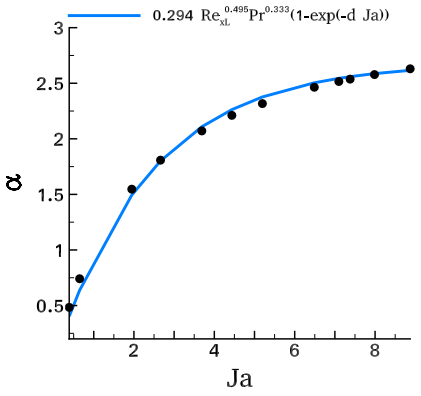

(c) Evolution with the Jakob number and keeping fixed the dimensionless numbers: $Pr = 1.022$, $Re_{x_L} = 85.7226$ and $\frac{\rho_l}{\rho_v} = 17.746$. // $d(\frac{\rho_l}{\rho_v}) = 0.4185$.

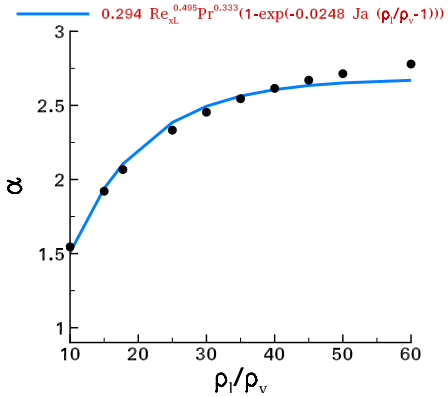

(d) Evolution with the density ratio and keeping fixed the dimensionless numbers: $Pr = 1.022$, $Re_{x_L} = 85.7226$ and $Ja = 3.69$.

Figure C.20. Evolution of the coefficient $\alpha\left(Re_{x_L}, Pr, Ja, \frac{\rho_l}{\rho_v}\right)$ for $x > x_L$ - Vaporization configuration.

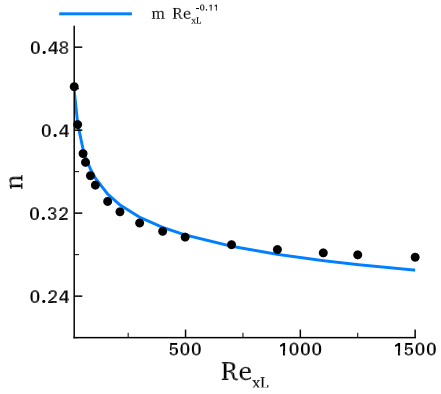

(a) Evolution with the Reynolds number and keeping fixed the dimensionless numbers: $Pr = 1.022$, $Ja = 3.69$ and $\frac{\rho_l}{\rho_v} = 17.746$. // $m(Pr, Ja, \frac{\rho_l}{\rho_v}) = 0.5879$.

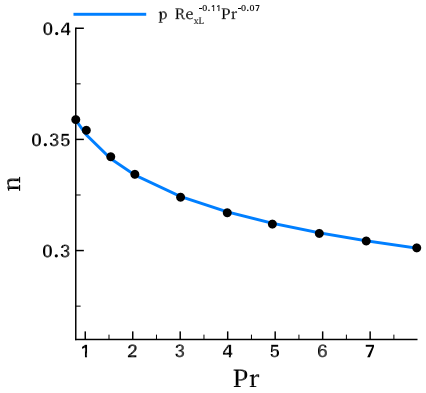

(b) Evolution with the Prandtl number and keeping fixed the dimensionless numbers: $Re_{x_L} = 85.7226$, $Ja = 3.69$ and $\frac{\rho_l}{\rho_v} = 17.746$. // $p(Ja, \frac{\rho_l}{\rho_v}) = 0.5739$.

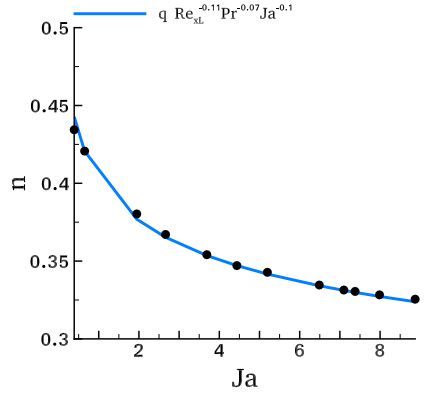

(c) Evolution with the Jakob number and keeping fixed the dimensionless numbers: $Pr = 1.022$, $Re_{x_L} = 85.7226$ and $\frac{\rho_l}{\rho_v} = 17.746$. // $q(\frac{\rho_l}{\rho_v}) = 0.6567$.

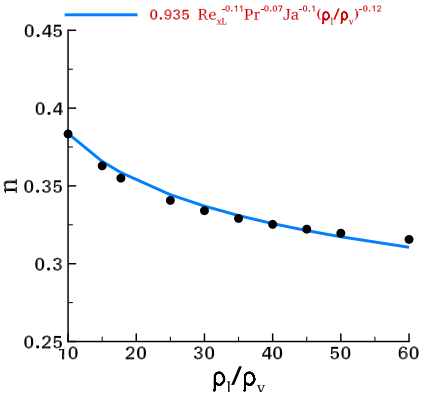

(d) Evolution with the density ratio and keeping fixed the dimensionless numbers: $Pr = 1.022$, $Re_{x_L} = 85.7226$ and $Ja = 3.69$.

Figure C.21. Evolution of the parameter $n\left(Re_{x_L}, Pr, Ja, \frac{\rho_l}{\rho_v}\right)$ for $x > x_L$ - Vaporization configuration.

References

[1] H. Blasius, Grenzschichten in Flüssigkeiten mit kleiner Reibung, Z. Math. u. Phys. 56 (1908) 1–37.
[2] R. Borges, M. Carmona, B. Costa, W. Don, An improved weighted essentially non-oscillatory scheme for hyperbolic conservation laws, J. Comput. Phys. 227 (2008) 3191–3211.
[3] P. Van, Carey. Liquid–Vapor Phase-Change Phenomena, second ed., (2008).
[4] R.D. Cess, E.M. Sparrow, Film boiling in a forced-convection boundary-layer flow, J. Heat Transf. 83 (3) (1961) 370–375.
[5] J.E. Dendy, Black box multigrid, J. Comput. Phys. 48 (1982) 366–386.
[6] R. Fedkiw, T. Aslam, B. Merriman, S. Osher, A non-oscillatory Eulerian approach to interface in multimaterial flows (The Ghost Fluid Method), J. Comput. Phys. 152 (1999) 457–492.
[7] F. Gibou, L. Chen, D. Nguyen, S. Banerjee, A level set based sharp interface method for the multiphase incompressible Navier-Stokes equations with phase change, J. Comput. Phys. 222 (2007) 536–555.
[8] F. Gibou, R. Fedkiw, L.T. Chieng, M. Kang, A second-order-accurate symmetric discretization of the Poisson equation on irregular domains, J. Comput. Phys. 176 (2002) 205–227.
[9] G. Huber, S. Tanguy, J.-C. Bra, B. Gilles, A time splitting projection scheme for compressible two-phase flows. Application to the interaction of bubbles with ultrasound waves, J. Comput. Phys. 302 (2015) 439.
[10] G. Huber, S. Tanguy, M. Sagan, C. Colin, Direct numerical simulation of nucleate pool boiling at large microscopic contact angle and moderate Jakob number, Int. J. Heat Mass Transf. 113 (2017) 662–682.
[11] N. Kaneyasu, I. Takehiro, Two-phase boundary-layer treatment of free-convection film boiling, Int. J. Heat Mass Transf. 9 (1966) 103–115.
[12] J.C.Y. Koh, Film condensation in a forced-convection boundary-layer flow, Int. J. Heat Mass Transf. 5 (1962) 941–954.
[13] J.C.Y. Koh, E.M. Sparrow, J.P. Hartnett, The two phase boundary layer in laminar film condensation, Int. J. Heat Mass Transf. 79 (1961) 69–82.
[14] B. Lalanne, N. Abi Chebel, J. Vejražka, S. Tanguy, O. Masbernat, F. Risso, Non-linear shape oscillations of rising drops and bubbles: experiments and simulations, Phys. Fluids 27 (2015) 123305.
[15] B. Lalanne, L. Rueda Villegas, S. Tanguy, F. Risso, On the computation of viscous terms for incompressible two-phase flows with level Set/Ghost Fluid Method, J. Comput. Phys. 301 (2015) 289–307.
[16] M. Lepilliez, E.-R. Popescu, F. Gibou, S. Tanguy, On two-phase flow solvers in irregular domains with contact line, J. Comput. Phys. 321 (2016) 1217–1251.
[17] P. Marmottant, E. Villermaux, On spray formation, J. Fluid Mech. 498 (2004) 73–111.
[18] J.-P. Matas, A. Delon, A. Cartellier, Shear instability of an axisymmetric air-water coaxial jet, J. Fluid Mech. 843 (2018) 575–600.
[19] D. Nguyen, R. Fedkiw, M. Kang, A boundary condition capturing method for incompressible flame discontinuities, J. Comput. Phys. 172 (2001) 71–98.
[20] S. Osher, J.A. Sethian, Fronts propagating with curvature-dependent speed: algorithms based on Hamilton-Jacobi formulations, J. Comput. Phys. 2 (1988) 12–49.
[21] E. Pohlhausen Der, Wärmeaustausch zwischen festen Körpern und Flüssigkeiten mit kleiner Reibung und kleiner Wärmeleitung, Z. Angew. Math. Mech. 1 (1921) 115–121.
[22] L. Prandtl, über Flüssigkeitsbewegung bei sehr kleiner Reibung, Proc. 3rd Intern. Math. Congr. Heidelberg, 1904, p. 484.
[23] M. Renksizbulut, M.C. Yuen, Experimental study of droplet evaporation in a high temperature stream, J. Heat Transf. 105 (1983) 384–388.
[24] M. Renksizbulut, M.C. Yuen, Numerical study of droplet evaporation in a high temperature stream, J. Heat Transf. 105 (1983) 389–397.

[25] E. Ruckenstein, E.J. Davis, The effects of bubble translation of vapor bubble growth in a superheated liquid, Int. J. Heat Mass Transf. 14 (1971) 939–952.
[26] L. Rueda-Villegas, S. Tanguy, G. Castanet, O. Caballina, F. Lemoine, Direct numerical simulation of the impact of a droplet onto a hot surface above the leidenfrost temperature, Int. J. Heat Mass Transf. 104 (2017) 1090–1109.
[27] L.E. Scriven, On the dynamics of phase growth, Chem. Eng. Sci. 10 (1959) 1–13.
[28] D.B. Spalding, Combustion and Mass Transfer: a Textbook with Multiple-Choice Exercices for Engineering Students, Pergamon Press, Oxford; New York, 1979.
[29] S. Tanguy, A. Berlemont, Application of a level set method for simulation of droplet collisions, Int. J. Multiph. Flow 31 (2005) 1015–1035.
[30] S. Tanguy, T. Menard, A. Berlemont, A level set method for vaporizing two-phase flows, J. Comput. Phys. 221 (2007) 837–853.
[31] S. Tanguy, M. Sagan, B. Lalanne, F. Couderc, C. Colin, Benchmarks and numerical methods for the simulation of boiling flows, J. Comput. Phys. 264 (2014) 1–22.
[32] M. Turkyilmazoglu, Stefan problems for moving phase change materials and multiple solutions, Int. J. Therm. Sci. 126 (2018) 67–73.
[33] A. Urbano, S. Tanguy, G. Huber, C. Colin, Direct numerical simulation of nucleate boiling in micro-layer regime, Int. J. Heat Mass Transf. 123 (2018) 1128–1137.
[34] L. Rueda Villegas, R. Alis, M. Lepilliez, S. Tanguy, A Ghost Fluid/Level Set Method for boiling flows and liquid evaporation: application to the leidenfrost effect, J. Comput. Phys. 316 (2016) 789–813.
[35] W.-M. Yan, C.-Y. Soong, Convective heat and mass transfer along an inclined heated plate with film evaporation, Int. J. Heat Mass Transf. 38 (1995) 1261–1269.

Bibliography

[1] R. Alis. *Simulation numérique directe de gouttes et de groupes de gouttes qui s'évaporent dans un écoulement laminaire ou turbulent.* PhD thesis, Université Fédérale Toulouse Midi-Pyrénées, 2019.

[2] G. Araya and L. Castillo. Dns of turbulent thermal boundary layers up to reθ= 2300. *International Journal of Heat and Mass Transfer*, 55(15-16):4003–4019, 2012.

[3] T. D. Aslam. A partial differential equation approach to multidimensional extrapolation. *Journal of Computational Physics*, 193(1):349–355, 2004.

[4] G.K. Batchelor. Heat transfer by free convection across a closed cavity between vertical boundaries at different temperatures. *Quarterly of Applied Mathematics*, 12(3):209–233, 1954.

[5] A. Bejan. *Convection heat transfer.* John wiley & sons, 1984.

[6] D.M. Bell and J.H. Ferziger. Turbulent boundary layer dns with passive scalars. *Near-Wall Turbulent Flows*, pages 327–336, 1993.

[7] A. Benkenida. *Développement et validation d'une méthode de simulation d'écoulements diphasiques sans reconstruction d'interfaces: application à la dynamique des bulles de Taylor.* PhD thesis, Toulouse, INPT, 1999.

[8] H. Blasius. Grenzschichten in flüssigkeiten mit kleiner reibung. *Z. Math. u. Phys.*, 56:1–37, 1908.

[9] T. Bonometti. *Développement d'une méthode de simulation d'écoulements à bulles et à gouttes.* PhD thesis, 2005.

[10] R.l Borges, M. Carmona, B. Costa, and W. S. Don. An improved weighted essentially non-oscillatory scheme for hyperbolic conservation laws. *Journal of Computational Physics*, 227(6):3191–3211, 2008.

[11] J. U. Brackbill, D. B. Kothe, and C. Zemach. A continuum method for modeling surface tension. *Journal of computational physics*, 100(2):335–354, 1992.

[12] R. D. Cess and E. M. Sparrow. Film boiling in a forced-convection boundary-layer flow. *Journal of Heat Transfer*, 83(3):370–375, 1961.

[13] P. Chassaing. *Turbulence en mécanique des fluides.* Cépaduès, 2000.

[14] I.-L. Chern, J. Glimm, O. McBryan, B. Plohr, and S. Yaniv. Front tracking for gas dynamics. *Journal of Computational Physics*, 62(1):83–110, 1986.

[15] A. J. Chorin. Numerical solution of the Navier-Stokes equations. *Mathematics of Computation*, 22(104):745–762, 1968.

[16] D. Coles. The law of the wake in the turbulent boundary layer. *Journal of Fluid Mechanics*, 1(2):191–226, 1956.

[17] B. J. Daly. Numerical study of two fluid rayleigh-taylor instability. *Physics of Fluids*, 10(2):297–307, 1967.

[18] D. S. Dandy and L. G. Leal. Buoyancy-driven motion of a deformable drop through a quiescent liquid at intermediate reynolds numbers. *Journal of Fluid Mechanics*, 208:161–192, 1989.

[19] V. Daru, P. Le Quéré, M.-C. Duluc, and O. Le Maitre. A numerical method for the simulation of low mach number liquid–gas flows. *Journal of Computational Physics*, 229(23):8844–8867, 2010.

[20] D. B. De Graaff and J. K. Eaton. Reynolds-number scaling of the flat-plate turbulent boundary layer. *Journal of Fluid Mechanics*, 422:319–346, 2000.

[21] S. Dellacherie. Numerical resolution of a potential diphasic low mach number system. *Journal of Computational Physics*, 223(1):151–187, 2007.

[22] J.E. Dendy. Black box multigrid. *Journal of Computational Physics*, 48(3):366–386, 1982.

[23] R. P. Fedkiw, T. Aslam, B. Merriman, and S. Osher. A non-oscillatory Eulerian approach to interfaces in multimaterial flows (the ghost fluid method). *Journal of Computational Physics*, 152(2):457–492, 1999.

[24] A. Ferrante and S. Elghobashi. On the physical mechanisms of drag reduction in a spatially developing turbulent boundary layer laden with microbubbles. *Journal of Fluid Mechanics*, 503:345–355, 2004.

[25] P. Germain. Cours de mécanique de l'école polytechnique. *Ellipses, Paris*, 1986.

[26] F. Gibou, L. Chen, D. Nguyen, and S. Banerjee. A level set based sharp interface method for the multiphase incompressible navier–stokes equations with phase change. *Journal of Computational Physics*, 222(2):536–555, 2007.

[27] F. Gibou, R. P. Fedkiw, L.-T. Cheng, and M. Kang. A second-order-accurate symmetric discretization of the poisson equation on irregular domains. *Journal of Computational Physics*, 176(1):205–227, 2002.

[28] J. Glimm, C. Klingenberg, O. McBryan, B. Plohr, D. Sharp, and S. Yaniv. Front tracking and two-dimensional riemann problems. *Advances in Applied Mathematics*, 6(3):259–290, 1985.

[29] D. Gueyffier, J. Li, A. Nadim, R. Scardovelli, and S. Zaleski. Volume-of-fluid interface tracking with smoothed surface stress methods for three-dimensional flows. *Journal of Computational physics*, 152(2):423–456, 1999.

[30] F. H. Harlow and J. E. Welch. Numerical calculation of time-dependent viscous incompressible flow of fluid with free surface. *Physics of Fluids*, 8(12):2182–2189, 1965.

[31] H. Hattori, T. Houra, and Y. Nagano. Direct numerical simulation of stable and unstable turbulent thermal boundary layers. *International Journal of Heat and Fluid Flow*, 28(6):1262–1271, 2007.

[32] J Hinze. 0. 1975 turbulence, 1959.

[33] C. W. Hirt and B. D. Nichols. Volume of fluid (vof) method for the dynamics of free boundaries. *Journal of Computational Physics*, 39(1):201–225, 1981.

[34] G. Huber, S. Tanguy, J.-C. Béra, and B. Gilles. A time splitting projection scheme for compressible two-phase flows. application to the interaction of bubbles with ultrasound waves. *Journal of Computational Physics*, 302:439–468, 2015.

[35] M. Ida. An improved unified solver for compressible and incompressible fluids involving free surfaces. part i. convection. *Computer Physics Communications*, 132(1-2):44–65, 2000.

[36] Y. Iritani, N. Kasagi, and M. Hirata. Heat transfer mechanism and associated turbulence structure in the near-wall region of a turbulent boundary layer. In *Turbulent Shear Flows 4*, pages 223–234. Springer, 1985.

[37] N. Jarrin. *Synthetic inflow boundary conditions for the numerical simulation of turbulence*. PhD thesis, University of Manchester, 2008.

[38] N. Jarrin, S. Benhamadouche, D. Laurence, and R. Prosser. A synthetic-eddy-method for generating inflow conditions for large-eddy simulations. *International Journal of Heat and Fluid Flow*, 27(4):585–593, 2006.

[39] J. Jeong, F. Hussain, W. Schoppa, and J. Kim. Coherent structures near the wall in a turbulent channel flow. *Journal of Fluid Mechanics*, 332:185–214, 1997.

[40] J. Jiménez, S. Hoyas, M. P. Simens, and Y. Mizuno. Turbulent boundary layers and channels at moderate reynolds numbers. *Journal of Fluid Mechanics*, 657:335–360, 2010.

[41] S. Y. Kadioglu, M. Sussman, S. Osher, J. P. Wright, and M. Kang. A second order primitive preconditioner for solving all speed multi-phase flows. *Journal of computational physics*, 209(2):477–503, 2005.

[42] N. Kaneyasu and I. Takehiro. Two-phase boundary-layer treatment of free-convection film boiling. *International Journal of Heat and Mass Transfer*, 9(2):103–115, 1966.

[43] M. Kang, R. P. Fedkiw, and X.-D. Liu. A boundary condition capturing method for multiphase incompressible flow. *Journal of Scientific Computing*, 15(3):323–360, 2000.

[44] W. M. Kays and M. E. Crawford. *Convective heat and mass transfert*. Number BOOK. McGraw-Hill, 1993.

[45] A. Keating, U. Piomelli, E. Balaras, and H.-J. Kaltenbach. A priori and a posteriori tests of inflow conditions for large-eddy simulation. *Physics of fluids*, 16(12):4696–4712, 2004.

[46] M. Klein, A. Sadiki, and J. Janicka. A digital filter based generation of inflow data for spatially developing direct numerical or large eddy simulations. *Journal of computational Physics*, 186(2):652–665, 2003.

[47] J. C. Y. Koh. Film condensation in a forced-convection boundary-layer flow. *International Journal of Heat and Mass Transfer*, 5(10):941–954, 1962.

[48] J. C. Y. Koh, E. M. Sparrow, and J. P. Hartnett. The two phase boundary layer in laminar film condensation. *International Journal of Heat and Mass Transfer*, 2(1-2):69–82, 1961.

[49] H. Kong, H. Choi, and J. S. Lee. Direct numerical simulation of turbulent thermal boundary layers. *Physics of Fluids*, 12(10):2555–2568, 2000.

[50] N. Kwatra, J. Su, J. T. Grétarsson, and R. Fedkiw. A method for avoiding the acoustic time step restriction in compressible flow. *Journal of Computational Physics*, 228(11):4146–4161, 2009.

[51] B. Lafaurie, C. Nardone, R. Scardovelli, S. Zaleski, and G. Zanetti. Modelling merging and fragmentation in multiphase flows with surfer. *Journal of Computational Physics*, 113(1):134–147, 1994.

[52] B. Lalanne, L. R. Villegas, S. Tanguy, and F. Risso. On the computation of viscous terms for incompressible two-phase flows with Level Set/Ghost Fluid Method. *Journal of Computational Physics*, 301:289–307, 2015.

[53] H. Le, P. Moin, and J. Kim. Direct numerical simulation of turbulent flow over a backward-facing step. *Journal of fluid mechanics*, 330:349–374, 1997.

[54] P. Le Quéré, R. Masson, and P. Perrot. A chebyshev collocation algorithm for 2d non-boussinesq convection. *Journal of computational physics*, 103(2):320–335, 1992.

[55] P. Le Quéré, C. Weisman, H. Paillère, J. Vierendeels, E. Dick, R. Becker, M. Braack, and J. Locke. Modelling of natural convection flows with large temperature differences: a benchmark problem for low mach number solvers. part 1. reference solutions. *ESAIM: Mathematical Modelling and Numerical Analysis*, 39(3):609–616, 2005.

[56] M. Lepilliez. *Simulation numérique des ballotements d'ergols dans les réservoirs de satellites en microgravité et à faible nombre de Bond*. PhD thesis, Université Paul Sabatier-Toulouse III, 2015.

[57] M. Lepilliez, E. R. Popescu, F. Gibou, and S. Tanguy. On two-phase flow solvers in irregular domains with contact line. *Journal of Computational Physics*, 321:1217–1251, 2016.

[58] D. Li, K. Luo, and J. Fan. Direct numerical simulation of heat transfer in a spatially developing turbulent boundary layer. *Physics of Fluids*, 28(10):105104, 2016.

[59] Q. Li, P. Schlatter, L. Brandt, and D. S. Henningson. Dns of a spatially developing turbulent boundary layer with passive scalar transport. *International Journal of Heat and Fluid Flow*, 30(5):916–929, 2009.

[60] K. Liu and R. H. Pletcher. Inflow conditions for the large eddy simulation of turbulent boundary layers: a dynamic recycling procedure. *Journal of Computational Physics*, 219(1):1–6, 2006.

[61] X.-D. Liu, R. P. Fedkiw, and M. Kang. A boundary condition capturing method for Poisson's equation on irregular domains. *Journal of Computational Physics*, 160(1):151–178, 2000.

[62] T. S. Lund, X. Wu, and K. D. Squires. Generation of turbulent inflow data for spatially-developing boundary layer simulations. *Journal of computational physics*, 140(2):233–258, 1998.

[63] S. P. MacLachlan, J. M. Tang, and C. Vuik. Fast and robust solvers for pressure-correction in bubbly flow problems. *Journal of Computational Physics*, 227(23):9742–9761, 2008.

[64] P. Marmottant and E. Villermaux. On spray formation. *Journal of fluid mechanics*, 498:73–111, 2004.

[65] J.-P. Matas, A. Delon, and A. Cartellier. Shear instability of an axisymmetric air–water coaxial jet. *Journal of Fluid Mechanics*, 843:575–600, 2018.

[66] I.V. Miroshnichenko and M.A. Sheremet. Turbulent natural convection heat transfer in rectangular enclosures using experimental and numerical approaches: A review. *Renewable and Sustainable Energy Reviews*, 82:40–59, 2018.

[67] D. Q. Nguyen, R. P. Fedkiw, and M. Kang. A boundary condition capturing method for incompressible flame discontinuities. *Journal of Computational Physics*, 172(1):71–98, 2001.

[68] W. F. Noh and P. Woodward. Slic (simple line interface calculation). In *Proceedings of the fifth international conference on numerical methods in fluid dynamics June 28–July 2, 1976 Twente University, Enschede*, pages 330–340. Springer, 1976.

[69] S. Osher and J. A. Sethian. Fronts propagating with curvature-dependent speed: algorithms based on hamilton-jacobi formulations. *Journal of Computational Physics*, 79(1):12–49, 1988.

[70] H. Paillère, P. Le Quéré, C. Weisman, J. Vierendeels, E. Dick, M. Braack, F. Dabbene, A. Beccantini, E. Studer, T. Kloczko, et al. Modelling of natural convection flows with large temperature differences: a benchmark problem for low mach number solvers. part 2. contributions to the june 2004 conference. *ESAIM: Mathematical Modelling and Numerical Analysis*, 39(3):617–621, 2005.

[71] M. Pamies. *Contrôle d'une couche limite turbulente au moyen d'un micro-sytème distribué*. PhD thesis, Lille 1, 2008.

[72] M. Pamiès, P.-E. Weiss, E. Garnier, S. Deck, and P. Sagaut. Generation of synthetic turbulent inflow data for large eddy simulation of spatially evolving wall-bounded flows. *Physics of Fluids*, 21(4):045103, 2009.

[73] S. Pandey, Y. G. Park, and M. Y. Ha. An exhaustive review of studies on natural convection in enclosures with and without internal bodies of various shapes. *International Journal of Heat and Mass Transfer*, 138:762–795, 2019.

[74] A.E. Perry and P.H. Hoffmann. An experimental study of turbulent convective heat transfer from a flat plate. *Journal of Fluid Mechanics*, 77(2):355–368, 1976.

[75] E. Pohlhausen. Der wärmeaustausch zwischen festen körpern und flüssigkeiten mit kleiner reibung und kleiner wärmeleitung. *ZAMM-Journal of Applied Mathematics and Mechanics/Zeitschrift für Angewandte Mathematik und Mechanik*, 1(2):115–121, 1921.

[76] S. B. Pope. *Turbulent flows*. Cambridge University Press, 2000.

[77] E.-R. Popescu, S. Tanguy, and C. Colin. On the influence of liquid/vapor phase change onto the nusselt number of a laminar superheated or subcooled vapor flow. *International Journal of Thermal Sciences*, 140:397–412, 2019.

[78] S. Popinet. An accurate adaptive solver for surface-tension-driven interfacial flows. *Journal of Computational Physics*, 228(16):5838–5866, 2009.

[79] L. Prandtl. Über flussigkeitsbewegung bei sehr kleiner reibung. *Verhandl. III, Internat. Math.-Kong., Heidelberg, Teubner, Leipzig, 1904*, pages 484–491, 1904.

[80] E. G. Puckett, A. S. Almgren, J. B. Bell, D. L Marcus, and W. J. Rider. A high-order projection method for tracking fluid interfaces in variable density incompressible flows. *Journal of Computational Physics*, 130(2):269–282, 1997.

[81] S. Rawat, A. Chouippe, R. Zamansky, D. Legendre, and E. Climent. Drag modulation in turbulent boundary layers subject to different bubble injection strategies. *Computers & Fluids*, 178:73–87, 2019.

[82] M. Renksizbulut and M. C. Yuen. Experimental study of droplet evaporation in a high-temperature air stream. *Journal of heat transfer*, 105(2):384–388, 1983.

[83] M. Renksizbulut and M. C. Yuen. Numerical study of droplet evaporation in a high-temperature stream. *Journal of Heat transfer*, 105(2):389–397, 1983.

[84] O. Reynolds. Xxix. an experimental investigation of the circumstances which determine whether the motion of water shall be direct or sinuous, and of the law of resistance in parallel channels. *Philosophical Transactions of the Royal society of London*, (174):935–982, 1883.

[85] W. J. Rider and D. B. Kothe. Reconstructing volume tracking. *Journal of Computational Physics*, 141(2):112–152, 1998.

[86] S. K. Robinson. Coherent motions in the turbulent boundary layer. *Annual Review of Fluid Mechanics*, 23(1):601–639, 1991.

[87] E. Ruckenstein and E. J. Davis. The effects of bubble translation on vapor bubble growth in a superheated liquid. *International Journal of Heat and Mass Transfer*, 14(7):939–952, 1971.

[88] L. Rueda Villegas. *Simulation numérique directe de l'effet Leidenfrost*. PhD thesis, École Doctorale Mécanique, Énergétique, Génie civil et Procédés (Toulouse . . . , 2013.

[89] G. Ryskin and L.G. Leal. Numerical solution of free-boundary problems in fluid mechanics. part 2. buoyancy-driven motion of a gas bubble through a quiescent liquid. *Journal of Fluid Mechanics*, 148:19–35, 1984.

[90] R. Saurel and R. Abgrall. A multiphase godunov method for compressible multifluid and multiphase flows. *Journal of Computational Physics*, 150(2):425–467, 1999.

[91] R. Scardovelli and S. Zaleski. Direct numerical simulation of free-surface and interfacial flow. *Annual Review of Fluid Mechanics*, 31(1):567–603, 1999.

[92] H. Schlichting et al. *Boundary-layer theory*. Springer, 1974.

[93] J.U. Schlüter, H. Pitsch, and P. Moin. Large-eddy simulation inflow conditions for coupling with reynolds-averaged flow solvers. *AIAA journal*, 42(3):478–484, 2004.

[94] L. E. Scriven. On the dynamics of phase growth. *Chemical engineering science*, 10(1-2):1–13, 1959.

[95] P. R. Spalart. Direct simulation of a turbulent boundary layer up to r θ= 1410. *Journal of fluid mechanics*, 187:61–98, 1988.

[96] P. R. Spalart and J. H. Watmuff. Experimental and numerical study of a turbulent boundary layer with pressure gradients. *Journal of Fluid Mechanics*, 249:337–371, 1993.

[97] P.R. Spalart, M. Strelets, and A. Travin. Direct numerical simulation of large-eddy-break-up devices in a boundary layer. *International Journal of Heat and Fluid Flow*, 27(5):902–910, 2006.

[98] D. B. Spalding. *Combustion and mass transfer: a textbook with multiple-choice exercises for engineering students*. Elsevier, 2013.

[99] M. Sussman, P. Smereka, and S. Osher. A level set approach for computing solutions to incompressible two-phase flow. *Journal of Computational physics*, 114(1):146–159, 1994.

[100] M. Sussman, K. M. Smith, M. Y Hussaini, M. Ohta, and R. Zhi-Wei. A sharp interface method for incompressible two-phase flows. *Journal of computational physics*, 221(2):469–505, 2007.

[101] S. Tanguy, T. Ménard, and A. Berlemont. A level set method for vaporizing two-phase flows. *Journal of Computational Physics*, 221(2):837–853, 2007.

[102] S. Tanguy, M. Sagan, B. Lalanne, F. Couderc, and C. Colin. Benchmarks and numerical methods for the simulation of boiling flows. *Journal of Computational Physics*, 264:1–22, 2014.

[103] H. Tennekes, J. L. Lumley, et al. *A first course in turbulence*. MIT press, 1972.

[104] A.A. Townsend. Equilibrium layers and wall turbulence. *Journal of Fluid Mechanics*, 11(1):97–120, 1961.

[105] S. O. Unverdi and G. Tryggvason. A front-tracking method for viscous, incompressible, multi-fluid flows. *Journal of Computational Physics*, 100(1):25–37, 1992.

[106] X. Wu. Inflow turbulence generation methods. *Annual Review of Fluid Mechanics*, 49:23–49, 2017.

[107] X. Wu and P. Moin. Transitional and turbulent boundary layer with heat transfer. *Physics of Fluids*, 22(8):085105, 2010.

[108] Z.-T. Xie and I. P. Castro. Efficient generation of inflow conditions for large eddy simulation of street-scale flows. *Flow, turbulence and combustion*, 81(3):449–470, 2008.

[109] W.-M. Yan and C.-Y. Soong. Convective heat and mass transfer along an inclined heated plate with film evaporation. *International Journal of Heat and Mass Transfer*, 38(7):1261–1269, 1995.

[110] D.L. Youngs. *Numerical Method for Fluid Dynamics*. Academic Press, 1982, ch. Time-dependent multi-material flow with large fluid distortion, pp. 273-285.

[111] H. Zhao, A. Wei, K. Luo, and J. Fan. Direct numerical simulation of turbulent boundary layer with heat transfer. *International Journal of Heat and Mass Transfer*, 99:10–19, 2016.